Understanding and ameliorating late-effects in childhood medulloblastoma survivors

Jemma Castle

A thesis submitted in part requirement for the degree of Doctor of Philosophy

Wolfson Childhood Cancer Research Centre

Newcastle University Centre for Cancer

Clinical and Translation Research Institute

Faculty of Medical Science

Newcastle University

September 2024

Declaration

I certify that no part of the material documented in this thesis has previously been submitted for a degree or other qualification in this or any other university. I declare that this thesis represents my own unaided work, carried out by myself, except where it is acknowledged otherwise in the thesis text.

Jemma Castle

September 2024

Acknowledgments

I would like to express my sincere gratitude to my PhD supervisors Dr Debbie Hicks, Dr Satomi Miwa and Professor Roderick Skinner for their invaluable guidance and support throughout my PhD.

My gratitude also goes out to my progression panel, Prof Anthony Moorman and Dr Jason Gill, for their valued input and advice throughout my PhD.

I would also like to thank past and present members of the Paediatric Brain Tumour Group for their input, guidance and contributions to this work. In particular, Dr Dean Thompson and Dr Alistair Poll for their assistance with bioinformatics data processing.

Furthermore, I am grateful to Dr Edward Fielder for his help and guidance with the *in vivo* assessments. Finally, thank you to the mice involved in this research (I appreciate you not biting me!).

Abstract

Medulloblastoma (MB) is the most common malignant paediatric brain tumour, with 5-year survival rates over 70%. Survivors frequently suffer a wide variety of late-effects due to their tumour and its multi-modal treatment: tumour resection, chemotherapy and craniospinal radiotherapy with posterior fossa boost (PFB). Treatment induces deleterious late-effects through damage to normal tissues and increases the risk of neurocognitive impairment, endocrine impairment, ototoxicity, secondary tumours, cardiotoxicity, poor physical function and premature ageing/frailty. Sadly, approaches to ameliorate treatment-induced late-effects are lacking; a paucity of appropriate model systems hinders their development. This thesis aims to develop clinically-relevant models of MB treatment to enable investigation of the biological mechanisms that underpin late-effect onset, and facilitate the appraisal of interventions.

To recapitulate childhood medulloblastoma radiotherapy and late-effect profile *in vivo,* age-equivalent mice received CT image-guided, human-equivalent cranial radiotherapy (CRT) or CRT+PFB and were longitudinally assessed for over 1 year. Following CRT, mice were significantly more frail, had reduced physical functioning and exhibited neurocognitive deficits. Receipt of PFB did not induce a more severe late-effect profile. The biological underpinnings of radiation-induced late-effects were explored, *ex vivo*. Assessment of transcriptional modifications 1 year post-irradiation, via RNA-sequencing, showed CRT did not induce consistent global changes, instead pathways including interferon-α/γ and epithelial-mesenchymal-transition were downregulated. Quantification of pro-inflammatory proteins, using immunohistochemistry, showed higher abundance following CRT, though response was not dose-dependent. Altered DNA methylation patterns are associated with premature ageing. Utilising a prebuilt epigenetic-clock, predicted age increased with chronological age, though this was more accurate in DNA from peripheral blood than brain tissue. CRT did not induce a significantly accelerated epigenetic age. To understand acute response to radiation-insult, human-equivalent radiation was delivered *in* vitro and the Luminex assay was utilised to develop a novel, multi-analyte assessment of molecular insult response to MB-equivalent radiation. Markers of inflammation increased 1 hour post-irradiation, and typically increased further at 48 hours. Increased inflammation was expected and is thought to play a major role in the development of radiation-induced late effects. To provide a baseline model for future investigation of chemotherapy-induced late-effects, a close-MB chemotherapy regimen was

developed *in vivo* that replicated the popular Packer-style chemotherapy. The development of clinically-relevant, treatment-induced late-effect models enables the elucidation of novel/target mechanisms underpinning MB late-effects and the development of novel interventions for their amelioration.

Abbreviations

ADHD	Attention deficit hyperactivity disorder
ALL	Acute lymphoblastic leukaemia
AT/RT	Atypical teratoid/rhabdoid tumours
BBB	Blood-brain barrier
BRIEF	Behaviour Rating Inventory of Executive function
CCNU	Lomustine
CCSS	Childhood Cancer Survivor Study
CCSs	Childhood cancer survivors
CIPN	Chemotherapy-induced peripheral neuropathy
CLA	Classical histology
CNS	Central nervous system
CpG	Cytosine-phosphate-guanine
CRT	Cranial radiation
CSF	Cerebrospinal fluid
CSI	Craniospinal irradiation
CT	Computed tomography
DEGs	Differentially expressed genes
DI	Discrimination index
DLT	Dose limiting toxicities
DN	Desmoplastic nodular histology
DNA	Deoxyribonucleic acid
dsDNA	double-stranded DNA
EAA	Epigenetic age acceleration
ECM	Extra-cellular matrix
EQD2	Equivalent dose in 2 Gy fractions
ex vivo	Outside the living body
FA	Fractional Anisotropy
FI	Frailty index
FSIQ	Full Scale Intelligence Quotient
GH	Growth hormone
GSEA	Gene Set Enrichment Analysis

Gy	Gray
HPG	Hypothalamus-pituitary-gonadal
HPT	Hypothalamus-pituitary-thyroid
HR	High-risk
HUI	Health Utilities Index
IHC	Immunohistochemistry
in silico	Within a computer
in vitro	Within the glass
in vivo	Within the living body
IP	Intraperitoneal
iPSCs	Induced pluripotent stem cells
IQ	Intelligence quotient
IV	Intravenous
LASA	Laboratory Animal Science Association
LCA	Large cell/anaplastic histology
LFS	Li-Fraumeni syndrome
LTM	Long-term memory
M.O.M	Mouse-on-mouse
M+	Metastatic disease
M0	Non-metastatic disease
MB	Medulloblastoma
MBEN	Medulloblastoma with extensive nodularity histology
MB_{Grp3}	MB group 3
MB_{Grp4}	MB group 4
MB_{SHH}	MB sonic hedgehog group
MB_{WNT}	MB wingless group
MEES	Medical, Educational, Employment and Social Questionnaire
MRI	Magnetic resonance imaging
MTD	Maximum tolerated dose
NC	Neurocognitive
NL	Neurological
NTR	near-total resection
PCA	Principal Component Analysis

PedsQL	Pediatric Quality of Life Inventory
PFB	Poster fossa boost
PFS	Posterior Fossa Syndrome
PL	Primary latency
~PND	Approximate postnatal days
PR	Perceptual reasoning
PS	Processing Speed
QoL	Quality of life
QoS	Quality of survivorship
RIN	RNA integrity number
RNA	Ribonucleic acid
RNAseq	RNA sequencing
ROS	Reactive oxygen species
rpm	Revolutions per minute
SARRP	Small animal radiation research platform
SASP	Senescence-associated secretory phenotype
SC	Sub-cutaneous
SD	Standard deviation
SDQ	Strengths and Difficulties questionnaire
SMN	Secondary malignant neoplasms
SR	Standard-risk
STM	Short-term memory
STR	Sub-total resection
VC	Verbal Comprehension
WCA	Whole-chromosome aberration
WHO	World Health Organisation
WISC	Wechsler Intelligence Scale for Children

Table of Contents

List of tables

List of figures

Chapter 1. Introduction

1.1. Medulloblastoma

1.1.1. Introduction

Medulloblastoma (MB) is the most common paediatric malignant embryonal tumour of the central nervous system (CNS; World Health Organisation [WHO] grade 4). With approximately 55 children diagnosed each year in the UK, MB accounts for 20% of all childhood CNS tumours (Northcott *et al.*, 2019) and is responsible for approximately 20% of all paediatric cancer deaths (Northcott *et al.*, 2019).

MB primarily occurs in children but can, rarely, occur in adults, with peak incidence between 6 and 8 years old. MB is more common in males, with an incidence rate of 1.7: 1 (male: female). MB tumours originate in the posterior fossa, typically within the cerebellum and often present having spread into the 4th ventricle (Figure 1.1). Standard-of care consists of multi-modal treatment, typically consisting of surgical resection, followed by craniospinal radiotherapy (for non-infants; defined as 3-5 years old at diagnosis depending on country) and chemotherapy. Current 5-year survival rates are over 70%, however prognosis is highly variable depending on clinico-pathological and molecular features (ranging from <40% for very high risk to >95% for favourable risk patients) (Pizer and Clifford, 2009; Millard and De Braganca, 2016; Ostrom *et al.*, 2018; Bailey *et al.*, 2025).

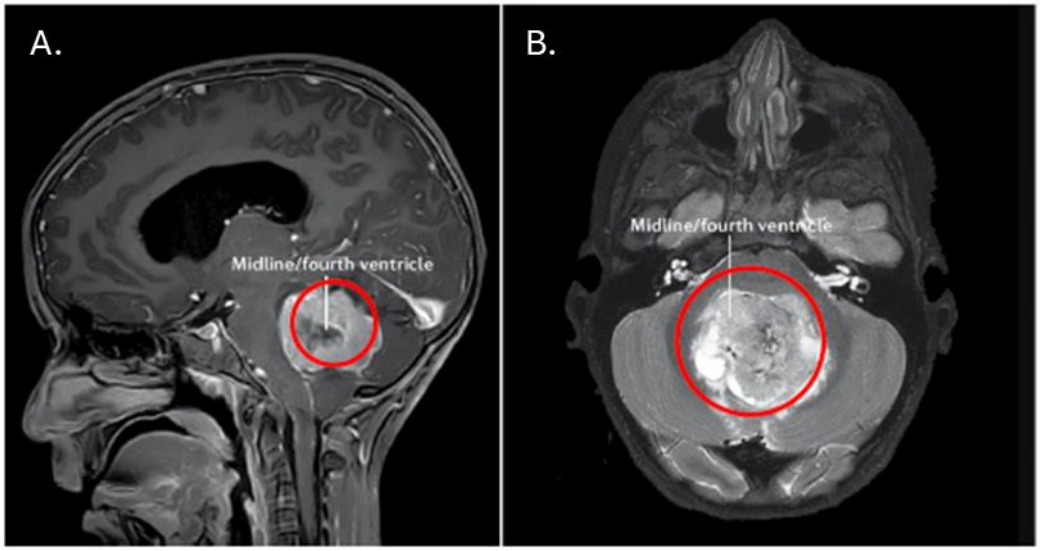

Figure 1.1. Cranial MRI scan showing tumour location of a patient with MB. A) Sagittal and B) transverse plane of cranial MRI showing tumour localisation to the midline/fourth ventricle. Adapted from Northcott et al.

1.1.2. Clinical presentation

MB patients present with varying severity of symptoms depending on the size and location of the tumour, which typically arise due to the tumour blocking cerebrospinal fluid (CSF) drainage. CSF is produced in the lateral ventricle, flows through the 3rd and 4th ventricles to the subarachnoid space and drains to the spinal cord (Bothwell;Janigro and Patabendige, 2019). As MB often spreads to the surface or base of the 4th ventricle, the tumour can block the drainage of CSF and increase intracranial pressure. Patients typically present with generic symptoms such as: headaches (particularly in the morning), nausea and fatigue, as well as more specific symptoms such as: blurred vision, hydrocephalous, increased head size and irritability. In infants, increased intracranial pressure results in an abnormal head shape and size through the splaying of sutures.

Due to the location of the tumour, patients also often display signs of cerebellar dysfunction such as poor co-ordination, difficulty walking and increased clumsiness (ataxia). As tumour size increases, symptoms can also include double vision, nystagmus (rapid, involuntary eye movements), facial weakness and hearing loss (Kim *et al.*, 2011).

1.1.3. Diagnosis

MB is diagnosed through a combination of assessments, including: 1) clinical symptoms, 2) magnetic resonance imaging (MRI) scans to determine the presence of a tumour and its location, 3) lumbar puncture to determine the presence of any tumour cells in the CSF, 4) histopathological assessment of the tumour following surgical resection and 5) molecular profiling of the tumour material following surgical resection (Northcott *et al.*, 2019).

1.1.3.1. Metastatic staging

One third of patients typically present with metastasised MB at diagnosis (Pizer and Clifford, 2009). Metastases typically spread from the primary tumour site through the CSF and occur either locally within the brain (cerebral subarachnoid space, third ventricle or lateral ventricle) or to the spinal cord (spinal subarachnoid space). In rare occasions MB can also spread outside of the craniospinal axis to the bone marrow, lymph nodes, liver or lungs (Pizer and Clifford, 2009). MB metastases are staged according to Chang's criteria based on location and align with the flow of CSF (Chang;Housepian and Herbert, 1969). A summary is shown in Table 1.1.

Stage	Description
M0	No evidence of tumour metastasis in the MRI scan or CFS
M1	Microscopic tumour cells observed in the CFS cytology
M2	Metastasis detected from MRI scan cerebellar or cerebral subarachnoid space or third or lateral ventricle
M3	Metastatic spread within the spinal subarachnoid space
M4	Metastatic spread outside the cerebrospinal axis

Table 1.1. Medulloblastoma metastatic staging system (Chang;Housepian and Herbert, 1969)

1.1.3.2. Histopathological assessment

Several tumour types can arise in the posterior fossa including ependymoma, astrocytoma, atypical teratoid/rhabdoid tumours (ATRT) and other embryonal tumours. Histopathological assessment of the tumour material is required for diagnosis of MB. There are four recognised WHO histopathological subgroups, comprising of classical (CLA), desmoplastic nodular (DN), MB with extensive nodularity (MBEN) and large cell/anaplastic (LCA) (Figure 1.2). DN and MBEN share similar histology and are often grouped together, collectively referred to as DN/MBEN.

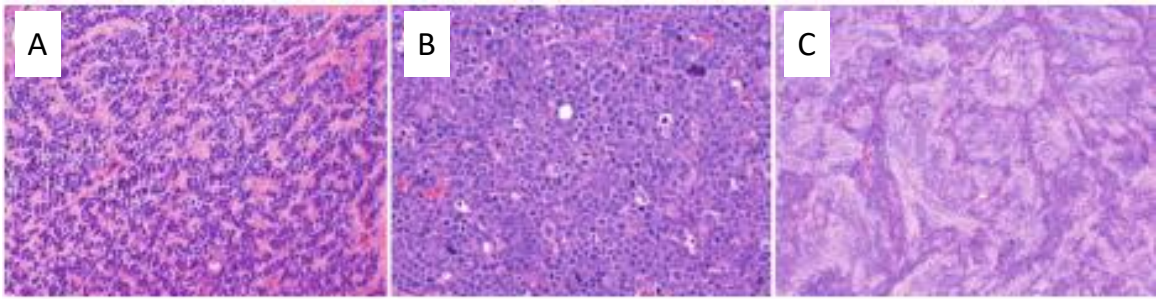

Figure 1.2. Histopathological classification of medulloblastoma. A) Classic: undifferentiated small cells in a sheet-like pattern, with mild-moderate pleomorphism (magnification ×200); B) Large cell/anaplastic (LCA): nuclear pleomorphism with a high mitotic count and abundant apoptosis, cell wrapping, a large cell phenotype (magnification ×400); C) Desmoplastic/nodular with extensive nodularity (DN/MBEN): nodules of neurocytic cells and internodular desmoplasia around embryonal cells showing variable nuclear pleomorphism, irregular regions of neurocytic cells against a neuropil-like matrix (magnification ×100). Adapted from Northcott et al.

1.1.3.3. Molecular profiling

MB is a biologically heterogeneous disease. The incorporation of histopathological assessment with genome-wide molecular analyses of the MB (epi)genetic has led to the classification into multiple molecular groups. In 2012, a global research consensus defined four principle molecular groups: Wingless (MB_{WNT}), Sonic Hedgehog (MB_{SHH}), Group 3 (MB_{Grp3}) and Group 4 (MB_{Grp4}) (Taylor *et al.*, 2012). The molecular groups form the genetically-defined medulloblastoma classification in the 2016 and 2021 WHO classifications of CNS tumours, alongside the histopathological characterisation (Louis *et al.*, 2016; Louis *et al.*, 2021). A summary of each molecular group is shown in Figure 1.3.

1.1.3.4. MB_{WNT}

MB_{WNT} is the least frequent subgroup and has an excellent prognosis (5-year survival >90%) (Ramaswamy *et al.*, 2016). Tumours are typically located in the cerebellar peduncle/cerebellopontine angle cistern or the midline with brainstem involvement (Perreault *et al.*, 2014). MB_{WNT} is typically characterised by loss of chromosome 6 and *CTNNB1* mutations, leading to over-activation of the WNT signalling pathway (Taylor *et al.*, 2012; Millard and De Braganca, 2016; Juraschka and Taylor, 2019; Northcott *et al.*, 2019).

1.1.3.5. MB_{SHH}

MB_{SHH} is defined by over activation of the SHH signalling pathway (*PTCH1*, *TERT*, *SMO*, *SUFU* mutations) (Taylor *et al.*, 2012; Millard and De Braganca, 2016; Juraschka and Taylor, 2019; Northcott *et al.*, 2019). Unlike the other molecular groups, MB_{SHH} are typically located in the cerebellar hemispheres (Perreault *et al.*, 2014). The overall prognosis for MB_{SHH} is intermediate, and depends on the age of the patient, and histo-molecular features of the tumour. Infant (<3 years old) patients have a good prognosis, whereas patients with *TP53*-mutated tumours (somatic mutations) have a poor prognosis (<50% survival) (Schwalbe *et al.*, 2017). Recent studies have reported heterogeneity; MB_{SHH} can be further classified into 4 subgroups (1-4) (Louis *et al.*, 2021).

1.1.3.6. MB_{Grp3} and MB_{Grp4}

MB_{Grp3} and MB_{Grp4} are less biologically distinct, and the underlying aetiology is not fully understood (Taylor *et al.*, 2012; Millard and De Braganca, 2016; Juraschka and Taylor, 2019; Northcott *et al.*, 2019). MB_{Grp3} and MB_{Grp4} have poor and intermediate prognoses, respectively (Taylor *et al.*, 2012; Millard and De Braganca, 2016; Juraschka and Taylor, 2019;

Northcott *et al.*, 2019), and are typically located in the midline 4th ventricle (Perreault *et al.*, 2014). Recent studies have reported heterogeneity and overlap between MB_{Grp3} and MB_{Grp4}. Sharma *et* al classified the clinicopathological and molecular features of MB_{Grp3} and MB_{Grp4} into 8 second-generation methylation subgroups (I-VIII,

Figure ***1.4***) supporting the heterogeneous biology between MB_{Grp3}/MB_{Grp4} (Sharma *et al.*, 2019). These second-generation methylation subgroups have been adopted into the 2021 WHO classification of CNS tumours, and display distinct demographic, clinical and molecular features (Louis *et al.*, 2021). Additionally, Williamson *et al* reported MB_{Grp3}/MB_{Grp4} tumours develop on a continuum (Williamson *et al.*, 2022).

Cytogenetic aberrations are more common among MB_{Grp3} and MB_{Grp4}, with key changes including loss of 17p and gain of 17q (collectively referred to as isochromosome 17q; i17q), gain of chromosome 7, loss of chromosome 8 and loss of chromosome 11 (Northcott *et al.*, 2012; Northcott *et al.*, 2017; Gajjar *et al.*, 2021). Amplification of *MYC* is almost exclusive to MB_{Grp3} and conveys a dismal prognosis (<5%) (Roussel and Robinson, 2013). Whole-chromosome aberration (WCA) signatures can improve risk stratification and be used to predict survival. Goschzik *et al* defined a favourable risk WCA signature (WCA-FR; defined as ≥ 2 of: gain of 7, loss of 8 and loss of 11) within standard-risk MB predicts a favourable prognosis with 100% 5-year PFS. Remaining tumours were classified as WCA-HR and had much poorer outcomes (68% 5-year PFB (Goschzik *et al.*, 2018). Incorporation of WCA groups with methylation subgroups and clinical features has led to further development of risk-stratified models (Goddard *et al.*, 2023; Mynarek *et al.*, 2023).

	Subgroup	WNT	SHH	Group 3	Group 4
Clinical Characteristics	% of Cases	10	30	25	35
	Age at Diagnosis				
	Gender Ratio (M:F)	1:1	1:1	2:1	3:1
	Anatomic Location				
	Histology	Classic, Rarely LCA	Desmoplastic, Classic, LCA	Classic, LCA	Classic, LCA
	Metastasis at Diagnosis (%)	5-10	15-20	40-45	35-40
	Recurrence Pattern	Rare; Local or metastatic	Local	Metastatic	Metastatic
	Prognosis	Very good	Infants good, others intermediate	Poor	Intermediate
Molecular Characteristics	Proposed Cell of Origin	Progenitor cells in the lower rhombic lip	Granule precursors of the external granule layer	Neural stem cells	Unipolar brush cells
	Recurrent Gene Amplifications	-	*MYCN* *GLI1* or *GLI2*	*MYC* *MYCN* *OTX2*	*SNCAIP* *MYCN* *OTX2* *CDK6*
	Recurrent SNVs	*CTNNB1* *DDX3X* *SMARCA4* *TP53*	*PTCH1* *TERT* *SUFU* *SMO* *TP53*	*SMARCA4* *KBTBD4* *CTDNEP1* *KMT2D*	*KDM6A* *ZMYM3* *KTM2C* *KBTBD4*
	Cytogenetic Events ■ Gain ■ Loss	6	3q, 9p 9q, 10q, 17p	1q, 7, 18 8, 10q, 11, 16q i17q	7, 18q 8, 11p, X i17q
	Other Recurrent Genetic Events	-	-	*GFI1* and *GFI1B* enhancer hijacking	*PRDM6*, *GFI1*, and *GFI1B* enhancer hijacking

Age: Infant Child Adult

Figure 1.3. Summary of the four consensus molecular subgroups (Juraschka and Taylor, 2019)

	Principle group	Group 3/4							
	Subgroup	**I**	**II**	**III**	**IV**	**V**	**VI**	**VII**	**VIII**
Demographics	**Frequency**	4%	13%	9%	10%	8%	9%	22%	25%
	Age								
	Gender	40 60	23 77	22 78	32 68	29 71	33 67	34 66	25 75
Other features	**Histology**	Classic > Desmoplastic	LCA, Classic	Classic > LCA	Classic	Classic	Classic	Classic	Classic
	Metastasis	35%	57%	56%	58%	62%	45%	45%	50%
	5-year OS	77%	50%	43%	80%	59%	81%	85%	81%
Molecular features	**Cytogenetics**	balanced	1q+, 8+, i17q	7+, 10q-, i17q	7+, 14+, 8-, 10-, 11-, 16-	7+, 16q-, i17q	7+, 8-, 11-, i17q	7+, 8-, i17q	i17q
	Driver events	GFI1/GFI1B act, OTX2 amp	MYC amp, GFI1/GFI1B act, KBTBD4/SMARCA4/CTDNEP1/KMT2D mut	MYC amp	no common driver event	MYC/ MYCN amp	PRDM6 act, MYCN amp	KBTBD4 mut	PRDM6 act, KDM6A/ZMYM3 / KMT2C mut

Figure 1.4. Second-generation methylation subgroups for MB_{Grp3}/MB_{Grp4}. International consensus second-generation methylation subgroups for MB_{Grp3}/MB_{Grp4} (subgroups I-VIII) display distinct demographic, clinical and molecular features (Hovestadt *et al.*, 2020).

.

1.1.4. Treatment

1.1.4.1. Surgery

Surgical excision of the tumour is carried out with the aim of achieving gross total resection (GTR). In some patients it is not possible to remove all of the tumour; patients are classed as having sub-total resection (STR) when there is ≥1.5cm^2 tumour remaining, and near-total resection (NTR) when there is <1.5cm^2 remaining. Patients with residual tumour (STR) are typically considered high risk and receive higher intensity chemotherapy and radiotherapy, however there is evidence that this may no longer be necessary (Thompson *et al.*, 2016). High risk patients are more likely to have STR, and hence STR is associated with poor survival, however, STR alone is not independently prognostic of worse outcomes (Keeling *et al.*, 2024).

1.1.4.2. Radiotherapy

Radiation therapy, or radiotherapy, after surgery greatly improves survival outcomes compared to surgery alone and forms an important part of current MB treatment and management (Northcott *et al.*, 2019). Radiation, the transmission of energy as electromagnetic waves or subatomic particles, can be categorised into non-ionising radiation and ionising radiation, based on the ability to strip electrons from atoms (ionise). Ionising radiation can be emitted in the form of particles (alpha, beta and neutron) or electromagnetic waves (gamma and X-ray). Alpha- beta- and neutron-particles have differing abilities to ionise, and penetrate objects, based on their size and charge (Donya *et al.*, 2014). A summary of the types of ionising radiation and their degree of penetrance provided in Figure 1.5.

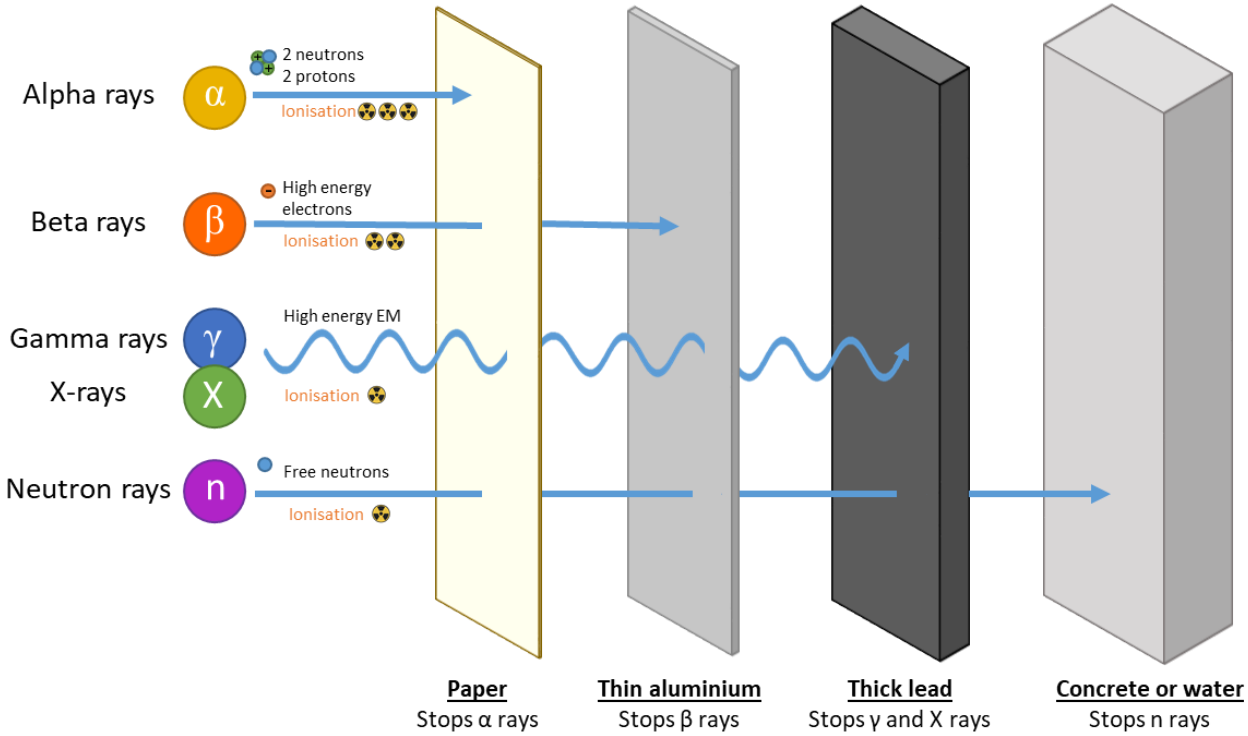

Figure 1.5. Types of ionising radiation. Ionising radiation can be emitted as either particles (alpha; α, beta; β, and neutron; n) or electromagnetic waves (gamma; γ, and X-rays; X).

Conventional MB radiotherapy consists of fractionated x-ray irradiation of the entire craniospinal axis, with an additional boost to the tumour site. Radiotherapy induces cell death through direct, indirect and bystander effects (summarised in

Figure 1.6). Ionisation of DNA molecules induces base modifications, single- and double-strand breaks, which, if unrepaired, prevent cell growth and induce cell death (Santivasi and Xia, 2014; Goldstein and Kastan, 2015). Tumour cells are typically associated with increased sensitivity to radiation due to high proliferation rates and impaired DNA damage response pathways (Goldstein and Kastan, 2015). Prior to the introduction of craniospinal irradiation (CSI), most MB patients would not survive (Bloom, 1982). The aim of radiotherapy is to eliminate any residual tumour following surgical resection and to reduce the risk of relapse by eradicating any microscopic deposits. MB typically spreads within the CNS and therefore patients usually receive radiation to the entire craniospinal axis, with an additional focal boost to the tumour site, within 3-4 post-surgery (Gottardo and Gajjar, 2006; Northcott *et al.*, 2019). Due to the adverse effects associated with radiotherapy, CSI is withheld or delayed in infants (typically patients under 3 years old but can also include under 5 depending on national conventions). Details of the current risk-stratified radiotherapy treatment protocols for non-infants are provided in section 1.1.5. A previous clinical trial (HIT-SIOP-PNET4; NCT01351870, running from 2001 – 2006) investigated the impact of hyper-fractionated radiotherapy to reduce tumour cell repopulation time between fractions (delivery of 1 Gy twice per day, compared to the conventional 1.8Gy daily fractions), however there was no survival advantage compared to standard radiotherapy delivery (Lannering *et al.*, 2012).

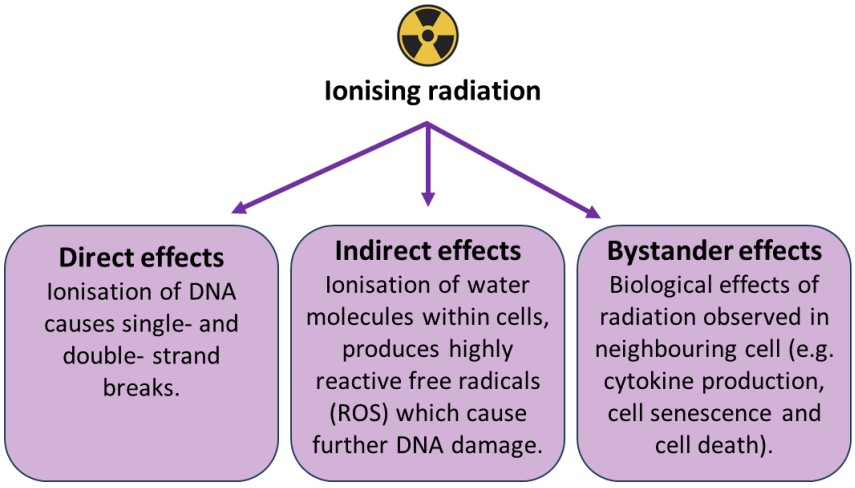

Figure 1.6. Ionising radiation induces damage by direct, indirect and bystander effects.

Receipt of conventional photon radiotherapy is associated with a plethora of debilitating long-term toxicities, which is discussed in detail in Chapter 1.2. The use of proton beam radiotherapy may offer an alternative. With typical photon radiation, the highest dose is received within centimetres of entry and attenuates exponentially though the tissue, depositing a dose before, within and after the target volume (tumour) (Hoffman and Yock, 2009). In contrast, proton radiation has a unique energy absorption profile and requires a lower entrance dose which rapidly decreases after the target volume; proton radiation results in minimal irradiation of non-target structures, whilst maintaining delivery of the lethal dose to the tumour (Hoffman and Yock, 2009). Studies have shown proton beam therapy to result in fewer long-term deficits whilst maintaining survival rates (Yock *et al.*, 2016; Pulsifer *et al.*, 2018). However, further large-scale trials are required to directly compare conventional and proton radiation therapy, to fully decipher the potential late-effect benefit.

1.1.4.3. Chemotherapy

Patients are treated with adjuvant chemotherapy during and after radiotherapy; chemotherapy is currently recommended for all patients regardless of risk status (Tait *et al.*, 1990; Millard and De Braganca, 2016). In the 1970s, chemotherapy was added to treatment regimens to increase survival rates by further eliminating remaining microscopic tumour, and since the 1990s the adoption of adjuvant chemotherapy alongside radiotherapy, has enabled a reduction in the CSI dose (from 36 Gy to 23.4 Gy for standard risk patients) (Evans *et al.*, 1990; Fossati;Ricardi and Orecchia, 2009; Northcott *et al.*, 2019).

Childhood MB chemotherapy regimens are complex, and often differ between treatment centres, with numerous clinical trials to assess the potency of new combinations. The most widely used chemotherapy drugs given before or during radiotherapy include cisplatin, vincristine, cyclophosphamide, lomustine (CCNU) and carboplatin *(Yock et al., 2016)*. Perhaps the mostly widely used chemotherapy regimen is the so-called Packer regimen (named after the esteemed paediatric oncologist Roger Packer), which consists of cisplatin, CCNU, and vincristine *(Packer et al., 1994)*. Variations of Packer-style chemotherapy are used within the current major MB clinical trials in Europe (SIOP-PNET5-MB; NCT02066220 and SIOP-HR-MB; EudraCT Number: 2018-004250-17) and the US (SJMB12; NCT01878617) *(Bailey et al., 2022)*. A summary of the chemotherapy regimens is shown in Table 1.2.

A combination of chemotherapy agents are typically used to target cells across multiple phases of the cell cycle. Classes of chemotherapy used in MB treatment include alkylating agents, mitotic inhibitors, antimetabolites and topoisomerase inhibitors. Alkylating agents are perhaps the most commonly used classes of chemotherapy drugs, and act in all phases of the cell cycle. Examples include cyclophosphamide, lomustine, thiotepa, and temozolomide. Alkylating agents introduce an alkyl group into DNA, typically at N-7 of guanine, causing crosslinking of DNA strands which prevents DNA replication and induces programmed cell death (Fischer, 2005). Platinum-containing agents (e.g. cisplatin and carboplatin) have a similar mechanism of action, and crosslink DNA strands with platinum (Dilruba and Kalayda, 2016). Mitotic inhibitors such as vinca alkaloids (e.g. vincristine) act during metaphase, these agents inhibit mitosis by binding tubulin which prevents microtubule formation and inducing programmed cell death (Banyal *et al.*, 2023). Antimetabolites, such as pemetrexed and gemcitabine, are particularly effective during S-phase; the nucleotide analogues are incorporated into DNA and inhibit DNA replication (Morfouace *et al.*, 2014). Moreover, topoisomerase II inhibitors (e.g. etoposide) also act during S-phase through preventing DNA ligation; DNA double strand breaks introduced during DNA synthesis remain and cells undergo apoptosis (Nitiss, 2009).

	Medulloblastoma clinical trials						
Chemotherapy agent	**SIOP-UKCCG-PNET3**	**HIT-SIOP-PNET4**	**SIOP-PNET5-MB**	**SIOP-HR-MB**	**ACN0331**	**SJMB03**	**SJMB12**
Vincristine	✓	✓	✓	✓	✓	✓	✓
Cisplatin		✓	✓	✓	✓	✓	✓
Cyclophosphamide	✓		✓	✓	✓	✓	✓
Etoposide	✓			✓R			
Carboplatin	✓		✓R	✓R			
Lomustine		✓	✓	✓	✓		
Thiotepa				✓R			
Temozolomide				✓R			
Pemetrexed							✓
Gemcitabine							✓

Table 1.2 Chemotherapy combination used in previous and ongoing clinical trials. Chemotherapy agents used in SIOP-UKCCG-PNET3 (Taylor *et al.*, 2003) HIT-SIOP-PNET4 [NCT01351870] (Lannering *et al.*, 2012), SIOP-PNET5-MB [NCT02066220] (Mynarek *et al.*, 2021), SIOP-HR-MB (Bailey *et al.*, 2022), ACNS0331 [NCT00085735] (Michalski *et al.*, 2021), SJMB03 [NCT00085202] (Gajjar et al., 2021 (Gajjar *et al.*, 2021)) and SJMB12 [NCT01878617]. R represents a chemotherapy agent included as part of a randomised arm of the trial.

1.1.4.4. Infant medulloblastoma

Infant medulloblastoma (iMB; patients under 3 years old at diagnosis but can also include children under 5 depending on national conventions) accounts for 25-35% of medulloblastoma. Unlike childhood MB, there is little consensus on iMB management treatment. iMB patients are treated with surgical resection and chemotherapy; patients typically do not receive CSI due to the high risk of impaired neurodevelopment leading to permanently disabling late-effects (Rutkowski *et al.*, 2010). Instead, CSI is avoided or delayed, through the use of intrathecal chemotherapy, high-dose intravenous chemotherapy followed by stem-cell rescue, or in combination with focal radiotherapy (Rutkowski *et al.*, 2005; Ridola *et al.*, 2007; Rutkowski *et al.*, 2010; von Bueren *et al.*, 2011; Müller *et al.*, 2014). Treatment must carefully balance morbidity and mortality, and unfortunately, iMB is associated with poor prognosis (<60% 5-year survival) (Hicks *et al.*, 2021).

iMB is typically risk-stratified based on histology; DN/MBEN has been shown to predict very good prognosis (>90% 5-year survival). iMB can be largely classified into iMB_{SHH} or iMB_{Grp3} (both approximately 40% of iMB) (Dhall *et al.*, 2008; Robinson *et al.*, 2018; Hicks *et al.*, 2021). iMB_{SHH} are typically SHH-*TP53* wildtype with DN/MBEN histology, though approximately 20% exhibit classic histology (Hicks *et al.*, 2021; Bailey *et al.*, 2025). iMB_{SHH} can be grouped into iMB_{SHH-1} and iMB_{SHH-2}; iMB_{SHH-2} is typically associated with poorer survival, though prognosis may also be treatment-dependant (Remke and Ramaswamy, 2018; Robinson *et al.*, 2018; Lafay-Cousin *et al.*, 2020; Mynarek *et al.*, 2020; Hicks *et al.*, 2021). iMB_{Grp3} typically have classic or LCA histology and a poor prognosis (Dhall *et al.*, 2008; Rutkowski *et al.*, 2010).

1.1.4.5. Acute side-effects

Successful delivery of chemotherapy and radiotherapy regimens is dependent on the management of acute their side effects (occurring during, immediately after or within 2 weeks of treatment). Treatment induces off-target tissue damage and can induce acute side-effects affecting most biological systems (De Braganca and Packer, 2013). Examples of dose limiting toxicities (DLT) include haematological toxicities (e.g. neutropenia, anaemia, leukopenia, and thrombocytopenia), gastrointestinal (e.g. nausea, vomiting and mucositis), hepatic toxicity (increased liver enzymes), nephrotoxicity and pulmonary toxicity. Acute toxicities during treatment are carefully managed through supportive care (such as blood transfusions, IV fluids), delaying of treatment or dose reduction (De Braganca and Packer, 2013).

1.1.5. Risk-stratified treatment

Non-infant medulloblastoma patients are risk-stratified using established clinical, pathological, and molecular risk-features. Current clinical trials across Europe and the US are delivering risk-adapted biomarker-driven therapy, which reduce therapy for favourable MB_{WNT} (SIOP-PNET5-MB; NCT02066220 and SJMB12; NCT01878617) and use intensified regimens for high-risk MB (HR-MB) patients (SIOP-HR-MB; EudraCT Number 2018-004250-17) (Bailey *et al.*, 2022).

High-risk features include metastatic disease, large cell/anaplastic (LCA) histology, sub-total resection (STR), as well as additional molecular biomarkers such as *TP53* mutation (only for MB_{SHH}) and *MYC/N* amplification. The presence of one or more high-risk factors confers higher disease risk, however, STR alone is not independently prognostic of poor survival outcomes, as already mentioned (Keeling *et al.*, 2024). Non-MB_{WNT} patients are stratified into high-risk (HR-MB) or standard-risk (SR-MB) groups dependant on the presence or absence of high-risk features, respectively. MB_{WNT} confers better prognosis and therefore patients are stratified into standard-risk (SR-MB) or favourable-risk (FR-MB) groups dependant on the presence or absence of high-risk features, respectively. A summary of current European clinical trial risk stratification is shown in Table 1.3.

Risk group	Risk stratification criteria
High-risk	Metastatic disease
	LCA pathology
	MYC amplification
	MB_{SHH} with *TP53* mutation or *MYCN* mutation
Standard-risk	Non-MB_{WNT} and no HR features
	MB_{WNT} (>16 years old with no HR features)
	MB_{WNT} (3-16 years old with HR features)
Favourable-risk	MB_{WNT} (3-16 years old with no HR features)

Table 1.3. A summary of the risk stratification criteria for the SIOP-E non-infant clinical trials. SIOP-PNET5-MB (Mynarek et al., 2021) and SIOP-Europe HR-MB (Bailey et al., 2022). HR denotes high-risk.

Patients typically receive the same chemotherapy and radiation boost to the tumour bed regardless of risk group but receive variable doses of CSI (Taylor *et al.*, 2004). In Europe, most non-infant MB patients are treated on the protocols developed in the standard-risk clinical trial (SIOP-PNET5-MB) (Mynarek *et al.*, 2021) or the high-risk clinical trial (SIOP-Europe HR-MB (Bailey *et al.*, 2022). A summary of the risk-stratified inclusion criteria is shown in Table 1.4. Briefly, standard risk patients receive 23.4 Gy craniospinal irradiation (CSI) with an additional boost to 54 Gy to the tumour bed. Conversely, patients with high-risk MB receive a higher radiotherapy dose, typically consisting of 36 Gy CSI with 54 Gy boost to the tumour bed (Table 1.4). In SIOP-Europe HR-MB, patients are randomised to receive either standard high risk treatment or intensified treatment consisting of increased CSI dose or high-dose chemotherapy with stem-cell rescue (R1-3, respectively; Table 1.4) (Bailey *et al.*, 2022). Within SIOP-PNET5-MB, favourable-risk patients (MB_{WNT} with no high-risk features) received de-escalated therapy of 18 Gy CSI with 54 Gy boost, followed by reduced chemotherapy (6 cycles rather than the standard 8). This trial aims to determine whether the severity of late-effects can be reduced, whilst maintaining high rates of overall survival (Mynarek *et al.*, 2021). Unfortunately, dose de-escalation strategies are not suitable for most MB patients, for whom the receipt of higher dose treatment (23.4-36 Gy) remains critical for survival. Consequently, there is an acute need for the improved understanding of the aetiology of MB late-effects, and the development of interventions strategies to alleviate the significant burden.

Risk group	Clinical trial	Risk factor	Treatment
High-risk	SIOP-Europe HR-MB	Presence of 1 or more HR feature	R1: 36 Gy CSI + 54 Gy PFB
			R2: 39 Gy CSI (HART) + 54 Gy focal
			R3: 36 Gy CSI + 54 Gy PFB with HR chemo with stem cell rescue
	SIOP-PNET5-MB	MB_{SHH} with TP53 mutation	LFS (M0): 54 Gy tumour bed only LFS (M+): 23.4 Gy CSI + 54 Gy focal (+ 54 Gy to intracranial mets, 45 Gy to spinal mets) No LFS: 36 Gy CSI + 54 Gy focal (+ additional dose to mets as above, if applicable)
Standard-risk	SIOP-PNET5-MB	non-MB_{WNT} with no HR features, or MB_{WNT} with HR features	23.4 Gy CSI + 54 Gy focal
Favourable-risk	SIOP-PNET5-MB	MB_{WNT} with no HR features	18 Gy CSI + 54 Gy focal

Table 1.4. A summary of radiotherapy regimens in the current SIOP-E non-infant clinical trials. SIOP-PNET5-MB (Mynarek *et al.*, 2021) and SIOP-Europe HR-MB (Bailey *et al.*, 2022)**.** HR features are summarised in Table 1.3. Patients in the SIOP-Europe HR-MB were randomised to receive either standard HR treatment (R1) or intensified treatment (R2 or R3). PFB = posterior fossa boost, LFS = Li-Fraumeni syndrome (germline TP53 mutation), M0 = non-metastatic disease, M+ = metastatic disease, 'mets' = metastases.

1.2. The long-term burden of medulloblastoma

Survival rates for childhood medulloblastoma are now over 70%, however, the quality of life (QoL) of the survivors is lower than that of their siblings and peers (Limond *et al.*, 2015; Chevignard *et al.*, 2017; King *et al.*, 2017). The harsh treatment modalities previously described cause damage to the normal healthy tissue, and result in the development of late-effects presenting months to years after the primary treatment. Treatment causes acute damage that may persist, or it can induce further complications that develop over a longer period of time.

The late-effect burden of MB treatment includes a wide variety of conditions that affect most systems of the body; examples include secondary tumours, endocrine impairment, neurological problems, premature ageing/frailty, cardiotoxicity and renal-toxicity (Figure 1.4) (Kiltie;Lashford and Gattamaneni, 1997; Kurt *et al.*, 2008). Nearly all survivors of childhood cancer experience at least 1 chronic health condition, and by 30 years post-diagnosis, many will experience severe late-effects that are disabling or life-threating (Figure 1.7)**.** Survivors of MB are at a particularly high risk of developing neurocognitive complications as a result of surgery and/or radiation to the brain (Armenian and Robison, 2013).

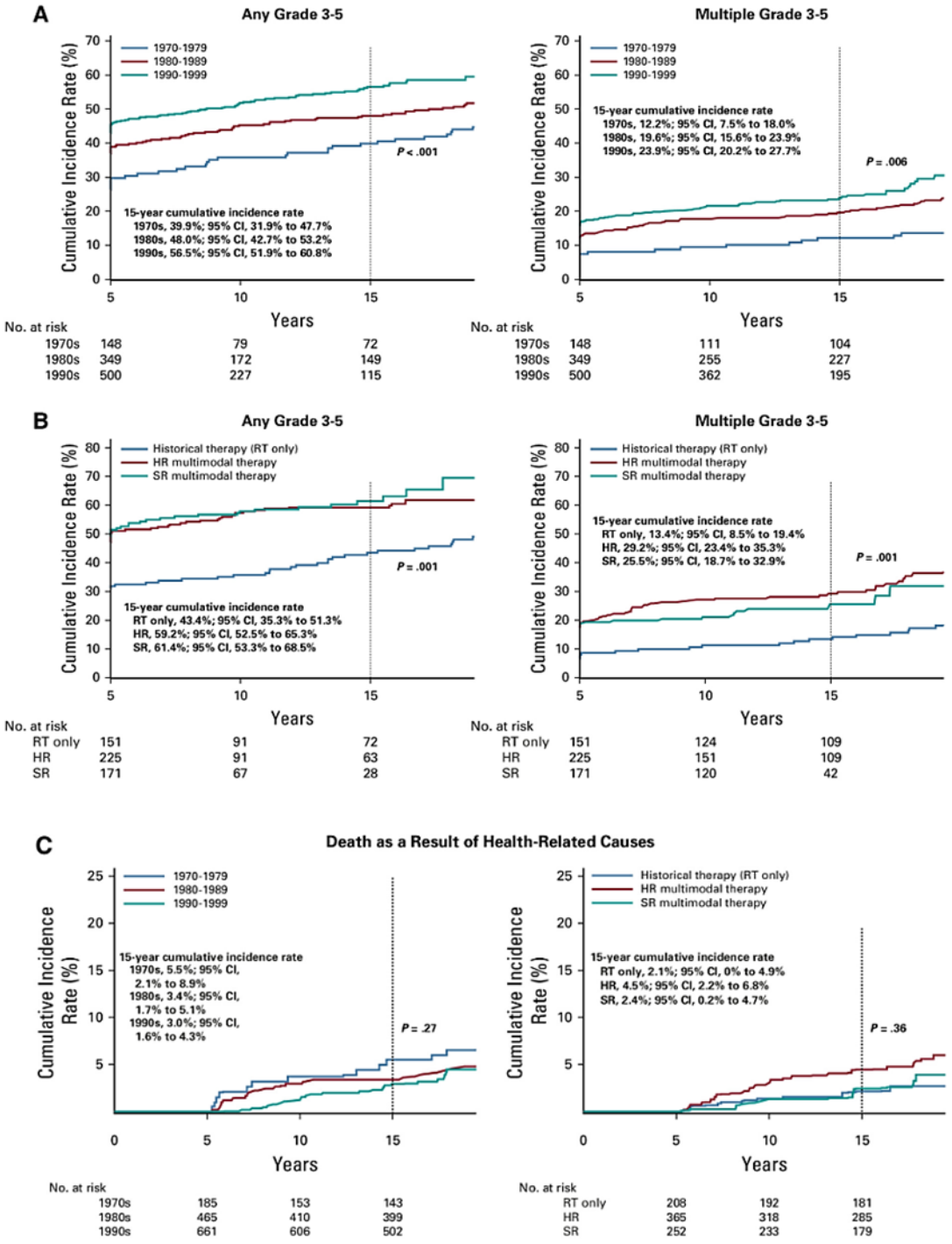

Figure 1.7. Medulloblastoma survivors experience severe, life-threatening health conditions. Fifteen-year cumulative incidence of A-B) severe, life-threatening, and fatal health conditions (grade 3-5) by A) treatment era and B) treatment exposure, and C) health-related mortality by treatment era and treatment exposure, among 5-year survivors of childhood medulloblastoma. HR, high risk; RT, radiotherapy; SR, standard risk (Salloum *et al.*, 2019).

1.2.1. Second malignant neoplasms

Secondary malignant neoplasms (SMNs) are the leading cause of death among adult survivors of central nervous system tumours (Morris *et al.*, 2007; Mertens *et al.*, 2008). MB survivors are at increased risk of developing SMNs. Typically, SMNs arise in the brain as a result of exposure to DNA damaging cranial radiation, with secondary gliomas and meningiomas being most common (Neglia *et al.*, 2006; Peterson *et al.*, 2006; Reulen *et al.*, 2011; Salloum *et al.*, 2019). Higher incidence of SMNs has been observed following adjuvant chemotherapy compared to radiotherapy alone (Packer *et al.*, 2013; Salloum *et al.*, 2019). Topoisomerase inhibitors (e.g., etoposide) and alkylating agents (e.g., cyclophosphamide) typically cause leukaemia rather than solid malignancies (Morris *et al.*, 2007). Genetic predisposition increases this risk further; patients with Li-Fraumeni syndrome (a germline mutation in tumour suppressor gene *TP53*) are highly likely to develop primary and secondary cancers (Suri *et al.*, 2013; Shin *et al.*, 2020). The developmental time of secondary tumours post-treatment can vary greatly (ranging from months to decades), and overall survival is extremely poor (Broniscer *et al.*, 2004; Edelstein *et al.*, 2011; Salloum *et al.*, 2019).

1.2.2. Endocrine impairment

Over half of MB survivors will develop an endocrine impairment as a result of CSI (Johnson *et al.*, 1994; Heikens *et al.*, 1998; Walter *et al.*, 1999; Ribi *et al.*, 2005; Frange *et al.*, 2009; Chevignard *et al.*, 2017). Endocrine impairment in MB survivors typically occurs due to radiation-induced damage of the pituitary gland, with the hypothalamus-pituitary-thyroid (HPT) and hypothalamus-pituitary-gonadal (HPG) axes also often affected (Johnson *et al.*, 1994; Heikens *et al.*, 1998; Walter *et al.*, 1999; Ribi *et al.*, 2005; Frange *et al.*, 2009; Chevignard *et al.*, 2017; Salloum *et al.*, 2019). Most commonly, growth hormone (GH) response is impaired. GH, produced by the pituitary gland, plays a vital role in growth and metabolism through stimulating insulin production (Stanley, 2012; Huang *et al.*, 2020). CSI leads to growth defects with survivors often exhibiting a premature ageing phenotype and short stature (Oeffinger *et al.*, 2006; Diller *et al.*, 2009b; Ness *et al.*, 2013). Additionally, survivors often experience delayed puberty, infertility, hypothyroidism and insulin-induced hypoglycaemia (Johnson *et al.*, 1994; Heikens *et al.*, 1998; Walter *et al.*, 1999; Ribi *et al.*, 2005; Frange *et al.*, 2009; Chevignard *et al.*, 2017).

1.2.3. Cardiovascular impairment

Adult survivors of childhood cancers have an 8-fold increased risk of developing a severe or life-threatening heart condition, including myocardial infarction and congestive heart failure (Oeffinger *et al.*, 2006). Survivors of childhood MB can experience reduced cardiovascular fitness, due to damage caused to the pericardium, myocardium, coronary arteries, valves and conduction system during combined chemotherapy and radiation treatment (Wolfe *et al.*, 2012; Martinez *et al.*, 2021). Development of cardiotoxicities are associated with high-risk therapy regimens, with incidence increasing 3-fold compared to that of radiotherapy alone (Oeffinger *et al.*, 2006). Chemotherapeutic agents such as anthracycline and cisplatin further increase the risk of cardiotoxicity development (Oeffinger *et al.*, 2006).

1.2.4. Neurophysiological impairment

Paediatric MB survivors can experience long-lasting neurological impairment from damage caused by the tumour itself, its surgical excision, or the subsequent radiotherapy and chemotherapy (Diller *et al.*, 2009a). Some patients develop obstructive hydrocephalus, resulting in vomiting, lethargy, headaches and double vision, although typically this can be resolved through perioperative CSF diversion (a shunt) (Lee *et al.*, 1994). The Childhood Cancer Survivor Study (CCSS) reported that over a third of childhood MB survivors experienced seizures and over 10% experienced a stroke by 30 years post-diagnosis; increased risk was associated with high-dose radiation to the brain, receipt of chemotherapy and/or recurrence of primary tumour (King *et al.*, 2017).

1.2.4.1. Posterior fossa syndrome

A relatively common side effect of surgery is Posterior Fossa Syndrome (PFS), which occurs in ~20% of cases. The exact cause of PFS development remains unclear, though risk factors include a midline tumour location and involvement of the brain stem (Law *et al.*, 2012; Avula *et al.*, 2015; Jabarkheel *et al.*, 2020). PFS, also referred to as cerebellar mutism, includes symptoms such as mutism, brainstem dysfunction, ataxia (poor balance), dysphagia (difficulty swallowing) and severe irritability. Duration and severity of symptoms vary greatly between patients, typically the mutism tends to be temporary, however, speech, language and neurocognitive impairments often remain (Law *et al.*, 2012; Jabarkheel *et al.*, 2020). The presence of PFS can also be used to predict the onset of later neurocognitive impairments (Northcott *et al.*, 2019).

1.2.4.2. Auditory and sensory impairment

Both cranial radiation and platinum-based chemotherapies (e.g. cisplatin and carboplatin) are associated with hearing loss (Grewal *et al.*, 2010; Harao *et al.*, 2020). Permanent hearing loss frequently occurs in children treated with cisplatin, with severity increasing with higher cumulative doses (Granowetter;Rosenstock and Packer, 1983; Packer *et al.*, 1994; Kortmann *et al.*, 2000; Grewal *et al.*, 2010). Ototoxicity typically occurs as a result of cranial radiation, and can be exacerbated with younger age, the presence of hydrocephalus or in combination with platinum-based chemotherapy (primary cisplatin) (Grewal *et al.*, 2010). By 30 years post-diagnosis, over a third of survivors experience deafness or hearing loss (King *et al.*, 2017). The development of cataracts leads to visual impairment; survivors are approximately 30 times more likely to develop cataracts than siblings (King *et al.*, 2017).

1.2.4.3. Physical functioning

Impaired physical functioning typically occurs during treatment and can improve over time; however, many patients experience lasting impairments (Packer *et al.*, 2003). Impaired physical functioning typically occurs in survivors who received cranial radiation, following receipt of chemotherapy or as a result of the tumour itself. Survivors often experience a wide range of neurological symptoms resulting in impaired gross motor skills such as balance and co-ordination, in addition to fine motor impairment and cranial nerve palsies (Chevignard *et al.*, 2017). Reduced physical function following irradiation has been demonstrated *in vivo* (Fielder *et al.*, 2019). The CCSS reported the majority of MB survivors (>60%) experience problems with balance, co-ordination, and/or tremors at 5 years post-diagnosis, with cumulative incidence increasing further (to >70%) by 30-years post-diagnosis (King *et al.*, 2017).

Chemotherapeutic drugs such as platinum-based agents (e.g. cisplatin) and vinca alkaloids (e.g. vincristine) can induce peripheral neuropathy (Armstrong *et al.*, 2009). Chemotherapy-induced peripheral neuropathy (CIPN) is a serious dose-limiting adverse effect that can result in permanent nerve damage leading to reduced muscular strength and walking difficulties. CIPN has been replicated *in* vivo; mice display impaired gait and reduced muscular endurance and balance (Geisler *et al.*, 2016; Liu *et al.*, 2018).

1.2.5. Premature ageing

Many survivors of childhood brain tumours appear frailer and prematurely aged compared to the general population (Ness *et al.*, 2013). A frail phenotype is characterised as low lean muscle mass, muscle weakness, slow walking speed, fatigue and the onset of chronic disease and mortality (Ness *et al.*, 2013). An increase in frailty is associated with reduced quality of life, and an increased prevalence of depression (Bray *et al.*, 2016; Lee;Chiu and Lee, 2016; Provencher *et al.*, 2016). The overall physical performance in adult survivors of brain tumours is typically akin to those decades older; survivors experience increased sensory loss, reduced leg and grip strength, as well as a diminished tolerance of exercise (Ness *et al.*, 2010). Assessment of frailty and premature ageing can be used as a predictor of morbidity across species (Rockwood *et al.*, 2017). The frailty index (FI) provides an overall picture of general health and wellbeing in both humans and mice. Whitehead *et al* developed an index of frailty to quantify premature ageing in mice through assessment of physical features associated with frailty, and subsequently showed this frailty index was comparable to the Rockwood frailty index used in humans (Whitehead *et al.*, 2014; Rockwood *et al.*, 2017). Assessment of frailty using this method provides an overview of overall physical function, however, can be subjective due to individual assessor judgement. Previous work by Fielder *et al* have shown whole-body irradiation of mice (3 doses of 3 Gy) promotes increased frailty (Fielder *et al.*, 2019). Frailty score can be used to predict mortality; mice displaying increased frailty also have higher mortality rates (Figure 1.8), something that is also seen in humans (Rockwood *et al.*, 2017; Fielder *et al.*, 2019).

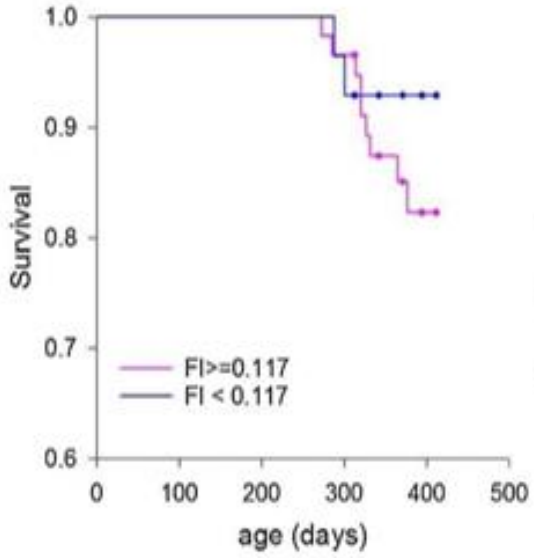

Figure 1.8. Whole-body irradiation induces premature frailty and earlier mortality. Frailty index (FI) can predict mortality. Mice were typically culled due to reaching the humane end point, rather than from natural causes (Fielder *et al.*, 2019).

1.2.6. Neurocognitive impairment

Radiation to the developing brain promotes the greatest risk of significant neurocognitive defects in MB survivors (Grill *et al.*, 1999; Packer *et al.*, 2003; Ellenberg *et al.*, 2009). Many survivors experience deficits affecting attention, working memory and processing speed which often result in intellectual disability and low levels of academic attainment that requires specialist education (Packer *et al.*, 2003; Chevignard *et al.*, 2017). Survivors experience a mean loss of IQ points of 2.5-3.9 per year and reach a plateau of impairment around two standard deviations below average (Walter *et al.*, 1999; Palmer *et al.*, 2001b; Ris *et al.*, 2001). Higher executive processes responsible for decision making, judgement and awareness are also generally poor; many survivors experience poor psychosocial satisfaction, and reduced independence in adulthood (Spiegler *et al.*, 2004; Maddrey *et al.*, 2005; Robbins *et al.*, 2012; Gupta *et al.*, 2022). These domains support the acquisition of new learning such that childhood brain tumour survivors acquire new information at half the rate of unaffected peers (Palmer *et al.*, 2001a). Cranial radiation leads to reduced neurogenesis in the hippocampus, resulting in reduced spatial memory (Winocur *et al.*, 2006; Wong-Goodrich *et al.*, 2010; Rao *et al.*, 2011; Schnegg *et al.*, 2013).

Neurocognitive impairment is associated with all CSI doses, though increased cranial radiation dose is associated with a greater risk of impaired neurocognitive function. 70-90% of survivors who received high-dose CSI demonstrate a significant impairment in global intellectual functioning, which are in turn strongly correlated with decreased quality of life (Walter *et al.*, 1999; Palmer *et al.*, 2001b; Ris *et al.*, 2001; Ramaswamy *et al.*, 2016). Impaired neurocognitive function is particularly severe when cranial radiation is received at a younger age. In infant patients, the risk of permanently disabling neurocognitive impairment is high, and consequently infant MB patients no longer receive CSI until they are over at least three years of age, sadly coming at the cost of reduced overall survival rates (Chapter 1.1.4.4) (Lafay-Cousin *et al.*, 2009; Chevignard *et al.*, 2017). Decreased neurocognition has also been linked to chemotherapeutic agents such as cisplatin and cyclophosphamide (Janelsins *et al.*, 2016; Zhou;Kavelaars and Heijnen, 2016; Chiu *et al.*, 2017; Flanigan *et al.*, 2017).

1.2.7. Assessing quality of survival

The late-effect burden experienced by survivors of cancer is collectively referred to as 'Quality of Survival' (QoS). QoS encompasses the long-term neurocognitive, endocrine, behavioural, medical, and emotional outcomes of cancer survival, and is broader than the subjective view of an individual survivor, termed quality of life (QoL) (Limond *et al.*, 2015).

Adult survivors of MB are less likely to reach major life milestones; survivors are less likely to live independently, get married or obtain a higher education degree compared to siblings, and are more likely to experience depression and anxiety (King *et al.*, 2017). Survivors are twice as likely to be unemployed, and those that are employed are often in lower paid, lower-skill jobs, with less career mobility (de Boer;Verbeek and van Dijk, 2006; Kirchhoff *et al.*, 2011; King *et al.*, 2017). Sensory impairment can greatly impact QoL; development of speech and language is often delayed or impaired, detrimentally impacting social interaction, communication and academic achievement (Grewal *et al.*, 2010).

QoS and QoL is assessed through a battery of direct and indirect assessments typically via neuropsychometric assessments and questionnaires, either in person or via online platforms. A summary of the questionnaires used within European clinical trials is available in Table 1.5.

Domain	Questionnaire
Health status	The Health Utilities Index (HUI)
Quality of life	The Pediatric Quality of Life Inventory (PedsQL) and Multidimensional Fatigue module
Behavioural difficulties	The Strengths and Difficulties questionnaire (SDQ)
Executive function	The Behaviour Rating Inventory of Executive function (BRIEF)
Demographic, endocrine, and medical information	Medical, Educational, Employment and Social Questionnaire (MEES)

Table 1.5. Indirect questionnaire-based assessments of QoL (Limond et al., 2015).

1.2.7.1. Assessing neurocognitive impairment

Typically, neurocognitive impairment is assessed during diagnosis, treatment, and follow-up, however, these assessments can be missed due the need for rapid treatment or the patients being too unwell. Neuropsychometric assessment is typically conducted by a neuropsychologist, or via an online platform. An overview of the assessments commonly used in clinical oncology protocols in Europe and the USA is provided in Table 1.6 (Limond *et al.*, 2015). A widely used assessment is the Wechsler Intelligence Scale for Children (WISC), which assesses individual components of intelligence: Working Memory (WM), Verbal Comprehension (VC), Processing Speed (PS) and Perceptual reasoning (PR). Together, these give a score for overall intellectual ability: Full Scale Intelligence Quotient (FSIQ). (Gomez;Vance and Watson, 2016).

Domain	USA	Germany	France	UK	Belgium	Italy	Netherlands	Norway
Perceptual/ Fluid reasoning	Block design (WISC-IV)	RPM	Block design Matrix reasoning (WISC-IV)	Block design Matrix reasoning (WISC-IV)	Block design (WISC-III)	Block design (WISC-III)	Block design (WISC-III)	Block design Matrix reasoning (WASI)
Short-term memory	-	Number recall (K-ABC I/II)	Digit span* (WISC IV or CMS)	Digit span* (WISC IV or CMS)	Digit span* (WISC III or CMS)	Digit span* (WISC III),	Digit span* (WISC III)	Digit span (WISC-IV)
Visual-motor skills	-	Visual motor integration (Beery VMI)	Visual motor integration (VMI)	Design Copy (WRAVMA)	Visual motor integration (VMI)	Visual motor integration (VMI)	Visual motor integration (VMI)	-
Motor skills	-	Purdue pegboard	Purdue pegboard	Pegboard (WRAVMA)	Finger tapping	Purdue pegboard	-	-
Semantic memory	Vocabulary (WISC-IV)	Vocabulary (WISC-IV)	Vocabulary (WISC-IV)	Vocabulary (WISC-IV)	Vocabulary (WISC-III)	Vocabulary (WISC-III)	Vocabulary (WISC-III)	Vocabulary (WASI)
Attention – vigilance and reaction times	-	Continuous performance test (CPT – short)	TEA-Ch/TEA/Mesulam	TEA-Ch/TEA	Amsterdam neuropsychology test battery	Continuous performance test (CPT)	TEA-Ch/TEA	Continuous performance test (CPT-II), Knox, SDMT
Processing speed	Coding and symbol search (WISC-IV)	-	Coding and symbol search (WISC-IV)	Coding and symbol search (WISC-IV)	Coding and symbol search (WISC-III)	Coding and symbol search (WISC-III)	Coding and symbol search (WISC-III)	-
Long-term memory	Stories, Dot locations, Faces (CMS) List learning (CVLT)	-	Stories, Dot locations, Faces (CMS) List learning (CMS) Rivermead behavioural memory test	Stories, Dot locations, Faces (CMS) List learning (CMS or CVLT), Word pairs (CMS)	Dot locations, Family pictures, Word pairs (CMS)	List learning (BVN), TEMA	RAVLT, RCFT	CAVLT-II, Visual Reproduction (WMS)
Reading	-	-	Local reading measure	Basic reading (WIAT-II)	-	Local reading measure	-	-

Table 1.6. Neuropsychometric assessments commonly used in clinical oncology protocols in Europe and the USA. TOMAL/TEMA: Test of memory and learning (name recall). CAVLT-II = Child auditory verbal learning test, CMS = Children memory scale, CPT= Continuous performance test, CVLT = California verbal learning test, K-ABC = Kaufman assessment battery for children, RAVLT = Rey auditory verbal learning test, RCFT = Rey Complex figure test and recognition trial, RPM = Raven's Progressive Matrices, SDMT = Symbol Digit Modalities Test, TEA = Test of everyday attention, TEA-Ch = Test of everyday attention for children, VMI = Visual motor integration, WASI = Wechsler abbreviated scale of intelligence, WISC-III = Wechsler intelligence scale for children, WISC-IV = Wechsler intelligence scale for children, WMS = Wechsler memory scales, WRAVMA = Wide range assessment of visual motor abilities, WIAT-II = Wechsler individual achievement test. NB: Several countries use additional tests in their national protocols.

1.3. The relationship between treatment and late-effects

It is well known that the intense treatment regimens childhood cancer survivors (CCSs) endure are significantly impacting their QoL (Evans *et al.*, 1990; Heikens *et al.*, 1998; Grewal *et al.*, 2010; Chevignard *et al.*, 2017). Despite the high risk of neurocognitive impairments, receipt of cranial irradiation is crucial for survival of MB and therefore remains standard of care for non-infants. Survivorship studies of completed European SR-MB clinical trials, SIOP/UKCCG-PNET3 (running from 1992- until 2000) and HIT-SIOP-PNET4 (NCT01351870, running from 2001 - 2006), assessed whether the respective treatment arms associated with neurocognitive outcomes (HIT-SIOP-PNET4 only) or QoL. SIOP/UKCCG-PNET3 showed the addition of pre-radiotherapy chemotherapy improved survival rates compared to radiotherapy alone, but there was no difference in QoL between the two treatment arms (Taylor *et al.*, 2003; Taylor *et al.*, 2004; Taylor *et al.*, 2005). Interestingly, QoL varied depending on MB subgroup (MB_{WNT}, MB_{SHH} and $MB_{Grp3/Grp4}$)(Bull *et al.*, 2014). Health-related QoL (HRQoL) was highest in patients with MB_{SHH} and poorest in patients with MB_{WNT}, although the cohort size was very small (Figure 1.9) (Bull *et al.*, 2014). Patients with MB_{SHH} had less IQ decline, and a lower incidence of cerebella mutism and motor defects (Bull *et al.*, 2014), which has also been recapitulated in recent larger studies (Moxon-Emre *et al.*, 2016; Jabarkheel *et al.*, 2020). Heterogeneous MB tumour biology may play a role in determining overall survivorship, however the enhanced QoL seen in survivors of MB_{SHH} tumours is likely due to the tumour location rather than biological subgroup differences; MB_{SHH} tumours are typically hemispheric, whilst $MB_{WNT,}$ MB_{Grp3} and MB_{Grp4} located in the midline (Teo *et al.*, 2013; Perreault *et al.*, 2014; Juraschka and Taylor, 2019).

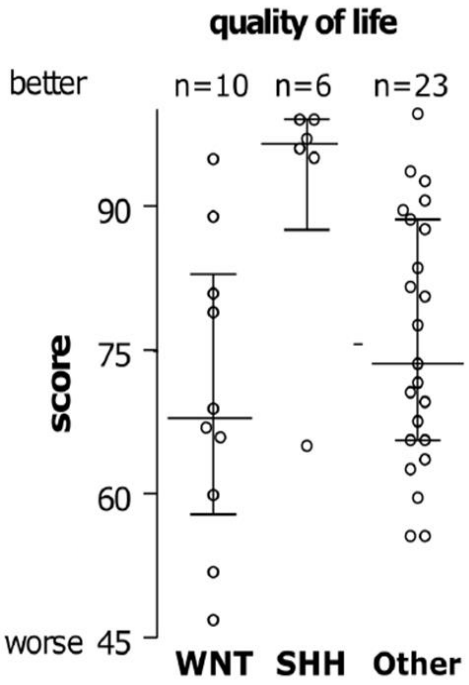

Figure 1.9. Tumour molecular subgroup affects QoL in MB survivors. Patients receiving the same treatment regimens had variable QoL, MB_{SHH} had the best QoL and MB_{WNT} the poorest. 'Other' depicts MB_{Grp3} and MB_{Grp4} combined (Bull *et al.*, 2014).

Later, HIT-SIOP-PNET4 aimed to compare hyper-fractionated radiotherapy (HFRT) with standard radiotherapy (STRT) in terms of survival benefit, and additionally whether either treatment arm had a benefit to QoS (Câmara-Costa *et al.*, 2015). There were no significant differences in overall survival and most measures of QoS between the two treatment arms, though verbal IQ was typically highly following HFRT (Câmara-Costa *et al.*, 2015). MB clinical trials SIOP/UKCCG-PNET3 and HIT-SIOP-PNET4 were completed prior to the introduction of molecular analysis, and consequently subsequent studies did not consider the new biological features of MB such as methylation subgroups (Kool *et al.*, 2012). Molecular annotation was conducted *post hoc* on remaining tumour material from the HIT-SIOP-PNET4 cohort, identifying distinct subgroup-specific risk models within the SR-MB patients (Goschzik *et al.*, 2018), however any relationships with late-effects have not yet been assessed.

SIOP-PNET5-MB (NCT02066220) is the first European MB clinical trial to assess dose de-escalation in FR-MB patients (Mynarek *et al.*, 2021). The trial aims to assess whether a reduced dose radiotherapy and chemotherapy regimen alleviates adverse effects, whilst still

maintaining overall survival. In addition to full clinico-molecular data, SIOP-PNET5-MB will also collect QoS outcome data (including assessment of health status (HUI3), quality of life (PedsQL) and neurological function (MEES)), and germline genotyping data.

Similarly, in the US SR-MB trial SJMB12, low risk patients will also receive therapy de-escalation, with extensive QoS outcome data collected (including assessments of fatigue, motor function and cognitive performance (e.g. BRIEF, WISC and CVLT)). These trials will enable future assessment of associations between clinical, treatment, tumour and host factors and the onset of late-effects, and further understanding into survivorship in MB patients. However, QoS data is not yet available from these trials and it cannot yet be concluded that dose de-escalation precipitates a benefit to late-effect development and as stated, only a minority of patients are eligible for such approaches. Therefore, the is a critical need for the use of model systems to i) test candidate interventions and ii) better understand the mechanisms of late-effect onset to discover novel targets for new intervention strategies.

1.4. Preclinical characterisation of MB treatment-related delayed adverse effects

Functional assessment of treatment-induced late-effects is essential to test candidate interventions and better understand the biological mechanisms underpinning the development of late-effects. The use of mammalian *in vivo* treatment injury models enables appraisal of MB therapy-induced late-effects in close-to-human physiological systems. Moreover, longitudinal appraisal of the overall physical effect of therapeutic insult provides a baseline for the future appraisal of intervention strategies and exploration of the underlying mechanisms of late-effect onset.

1.4.1. Modelling MB radiotherapy induced late-effects *in vivo*

Traditionally, irradiation to the murine brain is delivered via whole-head irradiation, whereby the body is lead-shielded from the radiation, with the head exposed (Wong-Goodrich *et al.*, 2010; Rodgers *et al.*, 2016; Ungvari *et al.*, 2017; de Guzman *et al.*, 2019; Tang *et al.*, 2019). However, delivery via this modality is not precise; non-target regions such as the mouth, ears and eyes are in the radiation field. Consequently, whole-head irradiation comes with high levels of acute toxicity, (e.g. damage to salivary gland, mouth ulceration, eye dryness, weight loss) (Jham and da Silva Freire, 2006; Brook, 2020) and therefore cannot achieve the high radiation doses relevant to MB. Moreover, whole-head irradiation cannot deliver targeted-radiation to specific brain regions, which negates the opportunity to deliver a posterior fossa boost dose. Thus, irradiation using these methodologies cannot fully recapitulate the dose and targeting of medulloblastoma regimens.

To date, previous *in vivo* studies have failed to fully recapitulate humanised MB cranial irradiation due to a failure to achieve either 1) the appropriate targeting, 2) the appropriate dose of radiation administered, 3) investigations in age-appropriate animals and 4) comprehensive, longitudinal late-effect assessment. A summary of previously published studies is provided in Table 1.7, and a detailed introduction to *in vivo* modelling of MB radiotherapy-induced late-effects is provided in Chapter 3.

Study Reference	Clinically relevant MB radiation dose	Juvenile	Targeted cranial irradiation	Assessment of late-effect profile	Long-term follow up
*This thesis and companion publication (Castle et al., 2024)**	✓	✓	✓	✓	✓
(Fielder *et al.*, 2019)	X	X	X	✓	✓
(Tang *et al.*, 2019)	✓	✓	X	X	✓
(Yuen *et al.*, 2021)	X	✓	X	X	X
(Sándor *et al.*, 2014)	X	✓	X	X	X
(Rao *et al.*, 2011)	✓	✓	X	✓	X
(Moravan et al., 2011)	✓	X	X	X	X
(de Guzman *et al.*, 2019)	X	✓	X	X	X
(Ungvari et al., 2017)	✓	X	X	✓	✓
(Yabluchanskiy et al., 2020)	✓	X	X	X	✓
(Wong-Goodrich *et al.*, 2010)	X	X	X	✓	X
(Tomé et al., 2015)	X	X	✓	✓	X
(Belcher et al., 2020)	✓	X	✓	X	X
(Baumann et al., 2012)	✓	X	✓	X	X
(Suckert et al., 2021)	✓	X	✓	X	X
(Lazarini et al., 2009a)	X	X	✓	X	✓
(Beera et al., 2018)	X	✓	✓	X	X
(Ruddy et al., 2020)	X	✓	X	X	X
(Zhang *et al.*, 2018)	X	✓	✓	X	X
(Zhou et al., 2017)	X	✓	X	X	X
(Casciati et al., 2016)	X	✓	X	X	✓
(Zanni *et al.*, 2021)	X	✓	X	X	X

Table 1.7. A summary of the in vivo radiotherapy literature in terms of clinical relevance to paediatric brain tumours (dose, developmental stage, targeting, late-effect assessment and follow up). The studies are summarised according to the following criteria: i) Use of a clinically-relevant radiation dose (single or cumulative) of 18 Gy or higher to the brain, ii) use of juvenile mice under PND 42, iii) delivery of targeted radiation to the brain or sub-region of the brain, iv) comprehensive assessment of the late-effect profile (>2 types of assessments [e.g. neurocognition, physical function, frailty]), v) long-term follow up (≥ 6 months post-irradiation). *The model developed during this thesis has now been published *(Castle et al., 2024)*.

1.4.2. Modelling MB chemotherapy induced late-effects in vivo

The mostly widely used chemotherapy regimens are modifications of Packer chemotherapy (consisting of cisplatin, CCNU, and vincristine; discussed in Chapter 1.1.4.3) (Packer *et al.*, 1994). However, there are currently no published *in vivo* studies that have recapitulated MB combination chemotherapy (Packer-style or any other combination) and assessed the resulting late-effects. Further details of *in vivo* chemotherapy modelling are provided in Chapter 5.

1.5. Understanding the mechanisms underpinning radiation-induced late-effects

1.5.1. Overview

1.5.1.1. The basic structure of the brain

The brain is complex and is organised into many substructures; an overview of the major brain structures is displayed in Figure 1.10. The brain comprises of two hemispheres, organised into four lobes each controlling discrete functions (*Brain Basics: Know Your Brain*, 2025). The frontal lobe, located at the front of the brain, controls high order functions such as decision-making and problem-solving. The motor cortex, located at the back of the frontal lobe, controls voluntary muscle function. The parietal lobe, which contains the somatosensory cortex, is responsible for sensory function and support reading, speech and arithmetic. The occipital lobes, located at the back of the brain, process visual information. Finally, the temporal lobe, located in front of the occipital lobe and under the frontal and parietal lobe, processing auditory information. The hippocampus, located within the temporal lobe, is involved in memory formation is particularly vulnerable to radiation (Turnquist;Harris and Harris, 2020a). The two hemispheres of the brain communicate through the corpus callosum, a large bundle of white matter fibres beneath the longitudinal fissure. MB typically originates in the cerebellum, located under the cerebral hemispheres, which co-ordinates voluntary movement and maintains balance (*Brain Basics: Know Your Brain*, 2025).

There are five major cell types within the brain: neurons, astrocytes, oligodendrocytes, microglia and endothelial cells (McKenzie *et al.*, 2018; Turnquist;Harris and Harris, 2020a). Neurons are primarily responsible for transmitting electrical signalling and are categorised and are supported by glial cells. Astrocytes, the most abundant type of glial cell within the brain, provide structural support, regulate neurotransmitters and maintain the blood-brain barrier (BBB). Oligodendrocytes provide the myelin sheath to neuronal axons and provide metabolic support, facilitating rapid electrical transmission. Microglia are primarily responsible for the immune response within the brain, are become activated following insults such as radiotherapeutic injury (McKenzie *et al.*, 2018; Turnquist;Harris and Harris, 2020a).(McKenzie *et al.*, 2018; Turnquist;Harris and Harris, 2020a). MB patients are particularly vulnerable to the damaging side-effects of radiation, due to typically receiving high doses (up to 36 Gy) to the whole brain, and a boost (up to 54Gy) to the tumour site (typically within the cerebellum).

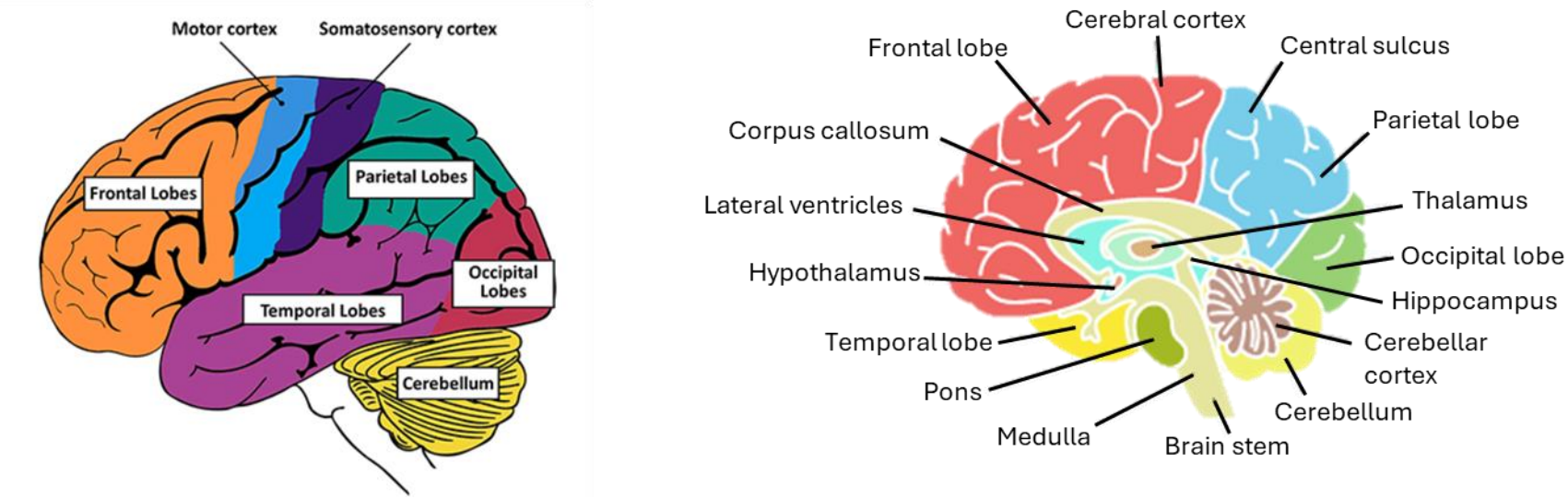

Figure 1.10. The human brain. Sagittal view of the human brain, labelled with the major structures. (Brain Basics: Know Your Brain, 2025). The brain is divided into 4 lobes: the frontal, parietal, temporal and occipital.

1.5.1.2. Radiation-induced brain injury

Early radiation-induced brain injury ranges from acute injury (oedema, headaches, drowsiness) and early-delayed (transient demyelination, reduced attention, and short-term memory loss). When damage is sustained for over 6 months, more permanent late-effects are present. Damage includes the development of abnormal vasculature, demyelination, gliosis and white matter necrosis, resulting in cognitive impairment (Greene-Schloesser *et al.*, 2012). The hippocampus is responsible for learning and memory. Radiation had been shown to reduce neurogenesis and maturation of neurons within the dentate gyrus and subgranular zone (SGZ) of the hippocampus, as well as the subventricular zone (SVZ) of the lateral ventricles (Monje *et al.*, 2002; Lazarini *et al.*, 2009b).

Elucidation of the biological mechanisms underpinning the development of radiotherapy-induced late-effects, provides the potential for the development of new therapies to ameliorate the late-effect burden faced by survivors. Moreover, through understanding the mechanisms involved in the stages of late-effect progression, biomarkers of risk can be identified for improved screening and potential intervention of high-risk patients. The prevention of treatment-related late-effects will lead to both improve overall survival and QoS (Bentzen, 2006; Begg;Stewart and Vens, 2011). The biological mechanisms underpinning the development of acute- and late-toxicities are not completely understood. Radiation destroys tumour cells through the induction of DNA damage; however, this also causes damage to the surrounding healthy tissue (Bentzen, 2006; Begg;Stewart and Vens, 2011). Damage to normal cells induces an inflammatory response, which can persist and induce injury through a wide range of mechanisms including: disruption of the blood-brain barrier, neuronal cell death, reduced neurogenesis, and the induction of a senescence-associated secretary phenotype (SASP) (Figure 1.11).

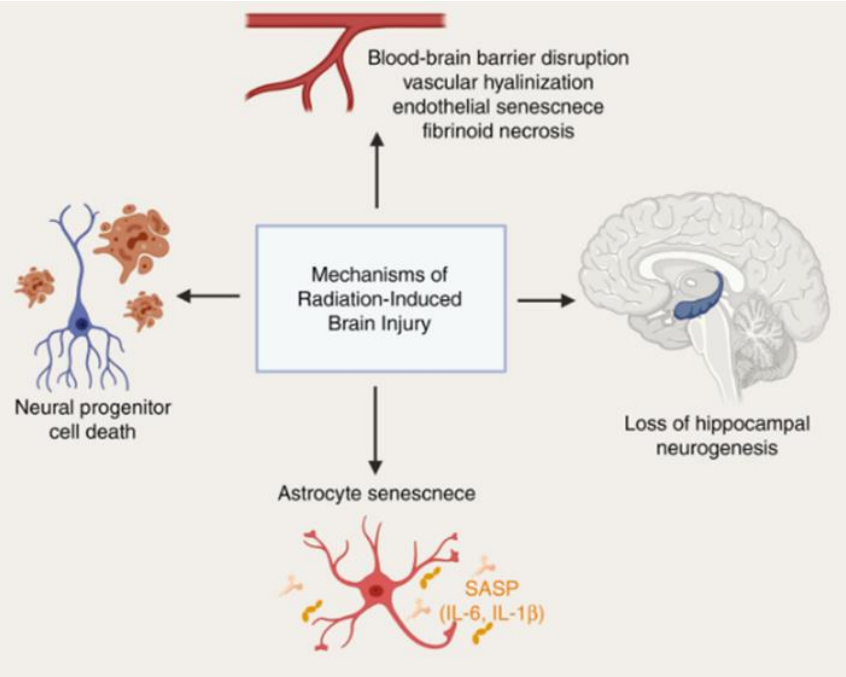

Figure 1.11. Overview of the mechanisms of radiation-induced brain injury (Turnquist;Harris and Harris, 2020b).

1.5.2. Molecular response to radiotherapeutic insult

1.5.2.1. DNA damage

Radiation induces DNA damage which typically leads to cell death, resulting in both direct and indirect tissue injury (Baskar *et al.*, 2014). The major types of DNA damage induced by radiation include base and sugar damage, single-strand breaks, double-strand breaks, clustered DNA damage, and covalent intra-strand or inter-strand crosslinking (Huang and Zhou, 2020). DNA damage that is not repaired induces programmed cell death (Figure 1.12). Tumour cells are particularly sensitive to DNA damage due to their highly proliferative nature and inability to repair.

Radiation can also cause indirect DNA damage in neighbouring cells and tissues through the release of free radicals (Baskar *et al.*, 2014). DNA damage can then further induce oxidative stress and inflammation that can persist for many months, together resulting in potentially irreversible damage to healthy tissue, both within the brain and systemically (Zhao;Diz and Robbins, 2007; Moravan *et al.*, 2011; Greene-Schloesser *et al.*, 2012; Lumniczky;Szatmári and Sáfrány, 2017).

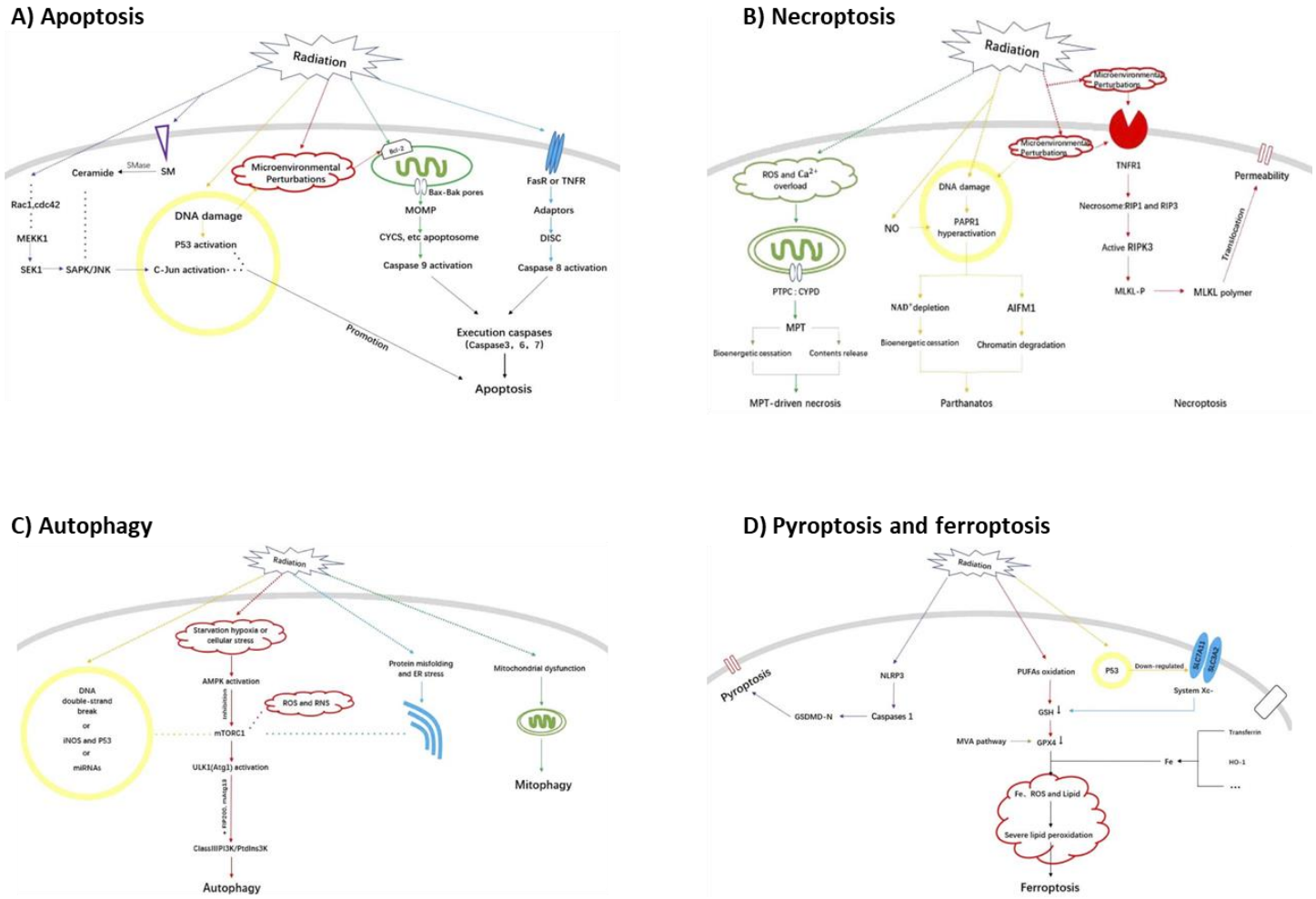

Figure 1.12. Radiation-induced programmed cell death. Radiation induces direct DNA damage, and indirect DNA damage through the production of free radicals. Following DNA damage, cells either undergo programmed cell death via A) apoptosis, B) necroptosis, C) autophagy or D) pyroptosis and ferroptosis (Ketelut-Carneiro and Fitzgerald, 2022).

1.5.2.2. Chronic inflammation

The biological mechanisms underpinning radiotherapy-induced late-effect development remain relatively undefined, though chronic inflammation is thought to play a major role. Radiation to the brain induces neuronal damage, activation of microglia and damage to the blood-brain barrier (BBB) leading to immune infiltration and an inflammatory response. DNA damage within microglia leads to their activation through the NFκB pathway, resulting in upregulation of MHC and CD68, and the release of pro-inflammatory cytokines (e.g. CCL2) (Lumniczky;Szatmári and Sáfrány, 2017). Consequently, peripheral macrophages are recruited through the BBB via CCL2 signalling. Moreover, radiation-induced damage in neurons induces the release of pro-inflammatory cytokines, which also activate microglia. Damaged neurons further recruit microglia; secretion of high-mobility group protein 1 (HMGB1) recruits activated microglia, and the expression of calreticulin induces phagocytosis of both damaged and healthy neurons. Additionally, radiation-induced damage induces upregulation of adhesion markers (e.g. intercellular adhesion molecule 1; ICAM-1) on endothelial cells within the brain microvasculature, which in turn recruits peripheral lymphocytes and monocytes. The pro-inflammatory response induced by damaged neurons and activated microglia also activates dendritic cells within the brain, which further induce an immune activation following migration to the lymph nodes (Lumniczky;Szatmári and Sáfrány, 2017). Activation of microglia, astrocytes, endothelial cells and T cells, leads to increased expression of pro-inflammatory cytokines (examples include TNF-α, IL-1β and IL-6), chemokines (such as CCL3/macrophage inhibitory factor 1) and reactive oxygen species (ROS). This results in a positive feedback loop and ultimately in chronic neuroinflammation (Streit;Mrak and Griffin, 2004; Moravan *et al.*, 2011; Lumniczky;Szatmári and Sáfrány, 2017).

In vivo mouse studies have shown that neuroinflammation can occur as soon as 4 hours after radiation and persist for up to 12 months (Chiang;McBride and Withers, 1993; Kyrkanides *et al.*, 1999). Neuroinflammation and ROS production have been linked to onset of neurocognitive decline; the use of FLASH radiation (ultra-rapid dose delivery) shows reduction in radiation-induced neuroinflammation can reduce neurocognitive decline in *in vivo* models (Montay-Gruel *et al.*, 2019; Simmons *et al.*, 2019).

1.5.2.3. Reactive oxygen species

Radiation can induce DNA damage indirectly through the production of free radicals, derived from the ionisation or excitation of water molecules within the cells (Baskar *et al.*, 2014). Within healthy brain tissues, radiation-induced damage leads to the release of reactive oxygen species (ROS), which results in both acute and chronic neuroinflammation (Bentzen, 2006; Begg;Stewart and Vens, 2011; Moravan *et al.*, 2011; Montay-Gruel *et al.*, 2019). ROS-induced neuroinflammation induces further damage and ROS production, and ultimately chronic inflammation (Ungvari *et al.*, 2013; Wang;Boerma and Zhou, 2016). Moreover, radiation can increase ROS production from mitochondria; radiation-induced mitochondrial damage leads to impaired respiration, and the overproduction of ROS from oxidative phosphorylation (Leach *et al.*, 2001; Shimura *et al.*, 2018). Neuronal cells are particularly vulnerable to ROS damage, due to their high fatty acid contents; radiation induces high levels of lipid peroxidation (Turnquist;Harris and Harris, 2020a), and ultimately neuronal degradation, resulting in neurocognitive decline and impaired physical functioning (Bentzen, 2006; Begg;Stewart and Vens, 2011; Moravan *et al.*, 2011; Montay-Gruel *et al.*, 2019).

1.5.2.4. Senescence-associated secretory phenotype

Moreover, radiation-induced DNA damage and oxidative stress can induce cellular senescence, whereby cells are in a persistent state of cell cycle arrest (Wang;Kohli and Demaria, 2020). Senescent cells secrete a wide variety of signalling factors including interleukins (e.g. IL-6 and IL-1β), chemokines, growth factors, and matrix metalloproteinases (MMPs), together referred to as the senescence-associated secretory phenotype (SASP) (Coppé *et al.*, 2010). SASP molecules are involved in multiple pathophysiological functions (summarised in Figure ***1.13***); SASP release is triggered through the stimulation of a variety of different pathways, and consequently, SASP production is highly variable and often context dependant (Herranz and Gil, 2018; Cuollo *et al.*, 2020). Release of SASP modifies the microenvironment and can lead to activation of nearby immune cells, often resulting in systemic chronic inflammation and ultimately tissue damage (Coppé *et al.*, 2010; Herranz and Gil, 2018; Sun;Coppé and Lam, 2018; Wang;Kohli and Demaria, 2020).

Following radiation to the brain, SASP significantly contributes towards neuroinflammation, neuronal death and ultimately cognitive decline. Astrocytes, activated in response to radiotherapeutic injury, release proinflammatory cytokines which can induce senescence in

endothelial cells. Senescent endothelial cells promote late-effect development by contributing to chronic inflammation through the release of SASP molecules including further proinflammatory cytokines, increased ROS production and upregulation of adhesion molecules (Rochfort and Cummins, 2015; Turnquist;Harris and Harris, 2020a). Proinflammatory cytokine IL-6 is thought play a major role in SASP in response to radiation (Coppé *et al.*, 2010). Following radiation, senescent astrocytes release SASP (including IL-6 and IL-1β) resulting in neurotoxicity and neurodegeneration (Turnquist *et al.*, 2019).

Pathway induction following radiotherapy is highly complex and still not fully understood. Given the diversity and complexity of mechanisms involved in the development of late-effects following radiotherapeutic insult, further investigation is required to elucidate potential therapeutic targets, and thus enable reduction of adverse effects, increase radiation tolerability, and improve QoL in survivors.

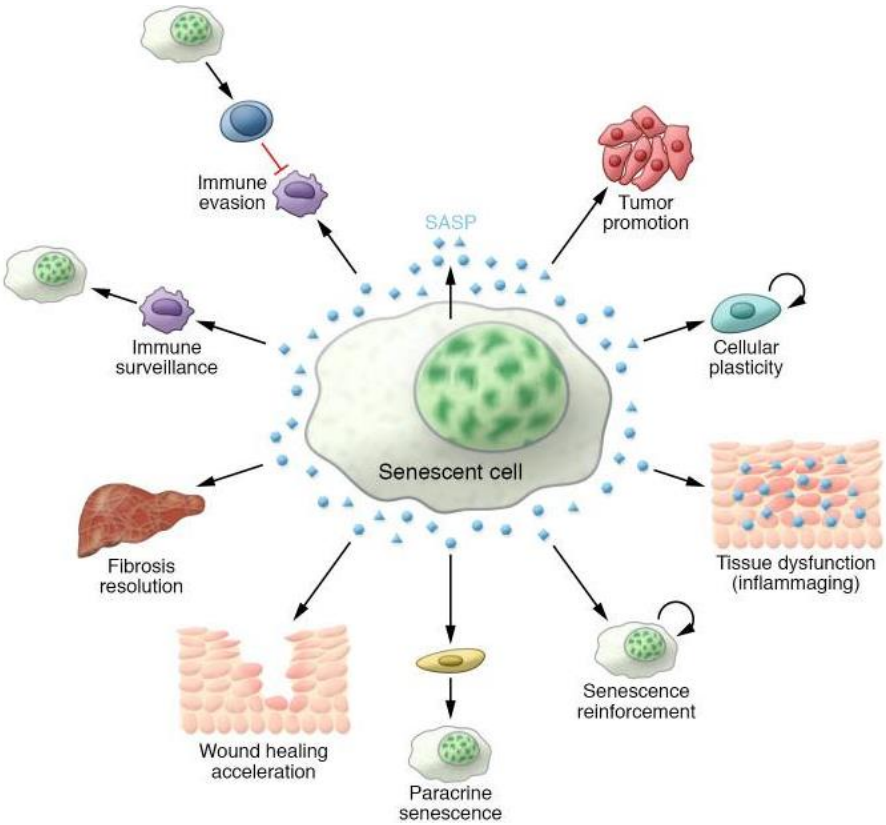

Figure 1.13. Schematic summary of the key functions of SASP (Herranz and Gil, 2018).

1.5.2.5. Radiation-induced perturbations of epigenetic methylation status

DNA methylation plays a major role in the control of gene expression and is considered a hallmark of ageing. DNA methylation patterns are established through the addition or removal of a methyl group to the fifth position of cytosine in DNA, facilitated by DNA methyltransferases (Miousse;Kutanzi and Koturbash, 2017). Whilst patterns of DNA methylation can vary greatly, they consist of conserved regions of unmethylated GC-rich regions with high densities of CpGs, known as CpG islands, that are often correlated with promoter regions. Changes in DNA methylation patterns occur with age and can be a useful tool in predicting the biological age of an individual; DNA methylation patterns can be influenced by external insult and have potential as predictive biomarkers of biological age and age-related diseases (Mozhui and Pandey, 2017; Kling;Wenger and Carén, 2020). External insult from ionising radiation can result in global methylation alterations, as well as gene-specific modifications (Miousse;Kutanzi and Koturbash, 2017). Damage of DNA base guanine, induced directly by radiation or subsequent ROS production, can inhibit methylation of adjacent cytosine and resulting in local hypomethylation (Rang and Boonstra, 2014). Moreover, methylation on damaged cytosine, may be lost during the DNA damage repair. ROS can also have bystander effects and interfere with DNA methyltransferases, inducing global methylation alterations (Miousse;Kutanzi and Koturbash, 2017). Alterations to methylation patterns can lead to an increased risk of cancer development, through genomic instability, activation of proto-oncogenes and silencing of tumour suppressor genes (Eden *et al.*, 2003; Donkena;Young and Tindall, 2010).

As a consequence of treatment, brain tumour survivors often experience a premature ageing phenotype, where their 'epigenetic age' is often older than their 'chronological age' (Field *et al.*, 2018; Kling;Wenger and Carén, 2020; Salameh;Bejaoui and El Hajj, 2020). Several epigenetic clocks have been developed to predict chronological age, through the assessment of variable CpG sites. Mathematical algorithms use the methylation status of genome-wide CpG sites to predict DNA methylation age (Mozhui and Pandey, 2017). Qin *et al* showed survivors of childhood cancers had a significantly higher estimated epigenetic age acceleration (EAA) compared to matched controls, and increased EAA was associated with prior treatment of radiotherapy or alkylating chemotherapy (Qin *et al.*, 2021). Moreover, within survivors the presence of unfavourable health conditions was also significantly associated with an increased EAA.

1.6. Aims of the study

Most childhood MB patients survive their tumour as a result of intensive multimodal treatment typically consisting of surgical resection, radiotherapy and chemotherapy. However, the receipt of such treatment often leaves survivors with debilitating late-effects. The receipt of radiation to the brain, particularly at a young age, poses the greatest risk of reduced quality of life, with many survivors experiencing poor neurocognitive outcomes and impaired physical functioning.

For a small subset of patients (e.g. favourable-risk MB_{WNT}) dose de-escalation may be possible, however, for many patients an intensive radiotherapy and chemotherapy schedule remains critical for survival. There is an urgent need for the development of interventions to prevent or ameliorate the late-effects that burden survivors throughout their adolescents and adulthood. However, the development of such interventions is hindered by a paucity of suitable experimental models. Previous *in vivo* models do not recapitulate MB radiotherapy, falling short of modelling one or more key components of i) delivering high-dose, targeted radiotherapy, (ii) using an equivalent age model and (iii) performing longitudinal and comprehensive long-term follow up.

The development of a suitable preclinical model will provide a platform to observe the progression of late effects and understand the biological mechanisms underpinning late-effect development, leading to identification of biomarkers and druggable interventions, as well as provide a baseline for the appraisal of future intervention strategies. Therefore, this study aims to:

1) Develop a baseline model that recapitulates childhood MB radiotherapy delivery/dose at an MB-equivalent developmental stage, using the Small Animal Radiation Research Platform (SARRP) to deliver highly targeted radiation to the brain and posterior fossa.
2) Longitudinally follow up irradiated mice to track the progression of late-effect development (physical functioning, premature ageing and neurocognition) up to the equivalent of human 40-50 years old.
3) Understand the biological response to radiotherapeutic insult *ex vivo*, to aid identification of key molecular pathway alterations and any potential further biomarkers for improved surveillance of late-effect development.

4) Develop an *in vitro* model for characterisation of the molecular insult response to MB radiotherapy, to provide a platform for identification of pharmacological targets and the appraisal of novel therapeutic interventions.
5) Establish the appropriate scheduling/dosing of MB-like chemotherapy to provide a pre-clinical platform for the future assessment of chemotherapy-induced late-effects.

Chapter 2. Materials and methods

2.1. In vivo murine studies

2.1.1. Ethical approval

The work was licensed by the UK Home Office (PBDAFDFB0 and P67C4EBE4) and complied with the guiding principles for the care and use of laboratory animals. Ethical approval was granted by Newcastle University Animal Welfare and Ethics Review Body.

2.1.2. Husbandry

Juvenile male C57BL/6J mice were purchased from Charles River post-weaning and maintained in groups of three littermates in individually ventilated cages. Cages contained sawdust, paper bedding and environmental enrichment. Mice were housed at 20 ± 2°C under a 12-hour light/12-hour dark photoperiod. They received standard rodent pelleted chow *ad libitum* (Special Diets Services, Witham, UK). Body weight was recorded at least weekly. Mice were humanely culled via schedule 1 methods.

2.1.3. Identification

Mice were identified by either radiofrequency identification (FRID, IMI-500 Read Only Transponder), ear-notching, or tail-marking.

2.1.4. Venepuncture

To enable blood withdrawal, mice were placed in a heated cabinet for 15 minutes prior to the procedure for better visualisation of the veins. Mice were placed in a restraint tube and a small incision (size 11 scalpel; Swann Morton) was made to one of the two lateral tail veins. Blood was collected in microvette 100 K3 EDTA capillary tubes (VWR, SARS20.1278). Following venepuncture, light pressure was applied to the incision site until bleeding ceased. Up to 10% total blood volume (TBV), and no more than 15% TBV in any 28 period was collected.

2.2. Physical functioning assessment

2.2.1. Forelimb grip strength

Physical functioning was assessed using the Grip Strength Test (BIO-GS3, BIOSEB) (Figure 2.1A). Mice were slowly lowered via the tail and gripped onto the device with their forepaws. The maximal peak force was recorded (grams, g), and the mean was calculated from three attempts.

2.2.2. Rotarod

To assess balance, co-ordination and endurance, mice were placed on the rotarod (Roto-Rod Series 8, IITC Life Science; Figure 2.1B), which began to rotate at an initial speed of 4 rpm, and gradually accelerated by 7.2 rpm per minute [12]. Time on the rod (seconds) was recorded automatically when mice fell from the rotarod. The landing area was padded with soft foam to minimise impact of falling. Quiet, low light conditions were used to minimise stress during testing. Mice were tested 3 times per day, for 2 consecutive days, with approximately 20-minute intervals between trials. The mean was calculated using scores across both days.

2.2.3. Hanging wire

Mice were gently lowered via the tail and suspended from the middle of a plastic wire (diameter 2 mm, and 30 cm in length) with their forelimbs and left to hang for up to 60 sec (Figure 2.1C). Success was measured as a mouse hanging for the total 60 sec, getting all 4 limbs onto the wire (time taken recorded), or reaching the end of the wire (time taken recorded). Failure was measured as a mouse falling before 60 sec. Mice were given up to 3 trials to succeed with 10 minutes rest between attempts. The wire was suspended 30 cm above a landing pad (20 cm depth of soft foam), which proved high enough to discourage deliberate dropping but reduced the impact from falling.

Figure 2.1. Assessments of physical functioning. A) Forepaw grip strength test, B) Balance and co-ordination (rotarod) and C) strength and co-ordination (hanging wire). Created using BioRender.

2.3. Frailty assessment

Frailty was assessed using a Rockwood-style frailty index as previously described (Fielder *et al.*, 2019). Briefly, 30 parameters of frailty (summarised in Table 2.1) were scored on a scale from 0 (no impairment) to 1 (severe impairment). Body temperature was recorded from the surface of the mid-abdomen using an infrared thermometer.

Body weight, body temperature and grip strength were scored according to degrees of standard deviation (SD) from the mean of age- and sex- matched controls (0: <1SD; 0.3: 1SD–2SD; 0.7: 2SD–3SD; 1: ≥3SD).

System and Parameter	Potential Deficits
Integument	
Alopecia	Hair loss due to age-related balding and/or barbering (fur trimming)
Loss of fur colour	Change in fur colour from black to grey
Dermatitis	Inflammation, over-grooming, barbering or scratching causing skin erosion. Can result in open sores anywhere on the body
Loss of whiskers	Loss of vibrissae (whiskers) due to aging and/or whisker trimming
Coat condition	Ruffled fur and/or matted fur. Ungroomed appearance. Coat does not look smooth, sleek, and shiny
Physical/musculoskeletal	
Tumours/masses	Development of tumours or masses anywhere on the body
Distended abdomen	Enlarged abdomen. May be due to tumour growth, organ enlargement, or intraperitoneal fluid accumulation
Kyphosis	Exaggerated outward curvature of the lower cervical/thoracic vertebral column. Hunched back or posture
Tail stiffening	Tail appears stiff, even when animal is moving in the cage. Tail does not wrap freely when stroked
Gait disorders	Lack of coordination in movement including hopping, wobbling, or uncoordinated gait. Wide stance. Circling or weakness
Tremor	Involuntary shaking at rest or during movement
Forelimb grip strength	A decline in forelimb grip strength
Body condition score	Visual signs of muscle wasting or obesity based on the amount of flesh covering bony protuberances
Vestibulocochlear/auditory	
Vestibular disturbance	Disruption in the ability to perceive motion and gravity. Reflected in problems with balance, orientation, and acceleration
Hearing loss	Failure to respond to sudden sound (e.g., clicker) indicative of hearing loss or impairment
Ocular/nasal	
Cataracts	Clouding of the lens of the eye. An opaque spot in the centre of the eye
Corneal opacity	Development of white spots on the cornea. Cloudy cornea
Eye discharge/swelling	Eyes are swollen or bulging (exophthalmia). They may exhibit abnormal secretions and/or crusting
Microphthalmia	Eyes are small and/or sunken. May involve one or both eyes
Vision loss	Vision loss, indicated by failure to reach toward the ground when lowered by the tail
Nasal discharge	Signs of abnormal discharge from the nose
Digestive/urogenital	
Malocclusions	Incisor teeth are uneven or overgrown. Top teeth grow back into the roof of the mouth or bottom teeth are long and easily seen
Rectal prolapse	Protrusion of the rectum just below the tail
Penile prolapse	Penis cannot re-enter the penile sheath.
Diarrhoea	Faeces on the walls of the home cage. Bedding adheres to faeces in cage. Faeces, blood, or bedding around the rectum
Respiratory	
Breathing rate/depth	Difficulty breathing (dyspnoea), pulmonary congestion (rales), and/or rapid breathing (tachypnoea)
Discomfort	
Mouse Grimace Scale	Measure of pain/discomfort based on facial expression. Assessment of five facial features: orbital tightening, nose bulge, cheek bulge, ear position (drawn back), or whisker change (either backward or forward)
Piloerection	Involuntary bristling of the fur due to sympathetic nervous system activation
Other	
Temperature	Increase or decrease in body temperature
Weight	Increase or decrease in body weight

Table 2.1. Parameters assessed during assessment of Frailty (Whitehead *et al.*, 2014)**.**

2.4. Assessment of neurocognitive function

2.4.1. Y-maze

The Y-maze was used to assess working memory(Maurice *et al.*, 1994). The maze consisted of 3 arms made of dark grey plastic; each arm was 40cm long, 5cm wide and 10cm high. Mice were placed in arm A and observed for 8 minutes; arm entry was manually recoded. Quiet, low light conditions were used to minimise stress during testing. Novel arm entries were calculated from the number of times a mouse entered a novel arm of the maze in 3 consecutive entries (e.g. A-B-C; Figure 2.2). Working memory was quantified by spontaneous alternation, which was defined as follows:

$$\text{Spontaneous alternation} = \frac{Novel\ arm\ enteries}{\text{Total arm enteries} - 2}$$

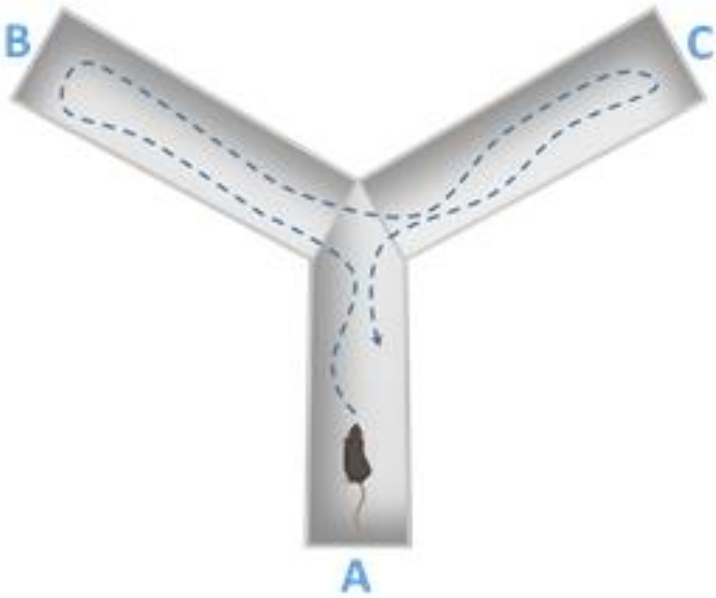

Figure 2.2. Working memory assessed using the Y-maze. Spontaneous alternation was defined as the frequency of a mouse entering a novel arm of the maze in 3 consecutive entries (e.g. A-B-C). Created using BioRender.

2.4.2. Barnes maze

Learning, short- and long-term memory was assessed using the Barnes maze as previously described (Figure 2.3) (Fielder *et al.*, 2020). The Barnes maze consisted of 20 holes, surrounded by four visual cues (square, circle, cross, triangle, Figure 2.3B). The target hole contained an escape box underneath. Target hole allocation was randomly assigned across visual cues and treatment groups. The maze was thoroughly cleaned and rotated 90° between each mouse and trial to remove potential olfactory cues. Briefly, testing consisted of 4 steps:

Day 1: Initial acclimatisation – the mouse was placed in an opaque holding chamber for 10 seconds, then gently guided to the target hole. The mouse stayed in the escape box for 2 minutes.

Day 1-4: Spatial acquisition (training period) – after 10 seconds in the holding chamber, the mouse attempted to locate the target hole for up to 3 minutes. If after 3 minute the mouse had entered the escape box, the mouse was gently guided in. The time taken to locate the target hole and enter the escape box was recorded, referred to as primary latency. The mouse remained in the escape box for 1 minute. Spatial acquisition was repeated for 4 trials per day for 4 days, with approximately 25 minutes between trials for memory consolidation.

Day 5: Probe 1 (short-term memory test) – 24 hours after the final day of spatial acquisition, the escape box was removed from the target hole and the mice explored the maze for 90 seconds. Primary latency was recorded.

Day 12: Probe 2 (long-term memory test) – 7 days after probe 1, the escape box was removed from the target hole and the mice explored the maze for 90 seconds. No training/testing took place on days 6-11. Primary latency was defined as the time taken to locate the target hole.

Mice were videoed during spatial acquisition, probe 1 and probe 2 for subsequent analysis.

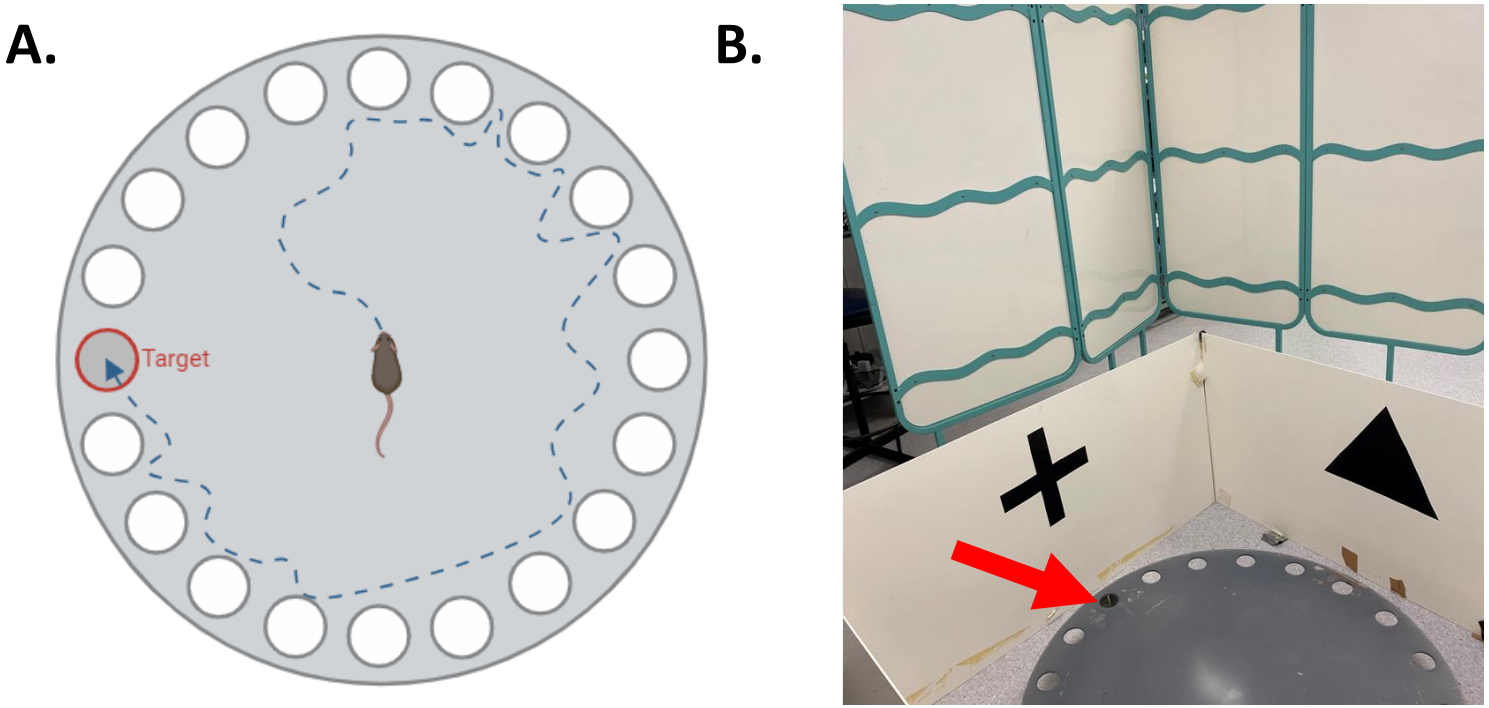

Figure 2.3. Learning and memory assessed via the Barnes maze. Red text/arrow depicts the target hole. Created using BioRender.

2.5. In vivo evaluation of cancer chemotherapeutics

Prior to administration of substances, animals were weighed and assessed to be in good general health. Chemotherapeutic agents (details provided in Table 2.2 were administered at 5ml/kg via intraperitoneal (IP) and intravenous (IV) injections using Micro-Fine+ U-100 0.5 ml Insulin Needle (Becton Dickinson) and adhering to Laboratory Animal Science Association (LASA) guidelines.

For IP injections, mice were restrained via the scruff and substances administered into the lower left and right quadrants of the abdomen. For repeated doses, injection site was alternated. For IV injections, mice were placed in a heated cabinet for 15 minutes prior to procedure for better visualisation of the veins. Mice were carefully placed in a restraint tube, with the tail exposed and the lateral tail veins were visualised. The substance was administered in up to two attempts. Following injection, light pressure was applied to the injection site until any bleeding ceased.

Compound	Product code	Brand (Supplier)	Vehicle	Administration route	Dose (per day, mg/kg)	Total dose (per cycle, mg/kg)	Dosing duration per cycle
Cisplatin	HY-17394	Generon (MedChemExpress)	0.5% CMC-Na/saline	IP	2	10	10 days
Vincristine sulfate	HY-N0488	Generon (MedChemExpress)	PBS	IP	1.5	1.5 - 3	2 – 4 days
Cyclophosphamide	HY-17420	Generon (MedChemExpress)	PBS	IV	60 - 200	60 - 200	2 days
CMC-Na	HY-Y0703	Cambridge bioscience (MedChemExpress)	saline	*Vehicle for cisplatin*			

Table 2.2. Details of chemotherapeutic agents and vehicles. Product code, supplier and vehicle for chemotherapeutic drugs used for the *in vivo* Packer-style chemotherapy regimens. Dose, total dose and duration varied across regimens (detailed in Chapter 6). CMC-Na: Sodium carboxymethyl cellulose (viscosity:800-1200mPa.s), PBS: phosphate buffered saline, IP: intraperitoneal injection, IV: intravenous injection.

2.6. Assessment of tolerability to chemotherapy

Body weight (grams) was recorded prior to the receipt of chemotherapy, daily during dosing, and then for 14 days following receipt of chemotherapeutic agents. Change in body weight for each animal was calculated in comparison to their starting weight for each cycle. Soaked food was provided if weight loss reached over 10%, and mice were humanely culled if weight loss could not be remedied with further supportive measures (e.g. diet gel and rehydration via saline injection) and weight loss reached over 25%.

General health was assessed daily during dosing, and then for 14 days following receipt of chemotherapeutic agents. Mice were scored on the following characteristics: activity, appearance, respiration, and hydration (Table 2.3). An overall score of 1 or less was considered normal, an overall score of 2 or more resulted in increased monitoring and the provision of soaked diet, and an overall score of 5 or more resulted in humane culling. Any individual characteristic scoring 3 resulted in immediate humane culling.

Power calculations were used to determine group size for the tolerability study. Accepting a type I error probability p=0.05 and a power of 80%, 4 – 6 animals per group are required to detect a 25% change in a two-sided comparison. Therefore, 6 mice per treatment regimen were used to ensure suitable power and mitigate a reduction in group size during treatment.

2.6.1. Frailty assessment

Frailty was assessed using a 30-parameter frailty index, as previously described in section 2.3.

	0	1	2	3
Activity	Normal, stands upright, explores, climbs	Active but avoids being upright on hind legs	Inactive, move around bottom of cage only	No activity, only moves when provoked
Appearance	Normal, well groomed	Patches of piloerected hair	majority of back fur piloerected	Mouse appears puffy
Respiration	Normal rapid mouse breathing	Brief periods of laboured breathing, abdominal breathing	Laboured abdominal breathing, no gasping	Laboured abdominal breathing with gasps >1 sec between breaths
Hydration	Skin doesn't tent when scruffed	Skin tents briefly but returns to normal	Skin tents and takes more than 2 seconds to return to normal	Skin tents and stays tented

Table 2.3. General health scoring. Any individual characteristic scoring 3 resulted in immediate humane culling. An overall score of 1 or less was considered normal, an overall score of 2 or more resulted in increased monitoring and the provision of soaked diet, and an overall score of 5 or more resulted in humane culling.

2.7. In vivo administration of X-ray radiation to mice

To facilitate the development of the *in vivo* model using the Small Animal Radiation Research Platform (SARRP; located at the University of Leeds), a cross-institutional collaboration was developed. Prof. Susan Short (University of Leeds) was responsible for the administration of the targeted cranial radiation. To facilitate the visualisation of the posterior fossa in young mice, a recently weaned (postnatal day [PND] 21) C57Bl/6J male mouse was humanely culled and a T2 Fast Spin Echo MRI was performed in the coronal, axial and sagittal planes (10 minutes per plane). To assess the optimal collimator size for the CRT and PFB irradiation doses, the mouse was transferred the SARRP and CT-imaged. Dose verification was carried out by end-to-end testing by NPL and Innovate UK.

Following recovery, mice were transferred to Newcastle University for subsequent assessment, where assessors were blind to the allocation of radiation group.

2.7.1. Delivery of MB-equivalent cranial irradiation

Mice received either CRT or CRT with PFB at human MB-equivalent doses and compared to sham-irradiated controls. All mice (n=36) were anaesthetised with isoflurane and placed into the SARRP, independent of receipt of radiation.

2.7.2. Acute toxicity

Mice were assessed for typical signs of ill health, as well as increased intracranial pressure including reduced mobility, hunching, decrease in food intake, hypersensitivity upon touching and handling, separation from cage mates. Mice were weighed daily during dosing and then for 14 days following receipt of radiation. Mice were humanely culled if weight loss exceeded 10%.

2.7.3. Evaluation of radiation-induced delayed toxicities

Following recovery from the irradiation (approximately two weeks), mice were transferred to Newcastle University (~PND 63) for subsequent assessment. Prior to transport, mice were assessed for good health and stabilisation of body weight. Mice were transported in travel boxes by an approved courier. On arrival in Newcastle, mice were provided with extra bedding and assessed for good health. If dehydration, or signs of distress occurred during transport, mice were treated with fluids (IP or SC) and/or soaked diet. Mice were housed in groups of 3 littermates and acclimatised for 2 weeks.

Mice were longitudinally assessed for physical functioning, frailty and neurocognitive function (methodologies previously detailed in chapter 2.2-2.4), for over one year (up to ~PND 394). Assessors were blind to allocation of radiation group. Body weight was assessed at least weekly. If more than 2 grams were lost in one week, animal weights were monitored daily, provided with soaked food, and humanely culled if weight loss continued for 3 consecutive days.

2.8. Ex vivo sample preparation

Brain tissue was harvested and typically split in half, then rapidly placed into the respective media. The brain was carefully removed from the skull and placed into a stainless-steel brain matrix (Fisher Scientific, 10-000-776) for microdissection with a scalpel (as shown in Figure 2.4). Briefly, a sagittal cut separated the left and rights hemispheres of the brain. Then, 3 coronal cuts separated each hemisphere into 4 sections containing the forebrain, hippocampus 1, hippocampus 2 and the cerebellum. For frozen storage, tissue was immediately placed into liquid nitrogen to flash-freeze then transported to a -80°C freezer for long-term storage. For fixation, tissue was placed in a Histosette I biopsy cassette (VWR, 720-0900) and placed in 4% paraformaldehyde (PFA; VWR, 9713.5000) for 24 hours, then transferred to 70% ethanol for long-term storage. The tissue cassettes were processed by Xin Xu (Histopathology Technician, Newcastle Biobank) using an automated benchtop tissue processor (Lecia TP1020) before paraffin wax embedding (Microm EC 350), both according to manufacturer's instructions. Blood was collected and placed on blue ice, before immediate processing.

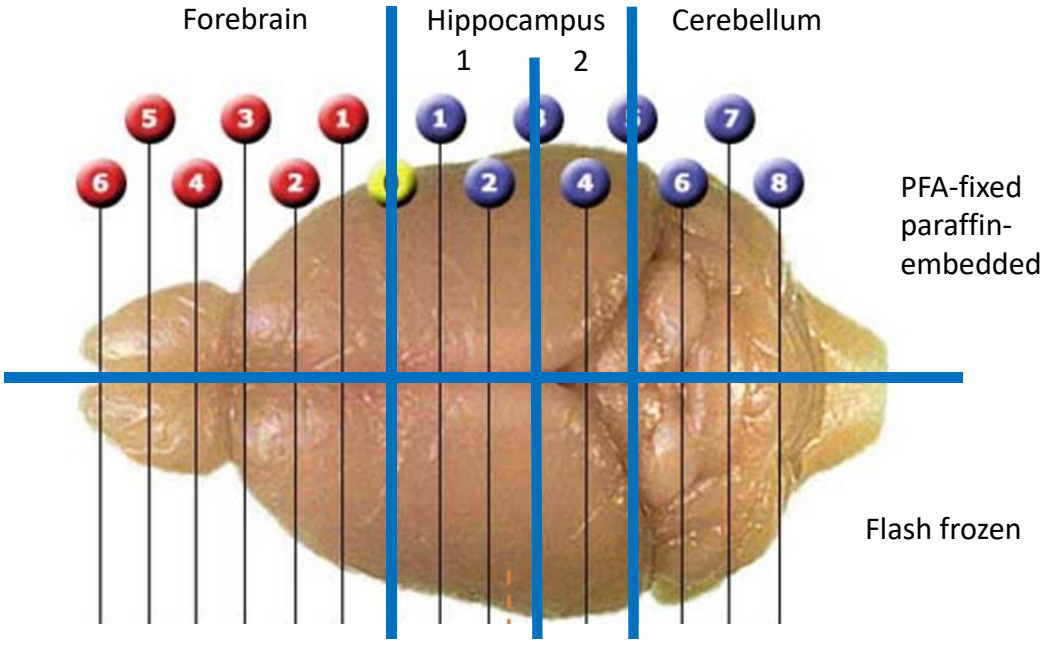

Figure 2.4. Microdissection plan of the mouse brain. Following removal from the skull, the brain was sectioned as per the blue lines into 8 sections (separation of the left and right hemispheres, then separated into: forebrain, hippocampus 1, hippocampus 2 and the cerebellum). The sections from the left side of the brain (bottom half of the image) were flash-frozen in liquid nitrogen and sections from the right side of the brain (top half of the image) were placed in PFA for 24 hours.

2.9. Nucleic acid extractions

2.9.1. DNA extraction

DNA was extracted from fresh blood and frozen tissue samples using the DNeasy Blood and Tissue Kit (Qiagen, 69506) following manufactures instructions, with an additional preliminary step was carried out for frozen tissues. Briefly, samples were thawed, then homogenised with 180 µL buffer ATL and 5 mm stainless steel ball (Qiagen, 69989) for 3 minutes at speed 30 in the TissueLyser LT (Qiagen, 85600). 20 µL proteinase K was added and samples were vortexed for 15 seconds then incubated at 56 °C for 1 hour until completely lysed. 200 µL buffer AL and 200 µL ethanol (96-100%) to each sample and vortexed to mix. Samples were transferred to DNeasy Mini spin column (in a 2 mL collection tube) and centrifuged at >6,000 x g (8,000 rpm) for 1 min. The flow through and collection tube were discarded. The column was placed in a clean collection tube, 500 µL buffer AW1 added into the column and centrifuged at >6,000 x g (8,000 rpm) for 1 minute. The flow through and collection tube were discarded. The column was placed in a clean collection tube, 500 µL buffer AW2 and centrifuged at >20,000 x g (14,000 rpm) for 3 minutes. The flow through and collection tube were discarded. The column was placed in a clean 1.5 mL Eppendorf, and 150 µL buffer AE added directly onto the column membrane. Samples were incubated for 5 minutes at room temperature, then centrifuged at >6,000 x g (8,000 rpm) for 2 minutes to elute the DNA.

2.9.2. DNA quantification

Quantification of double-stranded DNA (dsDNA) was assessed using the Qubit™ dsDNA Broad Range (BR) Assay kit (Invitrogen, Q32850) and the Qubit™ 2.0 Fluorometer (Invitrogen, Q32866), following manufacturer's instructions. Briefly, a working solution was prepared by diluting the Qubit™ dsDNA BR reagent 1:200 in Qubit™ dsDNA BR buffer. Standards and samples were prepared in thin-walled, clear 0.5 mL PCR tubes (ThermoFisher Scientific, Q32856). Standards were prepared by mixing 10 µL of Qubit™ standard with 190 µL working solution, and samples were by mixing 1 µL of Qubit™ standard with 199 µL working solution. The Qubit™ 2.0 Fluorometer was then calibrated using the standards, and a standard curve calculated. Each sample was placed in the Qubit™ 2.0 Fluorometer for quantification.

2.9.3. RNA extraction

RNA was extracted using the TRIzol method. Briefly, frozen tissue was homogenised as above with 1 ml TRIzol reagent (ThermoFisher Scientific, 15596026) and a 5mm stainless steel ball. 200 µL chloroform (ThermoFisher Scientific, J67241.AP) was added and samples were vortexed for 15 seconds, incubated for 2 minutes at room temperature then centrifuged at 12,000 x g for 15 minutes at 4°C. The upper, RNA-containing, aqueous layer was transferred to a clean 1.5 ml microfuge tube. 500 µL isopropanol (Fisher Scientific, 11453733) and 1 µL UltraPure Glycogen (ThermoFisher Scientific, 10814010) were added. Samples were mixed by inversion and then incubated at room temperature for 10 minutes. RNA was pelleted by centrifuged at 12,000 x g for 15 minutes at 4°C, and the supernatant removed. The pellet was then washed in 1 ml 75% ethanol, briefly vortexed and then centrifuged at 7,500 x g for 5 minutes at 4°C. The ethanol was removed, and then the microfuge tube was left open for any remaining ethanol to evaporate. One the RNA pellet was dried, 30 µL RNAase-free water was added and the sample was incubated at 50°C for 5 minutes to dissolve the pellet.

The RNA was then purified using the RNeasy MinElute Cleanup Kit (Qiagen, 74204) following manufacturer's instructions. Briefly, 70 µL RNAase-free water, 350 µL buffer RTL and 250 µL ethanol (96-100%) was added to each sample and mixed well with a pipette. Samples were then transferred to RNeasy MinElute spin columns, and centrifuged at ≥8000 x g (≥10,000 rpm) for 15 seconds. The flow through and collection tube were discarded. Samples were then washed with 500 µL buffer RPE, and centrifuged at ≥8000 x g (≥10,000 rpm) for 15 seconds. The flow through and collection tube were discarded. Next, 500 µL 80% ethanol was added to each column, samples were centrifuged at ≥8000 x g (≥10,000 rpm) for 2 minutes, and the flow through and collection tube were discarded. The column was placed in a clean collection tube, and centrifuged at full speed for 5 minutes to dry membrane. Finally, the column was placed in a clean 1.5 mL Eppendorf, and 14 µL RNase-free water added directly onto the column membrane. Samples were incubated for 5 minutes at room temperature, then centrifuged at full speed for 2 minutes to elute the RNA.

2.9.4. RNA quantification

The quantity and quality (RNA integrity number; RIN) of RNA was assessed using the RNA ScreenTape (Agilent, 5067-5576) with the 4200 TapeStation system (Agilent, G2991BA), following manufacturer's instructions. The RNA Sample buffer was brought to room

temperature for 30 minutes and the RNA ladder and RNA samples were thawed on ice. Samples were prepared as summarised in **Error! Reference source not found.**. Briefly, 1 µL of e ach RNA sample was added to 5 µL RNA sample buffer in either Optical Tube 8x Strip (Agilent, 401428) or 96-well sample plates (Agilent, 5042-8502), and covered with Optical Cap 8x Strip (Agilent, 401425) or 96-well Plate Foil Seal (Agilent, 5067-5154), respectively. Samples were vortexed (Agilent, IKA MS3 with 96-well sample plate adapter) for 1 minute, then briefly centrifuged to remove any bubbles. Samples were then denatured 72 °C for 3 minutes, then placed on ice for 2 minutes. Samples were then briefly centrifuged for 1 minute, then placed into the TapeStation for quantification.

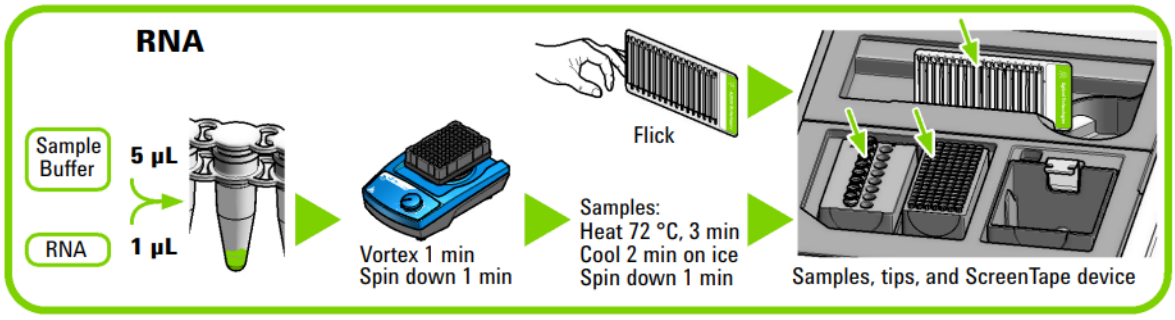

Figure 2.5. Sample preparation for quantification using the Agilent RNA ScreenTape Assay (Agilent TapeStation RNA ScreenTape Quick Guide).

2.10. Immunohistochemistry

Immunohistochemistry (IHC) was conducted on mouse brain tissue. Slide preparation, staining and analysis was conducted with technical assistance from Rachel Howarth (IHC Technician, Newcastle University Centre for Cancer). An overview of the IHC protocol is shown in

Figure 2.6 and detailed methodology is provided in sections 2.10.1-2.10.4.

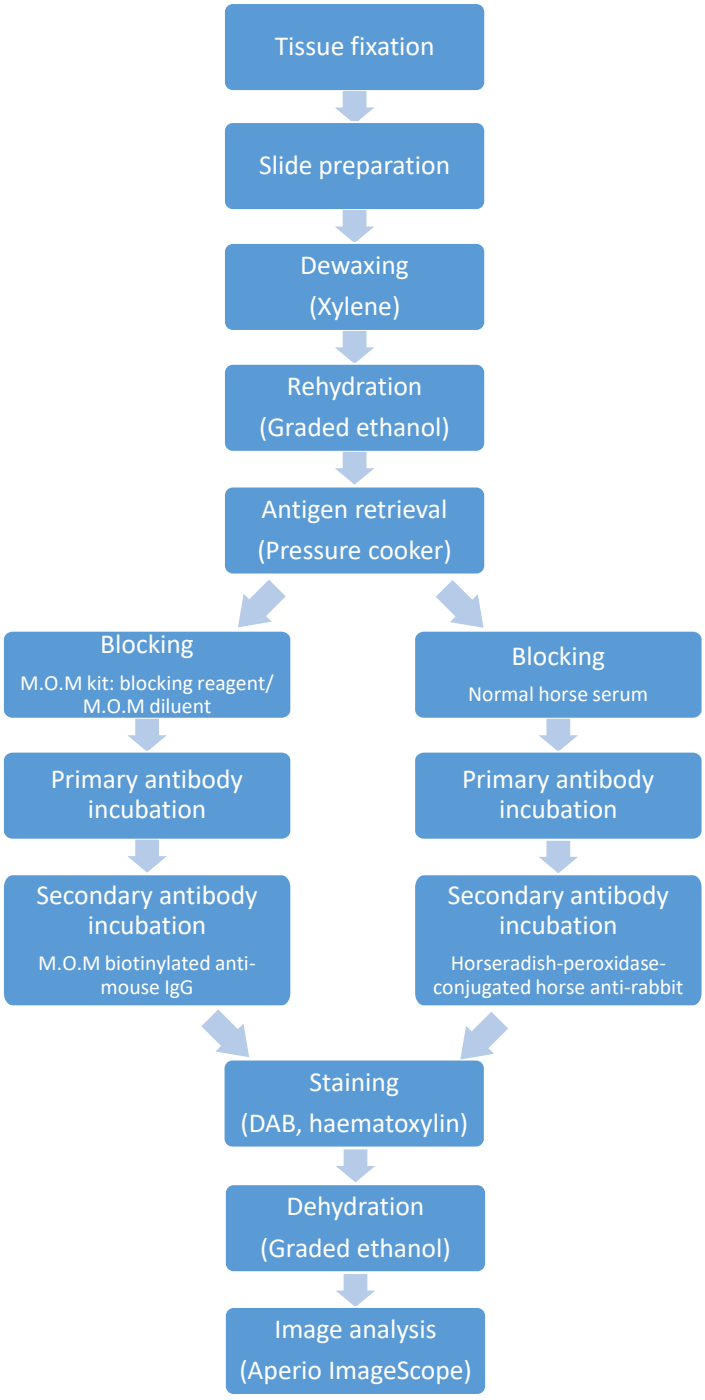

Figure 2.6. Immunohistochemistry protocol overview. Protocol varies based on the host species of the primary antibody. For mouse antibodies, a mouse-on-mouse (M.O.M) kit was used to minimise cross-reactivity.

2.10.1. Slide preparation

Tissue from the cerebellum and hippocampus of mice aged ~PND 394 (approximately a year after the receipt of CRT, CRT+PFB or sham irradiation; n=3 per group) was micro-dissected and fixed as described in chapter 2.8. Fixed tissue was sliced into 4 µm sections using a microtome (Microm HM315), placed on water and collected onto a glass slide. Samples were dewaxed in xylene and rehydrated through decreasing ethanol concentrations. Slides were placed in a pressure cooker for 20 minutes with either sodium citrate (pH 6) or Tris-EDTA (pH 9) buffer (see Table 2.4) for antigen retrieval, then rinsed in 1x Tris-buffered saline with Tween (TBST) for 5 minutes.

2.10.2. Primary antibodies

2.10.2.1. Mouse-on-mouse primary antibodies

Where appropriate, to minimise cross-reactivity, a mouse-on-mouse (M.O.M) immunodetection kit was used, following manufacturer's instructions. Details for all regents and antibodies are provided in Table 2.4. Briefly, slides were placed in a humidity chamber and blocked with M.O.M blocking reagents for 1 hours at room temperature, then incubated with M.O.M diluent for 5 minutes. 200 µL of diluted primary antibody (diluted in M.O.M diluent) was added to each slide and incubated for 30 minutes at room temperature. Next, slides were incubated with secondary antibody (M.O.M biotinylated anti-mouse IgG reagent) for 10 minutes at room temperature. Followed by staining with Vectastain Elite ABC reagents for 5 minutes at room temperature. Between each incubation step, slides were washed with TBST and Tris-Buffered Saline (TBS) for 2 minutes each.

2.10.2.2. Rabbit primary antibodies

Following antigen retrieval, 2.5% normal horse serum was applied to the tissue for 60 minutes at room temperature to block non-specific binding. Samples were then incubated overnight at 4°C with 200 µL of diluted primary antibody (diluted in TBS). Next, secondary antibody (horseradish-peroxidase-conjugated horse anti-rabbit) was applied for 30 minutes at room temperature. To eliminate endogenous peroxidase activity, samples were treated with 3% hydrogen peroxide for 10 minutes, then rinsed 3 times in TBST for 5 minutes per wash.

Antibody target	Primary antibody	Host species	Primary antibody dilution	Antigen retrieval buffer	Blocking agent	Secondary antibody
TNF-α	Anti-TNFα antibody (Abcam; ab1793)	Mouse	1:100	Sodium citrate (pH 6)	M.O.M. Mouse IgG Blocking Reagent from M.O.M. Immunodetection Kit (Vector Laboratories; PK-2200)	M.O.M. Biotinylated Anti-Mouse IgG Reagent from M.O.M. Immunodetection Kit (Vector Laboratories; PK-2200)
CCL-2/MCP-1	MCP-1 Monoclonal Antibody (ThermoFisher; MA5-17040)	Mouse	1:500	TRIS-EDTA (pH 9)	As above	As above
GFAP	GFAP Monoclonal Antibody (ThermoFisher; 53-9892-82)	Mouse	1:1000	Sodium citrate (pH 6)	As above	As above
ICAM-1	ICAM-1 Monoclonal Antibody (ThermoFisher; MA5407)	Mouse	1:100	Sodium citrate (pH 6)	As above	As above
MHC-II	MHC Class II Polyclonal Antibody (Thermo Fisher; PA5-116876)	Rabbit	1:500	Sodium citrate (pH 6)	2.5% normal horse serum (Vector Laboratories; MP-7452)	ImmPRESS HRP Horse Anti-Mouse (Vector Laboratories; MP-7452)
CD3	Anti-CD3 antibody (Abcam; ab16669)	Rabbit	1:100	Sodium citrate (pH 6)	As above	As above

Table 2.4. Immunohistochemistry reagent details. M.O.M = mouse-on mouse, HRP= horseradish peroxidase.

2.10.3. Counterstaining

Staining was visualised using 3,3'Diaminobenzidine (DAB). Upon oxidisation by hydrogen peroxide (a reaction catalysed by HRP), DAB forms a brown precipitate and can be visualised using a light microscope . Slides were rinsed for 5 minutes in running tap water, then counterstained with nuclear stain haematoxylin and blueing with Scott's tap water (to covert the soluble red component of haematoxylin into an insoluble blue).

2.10.4. Image analysis

IHC staining was visualised using the Lecia Scanscope console (20X magnification). Digital images were analysed using the Aperio ImageScope software (Lecia Biosystems, version 12.4.0.7018). Hippocampus and cerebellum regions were manually selected, and artefacts such as tissue folds and air bubbles were excluded.

Quantitative analysis of IHC staining was conducted using the positive pixel counting algorithm (version 9; Aperio ImageScope) to determine the number of weak (+), moderate (++), strong (+++) positive and negative (-) pixels. The number of ++/+++ and -/+ pixels were combined to create two groups: high and low protein expression, respectively. A positivity score was calculated by dividing the total number of positive pixels by the total number of pixels.

2.11. Transcriptomic and methylomic analysis

2.11.1. RNA sequencing

RNA was sequenced on the Illumina NovaSeq 6000 via the Inview Transcriptome Discover service (Eurofins Genomics). Library preparation was carried out following manufacturer's instructions. Briefly, total RNA was sent for library preparation and therefore no poly-A purification was required. For each sample 150ng mRNA was fragmented and strand-specific cDNA was synthesised. Next, adapters were ligated and then amplified using adapter specific PCR. Illumina paired-end read sequencing was carried out with average read depth of 30 million read pairs (read-mode: 2 x 150bp).

The raw RNAseq data was de-multiplexed and FASTQ files for each sample were downloaded from Eurofins Genomics for subsequent data processing and analysis (Figure 2.7). The FASTQ files underwent quality control using the FastQC program (Babraham Bioinformatics). FastQC provides an overview report of the quality of the raw sequencing data produced from high throughput sequencing. Poor quality data can be improved with trimming; however, this was not necessary in our dataset as data for all samples was of good quality. Quantification of the RNAseq data was carried out using Salmon (v0.8.10). Salmon uses quasi-alignment to quickly and accurately quantify transcript abundance, with less bias than more traditional full read alignment methods (previously described by Patro *et al* (Patro *et al.*, 2017)). Briefly, the reads are aligned to a reference transcriptome, the abundance calculated and then finally gene annotation is added (GENCODE vM31).

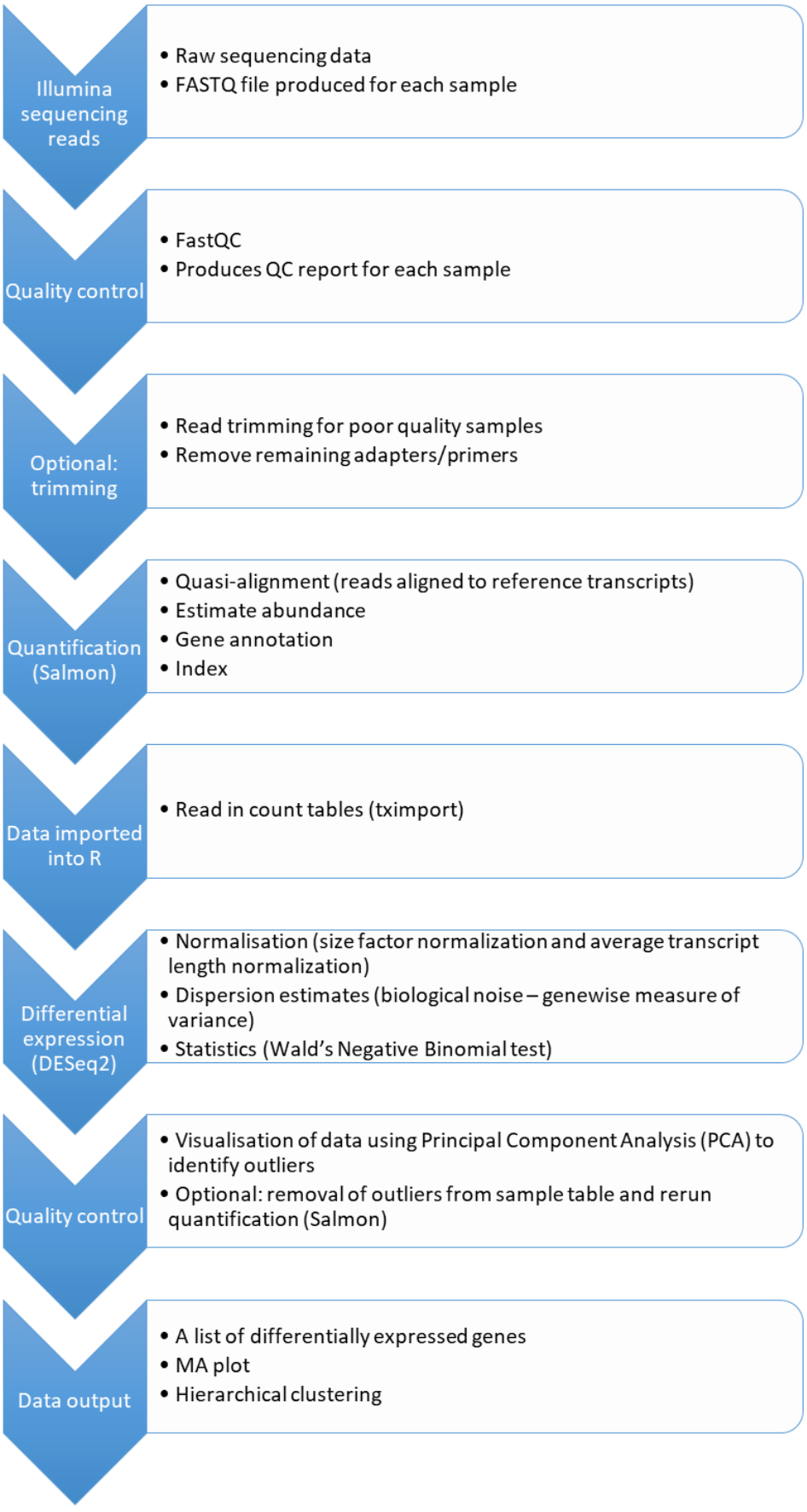

Figure 2.7. Overview of the RNAseq data analysis process.

2.11.2. Differential expression analysis

Differential gene expression analysis was carried out in R (version 4.2.2) using the package *DESeq2* (version 1.38.3). Briefly, the quantification files (quant; produced by Salmon) underwent normalisation (size factor normalisation and average transcript length normalisation) and dispersion estimation (gene-wise measure of variance to account for biological noise). The Wald's Negative Binomial test was then applied to determine whether genes were differentially expressed. Data was visualised using a Principal Component Analysis (PCA) and MA plots and filtered by log2 fold change *[abs (log2FoldChange) > 1]* and adjusted p-value *[padj < 0.05].*

2.11.3. Gene Set Enrichment Analysis

Gene Set Enrichment Analysis (GSEA) was carried out in R (version 4.2.2) using the package *fgsea* (fast pre-ranked gene set enrichment analysis; version 1.24.0), using a script kindly provided by Jack Goddard (PBTG Research Associate). Briefly, gene counts were ranked by p-value then underwent fgsea using the mouse hallmark gene sets (mh.all.v2023.1.Mm.symbols; Broad Institute) and the recommended settings (gene set size: *minSize = 15* and *maxSize = 500*). Bar plot enrichment scores and enrichment pathways were plotted using *ggplot2* (version 3.4.3).

2.11.4. DNA methylation analysis

Samples were sent to the Wellcome Trust Clinical Research Facility (Edinburgh) for genome-wide analysis of methylation sites, using the Infinium Mouse MethylationBeadChip Array (version MM285). The array contained a total of 296,070 probes, consisting of all genomic CpGs in the mouse genome (including all possible probe DNA strand and post-bisulfite converted strand combinations), CpGs selected to target genomic features/regions with known biology, and 28,011 random CpGs to account for unknown biology (Zhou *et al.*, 2022). The raw data was processed in R using the SeSAMe package (version 1.8.12 (Zhou *et al.*, 2018; Zhou *et al.*, 2022).

The processed data then underwent QC to 1) remove any unreliable probes ($p \geq 0.05$ for probe detection) and 2) correct for background (normal exponential out-of-band normalisation; Noob). Processed data consisted of beta-values for each probe site to indicate the methylation status (ranging from zero [no methylation] to one [methylation]).

To predict epigenetic age as a marker of accelerated ageing beyond chronological age, a prebuilt epigenetic clock and mouse tissue reference (1,239 DNA samples from 26 tissue/cell types) were utilised (developed by Zhou *et* al (Zhou *et al.*, 2022)). The mouse epigenetic clock predicted age using 347 CpG probes (mean absolute error of 1.2 months; n=706 mouse tissues) using the SeSAMe package (https://github.com/zwdzwd/sesame; (Zhou *et al.*, 2022)).

2.12. Tissue Culture

2.12.1. Cell maintenance

2.12.1.1. MRC-5 cell line

MRC-5 (human foetal lung fibroblasts, kindly gifted by Dr. Satomi Miwa [Newcastle University]) cells were expanded and maintained in Dulbecco's Modified Eagle's Medium (DMEM; Sigma D6429), supplemented with 10% foetal bovine serum (FBS; Gibco, 10500-064) and 1% penicillin-streptomycin (Sigma-Aldrich, P0781) and grown in a humidified incubator at 37°C and 5% CO_2. Cells were expanded in 75 cm^2 flasks (treated for cell attachment; Corning, 430641U) with 15 ml media and grown until they reached 80% confluency, when they were split additional flasks. Briefly, the media was aspirated from the flasks. To remove any remaining media from the cells, 3 ml warm phosphate-buffered saline (PBS) was washed over the cells, then aspirated. 3 ml warm 1x trypsin solution (Sigma, T4174) was applied to the adherent cells to allow detachment from the flask. Once detached, 6 ml of media was added to neutralise the trypsin. The cells suspended in trypsin-media was transferred to a 50 ml tube and centrifuged at 120 x g for 5 minutes. The trypsin-media supernatant was aspirated, and the pellet suspended in 1 ml warm media for subsequent counting.

2.12.1.2. AD2 WT1 cell line

AD2 WT1 (human induced pluripotent stem cells; iPSCs, kindly gifted by Prof. Lyle Armstrong [Newcastle University] (Chichagova *et al.*, 2023)) were expanded and maintained following WiCell Research Resources protocol (SOP-SH-002-G). Briefly, six-well plates were prepared with 1ml per well of Matrigel (10mg/mL; Corning, 354230) and DMEM/F-12 (Invitrogen, 11330) solution. Frozen cells were rapidly thawed at 37°C and centrifuged for 5 minutes at 200 x g. The pellet was resuspended in 12mL of mTeSR1 medium supplemented with 12µl ROCK inhibitor (Y-27632 dihydrochloride, BD Biosciences, 562822) and seeded into six-well plates (1ml per well) and additional 1ml of mTeSR1/ROCK was added to each well. iPSCs were grown in a humidified incubator at 37°C and 5% CO_2 until they reached 80% confluency, when they were split additional plates. The spent media was aspirated and refreshed with mTeSR1 media approximately every 4 days. Cells were passaged in 1:3 ratio, as per the WiCell protocol. Briefly, the media was aspirated from each well and cells were washed twice with 1mL of Versene (0.48mM EDTA solution; Fisher Scientific, 12569069), followed by 2mL of mTeSR1

media. Cells were collected, counted and seeded in fresh six-well plates (prepared as previously described).

2.12.2. Cell counting

The approximate number of living cells was counted until a haemocytometer and the Trypan blue exclusion test. Trypan blue is a dye that is not absorbed by living mammalian cells, once dead, the cells become permeable to the dye and appear blue. Briefly, 10 µL of cell solution was mixed with 10 µL 0.4 % Trypan blue solution (ThermoFisher Scientific) and then 10 µL of this mixture was placed onto the haemocytometer. The number of cells was counted manually under a microscope and cells per ml was calculated using the following formula:

$$\text{Total cells/ml} = \frac{\text{Total cells counted x Dilution factor x 10,000 cells/ml}}{Number\ of\ squares\ counted}$$

2.12.3. Storage of viable cells

To create stocks of viable cells, $1x10^6$ cells were resuspended in cold freeze media (MRC-5: FBS supplemented with 10% dimethyl sulfoxide; DMSO, and AD2 WT1: FBS supplemented with 0.1% ROCK inhibitor) and placed into a cryovial. To maintain viability, cells were frozen slowly; vials were placed in a Mr Frosty™ Freezing Container (ThermoFisher Scientific, 5100-0001) and transferred to a -80°C freezer. The Mr Frosty™ Freezing Container contains isopropanol to slow the freezing rate to 1°C/minute, the optimal freezing rate for preserving viable cells. Viable cell stocks were transferred to -152 °C freezer for long-term storage.

2.12.4. Cell line irradiation

Approximately $1x10^6$ MRC-5 cells were seeded in $75cm^2$ flasks 72 hours prior to irradiation. Separate flasks were seeded for each timepoint, in triplicate, and compared to non-irradiated controls. To prevent infection during cross-campus transport to the irradiator, flasks were sealed with parafilm, and the lids were replaced prior to return to the incubator. Non-irradiated controls experienced the same conditions as irradiated cells, including transit to radiator site, aside from exposure to radiation.

To replicate the high dose of radiation received by medulloblastoma patients, cells received a single dose of 36 Gy x-ray irradiation (RS320 irradiation system; Gulmay Medical) at a dose

rate of 2.52 Gy/min (14.4 minutes at 320 kV and 10 mA). Dose rate varies based on 1) the distance of samples from the X-ray tube, 2) the location of samples of the shelf and 3) the thickness of material placed between the X-ray tube and the samples. To ensure consistent radiation exposure, shelf height remained consistent (set at the lowest height to maximise the size of the focal region Figure 2.8A), location of samples of the shelf remained consistent (two flasks were placed within the focal region per irradiation period, Figure 2.8B). The thickness of material between samples and the X-ray tube remained consistent; samples were irradiated in 75cm^2 flasks with 15 ml media (3mm media depth).

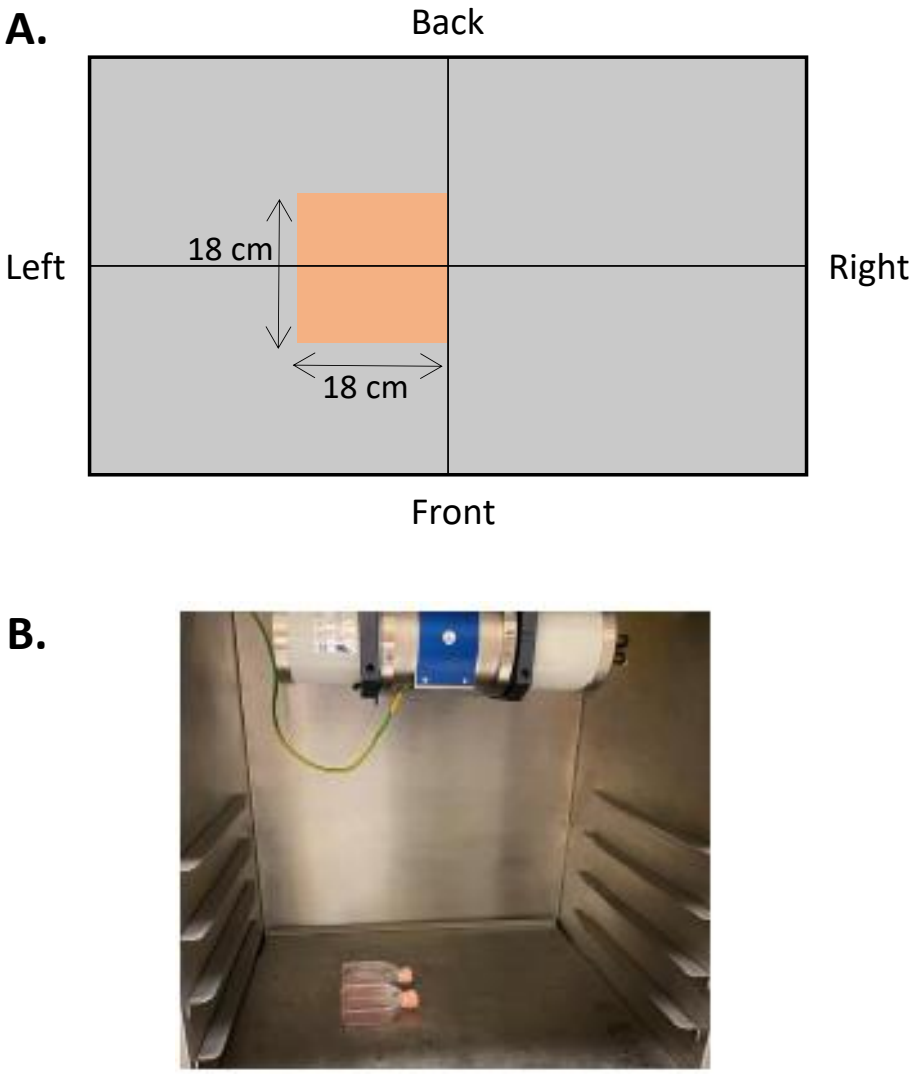

Figure 2.8. Inside the Gulmay RS320 X-Ray irradiator. A) The focal region (orange) of the irradiation field, B) Two 75cm^2 flasks were placed in the centre of the focal region for consistent irradiation.

2.13. Custom panel immunoassay

2.13.1. Assay protocol

The Luminex® Discovery Assay (R&D Systems) was utilised using a custom panel of four human pre-mixed multi-analyte kits to assess abundance of 57 analytes of interest in response to radiotherapeutic insult. Each kit (LXSAHM-25, -24, -12 and -06) contained unique analyte-specific antibodies pre-coated onto magnetic microparticles embedded with fluorophores at set ratios for each unique microparticle region. An overview of the assay principle is shown in Figure 2.9. Every assay plate consisted of a blank, six standards and the samples of interest (media) in duplicate. Assays were repeated for a total of 3 replicates.

Standard cocktails, containing known concentrations of each analyte, were reconstituted as per the Certificate of Analysis, combined to create standard 1 and then underwent a 3-fold serial dilution (with calibrator diluent RD6-52) series to create standards 2-6. Samples were centrifuged at 16,000 x *g*, then diluted 1:2 in calibrator diluent RD6-52.

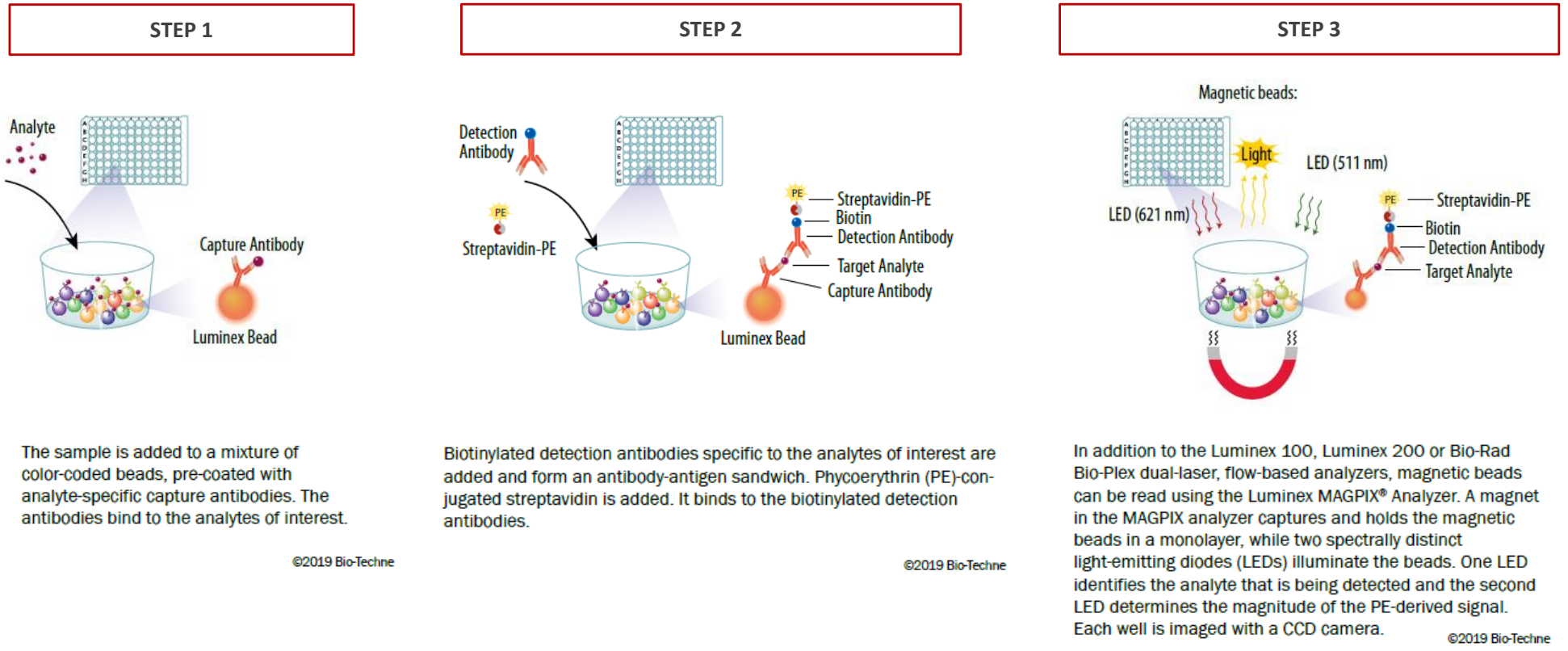

Figure 2.9. Luminex assay principle. Luminex assay users guide (bio-techne).

The Luminex assay was prepared as per the manufacturers' instructions (an overview is shown in Figure 2.10). Briefly, 50 µL microparticle cocktail was added to each well of a 96-well plate containing 50 µL of either a blank (calibrator diluent RD6-52), a standard (1-6) or a sample of interest and incubated for 2 hours at room temperature (RT) on a horizontal orbital microplate shaker set at 800 rpm to allow the immobilised antibodies to bind the analytes of interest. Next, the plate underwent a wash step to remove unbound substances; the plate was placed on a Bio-Plex Handheld Magnetic Washer (Bio-Rad Laboratories; 171020100), the liquid was carefully removed by one rapid 'flick' motion. Then, 100 µL wash buffer was added to each well, incubated for 1 min at RT and the liquid removed as above. This was repeated for a total of three washes. Next, 50 µL of a biotinylated antibody cocktail, specific to the analytes of interest, was added to each well, and incubated as above for 1 hour. The wash step was repeated to remove any unbound biotinylated antibody. Finally, 50 µL of a streptavidin-phycoerythrin conjugate (streptavidin-PE), which binds to the biotinylated antibody, was added to each well, and incubated as above for 30 minutes. After a final wash step to remove unbound streptavidin-PE, the microparticles were resuspended in buffer.

The abundance of microparticles was read using the Bio-Plex MAGPIX Multiplex Reader (Bio-Rad Laboratories), as per manufacturers' instructions (an overview is shown in step 3 of Figure 2.9). Briefly, the microparticles were held in a monolayer by a magnet within the analyser and illuminated by two spectrally distinct Light Emitting Diodes (LEDs). One LED excited the dye within each microparticle (to identify the region), and the second LED excited the PE (to measure the amount of analyte bound to the microparticle).

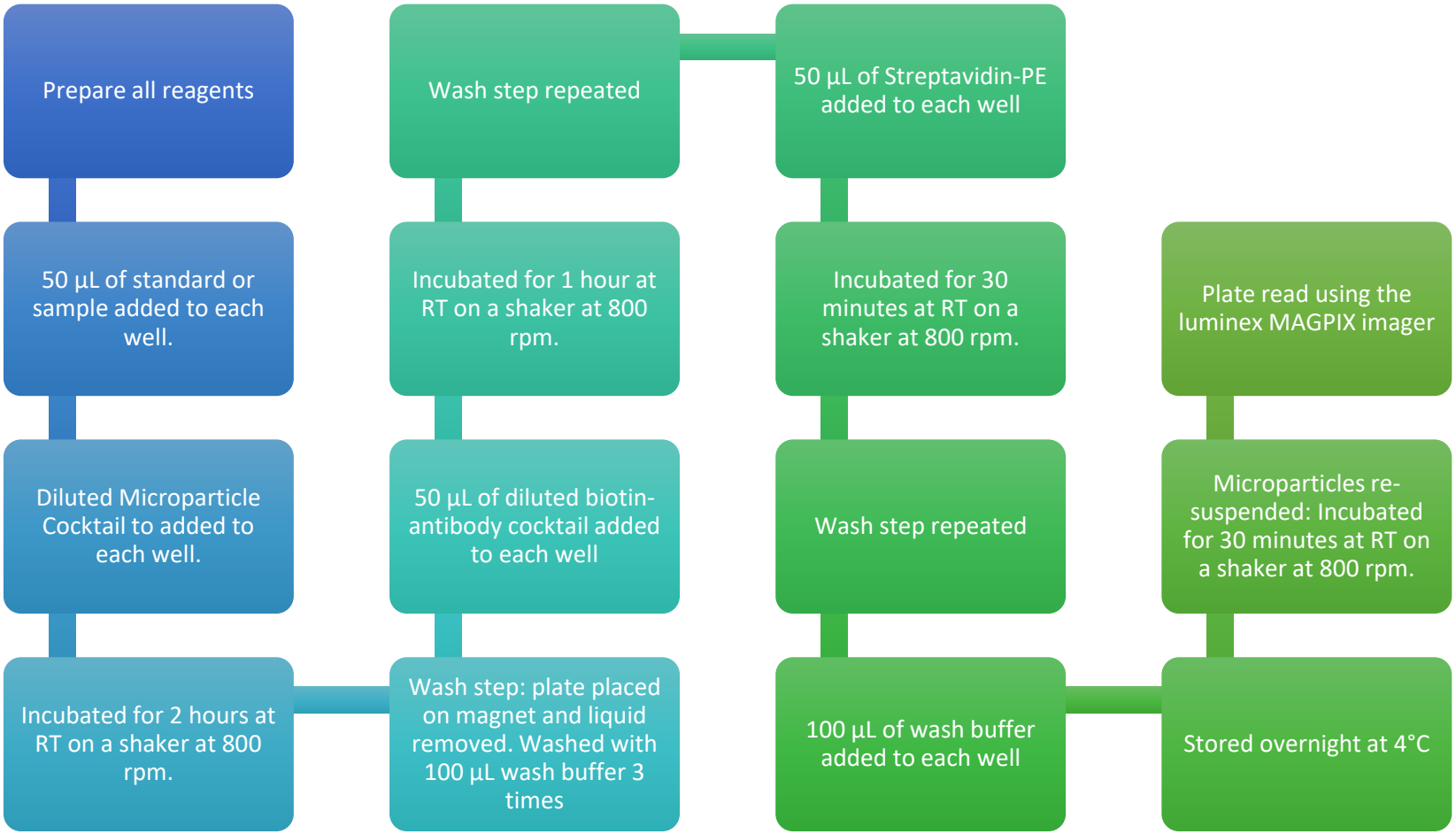

Figure 2.10. Overview of the Luminex assay preparation.

2.13.2. Data analysis

Concentrations for standard 1 were provided on the Certificate of Analysis, specific to each kit. For the remaining standards (2-6) a 3-fold dilution of concentrations was calculated. Readings (Median Fluorescence Intensity; MFI) for each sample and standard was calculated using the average of duplicate readings, minus the average MFI for the blank. A standard curve was created for each analyte using the xPONENT software, with a five-parameter logistic curve-fit. Resulting analyte concentrations were corrected for initial sample dilution, normalised to control cell count (average cell count after 1 hour with no irradiation). Fold change was calculated at 1 hour and 48 hours post-irradiation for each irradiation replicate (n=3) as follows:

$$Fold\ change = \frac{\text{normalised protein concentration following 36Gy}}{\text{mean normalised protein concentration following 0Gy}}$$

2.14. Statistical analysis

Statistical analyses and data visualisations were carried out using SPSS statistics (IBM, version 27) and R Studio (version 4.2.2). T-tests (independent and paired), linear regression and ANOVA with post-hoc Tukey tests were used to compare group means between continuous variables. Significant associations were defined as having a $p<0.05$. Where appropriate, the Benjamini-Hochberg procedure was used to correct for multiple testing. Kaplan-Meier plots and the log-rank test was used for survival analysis.

Chapter 3. Development of an in vivo model that recapitulates MB radiotherapy delivery and late-effect profile

3.1. Introduction

There is a critical need for the development of interventions to prevent or alleviate the burden of late-effects experienced by childhood medulloblastoma (MB) survivors, as previously discussed in Chapter 1. However, the development of such interventions is hindered by a lack of experimental models that can recapitulate MB radiotherapy dose, delivery, and late-effect profile in developmental stage-matched systems.

Craniospinal irradiation (CSI) is the mainstay of treatment for non-infant MB; MB is typically treated with high doses of CSI (up to 36 Gy) with a posterior fossa boost dose PFB (Spiegler *et al.*, 2004; Robbins *et al.*, 2012; Gupta *et al.*, 2022). However, both 23.4 and 36 Gy of CSI often results in a deleterious late-effect profile that significantly impacts the quality of life of survivors. Survivors suffer intellectual disability, low levels of academic attainment, poor psychosocial satisfaction, and reduced independence in adulthood (Spiegler *et al.*, 2004; Robbins *et al.*, 2012; Gupta *et al.*, 2022). High dose CRT promotes the greatest intellectual impairment; the mean loss of IQ points is between 2.5-3.9 per year (Walter *et al.*, 1999; Palmer *et al.*, 2001b; Ris *et al.*, 2001), reaching a plateau of impairment around two standard deviations below average. 70-90% of this group demonstrate a significant impairment in global intellectual functioning; many survivors experience attention deficits, slower processing speed and impaired working memory (Ramaswamy *et al.*, 2016), which are in turn strongly correlated with decreased quality of life (Walter *et al.*, 1999; Palmer *et al.*, 2001b; Ris *et al.*, 2001). Many survivors also experience impaired physical functioning (Piscione *et al.*, 2013), and neurological difficulties such as ataxia and co-ordination disorders, as well as reduced fine motor skills (Chevignard *et al.*, 2017).

Childhood MB patients typically receive up to 36 Gy CSI with 54 Gy to the posterior fossa (Ramaswamy *et al.*, 2016). Current *in vivo* models fail to fully recapitulate MB cranial irradiation due to 1) method of radiation delivery, 2) dose of radiation administered, 3) age at receipt of radiation and 4) follow-up of late-effects.

3.1.1. Preclinical delivery of a clinically relevant MB radiotherapy dose

Whole-body irradiation has been shown to induce late-effects such as increased frailty and reduced neurocognitive functioning (Fielder *et al.*, 2019), however radiation dose is limited to relatively low doses due to the acute toxicities associated with irradiating the entire body. 12 Gy is considered a very high dose of whole-body irradiation and is typically fatal (Ryu *et al.*,

2016), and therefore using this methodology it would not be possible to recapitulate the high doses childhood brain tumour patients receive.

In vivo whole-head irradiation is the most widely used model of brain tumour radiation protocols, as it more accurately replicates radiation regimens received by MB patients than whole-body irradiation. Typically, *in vivo* models receive radiation via similar methods to that of whole-body irradiation (either x-ray or gamma-rays), whereby the body is lead-shielded with the head exposed to the radiation (Wong-Goodrich *et al.*, 2010; Moravan *et al.*, 2011; Tomé *et al.*, 2015; Montay-Gruel *et al.*, 2017; Yousuf *et al.*, 2017; Belcher *et al.*, 2020). This method has enabled investigation of the effects of whole-head irradiation, however the specific dose the brain receives is difficult to accurately determine. The use of whole-head irradiation does in part model the radiotherapy received by childhood MB survivors. However, this modality includes irradiation of structures such as the eyes, ears and mouth and is associated with dose-limiting acute toxicities, (e.g. damage to salivary gland, mouth ulceration, eye dryness, weight loss) (Jham and da Silva Freire, 2006; Brook, 2020). The salivary glands are particularly radiosensitive, and decreased function can hinder eating and consequently body weight decreases indirectly of cranial radiation (Grundmann;Mitchell and Limesand, 2009; Deasy *et al.*, 2010). Moreover, childhood MB survivors can experience hearing and vision impairments, however as radiation planning typically spares the eyes and ears, these impairments typically arise from the tumour, surgery or chemotherapy, and therefore whole-head irradiation does not fully recapitulate the radiation-induced late-effect profile of brain tumour survivors.

Studies have typically delivered a single dose of ~7 Gy via whole-head irradiation (Ramanan *et al.*, 2009; Wong-Goodrich *et al.*, 2010; Sándor *et al.*, 2014; de Guzman *et al.*, 2019; Yuen *et al.*, 2021). Hormuth *et al* delivered a single dose of up to 40 Gy to rats, although made no comment on acute toxicity (Hormuth *et al.*, 2018), which would be expected at this dose. To minimise acute toxicity and enable delivery of higher, clinically relevant doses, radiation can be delivered in multiple fractions of lower doses; adult rodents received up to 40 Gy (Brown *et al.*, 2007; Lazarini *et al.*, 2009b; Rao *et al.*, 2011; Ungvari *et al.*, 2017; Tang *et al.*, 2019; Yabluchanskiy *et al.*, 2020).

Whole-head irradiation has been shown to induce cognitive defects in rodent brain tumour treatment models with both single dose and fractionated radiation at human-equivalent doses (de Guzman *et al.*, 2015; Nieman *et al.*, 2015; Tang *et al.*, 2019). Whole-head irradiation

models somewhat enable investigation into the effects of whole-brain irradiation received by MB patients. However, typical radiotherapy regimens for childhood MB treatment also involves an addition boost dose of radiation specifically targeted to the tumour bed (within the posterior fossa), the effects of which cannot be investigated using solely whole-head irradiation models. The cerebellum has a well-established role in co-ordinating voluntary movement, as well addition roles in neurocognitive function (Koziol *et al.*, 2014), and therefore, as this methodology cannot recapitulate the posterior fossa boost, it cannot accurately model childhood MB radiotherapeutic treatment.

3.1.2. Targeted cranial radiotherapy

Whole-body/whole-head irradiation cannot deliver targeted-radiation to specific brain regions, thus, irradiation using these methodologies cannot fully recapitulate the dose and targeting of medulloblastoma regimens. Targeted brain irradiation in rodents is now possible due to improvements in technology such as those demonstrated by the Small Animal Radiation Research Platform (SARRP, Xstrahl) (Wong *et al.*, 2008; Smoll, 2012). The SARRP utilises computed tomography to precisely deliver a known intensity of X-ray radiation to the target area, with very minimal radiation to non-target areas (<1mm precision) (Wong *et al.*, 2008). This precision enables radiation of specific structures, thus facilitating the delivery of a posterior fossa boost and sparing of the eyes and ears, more closely replicating MB targeting/dosing (Wong *et al.*, 2008). Targeted cranial irradiation has previously been utilised within the field of brain tumour research, delivering up to 54 Gy to the brain; however, these studies were designed to assess tumour burden and not the subsequent late-effect profile (Baumann *et al.*, 2012; Nimmervoll *et al.*, 2018).

3.1.3. Irradiation at an equivalent developmental stage

An additional challenge is delivering high-dose radiation to juvenile, developing, brains. Radiotherapeutic insult to the brain results in substantial damage to healthy tissue; radiation-induced DNA damage and oxidative stress induces chronic inflammation, neuronal cell death, reduced neurogenesis and disruption to the blood-brain barrier (Belka *et al.*, 2001). As significant brain development occurs in early childhood, young children are particularly vulnerable to the deleterious consequences of cranial radiation (CRT) used to treat a brain tumour (Greene-Schloesser *et al.*, 2012). Childhood MB incidence peaks between 3 and 8 years of age, and therefore patients receive CRT early during brain development. A younger age at receipt of radiotherapy is often associated with increased delayed toxicities and

adverse effects (Mulhern *et al.*, 1989; Kiltie;Lashford and Gattamaneni, 1997; Jenkin;Danjoux and Greenberg, 1998); in infants this is so severe that CSI is no longer given. However, *in vivo* irradiation studies typically use adult mice and therefore do not model the developmental stage of medulloblastoma (Wong-Goodrich *et al.*, 2010; Moravan *et al.*, 2011; Tomé *et al.*, 2015; Montay-Gruel *et al.*, 2017; Yousuf *et al.*, 2017; Belcher *et al.*, 2020). Rao *et al* demonstrated young, 1 month old mice, develop hippocampus-dependent learning deficits following receipt of 20 Gy fractioned whole-head irradiation (Rao *et al.*, 2011). To effectively recapitulate childhood MB radiotherapy and the subsequent late-effect profile in a preclinical model, the developmental stage must be considered, however, previous studies have typically utilised adult mice. Juvenile mice are particularly sensitive to treatment insults, and therefore, in addition to technical limitations from their small size, delivery of high-dose, targeted cranial radiation is particularly challenging. A benefit of using mouse models for *in vivo* late-effect studies is their shortened life-course, however, this renders only a short interval reflecting a juvenile developmental stage equivalent to paediatric MB onset (up to ~6-8 weeks old).

3.1.4. Assessment of the late-effect profile

The late effect profile can be readily assessed in rodent models. Physical function (such as muscular endurance, co-ordination and grip strength) is typically assessed *in vivo* using methods such as the treadmill, rotarod, grip strength and hanging wire tests. These assessments are relatively non-invasive and therefore can be employed longitudinally to assess physical function over the life-course.

Neurocognitive function is typically assessed *in vivo* using maze-based tests that utilise a mouse's innate instinct to explore novel environments (Kraeuter;Guest and Sarnyai, 2019). Y-maze and T-maze assess working memory by assessing the ability to enter novel arms. Both 'T' and 'Y' mazes consist of three tunnels in the shape of a 'T' and 'Y' respectively. The order of arm entry is recorded for a set time, and the proportion of novel arm choices provides the discrimination index (DI). It is generally assumed that a higher DI is due to better working memory, however environmental factors could also have an influence if the result if the test is not carried out correctly (Li *et al.*, 2018; Kraeuter;Guest and Sarnyai, 2019; Yoshizaki;Asai and Hara, 2020). The Y maze is most commonly used, but other cognitive tests include: Barnes maze, Morris water maze, and the open field test (Barnes, 1979; Sousa;Almeida and Wotjak, 2006; Vorhees and Williams, 2006). Morris water maze and the Barnes maze assess spatial learning and working memory by training the mouse to locate a target hole/platform and

assessing either the ability to retain learned behaviour or performance in the novel object recognition test (Barnes, 1979; Ennaceur and Meliani, 1992; Vorhees and Williams, 2006; Berta Sunyer *et al.*, 2007).

3.1.5. Long-term follow-up

Many of late-effects experienced by childhood MB survivors can present decades after treatment, and thus long-term follow-up is crucial. The shortened life course of rodents makes them an ideal model for long-term follow-up; Tang *et al* observed reduced brain growth and cognitive decline in rats, present 12 months after whole-head irradiation (30 Gy) (Tang *et al.*, 2019). However, longitudinal assessment and long-term follow-up is not typical, and therefore is lacking in the majority of published *in vivo* treatment-induced injury models.

To provide an essential foundation for the clinical development of neuro-interventional approaches, a novel, highly disease-relevant radiotherapeutic injury *in vivo* model was developed, which accurately recapitulates the early stage in development and radiotherapy schedule associated with MB treatment. The small animal radiation research platform (SARRP) was used to precisely deliver MB-like CRT with PFB via computed tomography (CT) imaging guidance (Wong *et al.*, 2008), at clinically relevant doses to mice of a MB human-equivalent age. To establish a baseline of radiotherapy-induced injury, the consequent toxicity and late-effect profile was longitudinally assessed.

3.2. Aims

The aim of this chapter is to establish an *in vivo* model that recapitulates childhood medulloblastoma cranial radiotherapy and late-effect profile.

1) Deliver childhood medulloblastoma-equivalent radiation, with a focus on replicating the radiation dose and target regions, in age-equivalent mice.
    a. Radiation targeting – deliver CRT with an additional boost dose to the posterior fossa. The SARRP enables precise delivery of radiation to the brain, as well as the ability to target specific substructures and therefore can recapitulate human radiation delivery.
    b. Radiation dose – deliver human-MB equivalent high-dose radiation, without severe acute toxicity for the subsequent induction of late-effects experienced by childhood MB survivors.
    c. MB-equivalent age – deliver cranial radiation to juvenile mice, for assessment of the impact of radiation on the developing brain.

2) Longitudinal assessment of the development of frailty, physical functioning deficits and neurocognitive impairment following cranial irradiation in juvenile mice.

3) Assessment of the additional impact (if any) of receipt of a posterior fossa boost on the late-effect profile.

3.3. Methods

3.3.1. Cranial radiation delivery

To facilitate the development of the *in vivo* model using the Small Animal Radiation Research Platform (SARRP; located at the University of Leeds), a cross-institutional collaboration with Prof. Susan Short was developed. Detailed methodologies are provided in 2.7.

3.3.2. Assessment of tolerability

Following recovery from the irradiation, mice were transferred to Newcastle University for subsequent assessment. Details of general husbandry are provided in 2.1.

Body weight was assessed at least weekly, whereby allocation of radiation group was unknown. Mice were humanely culled if excessive weight loss occurred (detailed in Chapter 2.7.3).

3.3.3. Delivery of MB-equivalent CRT and PFB

At age 28-37 PNDs (mean age of PND 33), mice were randomly allocated into 3 groups. As summarised in Table 3.1, the 3 groups consisted of: cranial (whole-brain) irradiation (CRT only, human-equivalent 38 Gy; n=12), cranial irradiation with an additional posterior fossa boost (CRT+PFB, human-equivalent 38 Gy with 11 Gy [49 Gy total to the posterior fossa]; n=12) and a control group that received sham-irradiation (sham, 0 Gy, n=12). Detailed methodologies are provided in 2.7.

Group	Radiation dose	Radiation schedule	Human-equivalent radiation dose
CRT only	Whole brain: 10F x 3 Gy (30 Gy)	5 days per week for 2 weeks	Whole-brain: 38 Gy
CRT + PFB	Posterior fossa only: 3F x 3 Gy (9 Gy)	3 consecutive days	PF only: 49 Gy
	Whole brain: 10F x 3 Gy (30 Gy)	5 days per week for 2 weeks	Whole-brain: 38 Gy
Sham	*Did not receive radiation*		

Table 3.1. SARRP irradiation regimen for each group. n=12 for each group.

3.3.4. Longitudinal assessment of the late-effects following CRT

3.3.4.1. Longitudinal assessment

Following recovery from cranial irradiation, mice were transferred to Newcastle University (aged ~PND 63) for subsequent assessment, where assessors were blind to the allocation of radiation group. After acclimatisation, mice received radiofrequency identification. Mice were longitudinally assessed for over one year (up to ~PND 394). A schematic overview of longitudinal assessment is shown in Figure 3.1 and the human-equivalent life stage for each time point is shown in Table 3.2.

3.3.4.2. Frailty

Frailty assessment was carried out using the Rockwood-style frailty index as previously described (Fielder *et al.*, 2019). Briefly, 30 parameters of frailty were scored on a scale from 0 (no impairment) to 1 (severe impairment). To minimise subjectivity, assessors (n=2) were kept the same throughout and blind to the allocation of radiation group. Detailed methodology is provided in 2.3. Frailty assessment was conducted at 4 timepoints (F1: ~PND 97, F2: ~PND 130, F3: ~PND 191 and F4: ~PND 233).

3.3.4.3. Physical functioning

Physical functioning was assessed using the forelimb grip strength test, rotarod (an assessment of balance, endurance and co-ordination) and the hanging wire (an assessment of muscular strength and co-ordination). Details of assessment protocols are provided in Chapter 2.2. Grip strength was assessed at 4 timepoints (G1: ~PND 97, G2: ~PND 130, G3:~PND 191 and G4: ~PND 233), the RotaRod at 2 timepoints (R1: ~PND 172 and R2: ~PND 249), and the hanging wire test at 2 timepoints (H1: ~PND 145 and ~PND 235).

3.3.4.4. Neurocognitive impairment

Neurocognitive function was assessed using the Y-maze (working memory) and the Barnes maze (learning, short- and long-term memory). Details are provided in Chapter 2.4. Mice were assessed using the Y-maze at two timepoints (Y1: ~PND 179 and Y2: ~PND 266). The Barnes maze was limited to one timepoint (~PND 369) due to the learning aspect of this assessment.

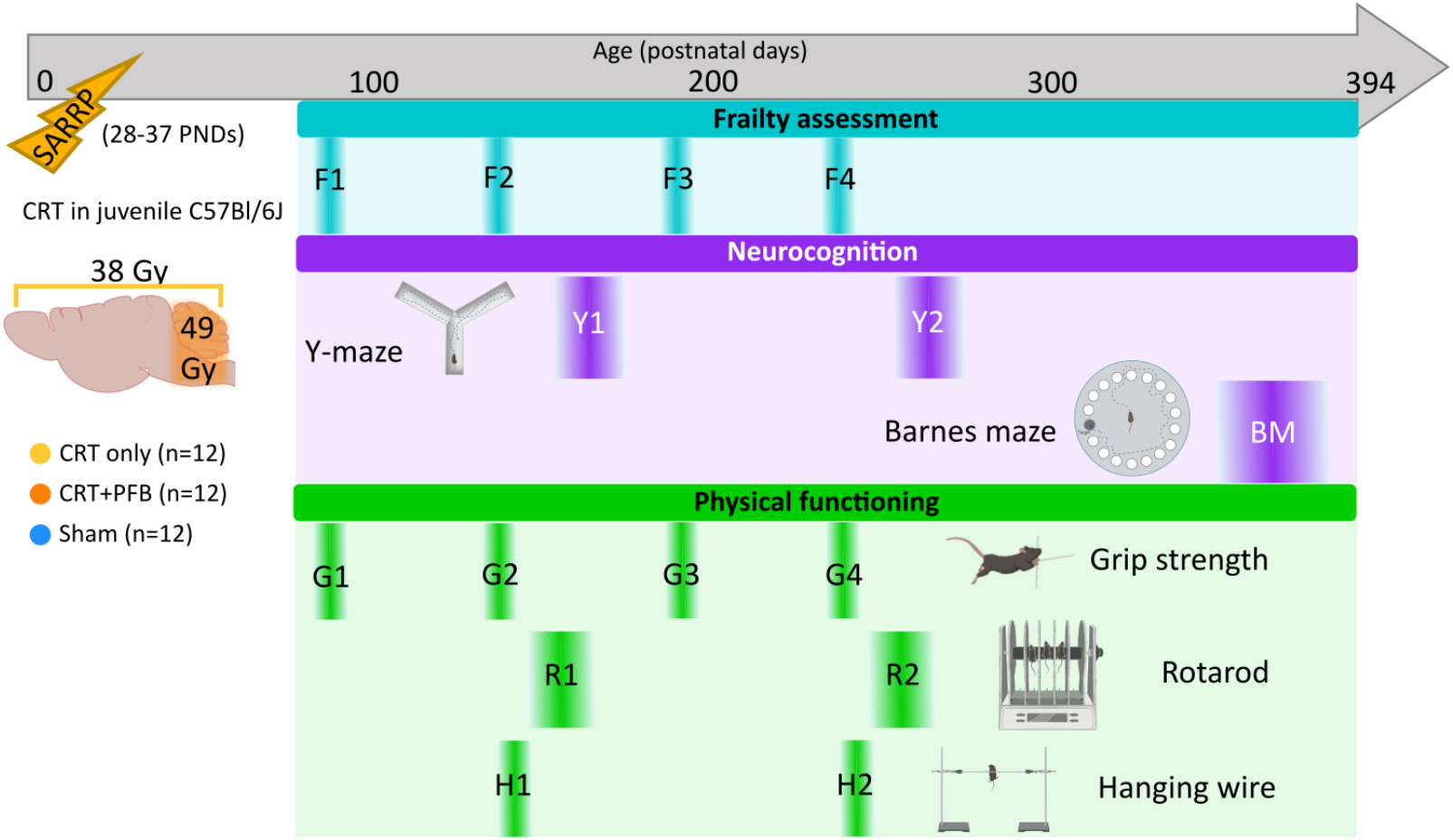

Figure 3.1. Schematic overview of the development of a clinically relevant, high-dose, targeted cranial-irradiation model. Juvenile C57Bl/6J mice (age 28-37 PNDs) received either CRT only (38 Gy human equivalent, n=12), CRT+PFB (total dose of 49 Gy to the posterior fossa, human-equivalent), or sham-irradiation (n=12) via the SARRP. Following irradiation, mice were subjected to longitudinal functional assessment. Assessments of frailty (frailty assessment at 4 timepoints [F1: ~PND 97, F2: ~PND 130, F3:~PND 191 and F4: ~PND 233]), neurocognition (Y-maze at two timepoints [Y1: ~PND 179 and Y2: ~PND 266] and Barnes maze [BM: ~PND 369]) and physical functioning (grip strength test at 4 timepoints [G1: ~PND 97, G2: ~PND 130, G3:~PND 191 and G4: ~PND 233], RotaRod at 2 timepoints [R1: ~PND 172 and R2: ~PND 249] and hanging wire at 2 timepoints [H1: ~PND 145 and H2: ~PND 235]) were carried out up to ~PND 394.

Timepoint	Mouse age (PNDs)	Life-stage equivalent	Approximate age-equivalent (years)
CRT	35-37	Juvenile	0-10
F1/G1	97	Early adulthood	20-30
F2/G2	130	Early adulthood	20-30
F3/G3	191	Early adulthood	20-30
F4/G4	233	Early middle age	30-40
R1	172	Early adulthood	20-30
R2	249	Early middle age	30-40
Y1	179	Early adulthood	20-30
Y2	266	Early middle age	30-40
BM	369	Middle age	40-50

Table 3.2. Mouse and human equivalent life-stage

3.4. Results

3.4.1. Delivery of targeted cranial irradiation

To facilitate the visualisation of the posterior fossa in young mice, a recently weaned (PND 21) mouse was humanely culled and a T2 MRI was performed. To assess the optimal collimator size for the CRT and PFB irradiation doses, the mouse was transferred the SARRP and CT-imaged.

A 10 x 10 mm collimator was used to deliver radiation to the whole brain. For radiation delivery to the posterior fossa, two sizes of collimator were assessed. A 5 x 5 mm collimator was deemed too small as it did not cover the entire posterior fossa region and therefore the larger, 10 x 10 mm collimator, was selected.

Irradiation of organs such as the ears, mouth and eyes can leads to high levels of acute toxicity. To minimise the development of acute toxicity, as well as closely recapitulate clinical radiation regimens, these organs were spared when planning the radiation coverage. To deliver CRT, an arc set-up from -60 to 60 degrees was used to avoid radiation to the oral cavity, ear and ear canal (**Error! Reference source not found.**). For delivery of the PFB dose, a set-up of two lateral beams produced high doses of irradiation to the ear and ear canal, and consequently this method of delivery was not used in our model. Instead, an arc set-up from -60 to 60 degrees was also used to deliver the high-dose boost to the posterior fossa, and radiation to the ear and ear canal was avoided (**Error! Reference source not found.**).

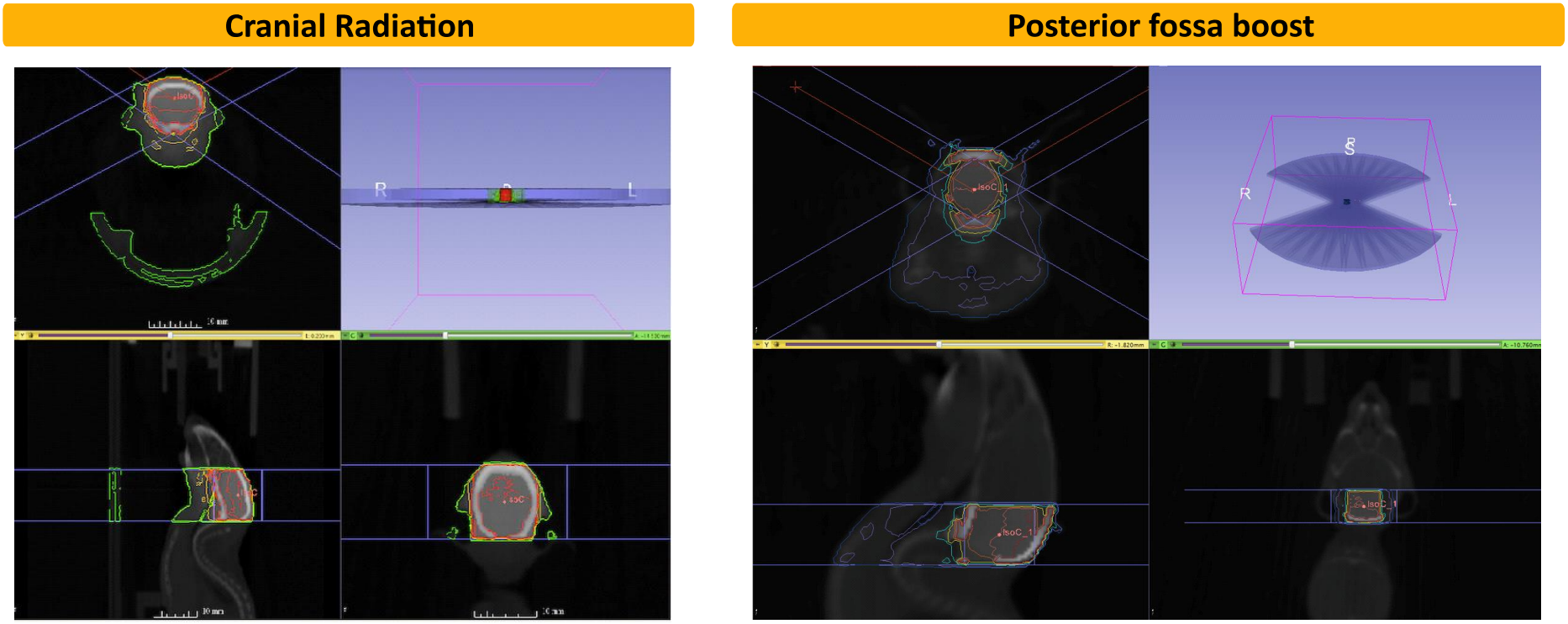

Figure 3.2 Delivery of CRT and PFB to the mouse brain. A representative image of dose distribution in each of the 3 planes for delivery of whole-brain radiation (CRT; left) and a posterior fossa boost (PFB; right) using the SARRP in a young mouse, using 2x 60-degree arc treatments and CT guidance. IsoC = isocentre. High dose volume shown by red outline.

3.4.2. Delivering a human MB-equivalent dose

At age 28-37 PNDs (mean age of PND 33), mice (n=36) were randomly allocated into 3 groups: cranial (whole-brain) irradiation (CRT only, human-equivalent 38 Gy; n=12), cranial irradiation with an additional posterior fossa boost (CRT+PFB, human-equivalent 38 Gy with 11 Gy [49 Gy total to the posterior fossa]; n=12) and a control group that did not receive any irradiation (sham, 0 Gy, n=12). Radiation protocols for each treatment group are summarised in Table 3.3.

The treatment for each group was staggered to ensure repeated doses of anaesthesia and cranial radiation was tolerated in young mice (Figure 3.3). First, the sham group were anaesthetised and placed into the SARRP daily for 5 days but received no irradiation. Daily anaesthesia was well tolerated in the sham group, and cranial irradiation was administered, starting with the CRT only group. Both the CRT and PFB doses were administered in 3 Gy fractions. 10 fractions of 3 Gy were applied to the whole-brain, replicating a human-equivalent dose of 38 Gy. The CRT+PFB group received an addition 3 doses solely to the posterior fossa (shown in Figure 3.3), prior to the receipt of CRT.

Group	Radiation Dose	Radiation schedule	Human-equivalent radiation dose
CRT only	Whole brain: 10F x 3 Gy (30 Gy)	5 days per week for 2 weeks	Whole-brain: 38 Gy
CRT + PFB	Posterior fossa only: 3F x 3 Gy (9 Gy)	3 consecutive days	PF only: 49 Gy
	Whole brain: 10F x 3 Gy (30 Gy)	5 days per week for 2 weeks	Whole-brain: 38 Gy
Sham		*Did not receive radiation*	

Table 3.3. SARRP irradiation regimen for each group. n=12 for each group

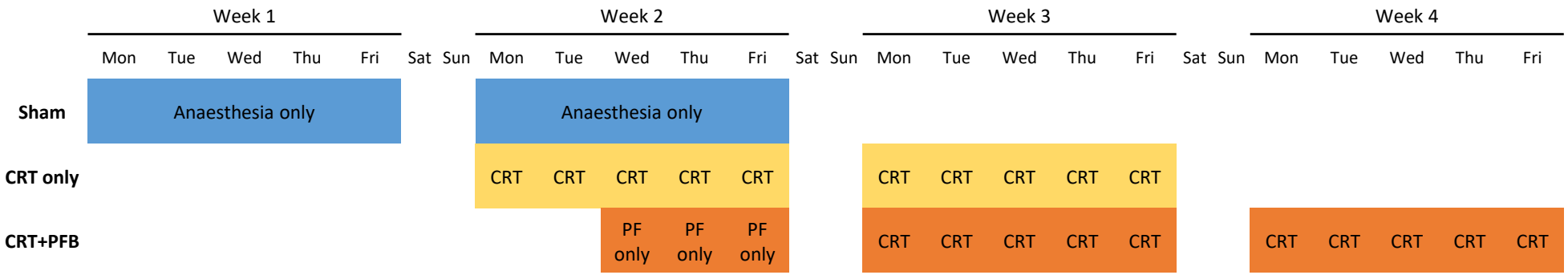

Figure 3.3. Timeline for the delivery of MB-equivalent cranial irradiation. To ensure repeated anaesthesia and cranial irradiation were tolerated in young mice, treatment groups were staggered. First, anaesthesia only was delivered to the sham group (n=12), followed by delivery of CRT only (n=12) and CRT+PFB (n=12).

3.4.3. Acute toxicity following cranial irradiation

CRT (+/- PFB) was delivered to cohorts of young mice at ~PND 33, representing a human-equivalent age of ~4 years. Surprisingly, no animals died due to severe acute toxicity (either during irradiation or up to 60 days after). Over the course of the experiment, 5 mice were humanely culled due to (i) injuries from fighting, (ii) procedure-related stress, (iii) a mass in the chest/neck region, and (iv) reaching the weight loss limits of the project licence (details are provided in Table 3.4). These deaths were not directly attributable to the receipt of CRT; however, it may have impacted sensitivity to stress and played an indirect role in the fighting, weight loss and procedural death.

Cause of death	n	Treatment group	Age (Postnatal day)
Injury (fighting)	1	CRT only	74
Injury (fighting)	1	CRT+PFB	75
Procedure	1	CRT only	150
Lump (chest/neck)	1	CRT only	232
Weight loss	1	CRT only	251

Table 3.4. Deaths over the course of the experiment.

3.4.4. Cranial irradiation was well tolerated

Following irradiation, mice thrived throughout their life course and continued to grow at the same rate as sham-irradiated controls (Figure 3.4). For each mouse, the change in body weight was calculated based on its starting weight, and the impact of CRT only and CRT+PFB was compared to sham; there was no significant difference in body weight between either group at any time point (appendix 1).

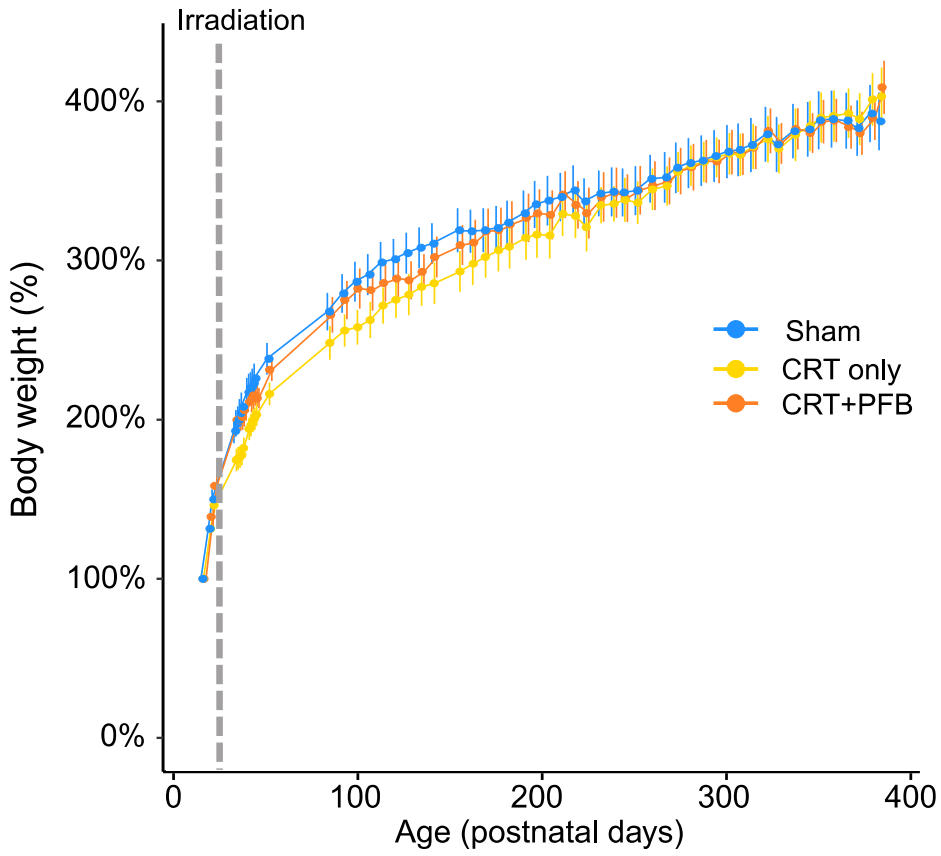

Figure 3.4. Clinically relevant, high-dose, targeted cranial irradiation is well tolerated, and mice thrive independent of posterior fossa boost. Mean body weight (+SEM) measured at least weekly over the course of the study, pre- and post-radiation (p-values given in Table 3.3). Receipt of cranial irradiation is depicted by the dotted line.

3.4.5. CRT with PFB has no additional impact on late-effect profile

Posterior fossa boost (PFB) did not have an additional deleterious impact over and above the receipt of CRT. Overall, premature ageing (frailty assessment, 30 criteria scored at time points F1-4), physical functioning (grip strength test at time points G1-2, rotarod at R1-2, and hanging wire at H1-2) and neurocognition (Y-maze at time points Y1-2, and Barnes maze) was equivalent between CRT only and CRT+PFB groups (Table 3.5). A significant difference in performance between CRT only and CRT+PFB groups, in any sub-measure of frailty, physical functioning or neurocognition, was very rare (3/170 measures tested, 1.8%; Table 3.5). Surprisingly, the CRT only group was worse in 2 of 3 measures, both of which were components of the 30-parameter frailty index (loss of fur colour and breathing rate; Table 3.5).

Given that the receipt of PFB is not associated with late-effect severity in this model, the CRT only and CRT+PFB groups were subsequently combined for further analyses (henceforth collectively referred to as “CRT”) for comparison against sham-irradiated mice.

Assessment		P-value (CRT only vs CRT+PFB)			
Frailty Index					
Time point		**F1**	**F2**	**F3**	**F4**
Body weight (score)		ns	ns	ns	ns
Body weight (g)		ns	ns	ns	ns
Loss of whiskers		ns	ns	ns	ns
Loss of fur colour		ns	0.004	ns	ns
Coat condition		ns	ns	ns	ns
Alopecia		ns	ns	ns	ns
Piloerection		ns	ns	ns	ns
Dermatitis		ns	ns	ns	ns
Breathing rate		ns	ns	ns	0.003
Mouse grimace scale		ns	ns	ns	ns
Cataracts		ns	ns	ns	ns
Corneal opacity		ns	ns	ns	ns
Microphthalmia		ns	ns	ns	ns
Eye discharge/swelling		ns	ns	ns	ns
Kyphosis		ns	ns	ns	ns
Tail stiffening		ns	ns	ns	ns
Vestibular disturbance		ns	ns	ns	ns
Vision loss		ns	ns	ns	ns
Gait disorder		ns	ns	ns	ns
Tremor		ns	ns	ns	ns
Hearing loss		ns	ns	ns	ns
Body temperature (score)		ns	ns	ns	ns
Body temperate (C)		ns	ns	ns	ns
Distended abdomen		ns	ns	ns	ns
Body condition score		ns	ns	ns	ns
Tumours		ns	ns	ns	ns
Prolapse (penile)		ns	ns	ns	ns
Prolapse (rectal)		ns	ns	ns	ns
Diarrhoea		ns	ns	ns	ns
malocclusions		ns	ns	ns	ns
Forelimb grip strength (score)		ns	ns	ns	ns
Average frailty score		ns	ns	ns	ns
Physical functioning					
Time point		**G1**	**G2**	**G3**	**G4**
Grip strength	Forelimb grip strength (g)	ns	ns	ns	ns
Time point		**R1**	**R2**		
Rotarod	Rotation (rpm)	ns	ns		
	Time (s)	ns	ns		
	Distance (m)	ns	ns		
Time point		**H1**	**H2**		
Hanging wire	Success after 1 attempt (%)	ns	ns		
	Success after 2 attempts (%)	ns	ns		
	Success after 3 attempts (%)	ns	ns		

Neurocognitive functioning			
Time point		**Y1**	**Y2**
Y-maze	Spontaneous alternation	ns	ns
Time point		**BM**	
Barnes maze	Primary latency – day 1	ns	
	Primary latency – day 2	ns	
	Primary latency – day 3	ns	
	Primary latency – day 4	ns	
	Primary latency – day 5	ns	
	Primary latency – day 12	ns	
	Total latency – day 1	ns	
	Total latency – day 2	ns	
	Total latency – day 3	ns	
	Total latency – day 4	ns	
	Total latency – day 5	ns	
	Total latency – day 12	ns	
	Primary errors – day 1	ns	
	Primary errors – day 2	ns	
	Primary errors – day 3	ns	
	Primary errors – day 4	ns	
	Primary errors – day 5	ns	
	Primary errors – day 12	ns	
	Total errors – day 1	ns	
	Total errors – day 2	ns	
	Total errors – day 3	ns	
	Total errors – day 4	0.01	
	Total errors – day 5	ns	
	Total errors – day 12	ns	

Table 3.5. Assessment of additional impact of PFB. Adjusted p-values comparing CRT only and CRT+PFB for all assessments of frailty, physical functioning (assessed via grip strength, rotarod and hanging wire), and neurocognitive function (assessed via Y-maze and Barnes maze). 'ns' represents a p-value ≥0.05, green text represents the CRT+PFB group performing significantly worse than CRT only group. Red text represents CRT only group performing significantly worse than CRT+PFB group.

3.4.6. CRT drives accelerated frailty

To assess whether CRT induced frailty in our model, the frailty index, a measure used to provide an overall picture of general health and wellbeing in both mice and humans, was utilised. Frailty was assessed longitudinally (at ~PND 97, 130, 191 and 233; time points F1-4 respectively, Figure 3.5) in our mice by scoring 30 age-related conditions on a scale of 0 (no frailty) to 1 (severe frailty) (Figure 3.6A), and calculating an average to produce a frailty index as described (Fielder *et al.*, 2019; Fielder *et al.*, 2022).

Vision loss, loss of fur colour, piloerection and high breathing rate were the most common parameters with indications of frailty following CRT (Figure 3.6A). Representative images of grimace, loss of fur colour and piloerection are shown in Figure 3.6B and C.

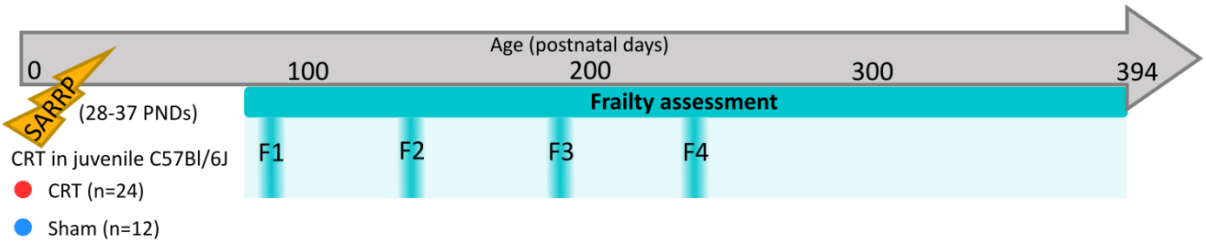

Figure 3.5. Timeline of longitudinal frailty assessment. Frailty was conducted at 4 timepoints (F1: ~PND 97, F2: ~PND 130, F3: ~PND 191 and F4: ~PND 233).

.

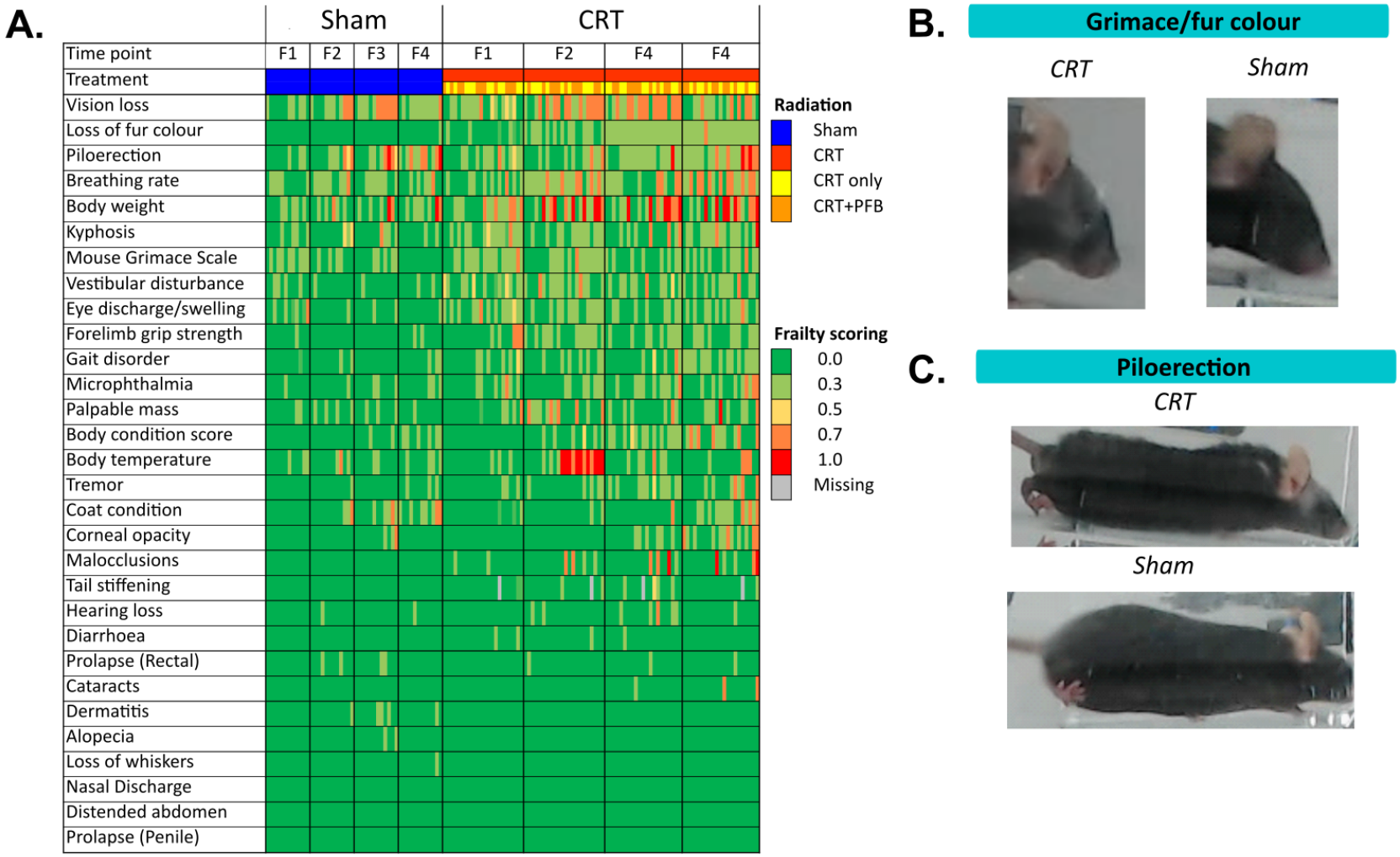

Figure 3.6. CRT drives accelerated development of frailty. A) Increased frailty scores following CRT. Heatmap showing frailty scores for all 30 frailty parameters following CRT or sham-irradiation. Individual frailty criteria were scored from 0 (no impairment, green) to 1 (severe frailty, red). Grey shading depicts missing data. B+C) Examples of commonly impaired features following CRT or sham-irradiation: grimace and loss of fur colour following CRT (B) and piloerection (bristling of hairs) following CRT (C).

Following cranial radiation, frailty manifested early; at F1 (~PND 97; human-equivalent age of ~22 years) frailty index was significantly higher in the CRT group than the sham-irradiated group (p=0.001; Figure 3.7). Increased frailty following cranial irradiation persisted and at all time points was significantly higher than sham-irradiation (F2, p=0.0001; F3, p=0.007 and F4, p=0.002, Figure 3.7).

As expected, the frailty index for sham-irradiated mice increased over the life course (r^2 = 0.101), representing a normal, healthy, ageing profile [52]. However, the rate of frailty index increase was significantly higher following CRT (r^2 = 0.166, p<0.0001) (Figure 3.7).

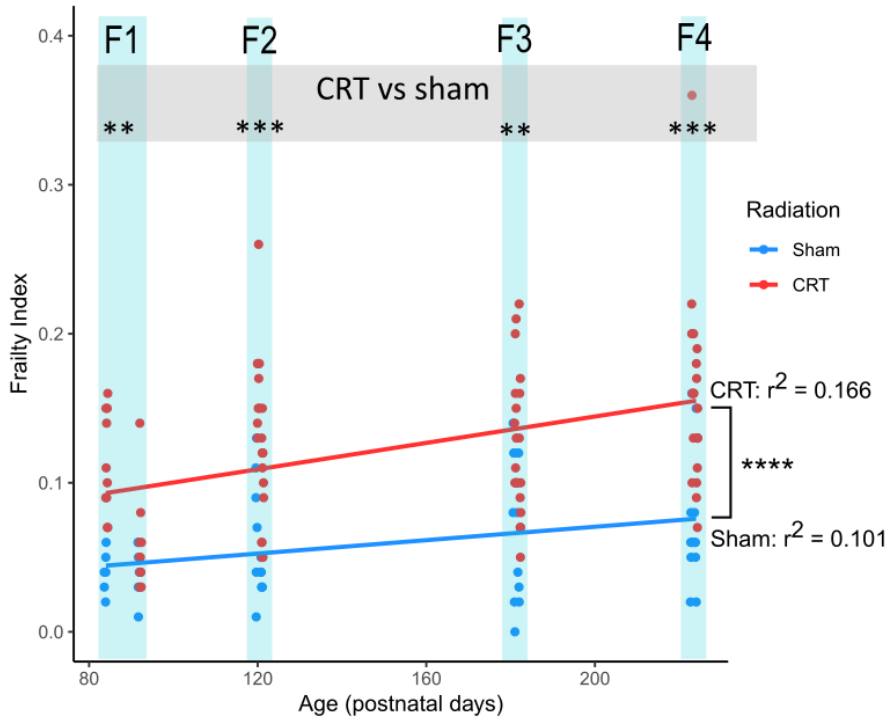

Figure 3.7. CRT drives accelerated frailty. Mean frailty index following longitudinal frailty assessment at F1-4. Each point represents individual mice scores for CRT (red) and sham (blue) groups. Rate of frailty increase is higher in CRT-treated mice. Goodness of fit is denoted by r^2, p-value represent linear regression. Significance is denoted by **: p<0.01, ***: p.0.001, ****: p<0.0001

3.4.6.1. PFB did not further increase frailty

Receipt of high-dose cranial radiation drives accelerated frailty, however the receipt of an additional dose to the posterior fossa did not increase this further. There was no significant difference in frailty between CRT only and CRT+PFB groups at any timepoint (F1, p=0.804; F2, p=0.849; F3; p=0.979 and F4, p=0.923; Figure 3.8A).

Whilst both CRT only and CRT+PFB groups had an increased rate of frailty with age compared to sham-irradiated mice (r^2=0.101), there was no significant difference between CRT only and CRT+PFB irradiated mice (r^2 = 0.167 and 0.164 respectively; Figure 3.8B).

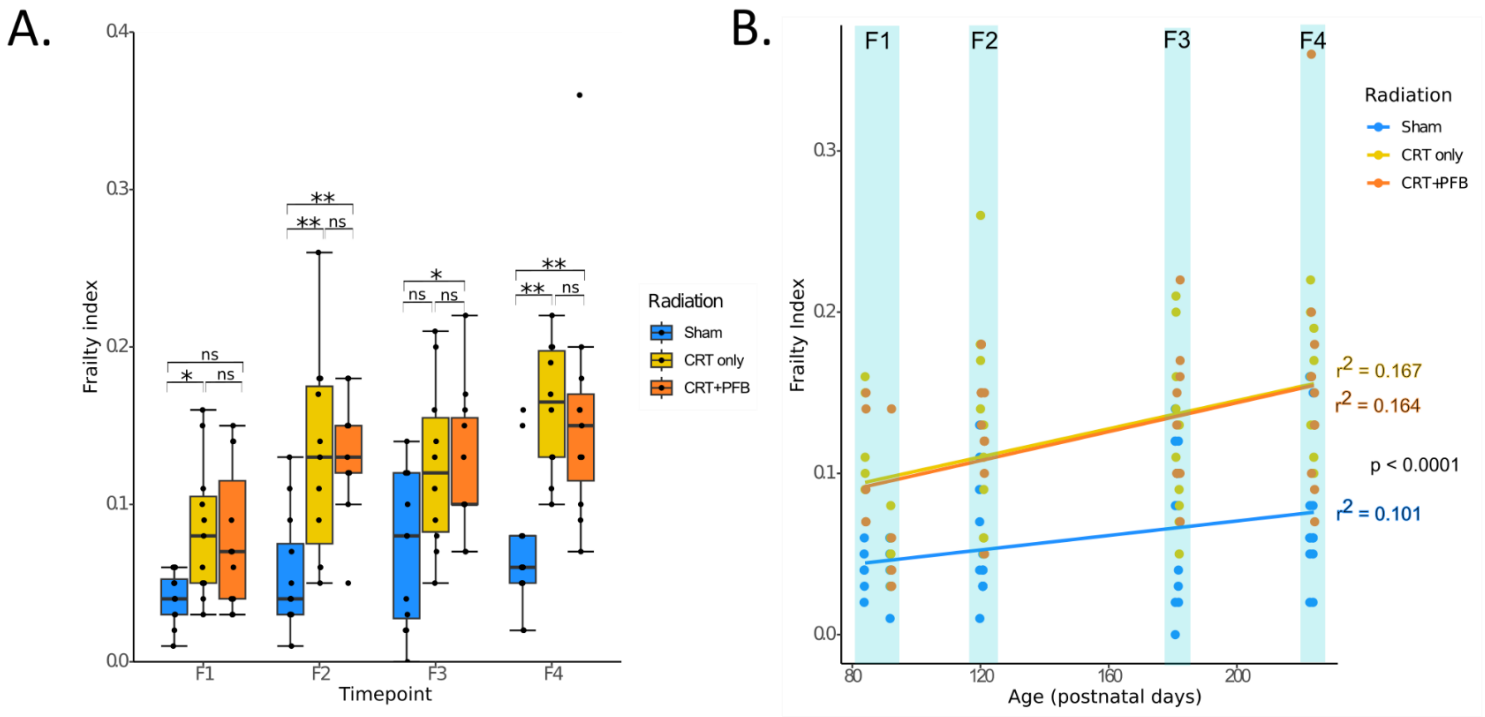

C.

	Sham			CRT only			CRT+PFB		
	F2	F3	F4	F2	F3	F4	F2	F3	F4
F1	0.155	0.053	**0.02**	**0.001**	**0.006**	**0.001**	**0.003**	**0.02**	**0.005**
F2	-	0.23	0.311	-	0.317	0.143	-	0.636	0.338
F3	-	-	0.97	-	-	**0.029**	-	-	0.163

Figure 3.8. Cranial-irradiation drives accelerated frailty, independent of receipt of PFB. A) CRT drives accelerated frailty, independent of receipt of PFB. Longitudinal frailty index (mean frailty score across all 30 criteria) at F1-4, where each point represents individual mice. Significance tested via one-way ANOVA with post-hoc Tukey, $p<0.05$ are in bold font. B) Frailty increases faster in CRT than sham-irradiation, independent of receipt of PFB. Scatterplot showing frailty index for each mouse, with linear regression lines. C) p-values following paired-t tests between all longitudinal frailty assessment points (F1-4), $p<0.05$ are in bold.

3.4.7. Physical function is impaired following cranial-irradiation

3.4.7.1. CRT induces poorer grip strength

Forelimb grip strength was assessed longitudinally using the grip strength test at ~PND 97, 130, 191 and 233 (time points G1-4, respectively; Figure 3.9). The grip strength of the CRT group was worse than sham-irradiated mice at all time points; this was significant at G2 (~PND 130, p=0.031) and G4 (~PND 233, p=0.006) (Figure 3.10A). Both CRT and sham-irradiated groups exhibited a similar rate of reduction in grip strength with age (r^2 = 0.262 and 0.273 respectively; Figure 3.10A).

Receipt of CRT, both with and without receipt of the high-dose boost to the posterior fossa, resulted in reduced forelimb grip strength than sham-irradiated mice. However, the receipt of the PFB did not reduce grip strength further; there was no significant difference in grip strength between CRT only and CRT+PFB groups at all timepoints (G1-4; Figure 3.10B).

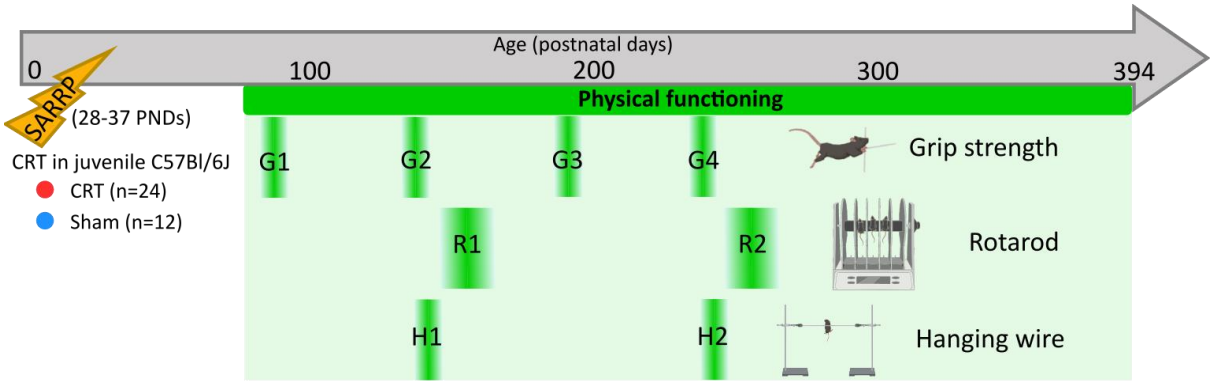

Figure 3.9. Timeline of physical functional assessments. Forelimb grip strength test was carried out at 4 timepoints (G1: ~PND 97, G2: ~PND 130, G3: ~PND 191 and G4: ~PND 233), RotaRod at 2 timepoints (R1: ~PND 172 and R2: ~PND 249) and hanging wire at 2 timepoints (H1: ~PND 145 and H2: ~PND 235).

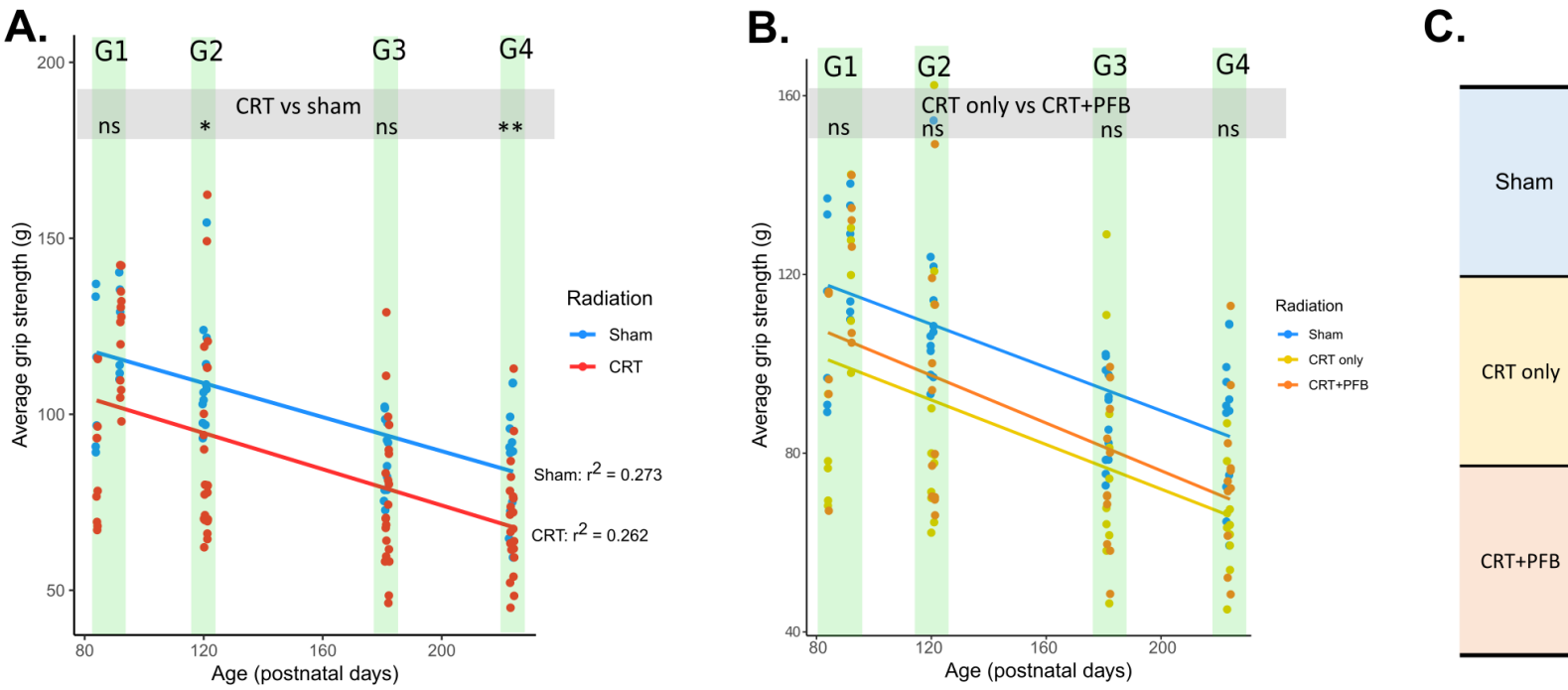

C.

		G1	G2	G3
Sham	G2	0.346	-	-
	G3	**0.0003**	**0.0003**	-
	G4	**0.0004**	**0.0001**	0.84
CRT only	G2	**<0.0001**	-	-
	G3	0.112	0.315	-
	G4	**0.006**	**0.033**	**0.038**
CRT+PFB	G2	**0.035**	-	-
	G3	**0.002**	0.135	-
	G4	**0.001**	0.125	0.96

Figure 3.10. Grip strength was poorer following CRT than sham-irradiation. Scatterplot showing longitudinal grip strength (mean of 3 attempts) at G1-4, where each point represents individual mice for A) CRT (red) and sham (blue) groups and B) CRT only (yellow), CRT+PFB (orange) and sham (blue) groups, with linear regression fit line. Significance was assessed via independent t-tests. Significance is denoted by *: $p<0.05$, **: $p<0.01$ and 'ns': $p\geq0.05$. Grip strength declines over time. Goodness of fit is denoted by r^2. C) p-values following paired-t tests between all longitudinal grip strength at assessment points (G1-4) following sham, CRT only and CRT+PFB irradiation; $p<0.05$ are in bold.

3.4.7.2. Balance, co-ordination and endurance

To assess endurance, and neurological function related to balance and co-ordination, the mice were subjected to the rotarod at ~PND 172 and ~PND 249 (timepoints R1 and R2, respectively, Figure 3.9). The CRT group were able to stay on the rotarod for significantly less time at both R1 (mean time 48.2 vs 70.7 s, p=0.003) and R2 (mean time 52.3 vs 70.2 s, p=0.026, Figure 3.11A). There was no age-associated decline in rotarod performance in either group; there was no significant difference between time on the rotarod at R1 and R2 for both CRT and sham groups (p=0.656 and p=0.807, respectively; Figure 3.11).

The additional dose to the posterior fossa did not further increase the deficit; there was no significant difference in time between CRT only and CRT+PFB group at either R1 or R2 (p=0.458 and p=0.120, respectively; Figure 3.11B). There was also no age-related decline in performance following receipt of CRT+PFB; there was no significant difference between time on the rotarod at R1 and R2 (p=0.085; Figure 3.11B).

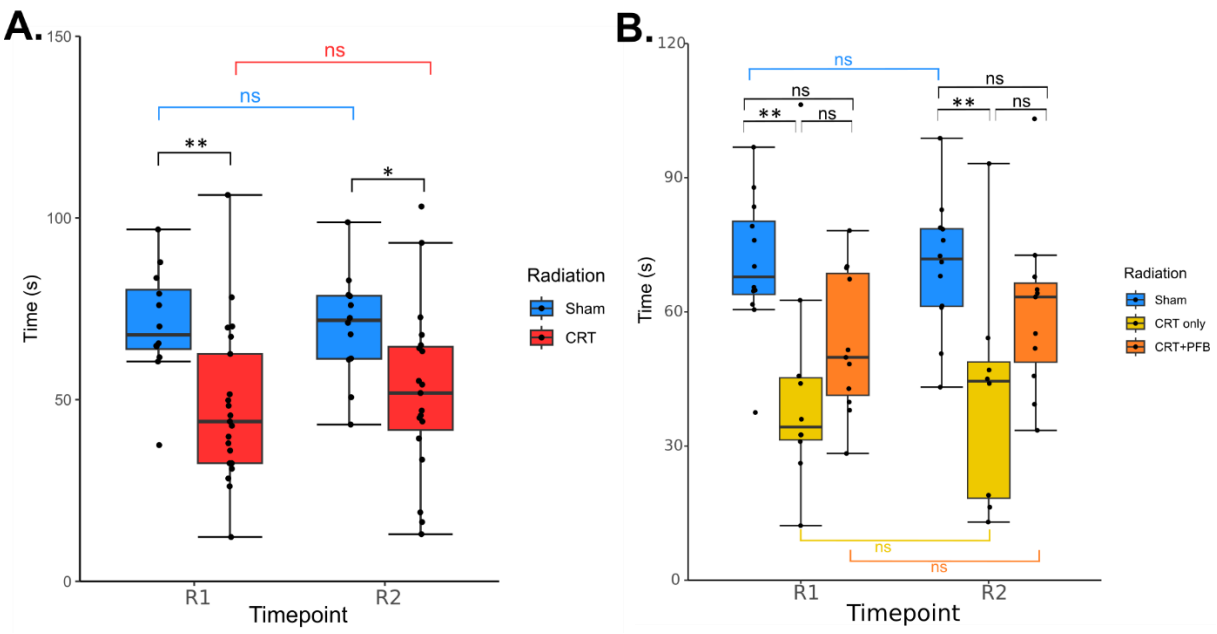

Figure 3.11. Balance, co-ordination and endurance is worse following CRT than sham-irradiation. Average time on the Rotarod (mean time across six trials) at R1 and R2. Each point represents individual mice. Significance was assessed via independent t-tests (black [at both R1 and R2]) and paired t-tests A) red (R1 vs R2 in the CRT group) and blue (R1 vs R2 in the sham-irradiation group), B) yellow (R1 vs R2 in the CRT only group), orange (R1 vs R2 in the CRT+PFB group) and blue (R1 vs R2 in the sham-irradiation group). Significance is denoted by *: p<0.05, **: p<0.01 and 'ns': p≥0.05.

As an additional assessment of forelimb grip strength and co-ordination, the mice were subjected to the hanging wire test at ~PND 145 and ~PND 235 (time points H1 and H2, respectively; Figure 3.9), and were given up to three attempts succeed (defined in Chapter 2.2.3). Performance was slightly poorer in the CRT group than the sham group, though there was no significant difference in mean success between the CRT and sham groups at either H1 or H2 (Figure 3.12A).

The receipt of PFB had no further decline on hanging wire performance. Surprisingly, CRT only typically had poorer performance than CRT+PFB, which was significantly worse at H2 (p=0.007 for both second and third attempts; Figure 3.12B).

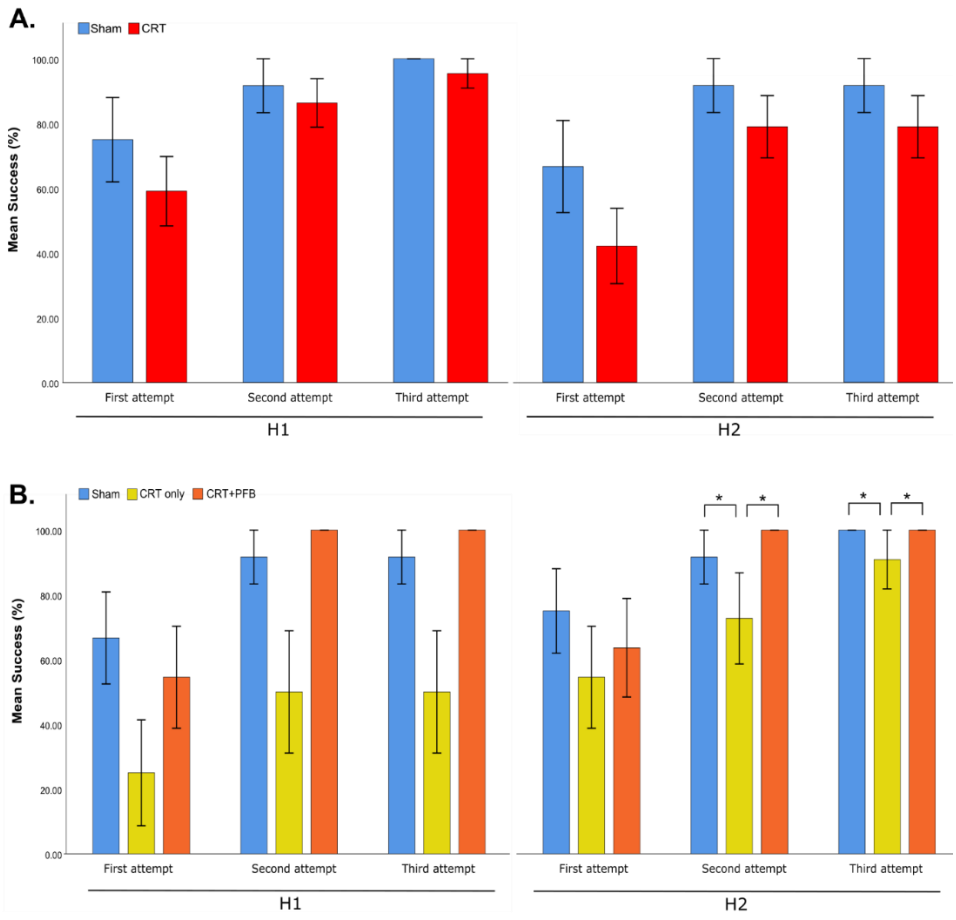

Figure 3.12. Forelimb grip strength and co-ordination following cranial irradiation. Mean success on the Hanging wire after up to three attempts at H1 and H2. Significance was assessed via independent t-tests between A) CRT and sham groups, and B) CRT only, CRT+PFB and sham groups. Significance is shown when p<0.05 and denoted by *.

3.4.8. CRT induces deficits in memory and learning

3.4.8.1. Working memory

To assess working memory, mice were subjected to the Y-maze at ~PND 179 and ~PND 266 (timepoints Y1 and Y2, respectively; Figure 3.13). Whilst at Y1, early in the life course, the CRT group performed equivalently to the sham-irradiated group (p=0.95), at Y2 (~PND 266; human-equivalent age ~36 years) spontaneous alternation was significantly lower than sham-irradiated mice (mean spontaneous alternation: 0.655 vs 0.781, p=0.009; Figure 3.14A).

The receipt of PFB had no additional impact on working memory; there was no significant difference in spontaneous alternation (SA) between CRT only and CRT+PFB groups at Y1 (mean SA: 0.643 vs 0.686, p=0.363; Figure 3.14B) or Y2 (mean SA: 0.630 vs 0.674, p=0.412; Figure 3.14B).

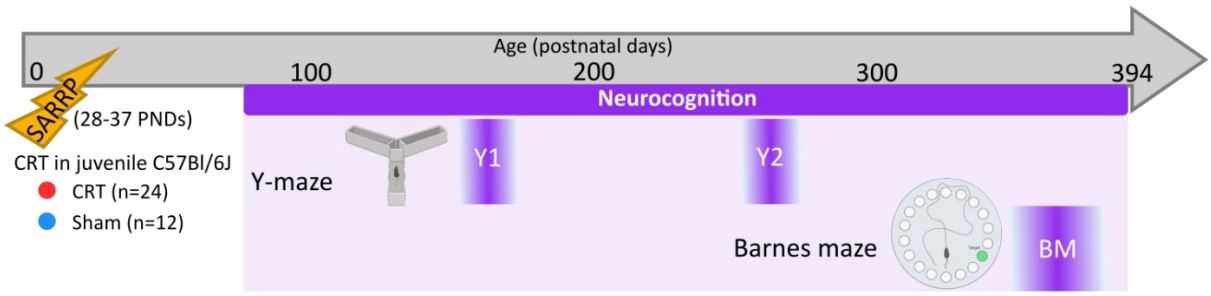

Figure 3.13. Timeline of neurocognitive assessment. Y-maze was carried out at two timepoints (Y1: ~PND 179 and Y2: ~PND 266) and Barnes maze at 1 timepoint (BM: ~PND 369). Brains were harvested at study endpoint (~PND 394).

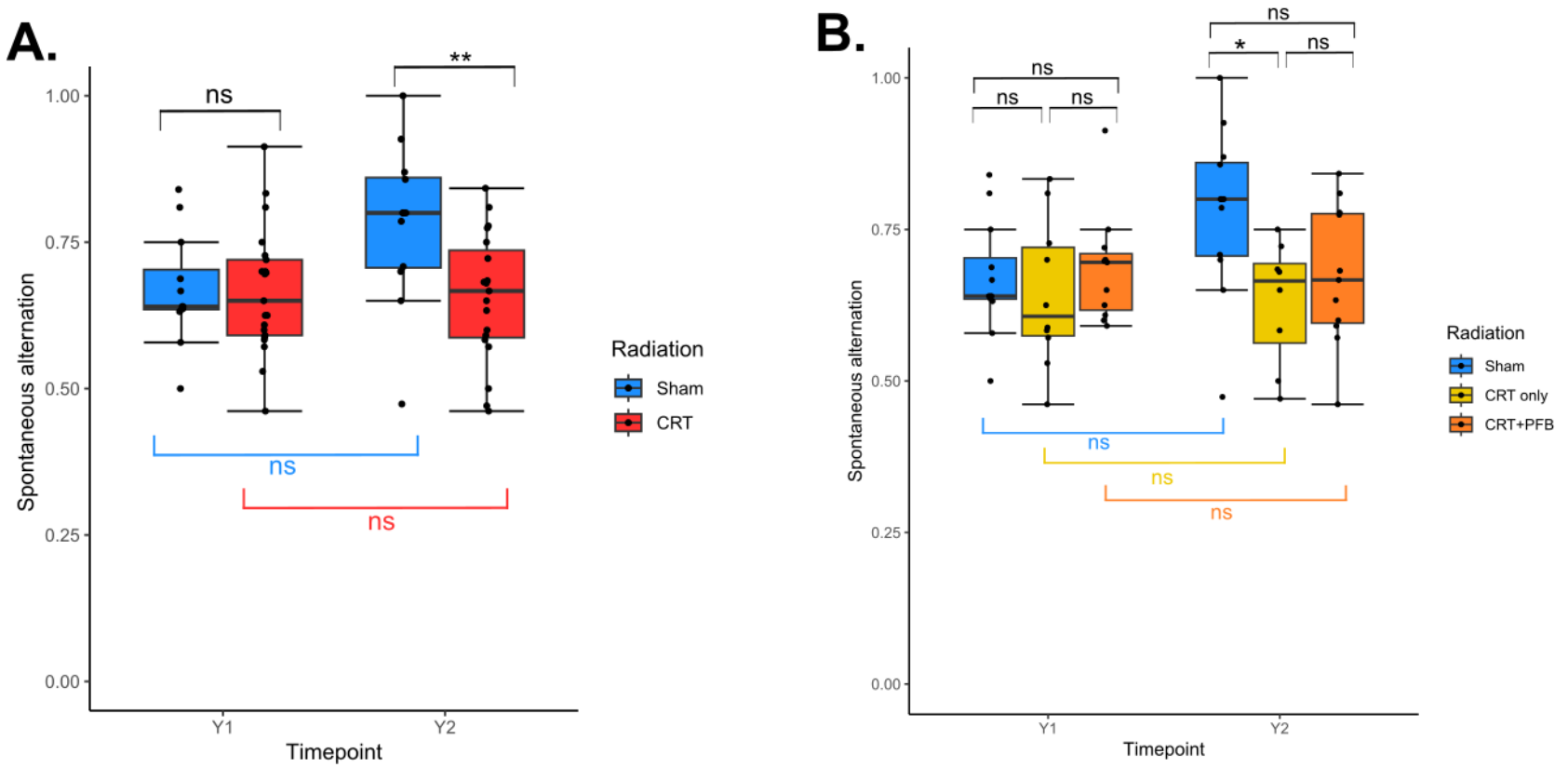

Figure 3.14. Working memory is poorer following CRT than sham-irradiation. Spontaneous alternation at Y1 and Y2, where each point represents individual mice. Significance was assessed via independent t-test (black [at both Y1 and Y2]) and paired t-tests (coloured [Y1 vs Y2]), following A) CRT (blue) and sham (red) irradiation and B) CRT only (yellow), CRT+PFB (orange) and sham (blue) irradiation. Significance is denoted by *: $p<0.05$, **: $p<0.01$ and 'ns': $p\geq0.05$.

3.4.8.2. Spatial learning and long-term memory

The ability to learn and retain learned behaviour was assessed using the Barnes maze at ~PND 369 (human-equivalent age of ~44 years; Figure 3.13). Mice were trained for four days to locate the target hole (spatial acquisition [day 1-4], four trials per day); search strategy and time to locate the target hole improved following. Mice in the CRT group were initially slower to locate the target hole; at day 1 and 2 primary latency (PL; time to locate the target hole) was significantly higher in the CRT group than the sham-irradiated group (day 1 PL: 58.9 vs 37.5 s [p= 0.04] and day 2 PL: 44.5 vs 24.6 s [p=0.028]; Figure 3.15A). Despite being initially slower on training days 1 and 2, the CRT group performed equivalently to the sham-irradiated group by the end of the spatial acquisition period; at day 3 and day 4 PL was equivalent in the CRT and sham-irradiated groups (p=0.333 and p=0.182, respectively; Figure 3.15A).

The receipt of PFB had no additional impairment to learning; mice performed equivalently on all training days (day 1-4) following receipt of CRT only and CRT+PFB (p=0.942, p=0.864, p=0.983 and p=0.385, respectively; Figure 3.15B).

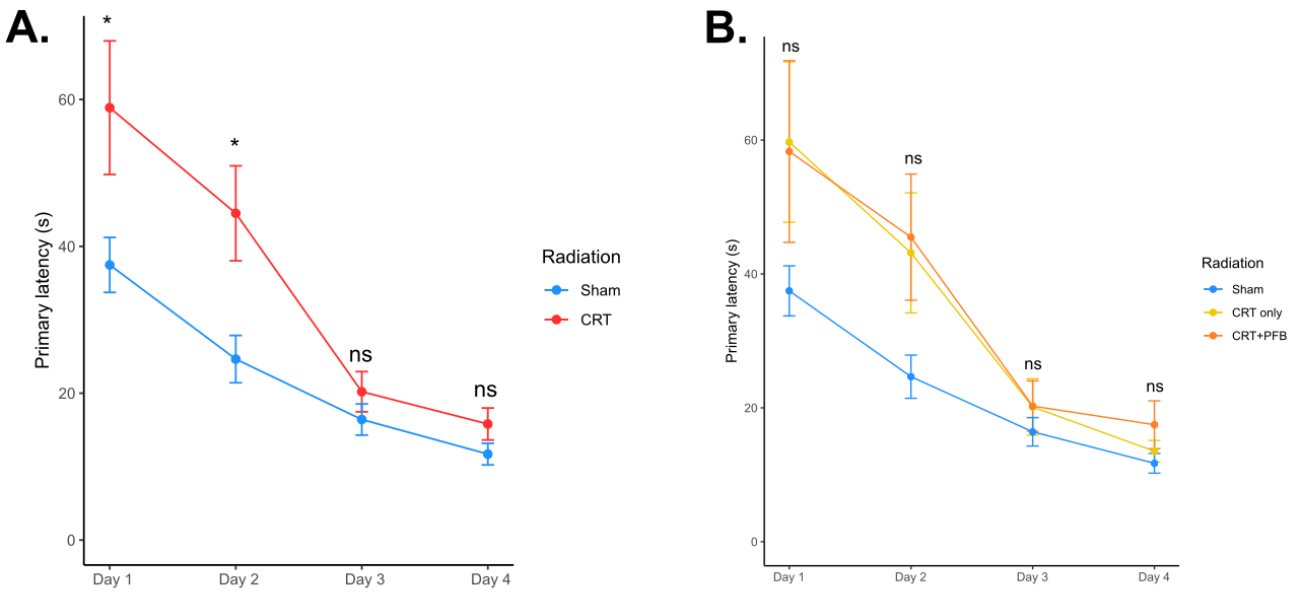

Figure 3.15. Mice receiving CRT showed initial learning deficits but overcame this by day 3. Mean time taken to find the target hole (primary latency, s) during spatial acquisition (day 1-4, four trials per day). Significance was assessed via independent t-tests between A) CRT (blue) and sham (red) irradiation and B) CRT only (yellow) and CRT+PFB (orange) irradiation. Significance is denoted by *: p<0.05 and 'ns': p≥0.05.

CRT induced deficits in long-term memory (LTM) but not short-term memory (STM, Figure 3.16A). A probe trial to assess STM function was performed one day after the spatial acquisition period (day 5). The CRT group showed no deficit in STM; PL was equivalent in CRT and sham-irradiated groups (day 5 mean PL: 11.6 vs 16.7 s, p=0.392). After 1 week, with no further training, a second probe trial was conducted to assess LTM (day 12). Despite having performed equally at day 5, mice that received CRT had impaired LTM and took significantly longer to locate the target hole; PL was significantly higher for the CRT group than sham-irradiated group (day 12 mean PL: 27.4 vs 10.9 s, p=0.029; Figure 3.16A).

The receipt of PFB had no additional impairment on short- or long-term memory; there was no significant difference in PL between CRT only and CRT+PFB at day 5 (mean PL: 13.9 vs 9.9 s, p=0.313) or day 12 (mean PL: 31.1 vs 24.6 s, p=0.647; Figure 3.16B).

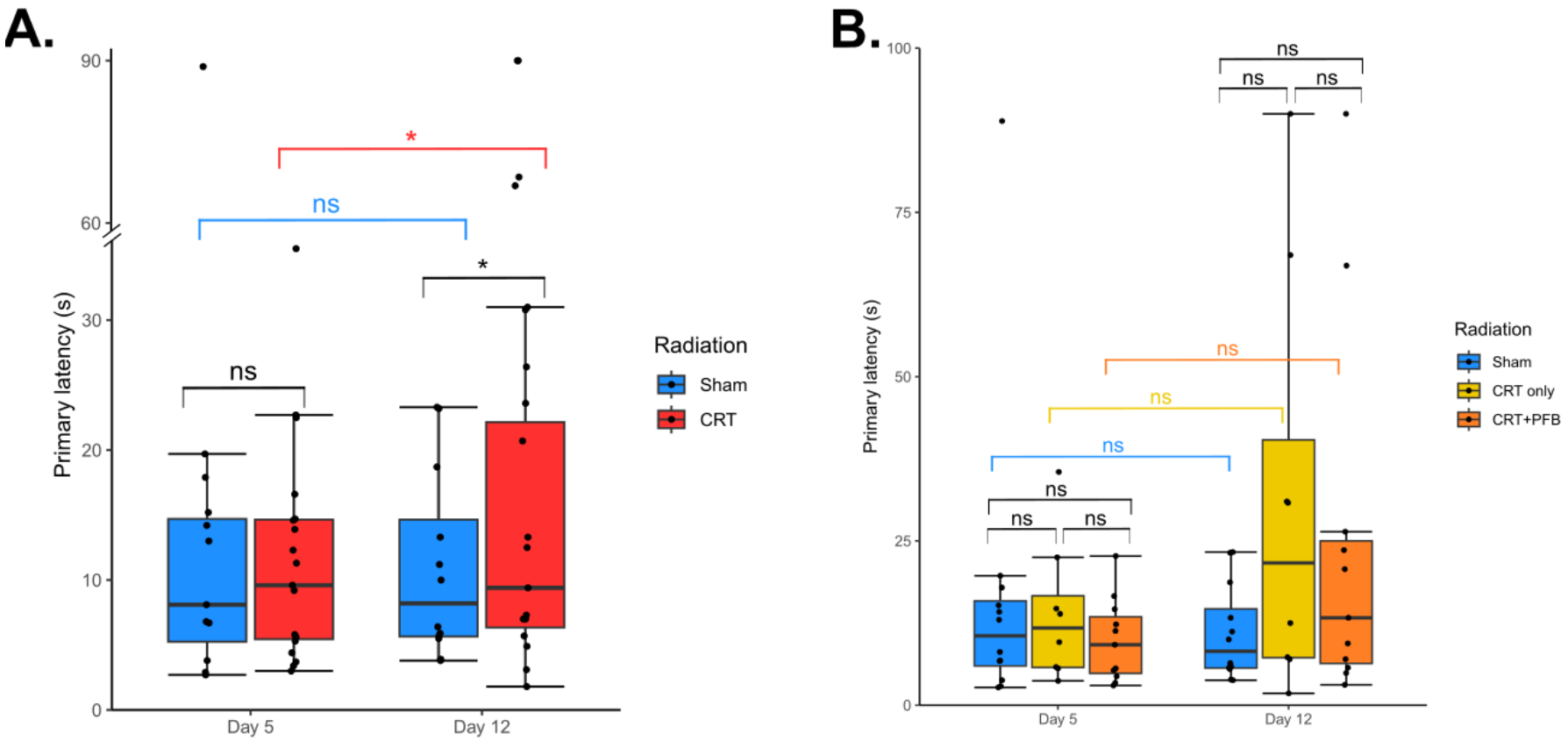

Figure 3.16. CRT drives deficits in long-term memory but not short-term memory. Primary latency on day 5 (short-term memory; STM) and day 12 (long-term memory; LTM), where each point represents individual mice. Significance was assessed via independent t-tests (black [at both day 5 and day 12]) and paired t-tests (coloured [day 5 vs day 12]), following A) CRT (blue) and sham (red) irradiation and B) CRT only (yellow), CRT+PFB (orange) and sham (blue) irradiation. Significance is denoted by *: $p<0.05$ and 'ns': $p\geq0.05$.

3.4.8.3. Brain weight

In our clinically-relevant model, CRT significantly reduced brain size versus sham-irradiation (mean weight: 0.45 g and 0.49 g respectively, p<0.001; Figure 3.17A). Receipt of PFB had no further impact on brain weight; there was no significant difference between CRT only and CRT+PFB (mean weight: 0.45 and 0.46 respectively, p=0.351; Figure 3.17B).

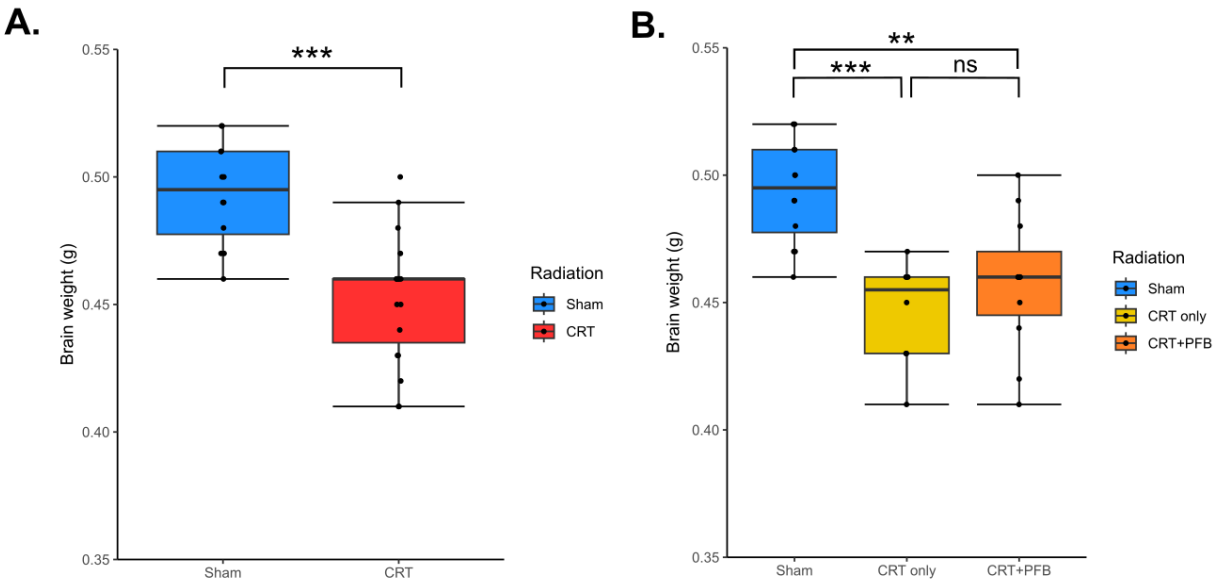

Figure 3.17. Brain weight is lower following CRT than sham-irradiation. Brain weight (g) at ~PND 394, where each point represents individual mice following A) CRT (red) or sham (blue) irradiation, and B) CRT only (yellow), CRT+PFB (orange) or sham (blue) irradiation. Significance was assessed via independent t-test. Significance is denoted by **: p<0.01, ***: p<0.001 and 'ns': p≥0.05.

3.5. Discussion

Survivors of childhood MB often experience a wide range of lasting effects due the cranial irradiation received to treat their primary tumour, leading to significantly impaired quality of life. There is a critical need for the development of interventions to prevent or alleviate the late-effect burden. However, a lack of experimental models that can recapitulate MB radiotherapy hinders their development; current *in vivo* models do not replicate radiotherapy delivery, dose and late-effect profile in developmental stage-matched systems.

3.5.1. Delivery of MB-equivalent radiotherapy

Traditionally, cranial irradiation is delivered to the murine brain via whole-head irradiation, whereby the body is lead-shielded from the radiation, and the head exposed (Wong-Goodrich *et al.*, 2010; Rodgers *et al.*, 2016; Ungvari *et al.*, 2017; de Guzman *et al.*, 2019; Tang *et al.*, 2019). However, delivery via this modality is not precise and non-target regions such as the mouth, ears and eyes are in the radiation field. Delivery of cranial radiation using the SARRP enables precise delivery of a known intensity of X-ray radiation to the target area, with very minimal radiation to non-target areas (<1mm precision) (Wong *et al.*, 2008). In our model, an equivalent (EQD2; equivalent dose in 2 Gy fractions, defined by Fowler (Fowler, 1989)) of 38 Gy cranial irradiation was delivered in 3 Gy fractions. The delivery of high-dose cranial irradiation has been conducted previously; Nimmervoll *et al* delivered 54 Gy in 2 Gy fractions using an orthovoltage irradiator or SARRP, and Morrissy *et al* delivered 36 Gy cranial irradiation in 2 Gy fractions using an image guided small animal irradiator (X-Rad 225CX). However, both models used tumour-bearing adult mice and no assessments of radiation-induced late-effects were conducted (Morrissy *et al.*, 2016; Nimmervoll *et al.*, 2018).

The SARRP utilises CT-guided imaging which also enables irradiation of sub-regions of the brain, and therefore has the potential for precise delivery of radiation to the posterior fossa, which would otherwise not be possible using whole-head irradiation methodologies. There is a current lack of *in vivo* model that deliver CRT with an additional PFB at human-MB equivalent doses. Tomé *et al* delivered a single dose of 10 Gy hippocampus-sparing irradiation using the SARRP to show the neurocognitive impact of avoiding the hippocampus and olfactory bulb in adult mice (Tomé *et al.*, 2015). In our model, in addition to CRT, an equivalent of 49 Gy was delivered to the posterior fossa (38 Gy CRT with 11 Gy PFB), close to the cranial radiotherapy doses received by MB patients.

Childhood MB patients often experience debilitating late-effects due to the receipt of CRT at a young age. Previous *in vivo* studies typically deliver CRT to adult mice, in this model CRT was delivered to cohorts of young mice at ~PND 33, representing a human-equivalent age of ~4 years (the youngest age MB patients typically receive CRT) (Dutta and Sengupta, 2016; Wang *et al.*, 2020). Surprisingly, no animals died due to severe acute toxicity (either during irradiation or up to 60 days after). Over the course of the experiment, 5 mice were humanely culled due to (i) injuries from fighting, (ii) procedure-related stress, (iii) a mass in the chest/neck region, and (iv) reaching the weight loss limits of the project licence. These deaths were not directly attributable to the receipt of CRT; however, it may have impacted sensitivity to stress and played an indirect role in the fighting, weight loss and procedural death. Stress was minimised where possible, including low stress handling and cage enrichment (Gurfein *et al.*, 2012). Whilst secondary malignant neoplasms (SMNs) are not uncommon following radiotherapy, these overwhelmingly occur within the irradiation field (Neglia *et al.*, 2006; Armstrong *et al.*, 2009; Packer *et al.*, 2013). The SARRP produces minimal scatter of radiation to non-target regions (Sayler *et al.*, 2013), and thus, as this mass was outside of the irradiated region, it was not considered an SMN (however no pathology was carried out to confirm this). A limitation of this model is a lack of pre-irradiation (baseline) assessments, however due to travel restrictions during the COVID-19 pandemic this was not possible.

3.5.2. Radiation-induced frailty

Survivors of childhood MB age prematurely and experience increased frailty (Oeffinger *et al.*, 2006; Diller *et al.*, 2009b; Ness *et al.*, 2013). To assess whether CRT induced frailty in our model, the frailty index was utilised. Mice were assessed at four timepoints from ~PND 97 to ~PND 233, an equivalent human age range of 22-33 years old (Dutta and Sengupta, 2016; Wang *et al.*, 2020). Following CRT, mice were more frail and aged quicker than the sham-irradiated group, mirroring the premature ageing observed in childhood cancer survivors. The use of the frailty index provided an overview of general health and can also be used as a predictor of mortality, in both human and mice (Whitehead *et al.*, 2014; Rockwood *et al.*, 2017). The mouse frailty index exhibits key features of the frailty index used in humans and is therefore useful to quantify clinically-relevant deficits relevant to human frailty and ageing. Frailty index can be influenced by stress, however in our study this was minimised by acclimatisation to handling prior to assessments, maintaining low levels of environmental noise and consistent assessors.

3.5.3. Physical functioning

Many survivors of childhood medulloblastoma experience below average physical functioning, particularly within motor functioning, exhibiting difficulties such as ataxia and co-ordination disorders, as well as reduced fine motor skills (Piscione *et al.*, 2013; Chevignard *et al.*, 2017; Varedi *et al.*, 2021; Gielis *et al.*, 2022). Whilst impaired physical functioning can result from the tumour itself, younger age at diagnosis and combination treatment (including surgical resection, chemotherapy, and cranial irradiation) have been identified as risk factors for neurological dysfunction (Gielis *et al.*, 2022). In our model, physical functioning was typically poorer following CRT than sham-irradiation, particularly forelimb grip strength, balance, co-ordination, and endurance. Despite the CRT group having poorer physical function when assessed via the grip strength test and rotarod, in the hanging wire test the CRT group performed equivalently to the sham-irradiated group. However, limitations with the hanging wire test may have resulted in inaccurate results. For example, on occasion the distance to fall was not enough of a deterrent; some mice, which appeared healthy and in good condition, opted to drop from the wire (and consequently were recorded as a failed attempt) rather than fell due to poor physical function.

Despite differences in the physical functioning of mice and humans (in particular, walking on 4 limbs vs 2 limbs), the functional basis of motor function is similar between species (Cenci;Whishaw and Schallert, 2002). In this model CRT induced poorer overall physical functioning, however some facets of human physical functioning were not assessed, and further testing may be required to fully conclude the burden of cranial radiation on physical functioning. Survivors of childhood MB frequently develop ataxia, whilst some features of ataxia were assessed in our model, including balance, co-ordination and gait, fine motor impairments were not recapitulated within this study. Gait was assessed within the frailty index; however, additional use of the stride test and kinematic analysis would provide specific assessment of walking pattern and fine motor function. Moreover, fine motor function can be assessed through Vermicelli handling test (to assess the use of paws and mouth), the single pellet reach test (the ability to reach and grasp) and adhesion removal test (somatosensory ability) (Schönfeld *et al.*, 2017a). These methodologies have previously been used to measure reduced fine motor function following traumatic brain injury, stroke and Parkinson's disease (Bouët *et al.*, 2007; Dunkerson *et al.*, 2014; Adkins *et al.*, 2015; Schönfeld *et al.*, 2017a; Schönfeld *et al.*, 2017b).

3.5.4. Neurocognitive impairment

In this model, brains were harvested at ~PND 394, equivalent to a human age of 46 years old (Dutta and Sengupta, 2016; Wang *et al.*, 2020). The brain weight of mice following CRT was significantly lower than sham-irradiated mice. A decrease in total brain volume following CRT has been linked with reduced neurogenesis, with the white matter particularly affected, however further investigation into the specific substructure vulnerabilities is required (Filley and Kleinschmidt-DeMasters, 2001; Nieman *et al.*, 2015). CRT has been shown to reduce brain volume in both humans and mice (Nieman *et al.*, 2015), which has also been linked to lower IQ scores in childhood MB survivors (Mulhern *et al.*, 1999).

Perhaps the most debilitating of late-effects is impaired neurocognitive function. Cranial radiation-induced neurocognitive impairment experienced by MB survivors, was mirrored within our *in vivo* model system; following CRT mice displayed reduced working memory and long-term memory function. Long term-memory function assessed via the Barnes maze at human-equivalent age of 44 years old (~PND 369), suggested impaired function following CRT. The reduced performance of the CRT group was presumably in part attributable to their worse physical functioning. There was no significant difference between CRT and sham-irradiated groups in the number of errors made prior to locating the target hole, despite the CRT taking longer. However, the distinction of errors can be subjective. Reduced LTM following CRT was expected and mirrors the late-effects experienced by childhood MB survivors. 70-90% of childhood brain tumour survivors demonstrate significant impairment in global intellectual functioning (Dennis *et al.*, 1996; Maddrey *et al.*, 2005), which is in turn strongly correlated with decreased quality of life, poor psychosocial satisfaction, and reduced independence in adulthood (Mitby *et al.*, 2003; Mulhern and Butler, 2004; Mabbott *et al.*, 2005; Gurney *et al.*, 2009). Reduced attention, slower processing speeds and poor working memory are characteristic of medulloblastoma patients who have received cranial radiotherapy (Anderson *et al.*, 1997; Mulhern *et al.*, 1999; Mulhern and Butler, 2004; Maddrey *et al.*, 2005; Brière *et al.*, 2008; Kahalley *et al.*, 2013; Câmara-Costa *et al.*, 2015; Hardy *et al.*, 2018). These domains support the acquisition of new learning such that childhood brain tumour survivors acquire new information at half the rate of unaffected peers (Palmer *et al.*, 2001a). The use of maze-based assessments such as the Y-maze and Barnes maze provide a general insight into neurocognitive function following cranial radiation, though more sophisticated testing would be required for appraisal of the specific domains of neurocognitive functioning.

3.5.5. Additional impact of PFB

In our model, the receipt of CRT with PFB had no additional impact of late-effect profile in comparison to receipt of CRT alone. A dose-dependent neurocognitive late-effect profile in response to cranial radiation is evident in childhood brain tumour survivors (Grill *et al.*, 1999). However, despite the CRT+PFB group receiving a higher dose to the posterior fossa, no additional deficit in our model was observed. Previous studies have reported a selective vulnerability of specific neuro-anatomical substructures to radiation injury, but have implicated radiation to hippocampus, frontal and temporal brain in determining neurocognitive function, rather than the posterior fossa (Armstrong *et al.*, 2010; Seibert *et al.*, 2017; Acharya *et al.*, 2022), supporting our findings.

Surprisingly, when significant differences between CRT only and CRT+PFB were present (for example, breathing rate and fur colour), it was typically the CRT only group that scored worse. This significance is likely due to smaller group size, and a larger proportion of mice being single-housed within the CRT only group than the CRT+PFB group (n=5/9 [56%] and n=2/11 [18%], respectively). Single housing is avoided where possible due to the associated increased effect on stress (HomeOffice, 2004), however in this study several animals required separation due to increased aggression following irradiation and transport from Leeds to Newcastle. Moreover, the individual components of the frailty index were not intended to assess individual characteristics and instead, together provide an assessment of overall health (Whitehead *et al.*, 2014; Rockwood *et al.*, 2017). However, as the significant components (e.g. increased breathing rate) may have underlying implications, affecting subsequent assessments, further specific evaluation is required to determine the extent of this.

3.6. Chapter Summary

Survivors of childhood MB often experience a wide range of deleterious late-effects as result of the cranial radiotherapy used to treat their original tumour. A novel, highly disease-relevant radiotherapeutic injury *in vivo* model was developed, which accurately recapitulates the early stage in development and radiotherapy schedule associated with childhood MB treatment. Receipt of CRT, particularly at a young age, results in a wide-range of deleterious late-effects that can drastically reduce the quality of life of childhood cancer survivors (Palmer *et al.*, 2001a; Palmer *et al.*, 2013; Chevignard *et al.*, 2017; King *et al.*, 2017).

Findings in this chapter show that *in vivo* delivery of childhood MB-equivalent cranial radiotherapy is both feasible and well tolerated. No mice suffered severe acute toxicity following CRT (human-equivalent 38 Gy) and CRT with PFB (human-equivalent 49 Gy), and no deaths were directly associated with the receipt of CRT. Despite the high radiation dose of the PFB, survival and body weight over the course of the study were equivalent to both the CRT only group and the non-irradiated controls.

To both facilitate the elucidation of novel/target mechanisms underpinning MB late-effects and the development of novel neuro-interventional strategies to alleviate the burden of surviving childhood MB, the late-effect burden induced in our childhood MB-equivalent radiotherapy model was longitudinally assessed. In this chapter, it can also be concluded that *in vivo* delivery of childhood MB-equivalent cranial radiotherapy induces an equivalent late-effect profile to that of childhood MB survivors (premature ageing, reduce physical functioning and impaired neurocognition). The receipt of an additional boost dose to the posterior fossa has no additional deleterious effect above that from cranial irradiation alone. Following CRT, mice were more frail and aged quicker than the sham-irradiated group, mirroring the premature ageing observed in childhood cancer survivors. Many survivors also experience impaired physical functioning, and neurological difficulties such as ataxia and co-ordination disorders. These deficits in physical functioning were mirrored in our model; mice that received CRT had poorer balance, co-ordination and endurance (assessed via the rotarod test) and forelimb grip strength (assessed via the grip strength test) compared with sham-irradiated.

Perhaps the most debilitating of late-effects is impaired neurocognitive function. Survivors often experience attention deficits, slower processing speed and impaired working memory

which results in intellectual disability, low levels of academic attainment, poor psychosocial satisfaction, and reduced independence in adulthood (Dennis *et al.*, 1996; Maddrey *et al.*, 2005; Chevignard *et al.*, 2017; Pazzaglia *et al.*, 2020). In our model, working memory and spatial learning and long-term memory was impaired following CRT.

To conclude, delivery of childhood MB-equivalent radiotherapy is tolerated *in vivo* and following longitudinal, multi-parameter assessments, invokes an equivalent late-effect profile to the human disease. Thus, our clinically-relevant model provides an essential platform that will both facilitate the elucidation of novel/target mechanisms underpinning MB late-effects and the development of novel neuro-interventional strategies to alleviate the burden of surviving childhood MB.

Chapter 4. *Ex vivo* interrogation of the biological underpinnings of radiation-induced late-effects

4.1. Introduction

Currently, there is limited understanding of how radiation-induced late-effects develop, and the underlying molecular response to cranial radiation is relatively undefined. Improved understanding the molecular response to cranial irradiation will enable identification of potential targets for the future development of new pharmacological interventions. Additionally, elucidation of the mechanisms involved across the stages of late-effect development will aid identification of biomarkers for screening of high-risk patients.

Cranial irradiation induces acute damage to healthy brain tissue; biological processes such as inflammation, oxidative stress, neuronal growth and repair, and DNA maintenance and repair have been implicated in the development of late-effects following radiotherapeutic insult (Dent *et al.*, 2003; Bentzen, 2006; Begg;Stewart and Vens, 2011). However, due to a previous lack of appropriate model systems, the specific role these pathways play in the development of late-effects, particularly when cranial irradiation occurs at a young developmental age, is yet to be fully explored. Radiotherapy causes damage to normal cells and induces an inflammatory response (previously described in section 1.5.2.2) which can persist and induce injury through a wide range of mechanisms including: disruption of the blood-brain barrier, microglia activation, induction of SASP, neuronal cell death and reduced neurogenesis. Pro-inflammatory signalling from the initial radiotherapeutic insult can persist for several months; radiation-induced damage triggers recruitment of activated immune cells (such as microglia, astrocytes, dendritic cells, peripheral lymphocytes and monocytes) which release pro-inflammatory cytokines (such as TNF-α, IL-1β and IL-6), and further induce cellular damage, thus creating a positive feedback loop and chronic neuroinflammation (Moravan *et al.*, 2011; Lumniczky;Szatmári and Sáfrány, 2017). However, the specific response following MB-equivalent radiation has not yet been fully explored. To characterise the late-molecular response to cranial radiation insult, whole-transcriptome sequencing was employed to identify late differential expression, in response to receipt of CRT+PFB.

Moreover, as previously discussed in chapter 3.5.2, survivors of childhood MB age prematurely and experience increased frailty (Oeffinger *et al.*, 2006; Diller *et al.*, 2009a; Ness *et al.*, 2013). DNA methylation patterns can be influenced by external factors, and have been associated with premature ageing which may provide a predictive biomarker of overall health (Mozhui and Pandey, 2017; Kling;Wenger and Carén, 2020). Whilst patterns of DNA methylation can vary greatly, they consist of conserved regions of unmethylated GC-rich

regions with high densities of CpGs, known as CpG islands, that are often correlated with promoter regions. Consequently, a number of epigenetic clocks have been developed to predict chronological age, through the appraisal of variable CpG sites. The development of epigenetic clocks has enabled the comparison of 'chronological age' with 'epigenetic age' and can be used as a measure of premature ageing (Field *et al.*, 2018; Salameh;Bejaoui and El Hajj, 2020). Mathematical algorithms use the methylation status of a number of genome-wide CpG sites to predict DNA methylation age (Mozhui and Pandey, 2017). Brain tumour survivors often experience a premature ageing phenotype, where their 'epigenetic age' is often older than their 'chronological age' (Field *et al.*, 2018; Kling;Wenger and Carén, 2020; Salameh;Bejaoui and El Hajj, 2020). Qin *et al* predicted epigenetic age through genome-wide methylation assessment of DNA obtained from a blood samples, and showed survivors of childhood cancers had a significantly higher estimated epigenetic age acceleration (EAA) compared to matched controls (Qin *et al.*, 2021). Increased EAA was associated with prior treatment of radiotherapy or alkylating chemotherapy. Moreover, within survivors the presence of unfavourable health conditions was also significantly associated with an increased EAA. Therefore, estimation of EAA may be a useful biomarker in the prediction of premature ageing, as well as the potential to predict the development of late-effects. In this chapter the relationship between cranial irradiation and epigenetic age in both a systemic and tissue-specific context will be explored as a potential future biomarker.

4.2. Aims

The aim of this chapter is to understand the biological mechanistic alterations that occur following cranial irradiation in an *in vivo* model of MB-equivalent cranial irradiation (the development of which is discussed previously in Chapter 3), to aid identification of potential biomarkers for the improved surveillance of late-effect development.

1) To understand the presence of late radiation-induced pro-inflammatory markers, immunohistochemistry (IHC) will be employed on brain tissue harvested 1 year post-irradiation.
    a. To determine whether the receipt of the additional PFB induces greater pro-inflammatory protein expression, IHC will be employed on cerebellum that received either sham, CRT or CRT+PFB.
    b. To assess whether radiation-induced pro-inflammatory protein expression differs between substructures, IHC will also be employed on hippocampal tissue.

2) To identify biological alterations that occurred following cranial irradiation, RNAseq will be employed on cerebellum 1 year post-radiation (CRT+PFB or sham). Differential expression and gene set enrichment analysis will be conducted to identify any major transcriptional alternations.

3) To assess whether cranial irradiation induced epigenetic age acceleration (EAA) in both a systemic and tissue-specific context, a pre-existing epigenetic clock will be utilised on peripheral blood and cerebellum following CRT+PFB or sham-irradiation. To understand the temporal response of EAA, samples taken at 6- and 13-months post-irradiation will be assessed.

4.3. Methods

4.3.1. Immunohistochemistry

Immunohistochemistry (IHC) was conducted on the cerebellum and hippocampus of mice aged ~PND 394 (approximately a year after the receipt of CRT, CRT+PFB or sham irradiation; n=3 per group). Details of e*x vivo* sample preparation are provided in chapter 2.8, and detailed IHC methodology (slide preparation, staining and analysis) is provided in chapter 2.10.

Fisher's Exact test was used to compare the protein expression between treatment groups using combined expression groups (high: ++/+++ and low: -/+). Independent t-tests and one-way ANOVA were used to compare positivity score between treatment groups.

4.3.2. RNA sequencing

RNA was extracted from cerebellum harvested at ~PND 394, as described in chapter 2.8. (*ex vivo* sample preparation) and 2.9.3 (RNA extraction). The quantity and quality (RNA integrity number; RIN) of RNA was assessed using the 4200 TapeStation system (details are provided in chapter 2.9.4). RNA sequencing (RNAseq) and expression analysis was conducted for the CRT+PFB (n=11) and sham-irradiation (n=12) groups, as described in chapter 2.11.

4.3.3. DNA methylation array

Peripheral blood was collected at ~PND 150 via venepuncture (as previously described in chapter 2.1.4) and immediately placed on ice until DNA extraction (within the same day). Brain tissue was harvested at ~PND 394, sliced and rapidly frozen as per details in chapter 2.8. DNA was extracted from fresh blood and frozen cerebellum samples using the DNeasy Blood and Tissue Kit (details provided in chapter 2.9.1) and quantified using the Qubit (details provided in chapter 2.9.2). DNA methylation array was conducted as described in chapter 2.11.4, for the CRT+PFB (peripheral blood [n=11] and cerebellum [n=11]) and sham-irradiation (peripheral blood [n=11] and cerebellum [n=7]) groups. Some samples were not sent for methylation array (despite passing QC) due to limited space on the array.

4.4. Results

4.4.1. Target selection

To explore the impact of cranial-irradiation on late radiation-induced pro-inflammatory markers within the cerebellum and hippocampus and employed IHC on brain tissue harvested 1-year post-irradiation. To understand the late molecular response following cranial irradiation targets were identified from the literature as key inflammatory markers to have altered expression up to a year after irradiation. 6 target proteins were identified that covered a range of neuroinflammation processes for initial assessment via IHC (details are provided in Table 4.1). Briefly, TNF-α was selected due to its central role in modulating the inflammatory, and chronic activity can contribute to tissue damage. CCL-2 promotes inflammation through recruitment of monocytes (which then differentiate into macrophages), and persistent expression has been associated with chronic inflammation. GFAP is expressed by activated astrocytes and is commonly used as a marker of CNS damage. ICAM-1, expressed by endothelial cells, mediates immune cells recruitment following radiation injury and has been linked to chronic tissue injury. Finally, MHC-II (expressed on antigen-presenting cells such as macrophages, dendritic cells and microglia) and CD3 (expressed on T-cells), promote pro-inflammatory signalling, highlighting active inflammation.

Target	Role
TNF-α	Pro-inflammatory cytokine
CCL-2/MCP-1	monocyte chemoattractant protein
GFAP	Marker of astrocyte activation
ICAM-1	intercellular adhesion molecule
MHC-II	Initiate immune response (present on antigen presenting cells)
CD3	T-cell marker

Table 4.1 Neuroinflammation targets selected for IHC.

4.4.2. Optimisation of immunohistochemistry protocols that use mouse-derived primary antibodies.

Immunohistochemistry (IHC) protocols were developed based on the literature and the recommended antibody dilutions obtained from the product suppliers. However, for primary antibodies that were derived from mouse, further optimisation was required. The initial protocols used for TNF-α, GFAP, CCL2 and ICAM-1 resulted in strong background staining (representative images shown in Figure 4.1A), as well as staining in the no primary negative control (red arrows; Figure 4.1A). As an anti-mouse secondary antibody was used, the strong background staining is likely a result of mouse-on-mouse (M.O.M) interactions, whereby the secondary anti-mouse antibody binds to IgG receptors in the mouse tissue as well as the mouse primary antibody. To optimise the IHC protocols, a M.O.M immunodetection kit was used for any mouse-derived primary antibodies to minimise these endogenous interactions (detailed provided in chapter 2.10.2.1). Moreover, primary antibody dilutions were increased which further improved the specificity of staining (Figure 4.1B).

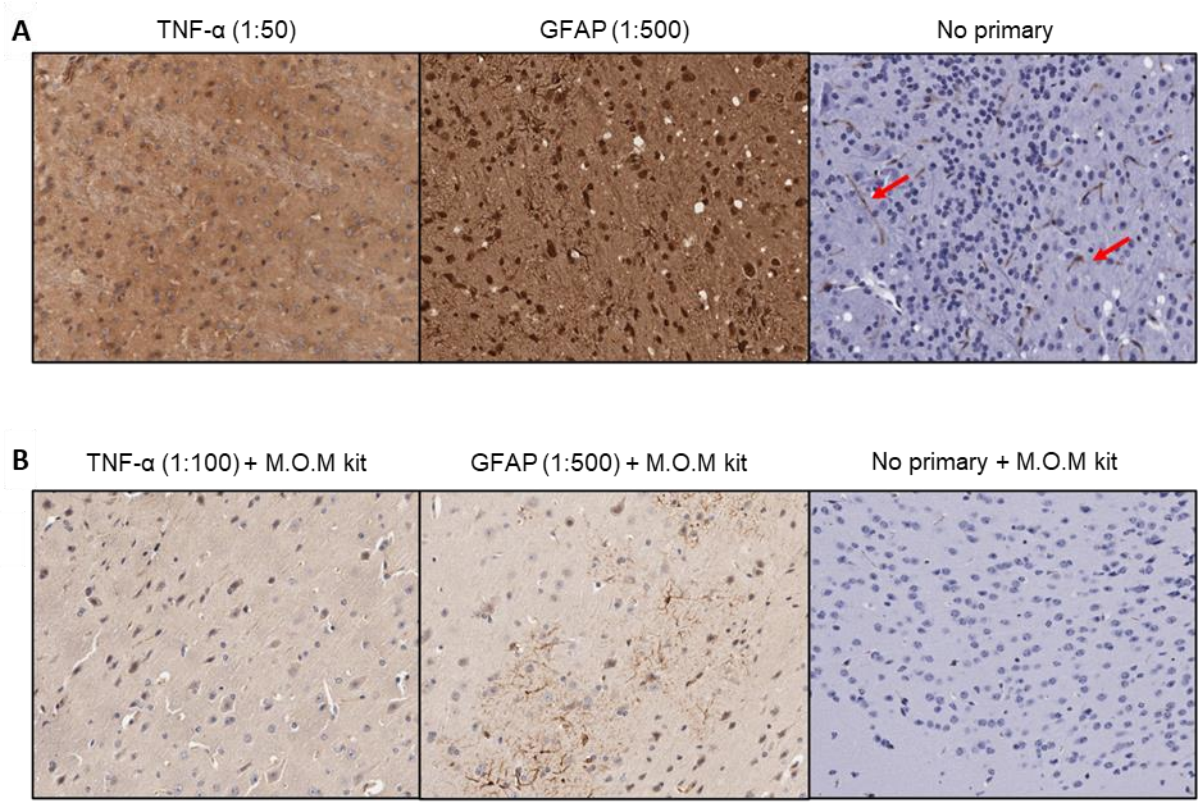

Figure 4.1. Optimisation of primary mouse antibodies for IHC on mouse tissue. A) Anti-TNF-α and anti-GFAP staining with no optimisation. B) Anti-TNF-α and anti-GFAP staining following optimisation of the IHC protocol (addition of mouse-on-mouse immunodetection kit and increased dilutions of the primary antibodies. Staining with no primary was used as a negative control. Red arrows indicate unexpected areas of staining.

4.4.3. Expression of pro-inflammatory proteins, 12 months post-cranial irradiation

Following IHC, the resulting images were assessed based on the proportion of low (+/-) and high (++/+++) positive pixels following CRT, CRT+PFB or sham-irradiation, to determine i) the dose-dependent impact within the cerebellum (0 Gy vs 37.5 Gy vs 48.75 Gy) and ii) spatial differences between the cerebellum and hippocampus within each treatment group. The human-equivalent radiation dose received by each group is summarised in Table 4.2.

Treatment group	Hippocampus dose	Cerebellum dose
CRT	37.5 Gy	37.5 Gy
CRT+PFB	37.5 Gy	48.75 Gy
Sham	0 Gy	0 Gy

Table 4.2. Summary of in vivo cranial irradiation doses for each treatment group. Doses displayed are human-equivalent total dose from fractioned, targeted radiation using the SARRP.

4.4.3.1. ICAM-1

Intracellular Adhesion Molecule 1 (ICAM-1) protein expression was visualised in cerebellum and hippocampal tissue sections taken from mice following CRT only, CRT+PFB or sham-irradiation (representative images are shown in Figure 4.2A). ICAM-1 was present in equivalent quantities across subregions of the brain; there was no significant difference in positivity score between the hippocampus and cerebellum for any of the treatment groups (Figure 4.2B+C). Surprisingly, the proportion of highly positive pixels (++/+++) in the hippocampus was significantly higher in the CRT+PFB group than CRT only group ($p=0.016$; Figure 4.2D), despite receiving the same dose of radiation to this region.

The positivity scores are highly variable within the hippocampus, particularly in the sham and CRT+PFB groups, suggesting variable baseline expression. As expected, baseline expression of ICAM-1 was low in the cerebellum; ENCODE transcription data suggests very low baseline expression in the cerebellum (appendix 2). There is a small increase in ICAM-1 expression within the cerebellum with increased radiation dose, although this was not significant. This suggests a dose-dependent effect and increased radiation may lead to increased ICAM-1 expression, though further investigation is required.

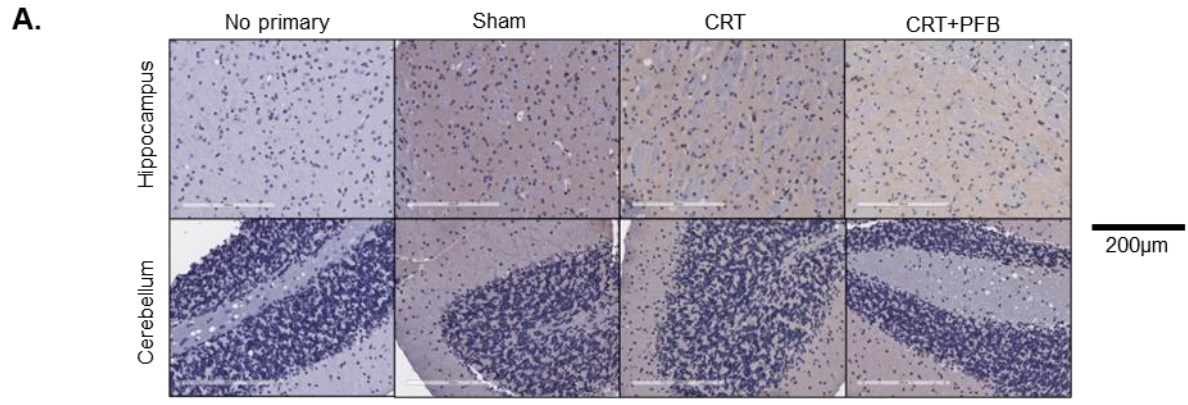

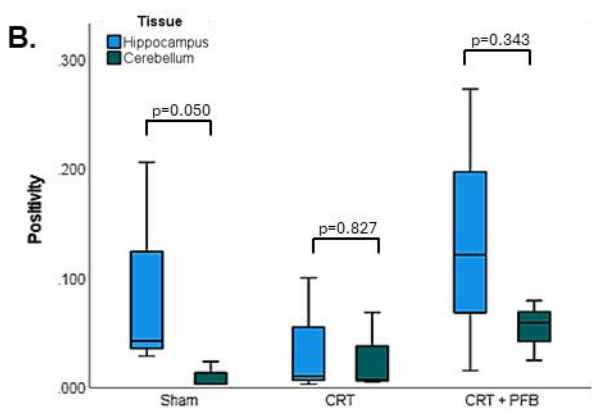

C.

Location	Treatment	p-value
Hippocampus	Sham vs CRT only	0.786
	Sham vs CRT+PFB	0.852
	CRT only vs CRT+PFB	0.485
Cerebellum	Sham vs CRT only	0.275
	Sham vs CRT+PFB	0.051
	CRT only vs CRT+PFB	0.513

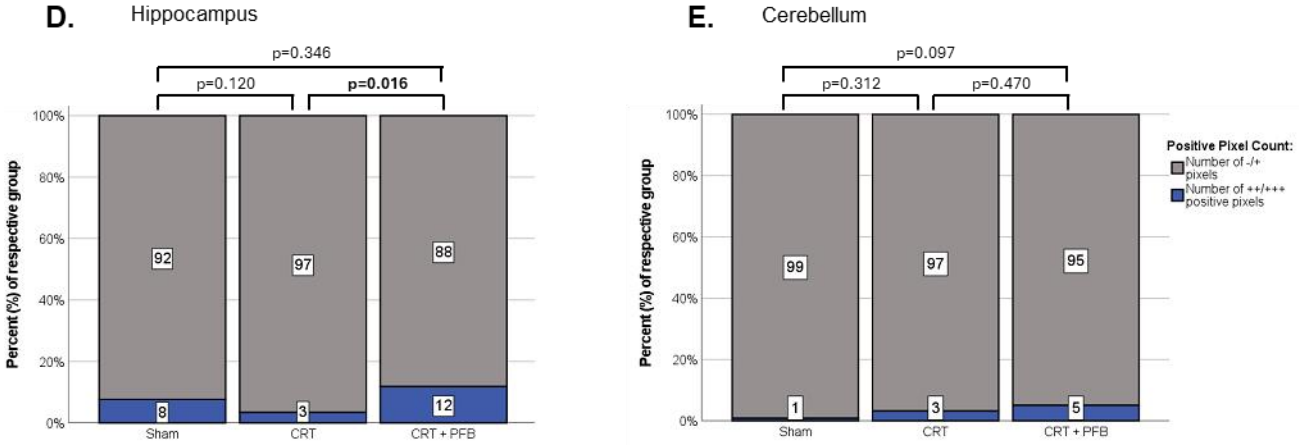

Figure 4.2 ICAM-1 protein levels in the hippocampus and cerebellum following CRT only, CRT+PFB or sham-irradiation. A) Images of the hippocampus and cerebellum following IHC staining for ICAM-1 (20x magnification), B) positivity score for the hippocampus and cerebellum for each treatment group. Significance was assessed between location for each treatment group via independent t-tests, C) table of p-values for comparison of positivity score between treatment groups at each location (significant assessed using one-way ANOVA with post hoc-Tukey). D+E) proportion of low (+/-) and high (++/+++) positive pixels in the hippocampus and cerebellum, protein expression between groups calculated using Fisher's exact test. P-values <0.05 were deemed as significant and are in bold text.

4.4.3.2. CCL2/MCP-1

Monocyte chemoattractant protein-1 (MCP-1, also known as CCL2), is expressed throughout the whole body, though baseline levels are relatively low in the brain (appendix 2; mouse ENCODE transcriptomic data). Expression of MCP-1 protein was higher in the hippocampus than the cerebellum, independent of receipt of radiation, though this was only significant in the CRT+PFB group (sham: p=0.05, CRT only: p=0.074 and CRT+PFB: p=0.045; Figure 4.3A-B). Receipt of radiation did not influence the level of MCP-1; there was no significant difference between treatment groups in either the cerebellum or hippocampus (Figure 4.3C-E). However, IHC was only conducted on brain tissue harvested approximately one year after radiation, and therefore any early alteration in expression of MCP-1 would have been missed.

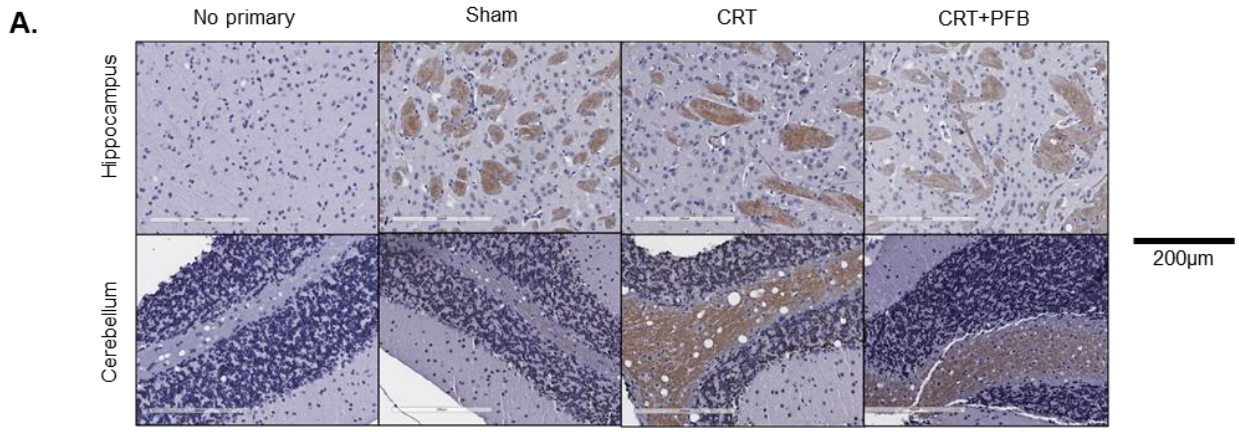

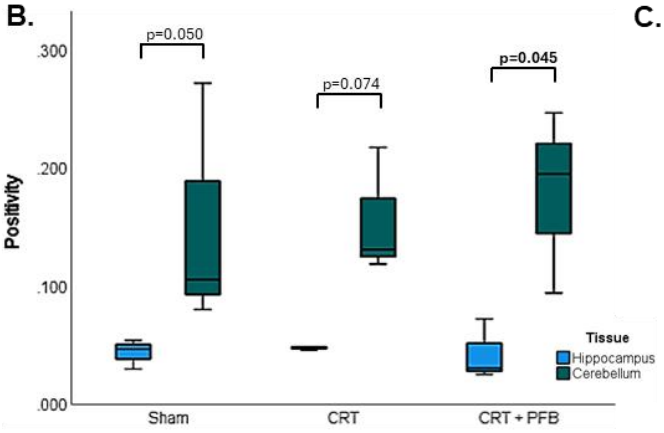

C.

Location	Treatment	p-value
Hippocampus	Sham vs CRT only	0.954
	Sham vs CRT+PFB	0.998
	CRT only vs CRT+PFB	0.933
Cerebellum	Sham vs CRT only	0.990
	Sham vs CRT+PFB	0.919
	CRT only vs CRT+PFB	0.937

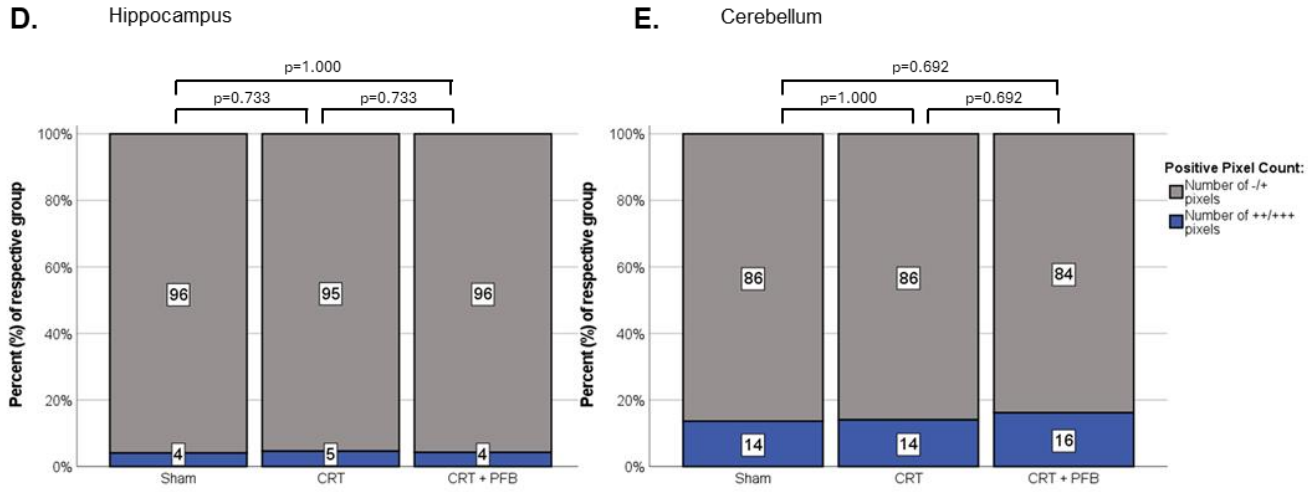

Figure 4.3 CCL2/MCP-1 protein levels in the hippocampus and cerebellum following CRT only, CRT+PFB or sham-irradiation. A) Images of the hippocampus and cerebellum following IHC staining for CCL2/MCP-1 (20x magnification), B) positivity score for the hippocampus and cerebellum for each treatment group. Significance was assessed between location for each treatment group via independent t-tests, C) table of p-values for comparison of positivity score between treatment groups at each location (significant assessed using one-way ANOVA with post hoc-Tukey). D+E) proportion of low (+/-) and high (++/+++) positive pixels in the hippocampus and cerebellum, protein expression between groups calculated using Fisher's exact test. P-values <0.05 were deemed as significant and are in bold text.

4.4.3.3. CD3

The abundance of the cluster of differentiation 3 (CD3) antigen, a marker of T-cells, was assessed in cerebellum and hippocampal tissue sections taken from mice roughly one year following either CRT only, CRT+PFB or sham-irradiation. Strong staining was observed across both brain region and all treatment groups (representative images are shown in Figure 4.4A). There was no significant difference in overall positivity score between the hippocampus and cerebellum in either radiation group (CRT only: p=0.482 and CRT+PFB: p=0.866; Figure 4.4B). However, in the sham-irradiation group CD3 abundance was visually lower within the cerebellum than the hippocampus, albeit this was not significant (p=0.05; Figure 4.4B).

Surprisingly, MHC-II protein expression is lower following CRT+PFB, despite this group receiving the highest dose of radiation. The proportion of strongly positive pixels is significantly lower in the CRT+PFB group compared to either sham group or CRT only in both the hippocampus (CRT only: p<0.001 and sham: p<0.001; Figure 4.4D) and the cerebellum (CRT only: p=0.014 and sham: p=0.259; Figure 4.4E). There was no significant difference in MHC-II abundance between CRT only and sham-irradiation groups, in either the brain region (Figure 4.4D+E). Baseline expression of CD3 within the brain is relatively low (ENCODE mouse transcriptomic data; appendix 2), however, T-cells cross the blood-brain barrier following an immune response.

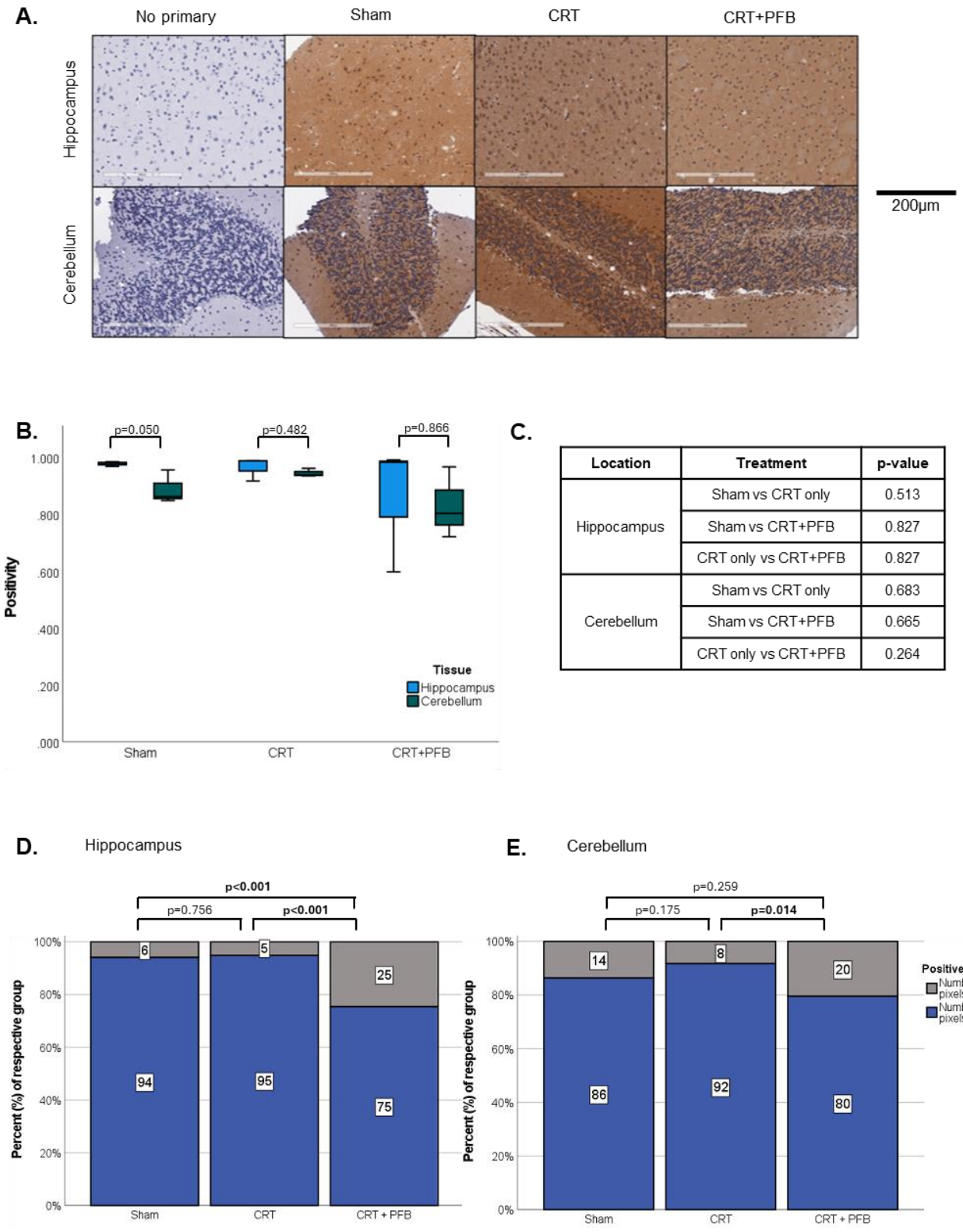

Location	Treatment	p-value
Hippocampus	Sham vs CRT only	0.513
	Sham vs CRT+PFB	0.827
	CRT only vs CRT+PFB	0.827
Cerebellum	Sham vs CRT only	0.683
	Sham vs CRT+PFB	0.665
	CRT only vs CRT+PFB	0.264

Figure 4.4. CD3 protein levels in the hippocampus and cerebellum following CRT only, CRT+PFB or sham-irradiation. A) Images of the hippocampus and cerebellum following IHC staining for CD3 (20x magnification), B) positivity score for the hippocampus and cerebellum for each treatment group. Significance was assessed between location for each treatment group via independent t-tests, C) table of p-values for comparison of positivity score between treatment groups at each location (significant assessed using one-way ANOVA with post hoc-Tukey). D+E) proportion of low (+/-) and high (++/+++) positive pixels in the hippocampus and cerebellum, protein expression between groups calculated using Fisher's exact test. P-values <0.05 were deemed as significant and are in bold text.

4.4.3.4. GFAP

Glial fibrillary acidic protein (GFAP) is a marker of neuroinflammation and astrocyte activation, and largely expressed within the cerebellum, cortex and frontal lobes of the brain (mouse ENCODE transcriptomic data; appendix 2). Levels of GFAP were higher in the hippocampus than the cerebellum; positivity score was significantly higher in the hippocampus for both sham and CRT+PFB groups, but not the CRT only group ($p=0.002$, $p=0.001$ and $p=0.923$, respectively; Figure 4.5A+B). Astrocytes are more abundant within the hippocampus than the cerebellum, and therefore it was expected that positivity score would be higher in the hippocampus, regardless of treatment group.

The level of GFAP in the hippocampus was not altered in response to radiation; there was no significant difference in overall positivity score or the proportion of highly positive pixels (++/+++) between either CRT only or CRT+PFB and the sham-irradiation groups (Figure 4.5C+D). Following irradiation, the level of GFAP in the cerebellum was higher than mice that received sham-irradiation; the proportion of highly positive pixels was higher in the CRT only and CRT+PFB groups ($p=0.034$ and $p=0.090$, respectively; Figure 4.5E). There does not appear to be a dose-dependent effect in either the hippocampus or the cerebellum.

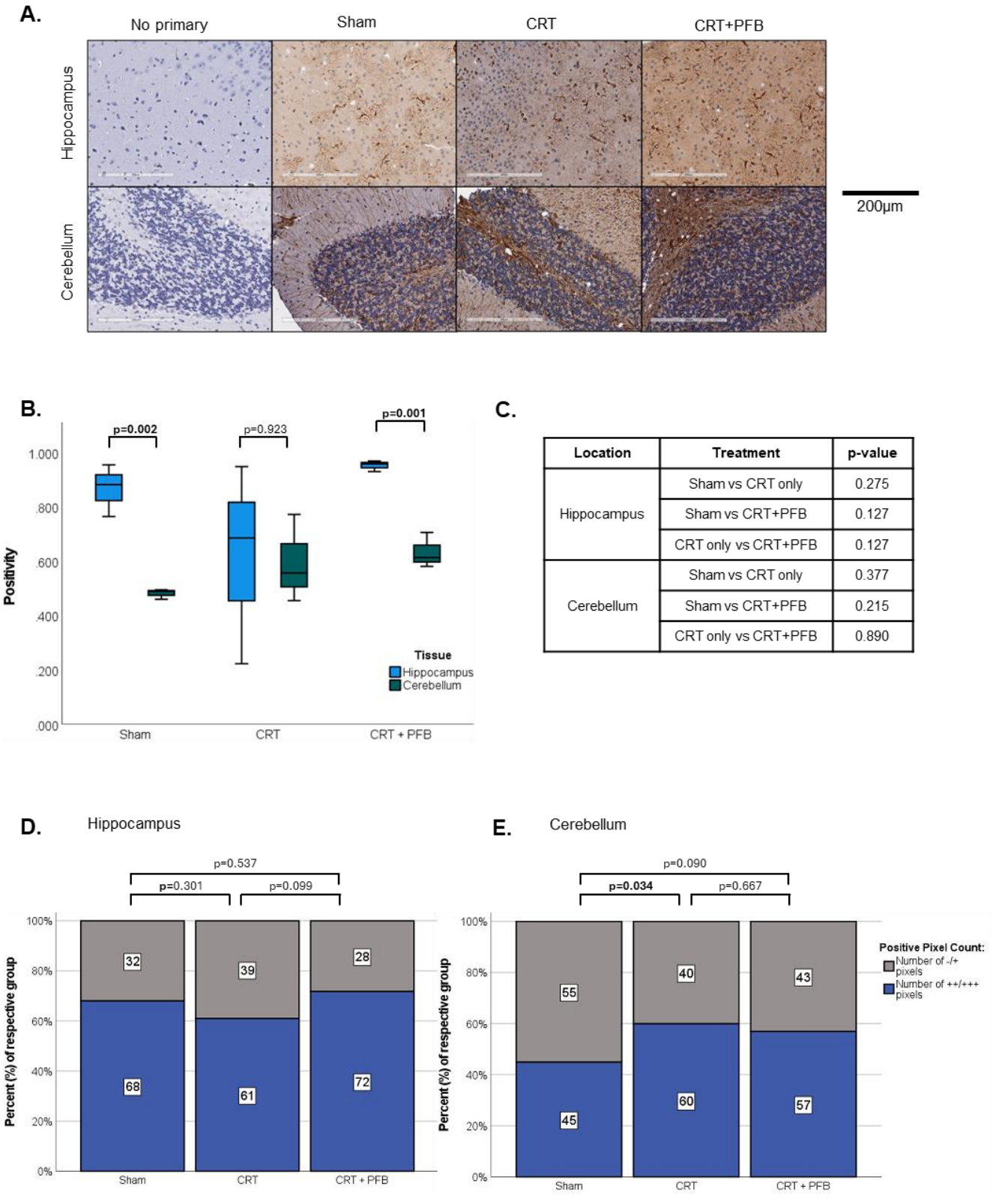

Location	Treatment	p-value
Hippocampus	Sham vs CRT only	0.275
	Sham vs CRT+PFB	0.127
	CRT only vs CRT+PFB	0.127
Cerebellum	Sham vs CRT only	0.377
	Sham vs CRT+PFB	0.215
	CRT only vs CRT+PFB	0.890

Figure 4.5. GFAP protein levels in the hippocampus and cerebellum following CRT only, CRT+PFB or sham-irradiation. A) Images of the hippocampus and cerebellum following IHC staining for GFAP (20x magnification), B) positivity score for the hippocampus and cerebellum for each treatment group. Significance was assessed between location for each treatment group via independent t-tests, C) table of p-values for comparison of positivity score between treatment groups at each location (significant assessed using one-way ANOVA with post hoc-Tukey). D+E) proportion of low (+/-) and high (++/+++) positive pixels in the hippocampus and cerebellum, protein expression between groups calculated using Fisher's exact test. P-values <0.05 were deemed as significant and are in bold text.

4.4.3.5. MHC-II

Major histocompatibility complex class II (MHC-II) are commonly found on antigen-presenting cell and are involved in initiating immune responses. The mouse ENCODE transcriptomic data (appendix 2) suggests there is very low baseline expression of MHC-II within the brain. Generally, the positivity scores for MHC-II expression were higher in the hippocampus than the cerebellum, though this was only significant in the ham-irradiation group (Figure 4.6A+B). Within the hippocampus, the abundance of MHC-II varied across the treatment groups; surprisingly, the proportion of highly positive pixels was significantly less in the CRT group compared to both the CRT+PFB and sham-irradiation groups ($p<0.001$ and $p=0.002$, respectively, Figure 4.6D). However, there was large variability in positivity scores within the hippocampal data from the CRT only group, which may have skewed the results, as data from the CRT+PFB group suggests increased expression of MHC-II within the hippocampus compared to the sham-irradiation group ($p=0.093$; Figure 4.6D). There was no evidence of a dose-dependent response within the cerebellum (Figure 4.6C+E).

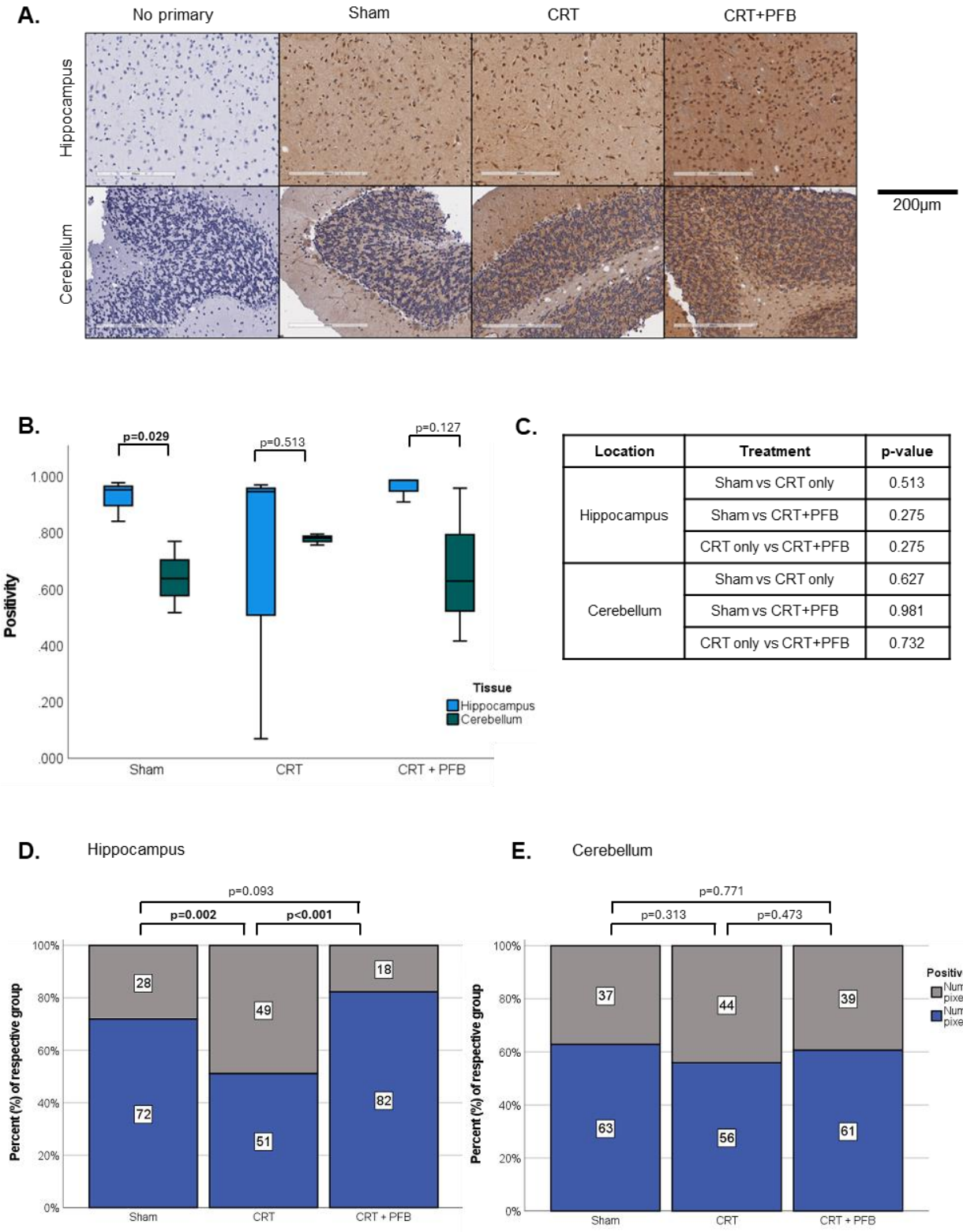

Location	Treatment	p-value
Hippocampus	Sham vs CRT only	0.513
	Sham vs CRT+PFB	0.275
	CRT only vs CRT+PFB	0.275
Cerebellum	Sham vs CRT only	0.627
	Sham vs CRT+PFB	0.981
	CRT only vs CRT+PFB	0.732

Figure 4.6. MHC-II protein levels in the hippocampus and cerebellum following CRT only, CRT+PFB or sham-irradiation. A) Images of the hippocampus and cerebellum following IHC staining for MHC-II (20x magnification), B) positivity score for the hippocampus and cerebellum for each treatment group. Significance was assessed between location for each treatment group via independent t-tests, C) table of p-values for comparison of positivity score between treatment groups at each location (significant assessed using one-way ANOVA with post hoc-Tukey). D+E) proportion of low (+/-) and high (++/+++) positive pixels in the hippocampus and cerebellum, protein expression between groups calculated using Fisher's exact test. P-values <0.05 were deemed as significant and are in bold text.

4.4.3.6. TNF-α

Tumour necrosis factor alpha (TNF-α) is a pro-inflammatory cytokine typically involved in acute inflammation. Expression of TNF-α protein is localised to subregions of the brain; positivity score was higher in the hippocampus than the cerebellum regardless of treatment group, though this was only significant in the CRT+PFB group (p=0.011; Figure 4.7A-C). This result is supported by the mouse ENCODE transcription data; baseline of TNF-α expression is low throughout the brain, with the lowest levels in the cerebellum.

There was no increase in expression in response to radiation, at this late time point. Surprisingly, following CRT only the proportion of highly positive pixels (++/+++) in the hippocampus was significantly lower than both the sham and CRT+PFB groups (p=0.025 and p=0.004 respectively; Figure 4.7D). The hippocampus of mice in the CRT only and CRT+PFB groups received the same dose (37.5 Gy) and therefore any increase in TNF-α is unlikely to be a consequence of radiation.

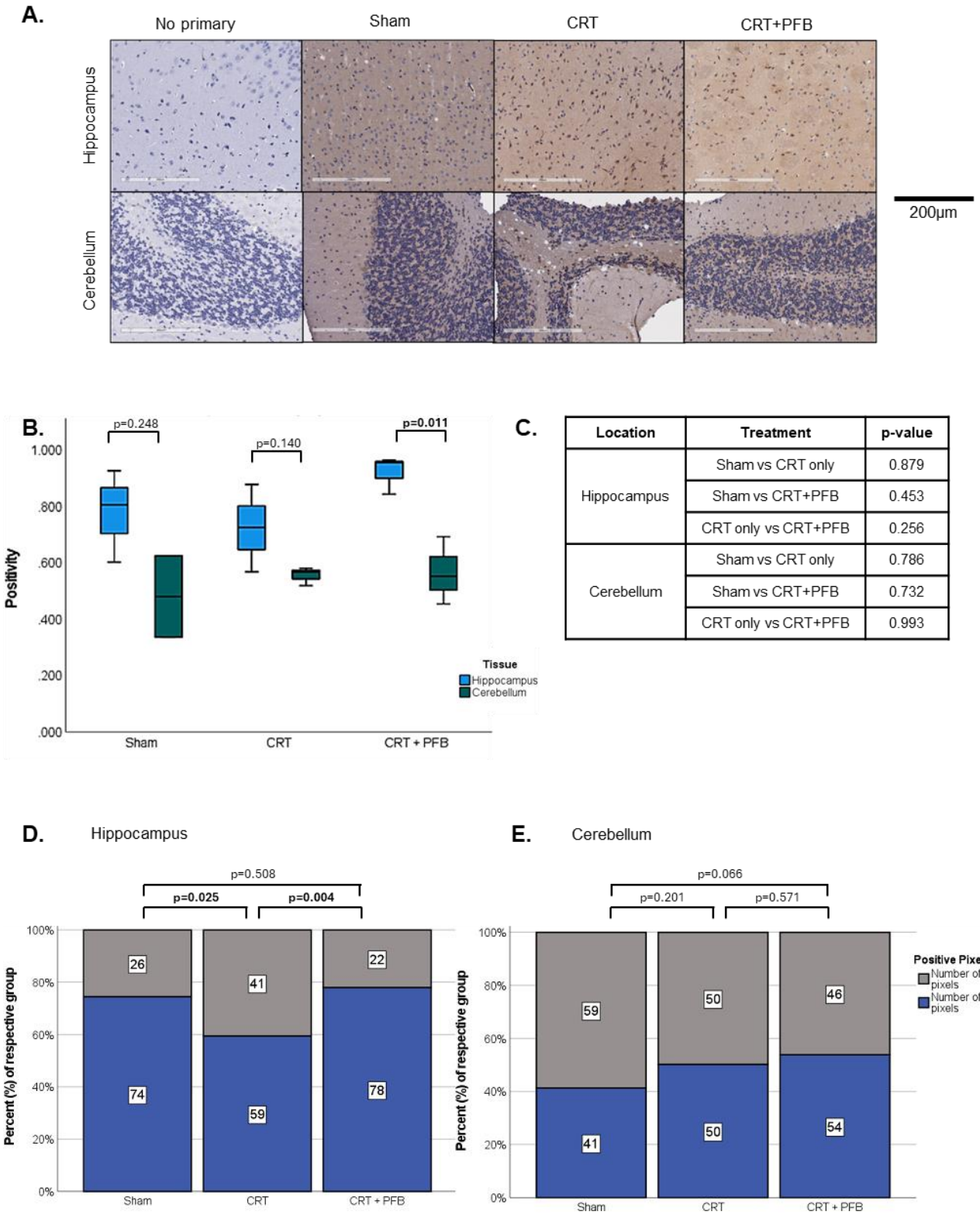

Location	Treatment	p-value
Hippocampus	Sham vs CRT only	0.879
	Sham vs CRT+PFB	0.453
	CRT only vs CRT+PFB	0.256
Cerebellum	Sham vs CRT only	0.786
	Sham vs CRT+PFB	0.732
	CRT only vs CRT+PFB	0.993

Figure 4.7. TNF-α protein levels in the hippocampus and cerebellum following CRT only, CRT+PFB or sham-irradiation. A) Images of the hippocampus and cerebellum following IHC staining for TNF-α (20x magnification), B) positivity score for the hippocampus and cerebellum for each treatment group. Significance was assessed between location for each treatment group via independent t-tests, C) table of p-values for comparison of positivity score between treatment groups at each location (significant assessed using one-way ANOVA with post hoc-Tukey). D+E) proportion of low (+/-) and high (++/+++) positive pixels in the hippocampus and cerebellum, protein expression between groups calculated using Fisher's exact test. P-values <0.05 were deemed as significant and are in bold text.

	Comparison	ICAM-1		CCL2		CD3		GFAP		MHC-II		TNF-α	
		score	prop	score	prop	score	prop	score	prop	score	prop	score	prop
Cerebellum	CRT only vs sham	ns	ns	ns	ns	ns	ns	ns	0.034	ns	ns	ns	ns
	CRT+PFB vs sham	ns	ns	ns	ns	ns	ns	ns	ns	ns	ns	ns	ns
	CRT only vs CRT+PFB	ns	ns	ns	ns	ns	0.014	ns	ns	ns	ns	ns	ns
Hippocampus	CRT only vs sham	ns	0.016	ns	ns	ns	ns	ns	ns	ns	0.002	ns	0.025
	CRT+PFB vs sham	ns	ns	ns	ns	ns	<0.001	ns	ns	ns	ns	ns	ns
	CRT only vs CRT+PFB	ns	ns	ns	ns	ns	<0.001	ns	ns	ns	<0.001	ns	0.004
CRT only	CB vs hippocampus	ns		ns		ns		ns		ns		ns	
CRT +PFB	CB vs hippocampus	ns		0.045		ns		0.001		ns		0.011	
Sham	CB vs hippocampus	ns		ns		ns		0.002		0.029		ns	

Table 4.3. Summary of IHC results. Comparison of protein abundance in cerebellum and hippocampus following CRT only, CRT+PFB or sham-irradiation. For positivity score [score], significance was assessed independent t-tests (between locations) and one-way ANOVA with post hoc-Tukey (between treatment groups). To test the significance between the proportion of low (+/-) and high (++/+++) positive pixels [prop] in the hippocampus and cerebellum, calculated using Fisher's exact test. P-values are displayed when <0.05, 'ns' depicts non-significant.

4.4.4. Transcriptional alternations following cranial irradiation

For non-biased assessment of the late molecular response to cranial irradiation, whole transcriptome sequencing was conducted on RNA extracted from the cerebellum harvested approximately 1 year after CRT+PFB or sham-irradiation.

4.4.4.1. RNA quality control

To maintain high quality sequencing only samples that met a minimum quantity of 150 ng and a RIN of 7 were sent for RNA sequencing (RNAseq; appendix 3). 91.3% (n=21/23) of samples passed quality control (QC) on the first attempt.

Two samples did not meet the QC criteria. For failed samples an additional section of tissue was chipped, and RNA extraction was repeated. Following re-extraction, the QC criteria was met by all samples (appendix 3).

4.4.4.2. Differential gene expression following cranial irradiation

First, quality control was conducted on the raw sequencing data using *FastQC.* Poor quality data can be improved with trimming; however, this was not necessary in this dataset as data for all samples was of good quality. All samples progressed to quantification (*Salmon*) and differential expression analysis (*DESeq2*).

Principal Component Analysis (PCA) was conducted to visualise similarities between samples. Unsupervised clustering was performed, and data points were plotted in 2-dimensions based on similarity with one another; samples that are closer in distance are more similar. Therefore, the PCA plot can be used to identify any outlying samples that may skew subsequent analysis. As illustrated in Figure 4.8, there are no obvious outliers following the RNAseq, and therefore no samples were removed from subsequent analysis.

Surprisingly, the samples did not form discrete clusters based on the receipt of radiation. As PCA derives two sets of principal components (PC1 and PC2) that summarise the variance between all the samples, this suggests that there is a lack of global changes consistent between the two groups, at this late time point.

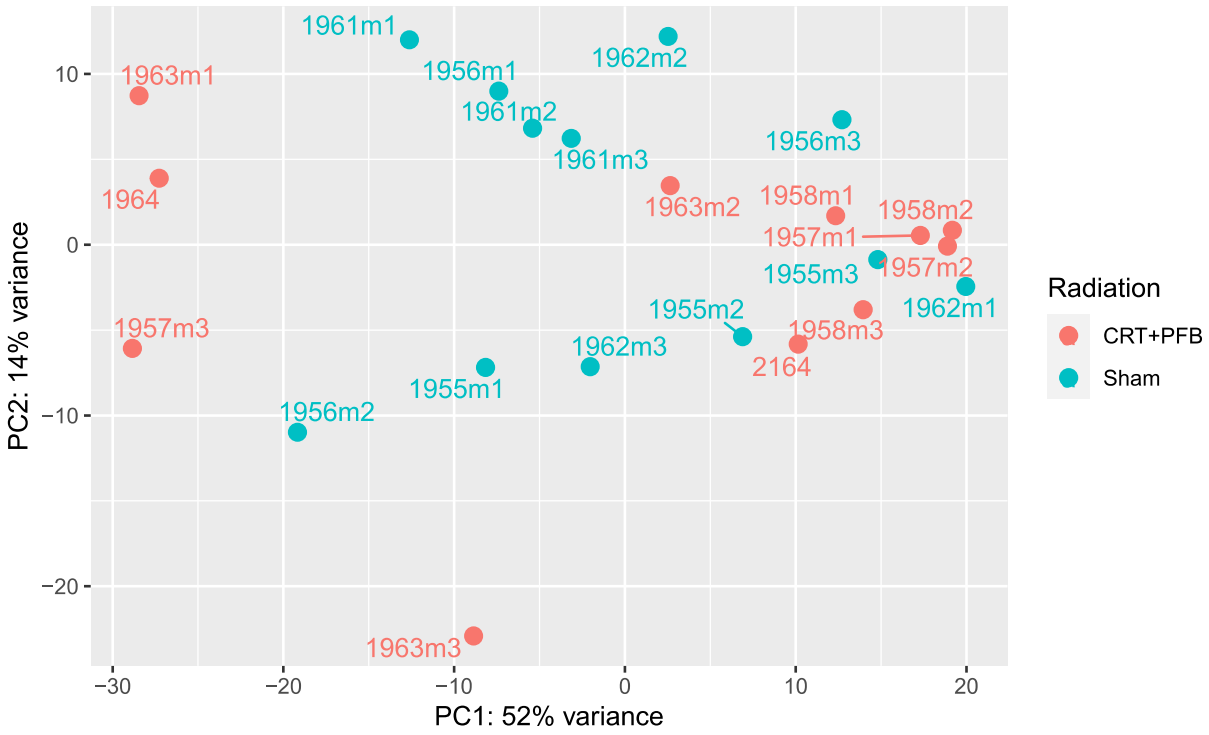

Figure 4.8. Principal component analysis of whole transcriptome sequencing of the cerebellum, approximately 12 months after CRT+PFB (red) or sham-irradiation (blue).

To identify key genes that were differentially expressed following CRT+PFB and sham-irradiation, genes were filtered by i) an expression fold change of 2 (*log2FoldChange > 1*; genes that were either up- or down-regulated by a factor of 2) and ii) adjusted p-value of less than 0.05. Following filtering, 15 genes were significantly differentially expressed following receipt of CRT+PFB, all of which had reduced expression compared to sham-irradiation: C*dh3, Or4e5, Ecrg4, Large2, Cldn2, Steap1, Lrrc71, Wfdc2, Pcolce, Slc28a3, Slc39a4, Ifi27l2a, Slc4a5, Folr1* and *Sult1c2.* Details of the differentially expressed genes (DEGs) are provided in Table 4.4.

Next, pathway analysis was conducted to identify any common pathways between the 15 DEGs. There were 2 common pathways shared between the DEGs: mineral absorption (*Steap1* and *Slc39a4*) and cell adhesion molecules (*Cldn2* and *Cdh3*).

Gene symbol	Gene name	Function	log2FoldChange	padj
Cdh3	Cadherin 3	Cell junction organization and ERK Signalling	-2.074	0.001
Or4e5	Olfactory receptor family 4 subfamily E member 5	Olfactory response	-4.697	0.005
Ecrg4	ECRG4 augurin precursor	Hormone regulation, CNS cell proliferation/senescence	-2.954	0.010
Large2	LARGE xylosyl- and glucuronyltransferase 2	Protein modification/metabolism	-2.008	0.010
Cldn2	Claudin 2	Cell junction organsation	-3.252	0.010
Steap1	Six transmembrane epithelial antigen of the prostate 1	Metabolism	-3.144	0.014
Lrrc71	Leucine rich repeat containing 71	-	-2.933	0.022
Wfdc2	WAP four-disulfide core domain 2	Innate immunity	-3.685	0.024
Pcolce	Procollagen C-endopeptidase enhancer protein	Collagen synthesis	-1.240	0.027
Slc28a3	Solute carrier family 28 (sodium-coupled nucleoside transporter), member 3	Nucleoside transporter, neurotransmission, vascular tone	-5.193	0.030
Slc39a4	Solute carrier family 39 (zinc transporter), member 4	Zinc/iron transportor	-2.611	0.035
Ifi27l2a	Interferon, alpha-inducible protein 27 like 2A	Immune response, metabolism, apoptosis	-1.339	0.035
Slc4a5	Solute carrier family 4, sodium bicarbonate cotransporter, member 5	Sodium bicarbonate cotransporter	-2.806	0.036
Folr1	Folate receptor alpha	Folate transport	-3.710	0.047
Sult1c2	Sulfotransferase family, cytosolic, 1C, member 2	Hormone/neurotransmitter regulation	-4.655	0.047

Table 4.4. Genes differentially expressed following CRT+PFB and sham-irradiation. Significant results were filtered for a fold change greater than 2 (log2FoldChange > 1) and adjusted p-value less than 0.05 (padj<0.05). Gene function obtained from GeneCards.org

4.4.4.3. Gene set Enrichment Analysis

The differential expression analysis suggests cranial irradiation does not induce in large-fold expression changes consistently across all samples, and instead may lead to smaller-fold expression alterations in numerous genes within the same pathways. These changes would be too subtle for detection using differential expression analysis, and therefore gene set enrichment analysis (GSEA) was conducted.

The RNAseq counts were ranked by p-value and for overrepresentation using mouse hallmark gene sets. GSEA calculates an enrichment score to reflect the level of overexpression within a gene set. Briefly, a score is calculated by walking down the genes list and increase the running-sum statistic when a gene within the genes set is encountered and decreasing it when a gene is not within the gene set.

5 pathways were significantly enriched following CRT+PFB: interferon-alpha and -gamma response, epithelial-mesenchymal transition, and oestrogen response (early and late) (Figure 4.9). Interestingly in our model, both early and late oestrogen response pathways were downregulated 12 months post CRT+PFB.

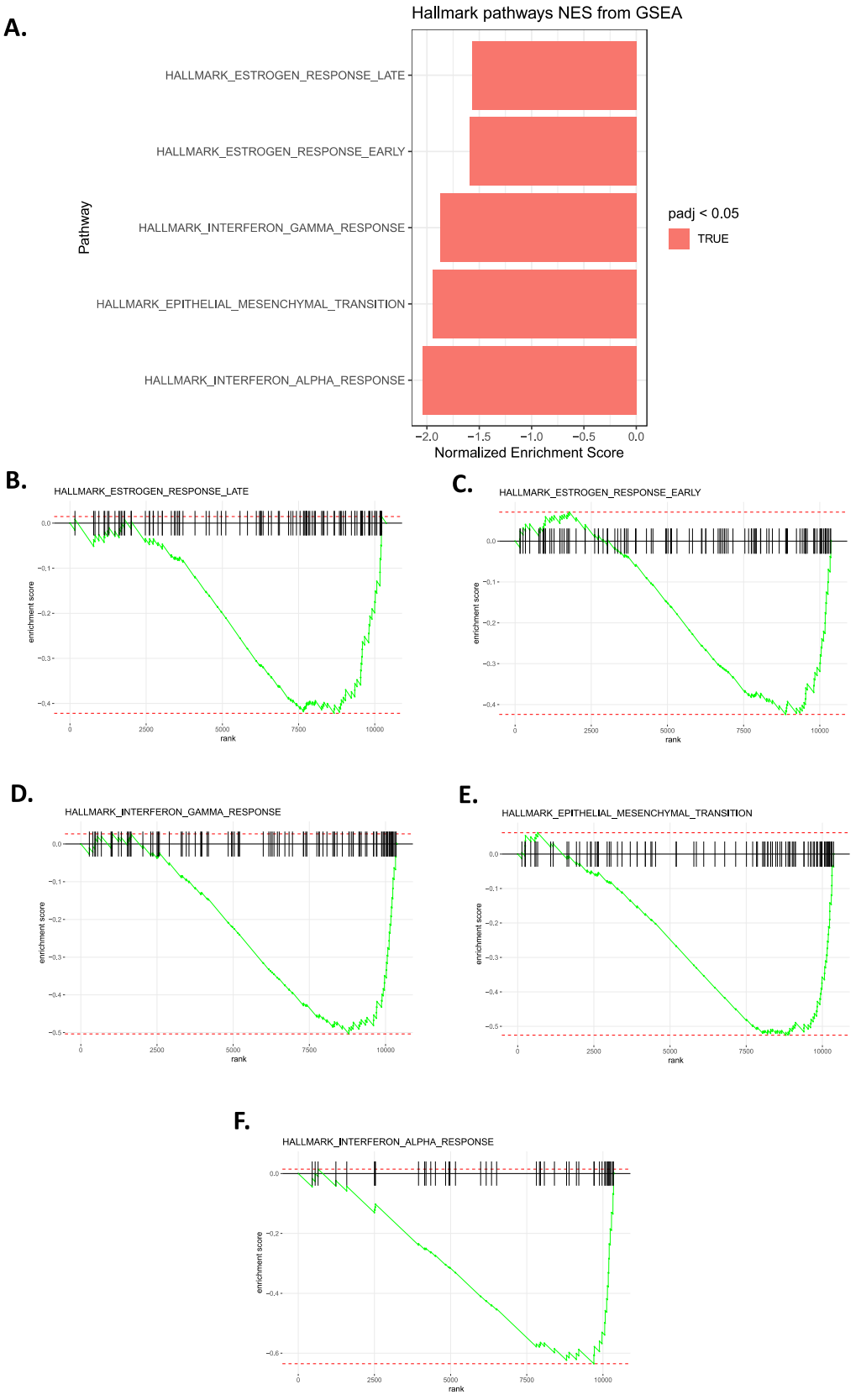

Figure 4.9. Hallmark pathways significantly downregulated following gene set enrichment analysis (GSEA). A) Pathways with a significant adjusted p-value following GSEA. All significant pathways (B-F) were downregulated following CRT+PFB (negative normalised enrichment score; NES)

4.4.5. Assessing premature ageing following CRT: the correlation between chronological age and epigenetic age

Assessment of genome-wide DNA methylation status in peripheral blood has previously been used to estimate epigenetic age acceleration (EAA) in childhood cancers survivors (CCS); survivors had a significantly higher EAA compared to matched controls. Increased EAA in CCS has also been associated with prior treatment of radiotherapy or alkylating chemotherapy, as well as the presence of poor health conditions. Therefore, estimation of EAA may be a useful biomarker to monitor premature ageing and late-effect development. To assess the effect of cranial radiation on epigenetic age, an epigenetic clock was utilised to predict the epigenetic vs chronological age of mice following CRT+PFB or sham-irradiation.

4.4.5.1. DNA quality control

Quantification of dsDNA was assessed using the Qubit dsDNA Broad Range (BR) Assay kit (details provided previously in chapter 2.9.2). Samples that met the minimum concentration and quantity requirements (50 ng/µL and 250 ng, respectively) were sent for array (raw data provided in appendix 4). Due to limited space on the array, some sham-irradiated samples were randomly excluded.

4.4.5.2. Assessment of premature ageing

DNA methylation was assessed on samples taken at age 5 months (~150 PNDs, from peripheral blood) and 13.1 months (~394 PNDs, from the cerebellum). At 5 months, there was no significant difference between the predicted epigenetic age following sham or CRT+PFB (mean age: 5.84 and 5.90 months, respectively; Figure 4.10). Interestingly, at 13.1 months, the mean epigenetic age was higher in the CRT+PFB group than in the sham group (mean age: 11.76 and 10.91 months, respectively; Figure 4.10 and Table 4.5), however this was not significant. At this later time point, the predicated epigenetic age exhibited a high level of variability in both treatment groups (sham: 2.48-22.61 [mean 10.91] months and CRT+PFB: 3.05-23.75 [mean 11.76] months; Table 4.5)

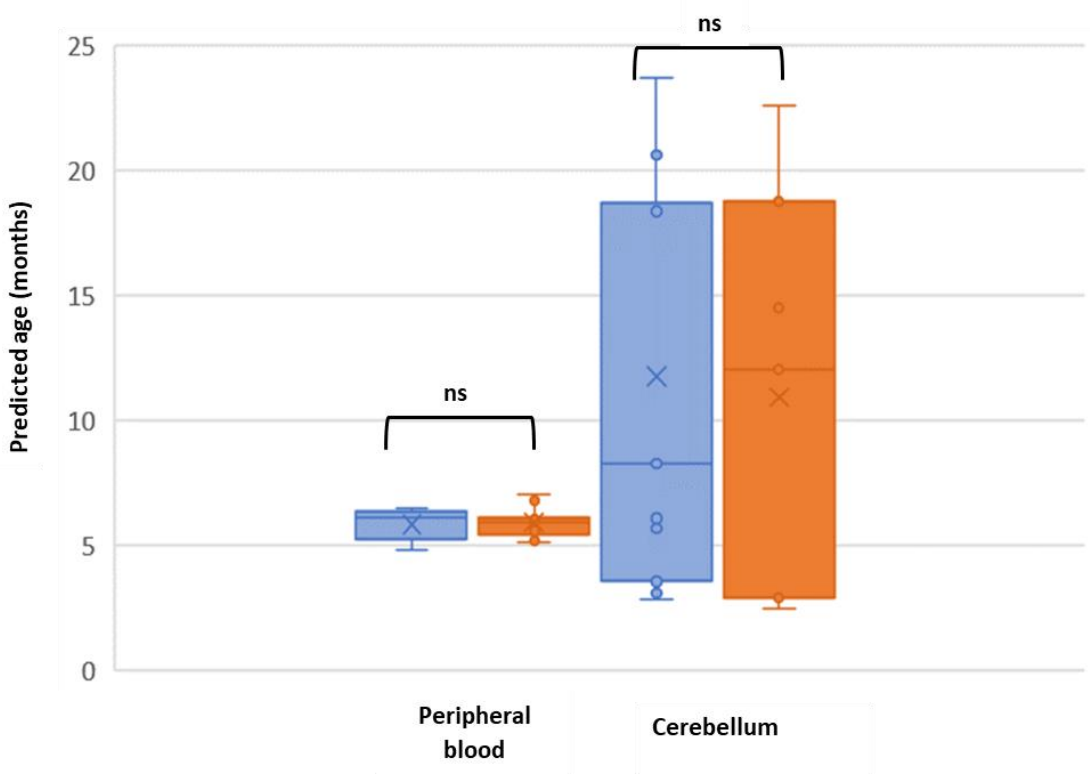

Figure 4.10. Predicted methylation age for DNA from peripheral blood (5 months; 150 PNDs) and cerebellum (13.1 months; 394 PNDs) following CRT+PFB (orange) and sham-irradiation (blue).

		DNA from peripheral blood		DNA from cerebellum	
Sample ID	Treatment group	Predicted age (months)	Difference from chronological age (months)	Predicted age (months)	Difference from chronological age (months)
1955m1	Sham	6.36	1.36	12.03	-1.10
1955m2	Sham	5.97	0.97	3.11	-10.02
1955m3	Sham	5.02	0.02		
1956m2	Sham	5.21	0.21	14.49	1.36
1956m3	Sham	6.31	1.31	22.61	9.48
1961m1	Sham	4.83	-0.17	2.87	-10.26
1961m2	Sham	6.27	1.27		
1961m3	Sham	6.12	1.12	18.78	5.65
1962m1	Sham	6.34	1.34		
1962m2	Sham	5.29	0.29	2.48	-10.65
1962m3	Sham	6.47	1.47		
Sham average		**5.84**	**0.84**	**10.91**	**-2.22**
1963m1	CRT+PFB	5.42	0.42	6.07	-7.06
1963m2	CRT+PFB	5.79	0.79	20.64	7.51
1963m3	CRT+PFB	6.8	1.8	8.28	-4.85
1964	CRT+PFB	5.58	0.58	23.75	10.62
2164	CRT+PFB	5.09	0.09	3.54	-9.59
1957m1	CRT+PFB	5.95	0.95	2.81	-10.32
1957m2	CRT+PFB	7.05	2.05	18.7	5.57
1957m3	CRT+PFB	6.01	1.01	5.68	-7.45
1958m1	CRT+PFB	5.17	0.17	18.48	5.35
1958m2	CRT+PFB	5.92	0.92	3.05	-10.08
1958m3	CRT+PFB	6.13	1.13	18.37	5.24
CRT+PFB average		**5.90**	**0.90**	**11.76**	**-1.37**

Table 4.5. Predicted epigenetic age from blood (taken at age 5 month, ~150 PNDs) and cerebellum tissue (harvested at 13.1 months, ~394 PNDs). Red text depicts a predicted age that is younger than the chronological age.

4.5. Discussion

4.5.1. The pro-inflammatory response 12 months post cranial irradiation

The receipt of radiation has been shown to increase pro-inflammatory protein expression, however overall, abundance was not consistently higher following CRT only and CRT+PFB compared to sham-irradiation. This suggests that inflammatory pathways may not still be increased one-year post-cranial irradiation, however, the assessment of more proteins is required to confirm this. Moravan *et al* identified proteins involved in neuroinflammation that were overexpressed up to one year following whole-head irradiation of adult mice (Moravan *et al.*, 2011). Moravan *et al* showed increased abundance of several inflammatory proteins was higher 6 months post-irradiation, with GFAP (a marker of activated astrocytes) abundant at 12 months. In our study, GFAP was also more abundant in the cerebellum following CRT only, compared to sham-irradiation. Astrocytes become activated in response to CNS insult, including stroke, tumours and neurodegenerative diseases. Astrocytes are involved in maintaining the blood-brain barrier, modulating synaptic transmission and following insult can induce neuroinflammation (Pekny and Nilsson, 2005). Interestingly, abundance of GFAP was significantly higher following CRT only in the cerebellum however not in the hippocampus, despite both regions receiving the same dose. This suggests that specific regions of the brain respond differently to radiation insult.

Investigation of pro-inflammatory proteins was limited due to the small sample size, and the late, single time point. In this study, the sample size for IHC was small (n=3 per treatment group and brain region) and therefore may not have been statistically powered to detect altered expression. IHC should therefore be repeated on the remaining samples from our *in vivo* model. However, as shown in the previous chapter, significant deficits in physical functioning and neurocognition developed much earlier, and therefore it is likely that most of the inflammatory signalling occurs early and was not present 12 months post irradiation.

4.5.2. Differential expression between CRT+PFB and sham-irradiation

Several DEGs are involved in expected key functions such as immune response *(Wfdc2, Ifi27l2a). Ifi27l2a* is involved in the regulation of microglia and neuroinflammation and has also been linked to premature ageing following stroke (Kim *et al.*, 2023). Surprisingly, in our model, these genes were significantly downregulated 12 months after CRT+PFB. Conversely, *Folr1* has a role in folate transport, with a known role in maintaining brain function and

reducing inflammation. A reduction in folate has been linked to cognitive impairment and neurodegeneration. Following pathway analysis, there were 2 common pathways shared between the DEGs: mineral absorption (*Steap1* and *Slc39a4*) and cell adhesion molecules (*Cldn2* and *Cdh3*). A decrease in mineral absorbance has been linked to increased risk of mild cognitive impairment as well as the development of Alzheimer's (Cherbuin *et al.*, 2014). *Slc39a4* expresses a zinc transporter (ZIP4) and is thought to play an essential role within the neuronal synapses (De Benedictis *et al.*, 2021). Whilst there is limited evidence on the exact role of ZIP4, the reduction on ZIP4 expression following CRT+PFB may play a role in reduced neurocognitive function (Takeda *et al.*, 2010). However, pathway analysis was only conducted on the 15 DEGs and may not provide a full illustration of all altered pathways.

Following gene set enrichment analysis, 5 pathways were significantly enriched following CRT+PFB: interferon-alpha and -gamma response, epithelial-mesenchymal transition, and oestrogen response (early and late). Interferon-alpha and –gamma response have been linked to neuroinflammation following radiation and brain injury, however surprisingly, these pathways were downregulated (negative enrichment score; NES) compared to sham-irradiation, 1 year post-irradiation, in this study. Epithelial-mesenchymal transition (EMT) plays an important role in development, wound healing and fibrosis (Lamouille;Xu and Derynck, 2014). Radiation has been shown to induce EMT through TGF-β signalling (Jung *et al.*, 2007; Liu *et al.*, 2014), though EMT is regulated by a variety of pathways including TGF-β, tyrosine kinase, WNT and SMO signalling, as well as inflammation and hypoxia (Lamouille;Xu and Derynck, 2014). However, surprisingly EMT was downregulated in the CRT+PFB group. Oestrogen signalling regulates a wide range of physiological functions, including reproduction, bone density, brain function, cholesterol mobilization, and control of inflammation (Liang and Shang, 2013). Oestrogen exhibits neuroprotective effects through reducing inflammation and oxidative stress, and increasing growth factor expression, and promoting cell survival, together resulting in modulation of learning, memory, and behaviour (Wallace *et al.*, 2006; Mitra *et al.*, 2023). Interestingly in our model, both early and late oestrogen response pathways were downregulated 12 months post CRT+PFB. Although the specific time oestrogen signalling is downregulated post-irradiation was not determined in our model, as shown in the previous chapter, mice exhibited impaired memory function following CRT, suggesting that reduced oestrogen signalling may have played a role in the

development of the neurocognitive deficits. Previous studies have suggested replacing reduced oestrogen can improve memory (Luine and Frankfurt, 2013).

However, RNAseq was conducted on tissue harvested at the end of the study (approximately a year after irradiation) and therefore is limited to only describing transcriptional response occurring during this late timeframe. As shown in the previous chapter, significant late-effects were already present at this timepoint, and therefore to fully elucidate the biological mechanisms that underpin late-effect onset, RNAseq at earlier timepoints should be conducted.

4.5.3. Using predicted epigenetic age as a biomarker for premature ageing

Alterations in DNA methylation signatures are a hallmark of ageing, and have been associated with premature ageing and the development of poor health conditions (Mozhui and Pandey, 2017; Field *et al.*, 2018; Kling;Wenger and Carén, 2020; Salameh;Bejaoui and El Hajj, 2020). The assessment of epigenetic age using DNA harvested from peripheral blood enables the assessment of distant radiotherapeutic effects on biological premature ageing. In a previous study by Qin *et al*, genome-wide DNA methylation assessment of collected from peripheral blood predicted childhood cancer survivors to have a higher epigenetic age than matched controls (Qin *et al.*, 2021).

In both the CRT+PFB and sham groups, the predicted age was close to the chronological age (a difference of 0.9 and 0.84 months, respectively). However, DNA from peripheral blood was only assessed at one time point (5 months old) and for a more complete picture on the utility as a future biomarker, predicted epigenetic age should also be considered at later time points. Interestingly, the predicted epigenetic age from DNA harvested from the cerebellum (at approximately 13 months old) was older in the CRT+PFB group, though this was not significant. There was large variance in the predicted epigenetic age from the cerebellum for both treatment groups (sham: 2.48-22.61 [mean 10.91] months and CRT+PFB: 3.05-23.75 [mean 11.76] months; Table 4.5). Zhou *et al* reported tissue-specific methylation signatures, which may account for the difference in variance between peripheral blood and cerebellum. The epigenetic clock used to predict age is based on the profiling of 26 tissue and cell types (including foetal brain, frontal lobe brain and hind brain) and therefore should provide a comprehensive epigenetic age prediction for most tissues (Zhou *et al.*, 2022). However, as the brain has higher levels of DNA methylation than most of tissues (Ehrlich *et al.*, 1982), and

therefore an epigenetic clock developed with numerous tissue types may not be the most suitable.

4.6. Chapter summary

This chapter aimed to further understand the late molecular alterations following cranial irradiation.

Through the IHC staining of pro-inflammatory proteins, an increased abundance of the astrocyte marker, GFAP, was observed within the cerebellum following CRT and surprisingly this was present within the hippocampus, despite receiving the same radiation dose. This suggests that in our model and at the timepoint assessed, response to cranial irradiation may be region specific, and further investigation is required to understand the differential response between regions of the brain.

Through the sequencing of the transcriptome following CRT, cranial irradiation was shown to not induce high expression fold changes in a uniform manner, instead, cranial irradiation induced low fold expression changes to multiple genes and that may alter overall pathway response. Pathways such as mineral absorption, cell adhesion, oestrogen response, and interferon alpha and gamma response were downregulated one year after CRT and therefore may be associated with the development of late effect such as frailty, reduced neurocognition, and impaired physical functioning.

Patterns of DNA methylation can provide an estimation into the biological epigenetic age and have potential as biomarkers of overall health. Epigenetic age was compared in both a systemic and tissue-specific context following *in vivo* MB-equivalent cranial irradiation. The epigenetic clock used could closely predict age from peripheral blood, however, was less accurate when using brain tissue. In our model there was no significant difference in the epigenetic age estimated from peripheral blood, however this may have been limited by the relatively early timepoint. The use of peripheral blood for estimation of epigenetic age provides a potential useful measure for the longitudinal assessment of premature ageing.

Chapter 5. Development of an *in vitro* model to assess response to radiotherapeutic insult

5.1. Introduction

Childhood MB survivors typically receive cranial-radiotherapy during treatment, which often results in late-effects as a result of damage caused to the healthy tissue. Radiation-induced brain injury ranges from acute injury (examples include oedema, headaches, drowsiness) to late injury such as cognitive impairment resulting from abnormal vasculature, demyelination and white matter necrosis (Greene-Schloesser *et al.*, 2012). Both direct and indirect damage occurs through the induction of DNA damage (Baskar *et al.*, 2014), which induces oxidative stress and an inflammatory response that can persist for many months, causing potentially irreversible damage to the healthy tissue within the brain (Zhao;Diz and Robbins, 2007; Moravan *et al.*, 2011; Greene-Schloesser *et al.*, 2012; Lumniczky;Szatmári and Sáfrány, 2017).

The exact mechanisms underpinning late-effect onset are unclear. Chronic inflammation, oxidative stress, impaired neurogenesis, cellular senescence and the senescence-associated secretory phenotype (SASP) have been indicated to play a role in cranial radiotherapy-induced late-effects (Turnquist;Harris and Harris, 2020b). Radiation-induced neuronal damage, and activated microglia/astrocytes release numerous pro-inflammatory cytokines (examples include TNF-α, IL-1β and IL-6), chemokines (such as CCL3/macrophage inhibitory factor 1) and reactive oxygen species, which further activate immune cells within the brain, resulting in chronic neuroinflammation (Streit;Mrak and Griffin, 2004; Lumniczky;Szatmári and Sáfrány, 2017).

Radiation-induced DNA damage and oxidative stress can induce cellular senescence, whereby cells are in a persistent state of cell cycle arrest (Wang;Kohli and Demaria, 2020). Senescent cells secrete a wide variety of signalling factors (examples include interleukins, chemokines and growth factors), proteases and ECM components, together referred to as the senescence-associated secretory phenotype (SASP) (Coppé *et al.*, 2010). Release of SASP modifies the microenvironment and can lead to activation of nearby immune cells (Coppé *et al.*, 2010; Wang;Kohli and Demaria, 2020). However, these pathways are complex and the exact mechanisms underpinning the development of late-effects remain elusive.

The biological mechanisms underpinning late-effect onset are currently unknown, as characterisation of the molecular response to cranial-irradiation insult is lacking. By understanding the exact mechanisms of late-effect development, target molecules can be identified for the development of future pharmacological interventions. In addition to

identification of targets, characterisation of the mechanistic response provides a baseline for the appraisal of novel interventions strategies to ameliorate late-effects.

5.2. Aims

The aim of this chapter is to develop an *in vitro* model to enable assessment of the molecular insult response to MB-equivalent radiotherapy. The development of a novel assay for the characterisation of the biological response to radiation will provide a useful tool for the identification of pharmacological targets and provide a baseline for the appraisal of novel interventions strategies to ameliorate late-effects.

1) Development of an *in vitro* model that recapitulate MB-equivalent radiotherapy dose.

2) Development of a novel assay using the Luminex system to characterise the biological response to radiation exposure.

5.3. Methods

5.3.1. Irradiation and sample collection

To understand the response to radiotherapeutic-insult within the brain, the aim was to develop novel assay using the Luminex system to characterise the biological response to radiation exposure, at a MB-equivalent radiation dose. Human iPSCs (AD2 WT1) were maintained as previously described in Chapter 2.12.1.2. Unfortunately, these cells did not survive irradiation, and it was decided assay development would take place using a cell line that could withstand irradiation, to facilitate future use in more biologically relevant cell lines.

To develop a novel assay to characterise the response to MB-equivalent radiotherapeutic-insult, an *in vitro* model was developed using a fast-growing human cell line (MRC-5; human foetal lung fibroblasts). MRC-5 cells were maintained as previously discussed in chapter 2.12. Cells were exposed to a single dose of 36 Gy (detailed methodology is provided in chapter 2.12.4). At 1-, 4-, 24- and 48-hours post-irradiation, 2 ml of media was collected, centrifuged at 300 x *g* for 10 minutes at 4°C to remove any cell debris, then frozen at -80°C in 200 µL aliquots. Total cell count was estimated as previously discussed in chapter 2.12.2. An overview of the irradiation and sample collection timeline is shown in Figure 5.1.

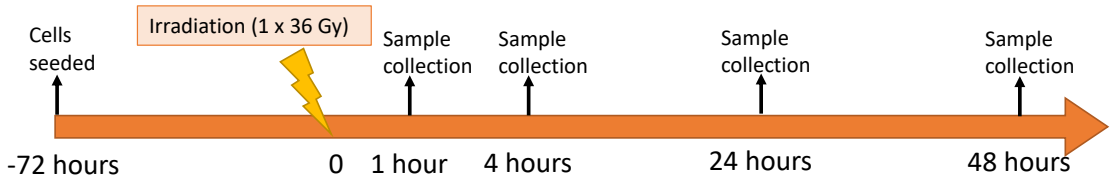

Figure 5.1 Timeline of irradiation and sample collection. Samples were seeded approximately 72 hours prior to irradiation. At 1-, 4-, 24- and 48-hours post-irradiation, 2 ml of media was collected, and the total number of cells counted.

5.3.2. Luminex assay

To assess the molecular response to radiotherapeutic insult, a custom panel immunoassay was developed using the Luminex® Discovery Assay (R&D systems). The Luminex assay utilises a magnetic-microparticle and antibody-based capture method to measure the abundance of multiple analytes at a time. A custom panel of four Human Pre-mixed multi-analyte kits was utilised to assess abundance of 57 analytes of interest in response to radiotherapeutic insult. A detailed methodology is provided in chapter 2.13.

5.4. Results

5.4.1. Development of assay to detect radiotherapeutic insult

To assess the molecular response to radiotherapeutic insult, a custom panel immunoassay was developed using the Luminex Discovery Assay (R&D systems). Analyte selection was based on the criteria summarised in Figure 5.2. From the 148 analytes available within the Human Luminex Discovery Assay, the first criterion for selection included a literature search to identify proteins with a role in the inflammatory response to radiotherapeutic insult (n=47). Additionally, any proteins known to be involved in the senescence associated secretory phenotype (SASP) were also included (n=37). The first criterion selected 68 proteins for further appraisal (17 proteins had both a known role in inflammatory response within the literature and were associated with the SASP). These proteins of interest were then further filtered for tissue-specific expression (n=67 selected), and exclusion of any proteins only expressed by T-cells, as these would not be detected within this assay (n=66 selected).

Due to technical limitations of the panel, some analytes could not be multiplexed together; to retain the greatest number of analytes, proteins enabling the widest coverage were selected. A total of 57 analytes were selected for inclusion in this custom panel, using four Human pre-mixed multi-analyte kits: LXSAHM-25, LXSAHM-14, LXSAHM-12 and LXSAHM-06 (details are provided in Table 5.1).

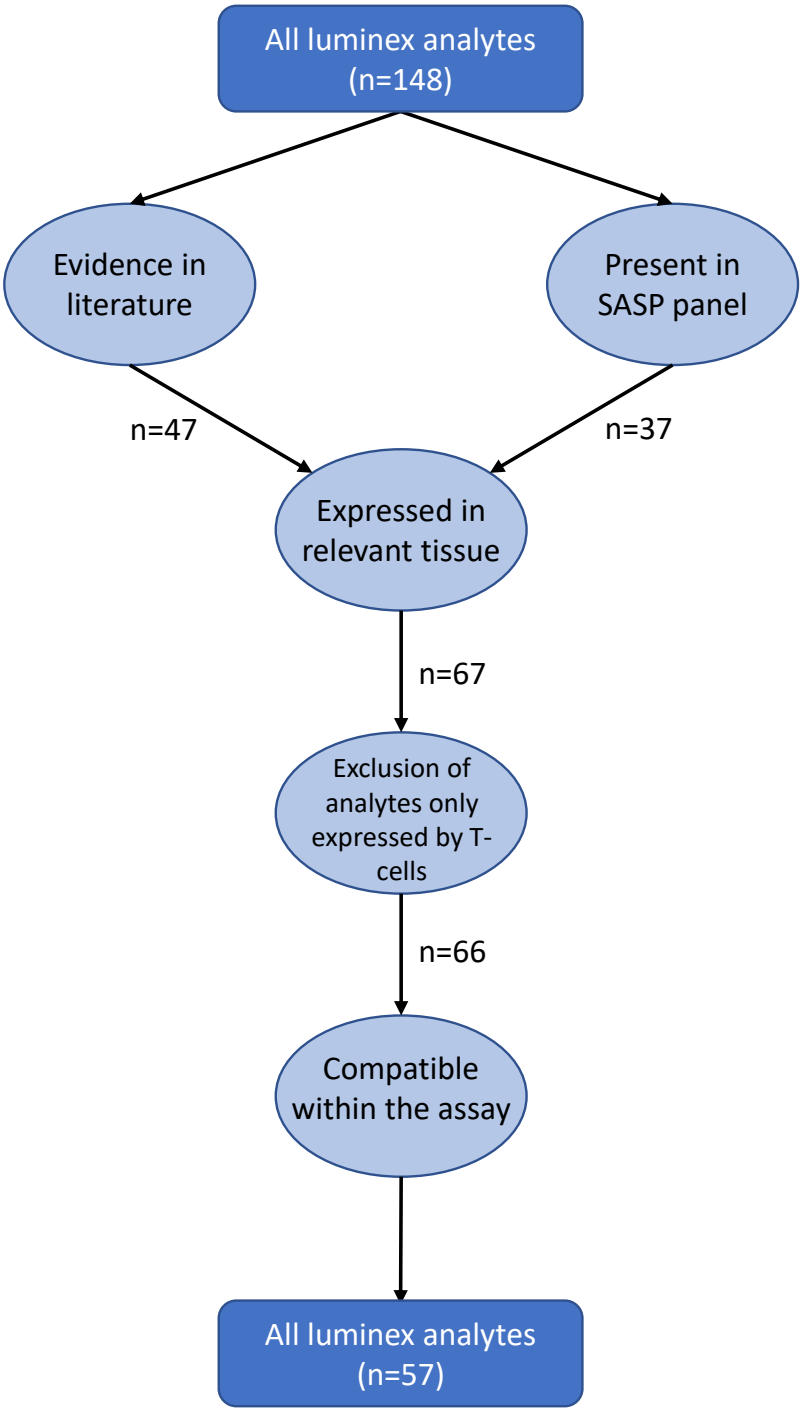

Figure 5.2. Analyte selection process for inclusion in the custom Luminex assay panel.

LXSAHM-25	LXSAHM-14	LXSAHM-12	LXSAHM-06
CXCL2/GRO beta/MIP-2/CINC-3	CCL2/JE/MCP-1	CCL7/MCP-3/MARC	NCAM-1/CD56
CD14	CCL4/MIP-1 beta	CD31/PECAM-1	BDNF
CCL22/MDC	IL-6	IFN-gamma	IL-7
IL-1 alpha/IL1F1	IL-10	IL-3	Osteopontin/OPN
Fas ligand/TNFSF6	MMP-2	MMP-8	IL-15
IL-17/IL-7A	MMP-7	SOST/Sclerostin	HGF
IL-2	TNF-alpha	CCL8/MCP-2	
RAGE/AGER	CCL3/MIP-1 alpha	GDNF	
GM-CSF	IL-1 beta/IL-1F2	IL-1 RI	
CD25/IL-2R alpha	IL-8/CXCL8	Lymphotoxin-alpha/TNF-beta	
M-CSF	MMP-1	S100B	
ADAMTS13	MMP-3	Tie-2	
IL-5	MMP-12		
G-CFS	VEGF		
Follistatin-like/FSTL1			
CXCL4/PF4			
VCAM-1/CD106			
ICAM-1/CD54			
CCL17/TARC			
GDF-15			
TNF RI/TNFRSF1A			
FAS/TNFRSF6/CD95			
IL-4			
CXCL1/GRO alpha/KC/CINC1			
IL-18/IL1F4			

Table 5.1. Analytes assessed using the Luminex Discovery Assay. A custom panel of 57 analytes was developed, using 4 Human premixed multi-analyte kits (LXSAHM-25, -14, -12, -06)

5.4.2. Cell survival post-irradiation

5.4.2.1. Irradiation of a biological-relevant cell line

To replicate the high dose of radiation received by medulloblastoma patients, a biological relevant cell line AD2 WT1 (human induced pluripotent stem cells; iPSCs) received a single dose of 36 Gy x-ray irradiation. Unfortunately, this dose was lethal, and resulted in total cell death. To facilitate the development of the Luminex assay, an easy-to-grow cell-line (MRC-5) that could withstand irradiation was utilised in parallel. Following optimisation, the objective was to then assess the response to radiotherapeutic injury in the more biologically relevant cell line. However, due to time constraints, this was not possible in the duration of this project.

5.4.2.2. Utilising a rapidly growing cell line for assay development

MRC-5 cells were seeded approximately 72 hours prior to receipt of a single radiation dose of 36 Gy and compared to controls that received 0 Gy. Cells were counted at 1-, 4-, 24- and 48-hours post irradiation, and normalised to the cell count 1-hour post-irradiation for each replicate to account for any variability within cell seeding.

As expected, the number of cells decreased across all timepoints following a high dose of radiation ($r= -0.38$, Figure 5.3), however this decrease was not significant ($p=0.23$), likely due to the variability between replicates. At 48 hours, the normalised cell count of irradiated cells was less than half that of non-irradiated controls (0.64 vs 1.38, respectively).

Non-irradiated cells continued to grow as expected ($r=0.46$), however, at 48 hours the cell count by was slightly lower than expected. MRC-5 cells have a doubling time of approximately 36 hours. Non-irradiated controls experienced the same conditions as irradiated cells, aside from exposure to radiation. Growth rate may have been disrupted due to practical limitations including time outside of the incubator and transport to the irradiator.

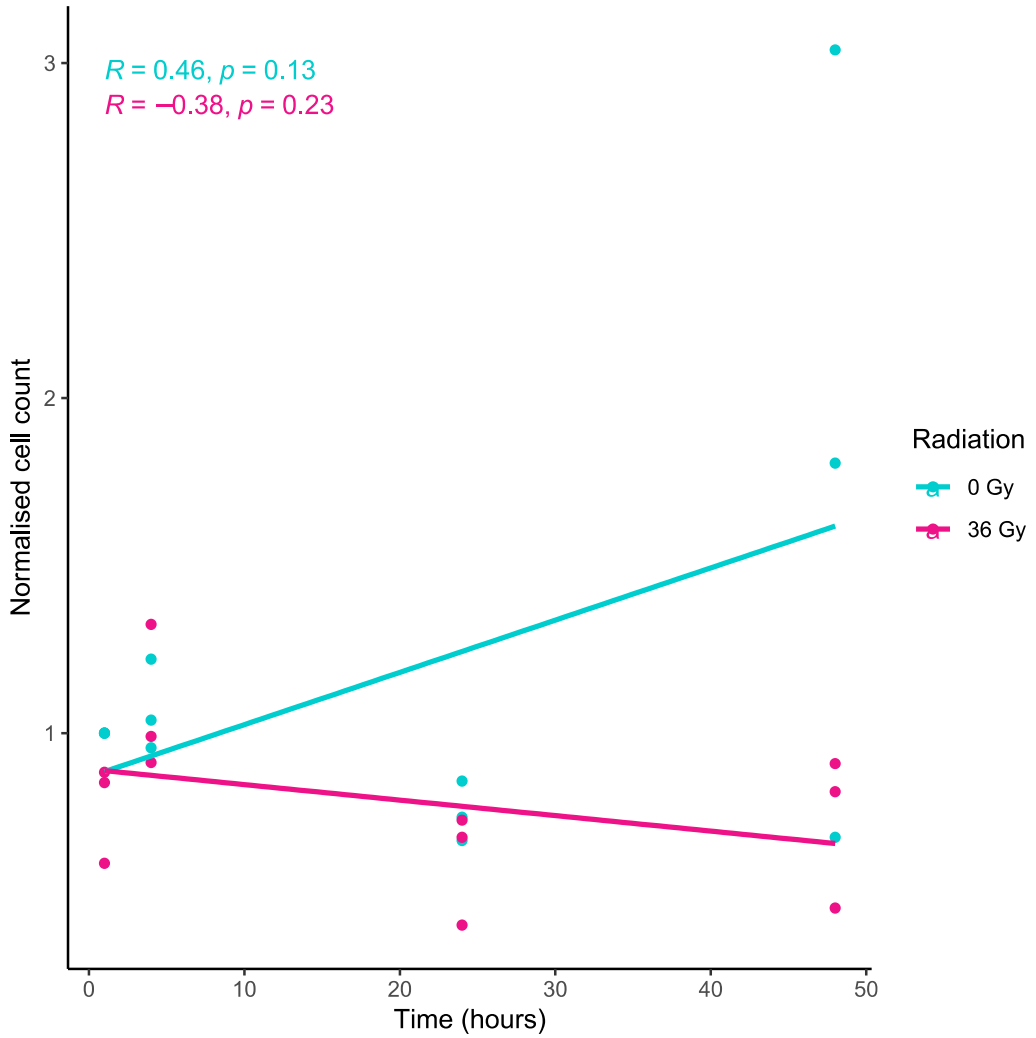

Figure 5.3. Normalised cell counts. Normalised cell counts (fold change) at 1-, 4-, 24-, and 48- hours following either a single dose of 36 Gy or 0 Gy irradiation. Cell counts were normalised to the estimated number of cells present 1 hour post 0 Gy, for each replicate (n=3).

5.4.3. High-dose radiation drives increased levels of pro-inflammatory markers

To assess the acute and late molecular response to radiotherapeutic insult *in vitro,* media was sampled 1- and 48-hours following either 36 Gy or 0 Gy radiation. The secretion of pro-inflammatory proteins from MRC-5 cells was assessed using a custom Luminex Discovery panel. Proteins were grouped into 6 groups to illustrate biological relevance: cytokines (n=23), inflammation markers (n=7), chemokines (n=10), cytokine receptors (n=5), matrix metalloproteinase (MMPs; n=6) and SASP marker (n=6). Categories provide a general overview at the level of the biological process, however there is duplication between groups, in particular with markers of inflammation and SASP.

The concentrations for 21/57 (36.8%; Table 5.2) analytes were outside the limit for quantification for all samples (both irradiated and control samples and at both time points) and therefore were excluded from subsequent analysis. The majority of excluded analytes (n=20/21, 95.2%) were below the limit of detection, and 1 analyte (4.8%; MMP-1) was above the limit of detection. Resulting analyte concentrations were normalised to the cell count, and the fold change between irradiated and non-irradiated cells, at their respective timepoints, was calculated.

Overall, the concentration of pro-inflammatory proteins increased following radiation (fold change greater than 1), which typically increased further 48 hours post-irradiation. They will be considered by biological process over the following sections.

Analyte	Biological process group	Reason for exclusion
G-CSF	Cytokines	Concentration below the lower limit
GM-CSF	Cytokines	Concentration below the lower limit
IFN-gamma	Cytokines	Concentration below the lower limit
IL1 alpha/IL1F1	Cytokines	Concentration below the lower limit
IL17/IL17A	Cytokines	Concentration below the lower limit
IL2	Cytokines	Concentration below the lower limit
IL4	Cytokines	Concentration below the lower limit
IL5	Cytokines	Concentration below the lower limit
CD14	Inflammation	Concentration below the lower limit
CD31/PCAM-1	Inflammation	Concentration below the lower limit
CCL7/MCP-3/MARC	Chemokines	Concentration below the lower limit
CCL17/TARC	Chemokines	Concentration below the lower limit
CCL8/MCP2	Chemokines	Concentration below the lower limit
CXCL4/PF4	Chemokines	Concentration below the lower limit
CD25/IL-2R alpha	Cytokine receptors	Concentration below the lower limit
RAGE/AGER	Cytokine receptors	Concentration below the lower limit
MMP-1	MMPs	Concentration above the lower limit
MMP-8	MMPs	Concentration below the lower limit
ADAMTS13	SASP	Concentration below the lower limit
Fas ligand/TNFSF6	SASP	Concentration below the lower limit
SOST/SCLEROSTIN	SASP	Concentration below the lower limit

Table 5.2. Analytes excluded from subsequent analysis. List of analytes that were outside the threshold of quantification (concentrations were above or below the concentrations of the standards).

5.4.3.1. Cytokine response

The concentration of 15 cytokines was assessed 1- and 48-hours post-irradiation, and a fold change in comparison to non-irradiated cells was calculated. An overview of the function of these cytokines is shown in Table 5.3. Cytokine concentration was increased 1-hour post-irradiation; 73.3% (n=11/15) of analytes had a fold change of greater than 1 in samples taken 1-hour post-irradiation (Figure 5.4). Increased cytokine protein expression was consistently higher than non-irradiated controls; at 48 hours 76.9% (n=10/13) of cytokines assessed had a fold change greater than 1. At the 48-hour timepoint, 2 analytes were excluded due concentrations outside the quantitative limit: HGF (the concentration was higher than the upper limit) and TNF-β (the concentration was below the lower limit). Increased cytokine expression typically leads to increased inflammatory signalling, this data suggests that a higher level of inflammation is still present 48 hours after cells are exposed to irradiation.

For the majority of cytokines, the level of protein increased over time; 69.2% (n=9/13) had a higher concentration 48-hours post-irradiation than at 1-hour post-irradiation, though this was only significant for FSTL1 ($p=0.023$). Whilst not significant, abundance of GDF-15, IL-6 and VEGF were visually increased at 48 hours post-irradiation (2.89, 3.51 and 3.04 fold increase, respectively.

Conversely, 28.6% (n=4/14; IL-1β, IL-3, IL-10 and TNF-α) analytes had a reduced expression at 48-hours, despite an initial increase in expression at 1-hour post-irradiation, though this decrease was only significant for IL-10 ($p=0.047$).

Analyte	Name	Function
FSTL1	Follistatin-like 1	Immune regulation
GDF-15	Growth differentiation factor 15	Macrophage inhibition
HGF	Hepatocyte growth factor	Regulates cell growth/motility
IL-1β/IL-1F2	Interleukin 1 beta	Pro-inflammatory signalling
IL-3	Interleukin 3	Pro-inflammatory signalling
IL-6	Interleukin 6	Pro-inflammatory signalling
IL-7	Interleukin 7	Pro-inflammatory signalling
IL-8/CXCL8	Interleukin 8	Pro-inflammatory signalling
IL-10	Interleukin 10	Anti-inflammatory
IL-15	Interleukin 15	Pro-inflammatory signalling
IL18/IL1F4	Interleukin 18	Pro-inflammatory signalling
M-CSF	Macrophage colony-stimulating factor	Macrophage stimulation
TNF-α	Tumour necrosis factor alpha	Pro-inflammatory signalling
TNF-β	Tumour necrosis factor-beta/ lymphotoxin-alpha	Proliferation and pro-inflammatory signalling
VEGF	Vascular endothelial growth factor	Vascular permeability/angiogenesis

Table 5.3. Overview of cytokine function

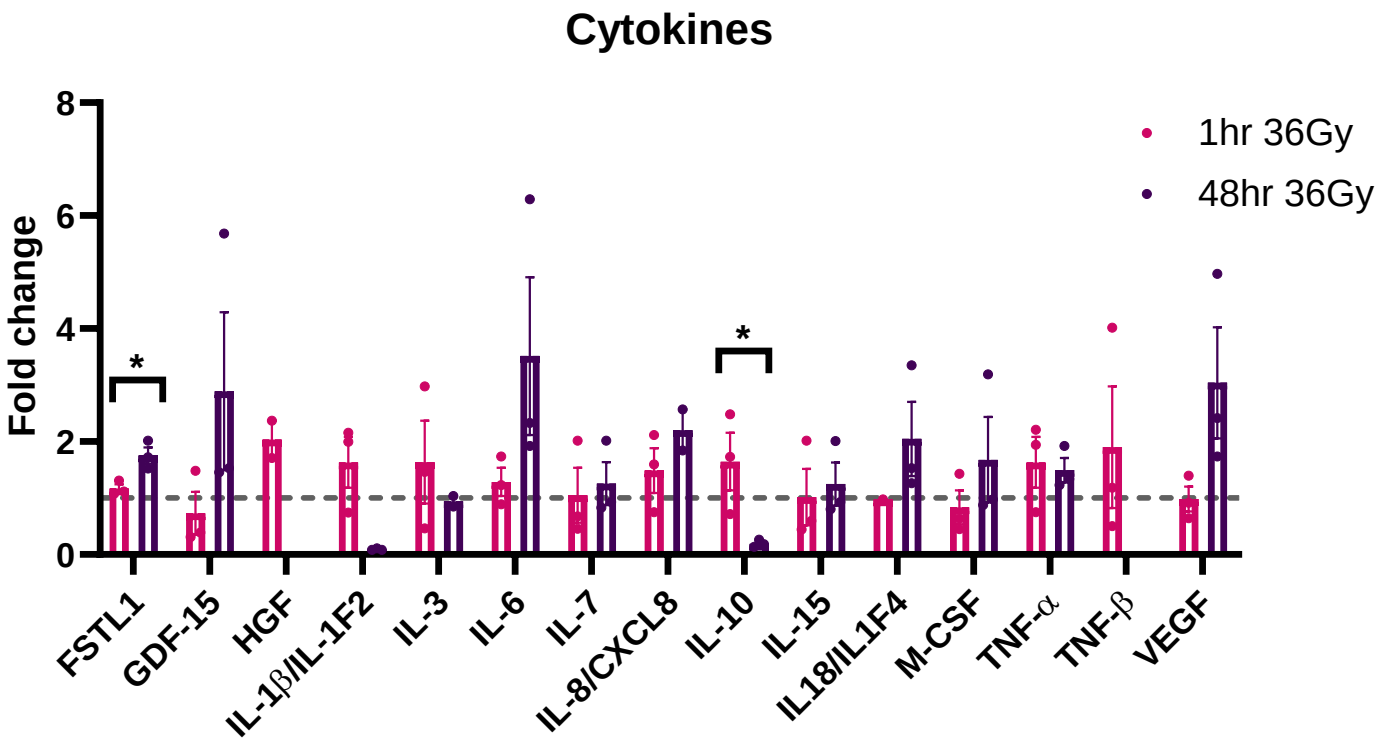

Analyte	Mean fold change	
FSTL1	1.17	1.75
GDF-15	0.73	2.89
HGF	2.04	
IL-1β/IL-1F2	1.63	0.09
IL-3	1.64	0.94
IL-6	1.29	3.51
IL-7	1.05	1.26
IL-8/CXCL8	1.49	2.21
IL-10	1.64	0.19
IL-15	1.02	1.25
IL18/IL1F4	0.98	2.05
M-CSF	0.84	1.68
TNF-α	1.63	1.50
TNF-β	1.90	
VEGF	0.98	3.04

Figure 5.4. Cytokine response following 36 Gy irradiation. Fold change concentration (relative to 0 Gy) at 1 hour and 48 hours post-irradiation, normalised to cell count. Points show individual replicates, error bars depict SEM and grey line depicts a fold change of 1. Significance between 1 hour and 48 hour time points was assessed via 2-sided independent t-test, p-values are shown when $p<0.05$ (denoted by *).

5.4.3.2. Inflammation markers

Several markers of inflammation (BDNF, S100B, NCAM-1/CD56, and TIE-2) were quantified 1- and 48-hours post-irradiation. An overview of the inflammatory proteins assessed is shown in Table 5.4. Increased inflammation was present following radiation; all markers of inflammation had a fold change greater than 1 at both 1 and 48 hours following 36 Gy of radiation Figure 5.5). Following the initial increase in protein concentration 1 hour after radiation, this response was sustained and concentrations further increased for all 4 proteins at the 48 hour sample time, though this was only significant for BDNF (brain-derived neurotropic factor; p=0.021).

Analyte	Name	Function
BDNF	Brain-derived neurotrophic factor	Neuronal survival/growth
NCAM-1/CD56	Neural cell adhesion molecule 1	Neural cell adhesion
S100B	S100 calcium-binding protein B	Astrocyte/microglia activation
TIE-2	Angiopoietin-1 receptor	Vascular stability

Table 5.4. Overview of the inflammation markers.

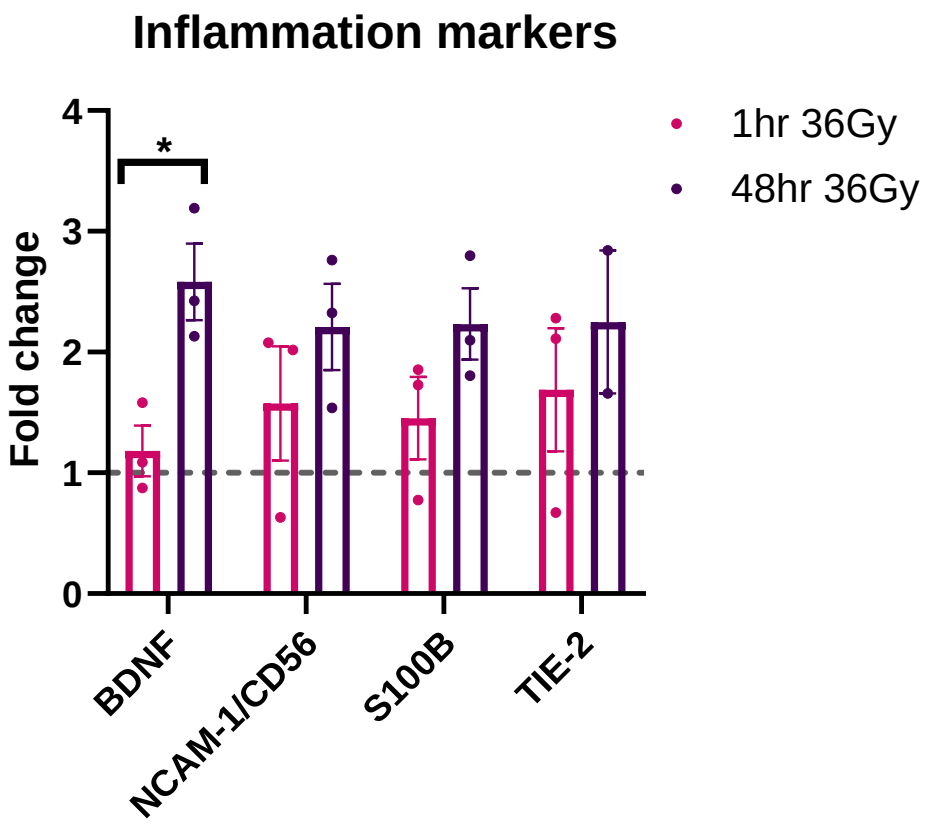

Analyte	Mean fold change	
BDNF	1.18	2.58
NCAM-1/CD56	1.58	2.21
S100B	1.45	2.23
TIE-2	1.69	2.25

Figure 5.5. Inflammation marker response following 36 Gy irradiation. Fold change concentration (relative to 0 Gy) at 1 hour and 48 hours post-irradiation, normalised to cell count. Points show individual replicates, error bars depict SEM and grey line depicts a fold change of 1. Significance between 1 hour and 48 hour time points was assessed via 2-sided independent t-test, p-values are shown when $p<0.05$ (denoted by *)

5.4.3.3. Chemokines

Chemokines play an important role in inflammation, through their role in stimulating the migration of leukocytes (Hughes and Nibbs, 2018). Concentration of 6 chemokine proteins (CCL2, CCL3, CCL4, CCL22, CXCL1, and CXCL2) was quantified 1- and 48-hours post-irradiation. An overview of chemokines assessed is shown in Table 5.5). Concentration for most chemokines was higher 1-hour post-irradiation compared to the non-irradiated controls; fold change was greater than 1 for 83.3% (n=5/6) of chemokine protein assessed (Figure 5.6). Typically, chemokine protein concentration increased further at 48 hours post-irradiation (n=4/6, 66.7%), a significant increase was seen for CXCL2 ($p=0.012$).

Conversely, CCL3 and CCL4 (macrophage inflammatory protein 1α and β, respectively) were initially increased; 1 hour-post irradiation protein concentration was 1.65 and 1.68 times higher, respectively, than non-irradiated controls. However, at 48-hours post-irradiation, protein concentration was lower than both the 1 hour irradiated cells, and approximately half that of 48 hour non-irradiated cells (fold change = 0.59 and 0.45 for CCL3 and CCL4, respectively). This suggests CCL3 and CCL4 play an early role in modulating immune response.

Analyte	Name	Function
CCL2/JE/MCP-1	Monocyte chemoattractant protein 1	Macrophage/monocyte recruitment
CCL3/MIP-1α	Macrophage inflammatory protein 1 alpha	Pro-inflammatory signalling
CCL4/MIP-1β	Macrophage inflammatory protein 1 beta	Pro-inflammatory signalling
CCL22/MDC	Macrophage-derived chemokine	Pro-inflammatory signalling
CXCL1/GROα	CXC motif chemokine ligand 1	Pro-inflammatory signalling
CXCL2/GROβ	CXC motif chemokine ligand 1	Pro-inflammatory signalling

Table 5.5. Overview of the chemokines.

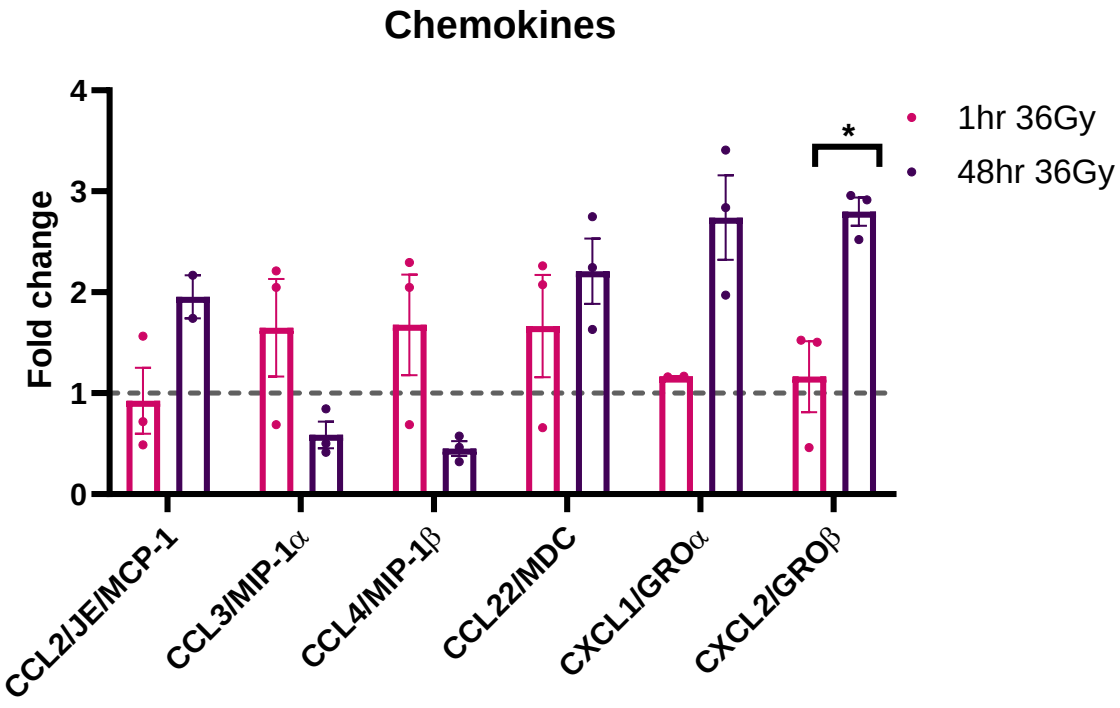

Analyte	Mean fold change	
CCL2/JE/MCP-1	0.92	1.96
CCL3/MIP-1α	1.65	0.59
CCL4/MIP-1β	1.68	0.45
CCL22/MDC	1.67	2.21
CXCL1/GROα	1.17	2.74
CXCL2/GROβ	1.16	2. 8

Figure 5.6 Chemokine response following 36 Gy irradiation. Fold change concentration (relative to 0 Gy) at 1 hour and 48 hours post-irradiation, normalised to cell count. Points show individual replicates, error bars depict SEM and grey line depicts a fold change of 1. Significance between 1 hour and 48 hour time points was assessed via 2-sided independent t-test, p-values are shown when $p<0.05$ (denoted by *).

5.4.3.4. Cytokine receptors

To further determine the level of inflammation occurring post-irradiation, concentrations of 3 cytokine receptors (Fas, IL-1 R1 and TNF R1; Table 5.6) were assessed. Expression of the cytokine receptors assessed typically occurred later; at 1-hour post-irradiation 66.7% (n=2/3; Fas and TNF R1) proteins had a fold change less than 1 (0.86 and 0.91, respectively; Figure 5.7). Yet after 48-hours, concentrations for all proteins were around 2-fold higher than non-irradiated controls (Fas: 2.10, IL-1 R1: 1.57 and TNF R1: 1.72).

Analyte	Name	Function
Fas/TNFRSF6/CD95	Tumour necrosis factor receptor superfamily member 6	Apoptosis/immune regulation
IL-1 R1	Interleukin 1 receptor type 1	Pro-inflammatory signalling
TNF R1/ TNFSFR1A	TNF receptor superfamily member 1A	Pro-inflammatory signalling

Table 5.6 Overview of the cytokine receptors.

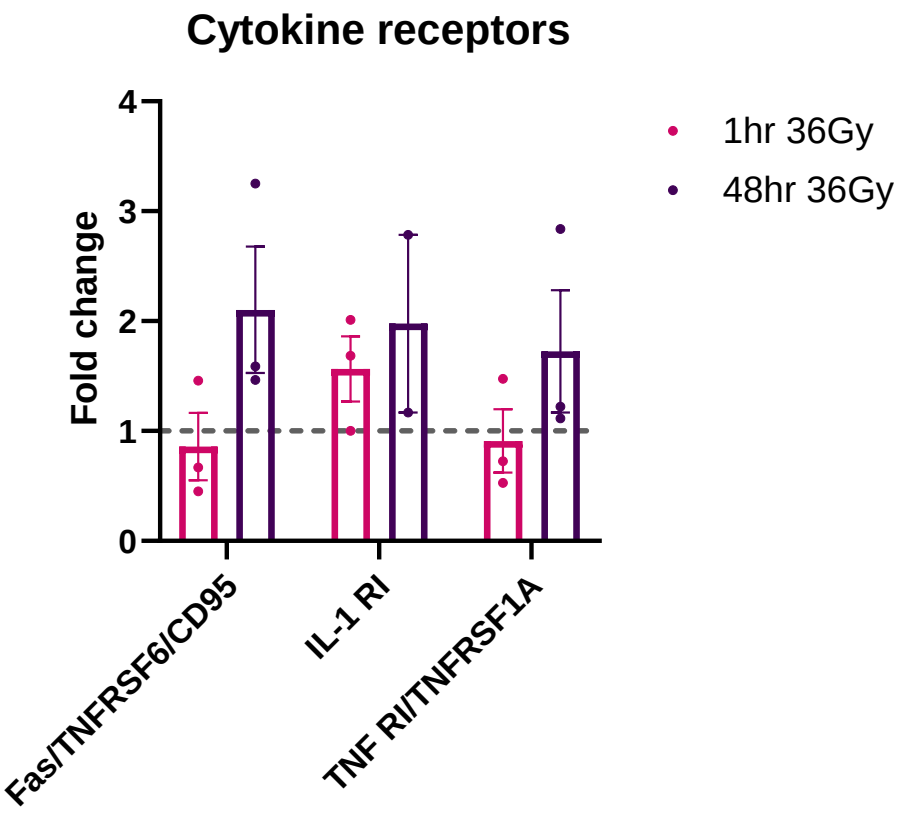

Analyte	Mean fold change	
Fas/TNFRSF6/CD95	0.86	2.10
IL-1 RI	1.57	1.98
TNF RI/TNFRSF1A	0.91	1.72
Fas/TNFRSF6/CD95	0.86	2.10

Figure 5.7. Cytokine receptor response following 36 Gy irradiation. Fold change concentration (relative to 0 Gy) at 1 hour and 48 hours post-irradiation, normalised to cell count. Points show individual replicates, error bars depict SEM and grey line depicts a fold change of 1. Significance between 1 hour and 48 hour time points was assessed via 2-sided independent t-test, p-values are shown when $p<0.05$.

5.4.3.5. Matrix metalloproteinase

Matrix metalloproteinases (MMPs) are enzymes involved in the regulation of extracellular matrix (ECM), as well as both acute and chronic inflammation through the release of membrane-anchored cytokines, growth factors and chemokines (Klein and Bischoff, 2011). The protein level of 4 MMPs was assessed: MMP-2, -3, -7 and -12 (Table 5.7). All MMPs were abundant 1-hour post-irradiation; concentration was 1.56-, 1.61-, 1.21- and 1.67-fold higher than non-irradiated controls, respectively (Figure 5.8). At 48 hours post-irradiation, levels of MMP-2, -3 and -7 further increased (2.30, 2.38 and 1.94 fold higher than non-irradiated controls), though this was not significant.

Conversely, protein expression of MMP-12 reduced; at 48-hours post-irradiation, MMP-12 concentration was 0.38 fold lower than non-irradiated controls, however this was not significant. A decrease in the level of MMP-12, in combination with decreased levels of CCL3 and CCL4 (section 5.4.3.3), suggest a reduced expression of macrophage simulation at 48 hours.

Analyte	Name	Function
MMP-2	Matrix metalloproteinase-2 /gelatinase A	ECM degradation, inflammation
MMP-3	Matrix metalloproteinase-3/ Stromelysin-1	ECM degradation, inflammation
MMP-7	Matrix metalloproteinase-7/ Matrilysin	ECM degradation, inflammation
MMP-12	Macrophage-specific Matrix metalloproteinase-12	ECM degradation, inflammation

Table 5.7. Overview of the matrix metalloproteinases.

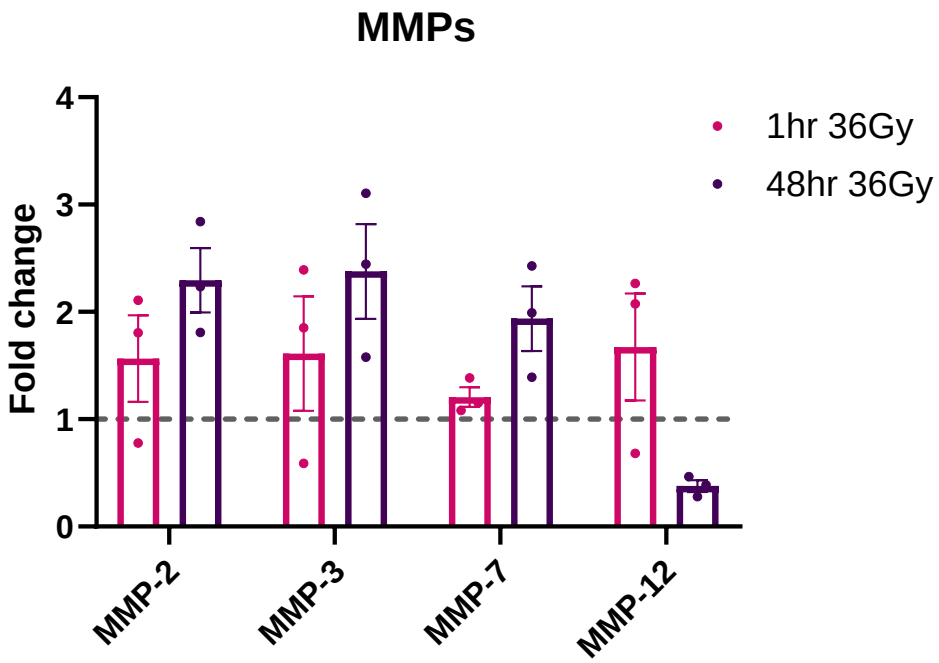

Analyte	Mean fold change	
MMP-2	1.56	2.30
MMP-3	1.61	2.38
MMP-7	1.21	1.94
MMP-12	1.68	0.38

Figure 5.8. MMPs response following 36 Gy irradiation. Fold change concentration (relative to 0 Gy) at 1 hour and 48 hours post-irradiation, normalised to cell count. Points show individual replicates, error bars depict SEM and grey line depicts a fold change of 1. Significance between 1 hour and 48 hour time points was assessed via 2-sided independent t-test, p-values are shown when $p<0.05$.

5.4.3.6. SASP

The senescence-associated secretory phenotype (SASP) is a fundamental feature of cellular senescence and encompasses tissue remodelling and pro-inflammatory signalling compounds (Cuollo *et al.*, 2020). A further 4 proteins characterised as markers of SASP (GDNF, ICAM-1, OPN and VCAM1; Table 5.8) was assessed, although there is considerable cross-over with analytes in categories previously discussed. At 1 hour post-irradiation, levels of SSAP marker expression was variable; GDNF and OPN levels were high than non-irradiated controls (1.48 and 1.34 fold respectively; Figure 5.9), whereas cell adhesion molecules ICAM-1 and VCAM-1 were present at lower levels than non-irradiated controls (0.22 and 0.51, respectively). Conversely, at 48-hours all SASP markers assessed were present at a higher level than non-irradiated controls (GDNF: 4.03, ICAM-1: 3.20, OPN: 1.61 and VCAM-1: 2.07 fold higher), though this was not significantly higher than at 1 hour post-irradiation.

Analyte	Name	Function
GDNF	Glial cell derived neurotrophic factor	Neuronal survival
ICAM-1/CD54	Intercellular adhesion molecule 1	Leukocyte-endothelial transmigration
OPN	Osteopontin	Pro-inflammatory signalling
VCAM1/CD106	Vascular cell adhesion molecule 1	Pro-inflammation, cell adhesion

Table 5.8. Overview of SASP markers function.

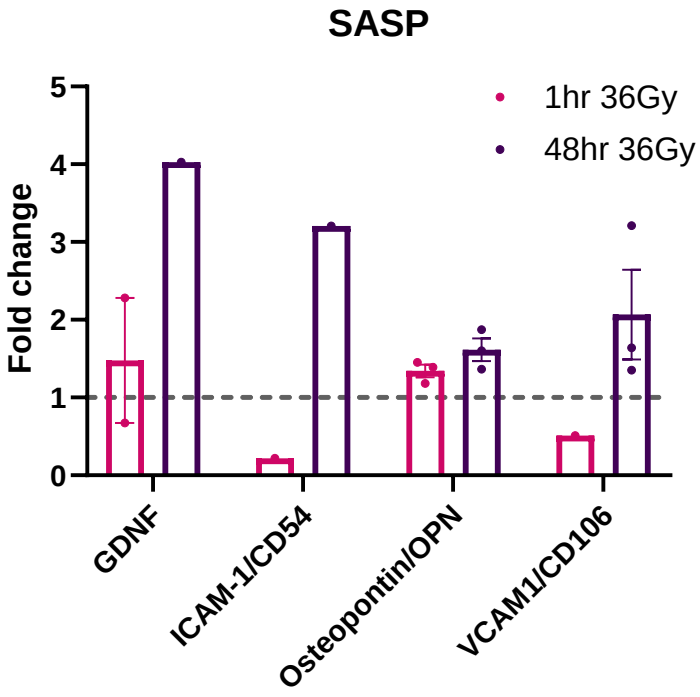

Analyte	Mean fold change	
GDNF	1.48	4.03
ICAM-1/CD54	0.22	3.20
Osteopontin/OPN	1.34	1.61
VCAM1/CD106	0.51	2.07

Figure 5.9. SASP response following 36 Gy irradiation. Fold change concentration (relative to 0 Gy) at 1 hour and 48 hours post-irradiation, normalised to cell count. Points show individual replicates, error bars depict SEM and grey line depicts a fold change of 1. Significance between 1 hour and 48 hour time points was assessed via 2-sided independent t-test, p-values are shown when $p<0.05$.

5.4.4. Assay limitations

The development of the custom panel of 57 analytes using the Luminex Discovery, enabled an insight into the inflammatory and SASP response to irradiation, as well as highlight potential key proteins involved in modulating insult response. However, as only 57 analytes were included within this assay, it was not possible to capture all proteins, and key drivers may have been missed. Of the 57 analytes selected, 21 were excluded from analysis, the vast majority (n=20/21) due to a concentration below the detectable limit. This suggests these analytes are not highly expressed in response to radiation insult and are unlikely to play a major role in modulating the response to radiation in this cell line. However, assay development utilised MRC-5 fibroblasts, and therefore excluded analytes may still play a role in modulating radiation-insult response and further appraisal of more biologically relevant, brain-derived cell lines is required.

To understand both the acute and chronic molecular response to radiation, samples were collected at 1- and 48-hours post-irradiation. To further elucidate the temporal response to radiotherapeutic insult, assessment of additional time points are required. This assay provides an insight into the level of inflammation that has occurred up to the time of sample collection, however, it is not possible to decipher the level of inflammatory signalling specifically at this timepoint.

An additional limitation of this study was due to the location of the irradiator. All flasks (both experimental and control) were transported across campus to receive either 36 Gy or 0 Gy radiation. The impact of this transport was minimised where possible, however, it is likely to have caused cellular stress. The control cells were exposed to the same environmental conditions as the irradiated samples (excluding radiation), and therefore for subsequent analysis irradiated samples were normalised to control samples. Transport-related stress may have induced a stress response in non-irradiated cells, and therefore may have partially masked radiation-related stress. Samples collected at the 48 hour time point were less likely to have been affected, and this may partially account for the increase in normalised analyte concentrations seen at 48 hours.

Overall, this model provides a useful insight into the biological response to radiation, as insult response was generally as expected, however, to account for tissue dependant features, this assay should next be utilised on more biologically relevant, brain-derived cell lines.

5.5. Discussion

The biological mechanisms underpinning radiotherapy-induced late-effects remains are relatively undefined. Radiation induces neuronal damage, and activates microglia/astrocytes to release numerous pro-inflammatory cytokines, chemokines and reactive oxygen species, which further activate immune cells within the brain, resulting in chronic neuroinflammation (Streit;Mrak and Griffin, 2004; Lumniczky;Szatmári and Sáfrány, 2017). Chronic inflammation, oxidative stress, impaired neurogenesis, cellular senescence and the senescence-associated secretory phenotype (SASP) have been indicated to play a role in cranial radiotherapy-induced late-effects (Turnquist;Harris and Harris, 2020b). Within this chapter, a novel assay was developed to investigate radiation-insult response. 57 analytes were selected for inclusion within the assay and were grouped into six biological groups: cytokine response, inflammation markers, chemokines, cytokine receptors, matrix metalloproteinases (MMPs) and SASP. For ease of visualisation analytes were analysed within these groups to provide an overview at the level of biological process, however there is considerable overlap between groups, in particular with markers of inflammation and SASP.

As expected, the concentration of pro-inflammatory proteins increased following irradiation, which typically increased further 48-hours post-irradiation. The majority of cytokines quantified exhibited increased expression 1-hour (73.3%, n=11/15) and 48-hours (76.9%, n=10/13) post-irradiation. For the majority of cytokines, the level of protein increased over time; 69.2% (n=9/13) had a higher concentration 48-hours post-irradiation than at 1-hour post-irradiation, though this was only significant for FSTL1 ($p=0.023$). FSTL1 plays a role in immune regulation through promoting cytokine production and the proliferation of inflammatory cells, and has been linked to the development of multiple diseases such as those affecting the cardiovascular system, osteo- and rheumatoid-arthritis (Mattiotti *et al.*, 2018; Li *et al.*, 2020). Whilst in this experiment used MRC-5 cells, FSTL1 is strongly expressed in the brain, and has been linked to impaired neurodevelopment through the increasing astrocyte activation (Yamada *et al.*, 2018). Moreover, at 48-hours post-irradiation, abundance of GDF-15 was increased (2.89-fold), however this was not significant. GDF-15 is typically expressed at low levels, which is upregulated in response to ROS, hypoxia and inflammation, to modulate the immune response and limit tissue damage (Jiang *et al.*, 2021; Siddiqui *et al.*, 2022). Conversely, 28.6% (n=4/14; IL-1β, IL-3, IL-10 and TNF-α) analytes had a reduced expression at 48-hours, despite an initial increase in expression at 1-hour post-irradiation, though this

decrease was only significant for IL-10 (p=0.047). IL-10 plays a role in regulating the immune response through inhibition of T helper type 1 and type 2 cells (Th1 and Th2) and enhances differentiation of regulatory T-cells (Tregs) (Saraiva and O'Garra, 2010), and can inhibit production of many pro-inflammatory cytokines including IL-1β, IL-6, TNF-α, and IFN-γ (de Waal Malefyt *et al.*, 1991; Moore *et al.*, 2001; Batista *et al.*, 2009; Porro;Cianciulli and Panaro, 2020). IL-10 also play a key role in modulating inflammation within the brain (Porro;Cianciulli and Panaro, 2020). Within this assay using MRC-5 cells, at 48 hours post-irradiation the concentration of IL-10 was very low, which, in combination with increased expressed of pro-inflammatory cytokines, suggests that high levels of inflammation persist days after radiation exposure.

To further determine the level of inflammation occurring post-irradiation, concentrations of 3 cytokine receptors were assessed (Fas, IL-1 R1 and TNF R1). Expression of the cytokine receptors assessed typically occurred later; at 1-hour post-irradiation 66.7% (n=2/3; Fas and TNF R1) proteins had a fold change less than 1. Yet after 48-hours, concentrations for all proteins were around 2-fold higher than non-irradiated controls. This delayed response highlights the need for multiple timepoints when assessing the response to radiation. Fas drives apoptosis cell death, by 48 hours concentration of Fas is 2.10 fold higher than in non-irradiated cells. Interesting, this increased concentration of Fas is in line with the level of cell death shown in the previous section; normalised cell count of irradiated cells was approximately half that of non-irradiated controls (0.64 vs 1.38, respectively; 5.4.1).

Moreover, markers of inflammation showed a similar trend following irradiation: all analytes (BDNF, S100B, NCAM-1/CD56 and TIE-2) had a fold change greater than 1 at both 1 and 48 hours, compared to non-irradiated controls. Inflammation was highest at the 48 hour timepoint, however this was only significant for BDNF. BDNF, brain-derived neurotropic factor, is primarily associated with promoting neuronal survival, growth and maintenance within the brain, and has been linked to maintaining synaptic plasticity and cognition (Zhao *et al.*, 2017). BDNF is thought to have anti-inflammatory effects on microglia, and reverse effectors such as IL-6 and TNF-α (Charlton *et al.*, 2023). BDNF can also be expressed by non-CNS tissue and protect against stimuli such as inflammation and hypoxia (Prakash and Martin, 2014; Hartman *et al.*, 2015). The increased level of BDNF in MRC-5 cells 48 hours post-irradiation suggests this protective response does not occur immediately, though additional timepoints are required to assess the exact timing of this response.

SASP, a fundamental feature of cellular senescence, encompasses pro-inflammatory signalling and factors of tissue remodelling (Cuollo *et al.*, 2020). GDFN (glial cell derived neurotrophic factor) protein expression was increased 1 hour post-irradiation and considerably elevated by 48 hours (1.48 and 4.03 fold, respectively). GDFN is a growth factor that promotes cell survival (including neuronal cells and foetal lung cells) thus elevated GDFN levels post-irradiation suggests a protective response is initiated early and progressively increases over time (Airaksinen and Saarma, 2002; Fromont-Hankard *et al.*, 2002). Conversely, levels of cell adhesion molecules (ICAM-1 and VCAM-1) were lower than non-irradiated controls 1 hour post-irradiation (0.22 and 0.51 fold, respectively), yet by 48 hours were considerably higher (3.2 and 2.07 fold, respectively). ICAM-1 and VCAM-1 promote inflammation through cell adhesion and leukocyte-endothelial transmigration in response to pro-inflammatory cytokines, activated mainly by TNF-α, IL-1β and IFN-γ depending on the cell type (Kong *et al.*, 2018; Bui;Wiesolek and Sumagin, 2020). In this assay, levels of ICAM-1 and VCAM-1 were as expected; increased ICAM-1 and VCAM-1 protein expression was present at 48 hours but not at 1 hour post-irradiation, whereas IL-1β and TNF-α levels were highest 1-hour post-irradiation. The level of IFN-γ not quantifiable in this assay; activation of ICAM-1 through IFN-γ typically occurs within macrophages (Bui;Wiesolek and Sumagin, 2020).

5.6. Chapter Summary

In this chapter a model was developed which provides the basis for *in vitro* investigation into the acute and chronic molecular response to radiotherapeutic insult, and a platform for the future appraisal of pharmacological interventions to modulate and protect against radiotherapeutic-insult. Delivery of an MB-equivalent high dose of radiation was tolerated in MRC-5 cells, and cells continue to grow, albeit at a slower rate than non-irradiated controls. Through the development of a custom Luminex Discovery panel, markers of inflammation were increased at 1 hour post-irradiation, and this typically increased further at 48 hours. Increased inflammation was expected and is thought to play a major role in the development of radiation-induced late effects.

Through the use of a panel of 57 analytes, it has been shown that response to radiotherapeutic insult is not uniform and a temporal response is present; whilst most inflammatory proteins increased in concentration by 48 hours, several had decreased. This assay was developed using a fast-growing, non-brain derived cell line and therefore, despite being indicated in the literature to play a role the inflammatory/SASP response to radiotherapeutic insult, 20 analytes were excluded from subsequent analysis as the concentration was below the level of detection. Though these analytes may not modulate radiotherapeutic-insult response in MRC-5 cells, they may still play a role within the response to cranial-irradiation and therefore should be explored within more biologically relevant, brain-derived cell lines.

Chapter 6. Development of an in vivo model of MB chemotherapy-induced late-effects

6.1. Introduction

Childhood MB patients receive multimodal therapy, including the receipt of adjuvant chemotherapy, which is currently recommended for all patients regardless of risk status (Tait *et al.*, 1990; Millard and De Braganca, 2016). The combination of chemotherapy with radiotherapy has significantly improved 5-year event-free survival (EFS) when compared to radiotherapy alone (74.2% vs 59.8%; SIOP/UKCCSG-PNET3) (Taylor *et al.*, 2003), and has enabled a reduction in the intensity of radiotherapy regimens for standard risk patients (from 36 Gy to 23.4 Gy CSI) (Evans *et al.*, 1990; Northcott *et al.*, 2019). However, the receipt of multimodal therapy has led to increased morbidity and mortality among MB survivors (Salloum *et al.*, 2019). Survivors often experience late-effects including ototoxicity, peripheral neuropathy, cardiotoxicity and secondary malignant neoplasms as a result of adjuvant chemotherapy (Gurney *et al.*, 2003; Diller *et al.*, 2009a). However, the development of such late-effects is currently not well defined, and model systems recapitulating MB-equivalent chemotherapy-induced late-effects, particularly in combination with receipt of radiotherapy, are lacking. Chemotherapy-induced late-effects poses a large problem within cancer research; understanding and preventing chemotherapy-induced neurotoxicity and neuropathy is a theme of the 2023 Cancer Grand Challenges.

Childhood MB chemotherapy regimens are complex, and often differ between treatment centres, with numerous clinical trials to assess the potency of new combinations. The most widely used chemotherapy drugs given before or during radiotherapy include cisplatin, vincristine, cyclophosphamide, lomustine (CCNU) and carboplatin (Yock *et al.*, 2016). Perhaps the mostly widely used chemotherapy regimen is the ‘Packer Regimen’ (named after Roger Packer), which consists of two alternating regimens, summarised in Table 6.1. Variations of Packer-style chemotherapy are used within the current major MB clinical trials in Europe (SIOP-PNET5-MB; NCT02066220) and the US (SJMB12; NCT01878617).

Currently, there are no models that recapitulate Packer-style or indeed any contemporary combination chemotherapy *in vivo*. Nimmervoll *et al* established a preclinical model of supratentorial ependymoma using a combination of etoposide, cisplatin, and vincristine (Nimmervoll *et al.*, 2018) and Mañas *et al* used a combination of cisplatin, vincristine, etoposide, cyclophosphamide, carboplatin to model high-risk neuroblastoma chemotherapy (Mañas *et al.*, 2022). Both groups aimed to investigate tumour response and overall survival, and consequently no treatment-associated acute toxicities or late-effects were reported. The

amelioration of late-effects is hindered through a paucity of knowledge in their development, and a lack of an appropriate baseline model for the appraisal of potential interventions.

Regimen	Dug	Frequency	Dose
Regimen A (cycles 1, 3, 5, 7)	Lomustine	Day 0	75 mg/m^2
	Cisplatin	Day 1	75 mg/m^2
	Vincristine	Day 1, 7, 14	1.5 mg/m^2
Regimen B (cycles 2, 4, 6, 8)	Cisplatin	Day 0	75 mg/m^2
	Vincristine	Day 1	1.5 mg/m^2
	Cyclophosphamide	Day 21 and 22	1000 mg/m^2

Table 6.1. Overview of Packer chemotherapy. Starting 6 weeks post-radiotherapy, MB patients typically receive 8 cycles of Packer chemotherapy, alternating between regimen A and regimen B.

6.2. Aims

In this chapter the aim is to develop an *in vivo* model that recapitulates Packer-style MB chemotherapy, to provide a baseline model for further investigation of chemotherapy-induced late-effects, for the development of improved surveillance strategies and pharmacological interventions.

1) *In vivo* delivery of Packer-style chemotherapy, through modification of a previously published *in vivo* regimen.

2) Assessment of chemotherapy tolerability through measurement of body weight and frailty assessment.

6.3. Methods

6.3.1. Chemotherapy administration

Male C57Bl/6 mice were purchased at approximately 4-5 weeks old and received chemotherapy at 5-7 weeks old (human equivalent approximately 6-14 years old). Stocks of chemotherapeutic agents were made fresh for each cycle. Diluted cisplatin was stored at 4°C during dosing (day 1-5). Details of injection methodology is provided in Chapter 2.5.

6.3.2. Chemotherapy regimen design

To recapitulate MB chemotherapy, a regimen based on Packer regimen B was designed. Packer regimen B is comprised of the most widely used MB chemotherapeutic agents: cisplatin (day 0, 75 mg/m^2), vincristine (day 1, 1.5 mg/m^2) and cyclophosphamide (1000 75 mg/m^2). As there was no evidence of *in vivo* delivery of this regimen in the literature, this regimen was a refinement of a previously published *in vivo* ependymoma regimen of cisplatin, vincristine, and etoposide (Table 6.2 (Nimmervoll *et al.*, 2018)).

To recapitulate Packer regimen B chemotherapy, cyclophosphamide was added, and the dose increased incrementally, alongside an additional dose of vincristine. Etoposide is not widely used in the treatment of childhood MB and was therefore not included in this regimen. To minimise potential toxicity, modifications were made incrementally across 4 optimisation regimens (regimen 1-4). Once one cycle of the regimen was deemed to be tolerated, a second cycle of the same regimen was administered (to the same mice, following sufficient recovery) and the next regimen began (to a new group of mice, n=6 per regimen). One cycle lasted 10 days and the second cycle began following stabilisation of body weight and recovery from any weight loss.

Dug	Frequency	Dose	Route
Cisplatin	Day 1-5	2 mg/kg	IP
Etoposide	Day 1-3	6 mg/kg	IP
Vincristine	Day 5	1.6 mg/kg	IV

Table 6.2. Chemotherapy dosing schedule by Nimmervoll *et al*. IP = Intraperitoneal injection and IV = intravenous injection (tail vein).

6.3.3. Assessment of tolerability to chemotherapy

Body weight (grams) was recorded prior to the receipt of chemotherapy. Body weight and general health was assessed daily during dosing and then for 14 days following receipt of chemotherapeutic agents. Frailty assessment was conducted 2 weeks following completion of dosing to allow sufficient recovery from any acute toxicity. Details of assessments are provided in Chapter 2.6.

6.4. Results

6.4.1. Chemotherapy dosing development

The addition of cyclophosphamide at day 10 was added with a starting dose at 1/5th of the maximum tolerated dose (MTD) (Aston *et al.*, 2017). To achieve the higher doses associated with human MB chemotherapy, cyclophosphamide dose was increased incrementally in each regimen up to a final dose at 2/3rd MTD. An additional dose of vincristine was also assessed. An overview of the optimisation regimens (regimen 1-4) is shown in Table 6.3.

Once one cycle was deemed to be tolerated, a second cycle of the same regimen was administered (to the same mice, following sufficient recovery) and the next regimen began (new group of mice). An overview of the workflow is shown in Figure 6.1.

Regimen	Drug	Day	Dose (per day, mg/kg)	Total dose (per cycle, mg/kg)	Route	Reasoning
1	Cisplatin	1-5	2	10	IP	Addition of cyclophosphamide to previously published regimen, modified by removing etoposide and adding cyclophosphamide at 1/5th MTD
	Vincristine	5	1.5	1.5	IP	
	Cyclophosphamide	10	60	60	IV	
2	Cisplatin	1-5	2	10	IP	Regimen 1 + increased dose of cyclophosphamide at ½ MTD
	Vincristine	5	1.5	1.5	IP	
	Cyclophosphamide	10	150	150	IV	
3	Cisplatin	1-5	2	10	IP	Regimen 2 + extra dose of vincristine
	Vincristine	3+5	1.5	3	IP	
	Cyclophosphamide	10	150	150	IV	
4	Cisplatin	1-5	2	10	IP	Regimen 3 + increased dose of cyclophosphamide at desired concentration
	Vincristine	3+5	1.5	3	IP	
	Cyclophosphamide	10	200	200	IV	

Table 6.3. Development of dosing schedule. The intensity of CTX dosing regimen was incrementally increased from a modified published regimen (yellow; regimen 1) to the desired regimen (green; regimen 4). Red text depicts the new element (drug, dose) being assessed in each regimen.

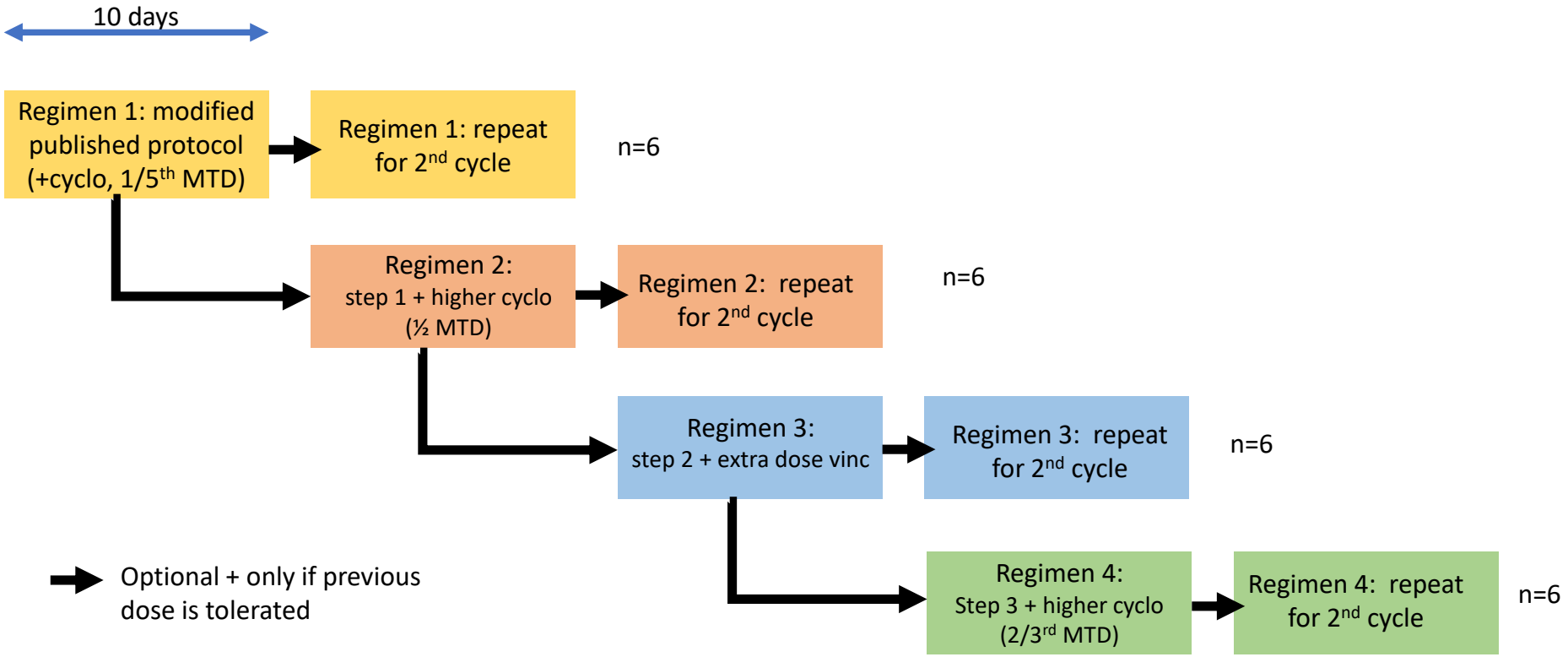

Figure 6.1. Workflow of dosing optimisation. Details of each regimen are shown in Table 7.1. Once the cycle is deemed to be tolerated, a second cycle of the same regimen was administered (same mice) and the next regimen began (new mice).

6.4.2. Chemotherapy dosing regimen

6.4.2.1. Optimisation step 1

Step 1 consisted of the administration of cisplatin (day 1-5; 2 mg/kg, IP), vincristine (day 5; 1.5 mg/kg, IP) and cyclophosphamide (day 10; 60 mg/kg, IV). Regimen 1 was applied to two groups (n=3 for each). First, regimen 1 was given to 3 mice, aged approximately 5 weeks old with no minimum weight criteria (regimen 1_A). Unfortunately, this was not well tolerated, and despite supportive measures (additional food and rehydration with saline injection), one mouse was humanely culled prior to cyclophosphamide administration, and the remaining two mice culled following cycle 1 (Figure 6.2).

To mitigate excessive toxicity in young mice, a minimum starting weight of 20g was set, to promote resilience. In group 2, mice were dosed at approximately 6 weeks old with a minimum starting weight of 20g (regimen 1_B). This was well tolerated, and all mice (n=3) tolerated two cycles of regimen 1 (Figure 6.2). Therefore, it was concluded that cyclophosphamide could be delivered *in vivo* in combination with cisplatin and vincristine, when given at a dose of 60 mg/kg, and the optimisation could proceed to the increased cyclophosphamide dose.

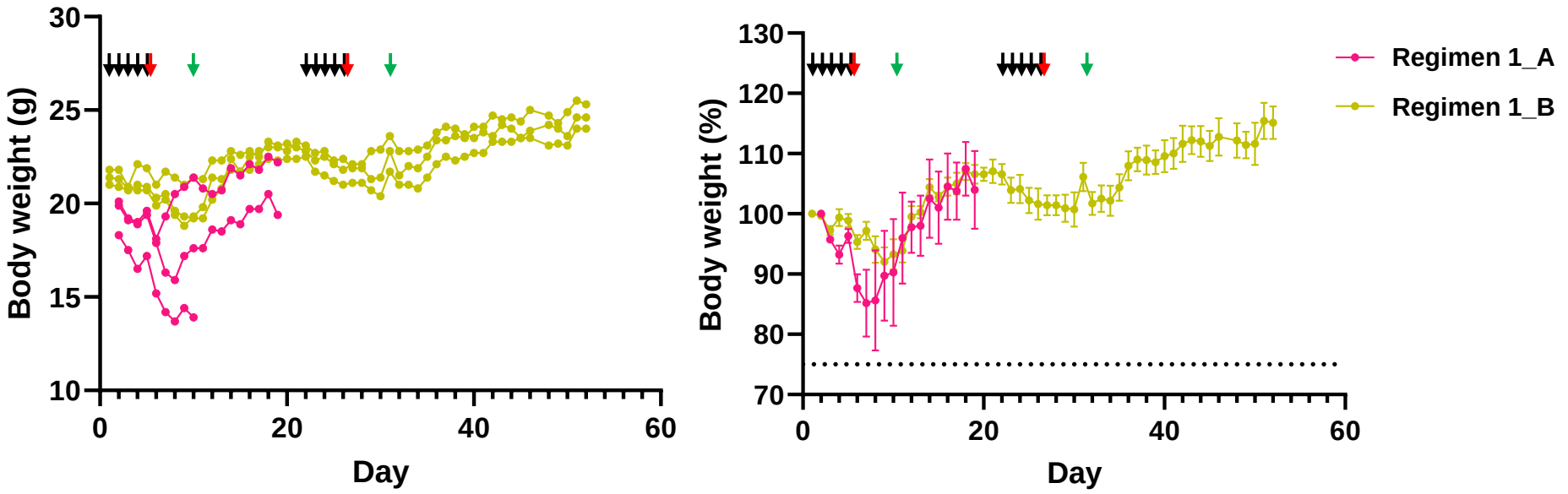

Figure 6.2. Step 1 (cyclophosphamide in combination with cisplatin and vincristine) was well tolerated. Body weight (individual, g; left and % mean ± SEM; right) following administration of cisplatin (2 mg/kg, IP; black), vincristine (1.5 mg/kg, IP; red) and cyclophosphamide (60 mg/kg, IV; green). Regimen 1 was conducted in two groups (n=3 for each): Regimen 1_A mice were dosed at 5 weeks old with no minimum weight criteria; Regimen 1_B mice were dosed at 6 weeks old with a minimum starting weight of 20g.

6.4.2.2. Optimisation step 2

As the combination of cyclophosphamide with cisplatin and vincristine was well tolerated, following the addition of a minimum weight criterion, the dose of cyclophosphamide was increased from 60 mg/kg to 150 mg/kg (1/5th to 1/2 of the MTD). Step 2 consisted of the administration of cisplatin (day 1-5; 2 mg/kg, IP), vincristine (day 5; 1.5 mg/kg, IP) and cyclophosphamide (day 10; 150 mg/kg, IV). Mice (n=6) were dosed at approximately 6 weeks old, once a minimum weight of 20g was reached (Figure 6.3). One mouse (m5) was humanely culled at day 7 (before receipt of cyclophosphamide) due to weight loss. However, all remaining mice (n=5) tolerated regimen 2 well and received two cycles. All mice exhibited weight loss during receipt of chemotherapy, though this was within the expected limits and mice recovered once the dosing period ended. As two cycles of regimen 2 was well tolerated, the optimisation process progressed to the next step.

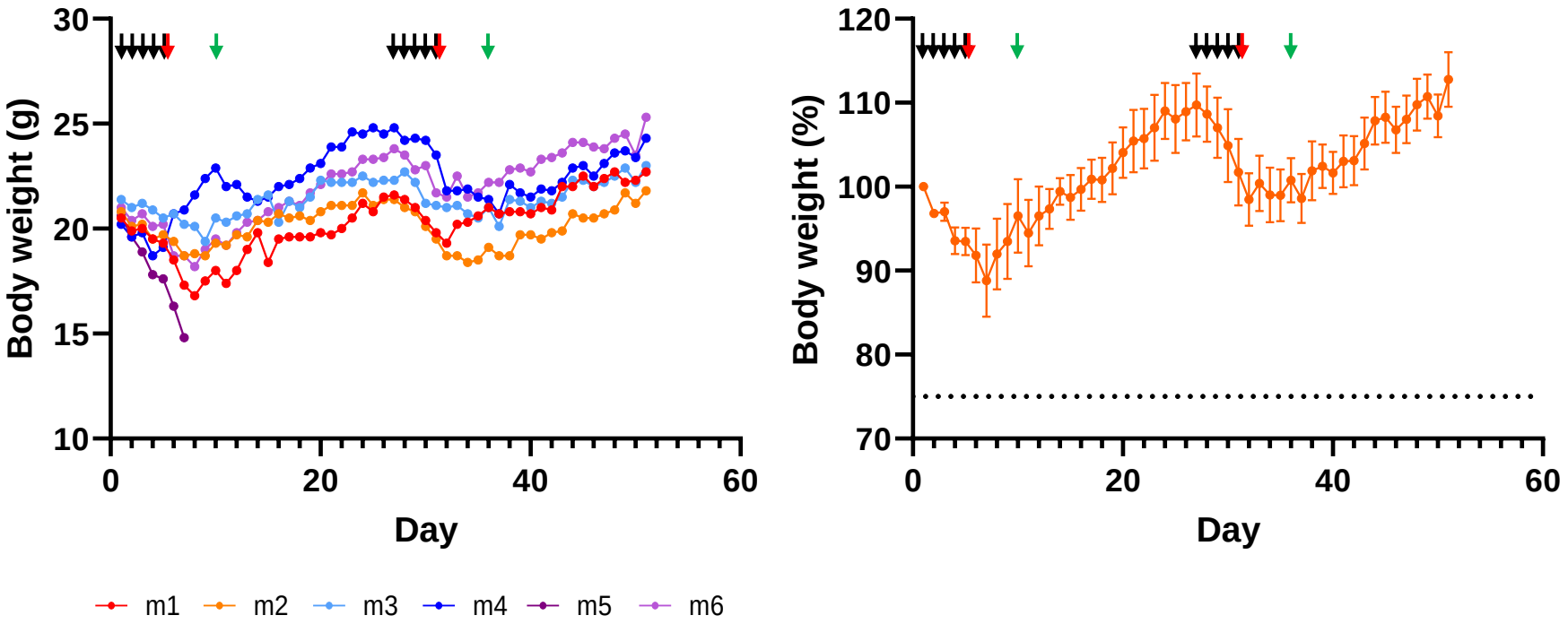

Figure 6.3. Step 2 (increasing cyclophosphamide dose) was well tolerated. Body weight (individual, g; left and % mean ± SEM; right) following administration of cisplatin (2 mg/kg, IP; black), vincristine (1.5 mg/kg, IP; red) and an increased dose of cyclophosphamide (150 mg/kg, IV; green). Regimen 2 was well tolerated; 5/6 mice tolerated 2 cycles of regimen 2 and survived until the study end point (day 52; 1 mouse was humanely culled at day 7).

6.4.2.3. Optimisation step 3

As the increased dose of cyclophosphamide, in combination with cisplatin and vincristine, was well tolerated, an additional dose of vincristine was added to the regimen to provide a higher cumulative dose and better recapitulate childhood MB chemotherapy. Step 3 consisted of the administration of cisplatin (day 1-5; 2 mg/kg, IP), vincristine (day 3 and day 5; 1.5 mg/kg, IP) and cyclophosphamide (day 10; 150 mg/kg, IV). Mice (n=6) were dosed at approximately 7 weeks old, once a minimum weight of 20g was reached.

Unfortunately, the additional dose of vincristine was not tolerated; body weight rapidly declined from day 5 despite mice receiving supportive care (additional food and rehydration with saline injections) (Figure 6.4). All mice were humanely culled on day 8 due to poor general health and extensive weight loss.

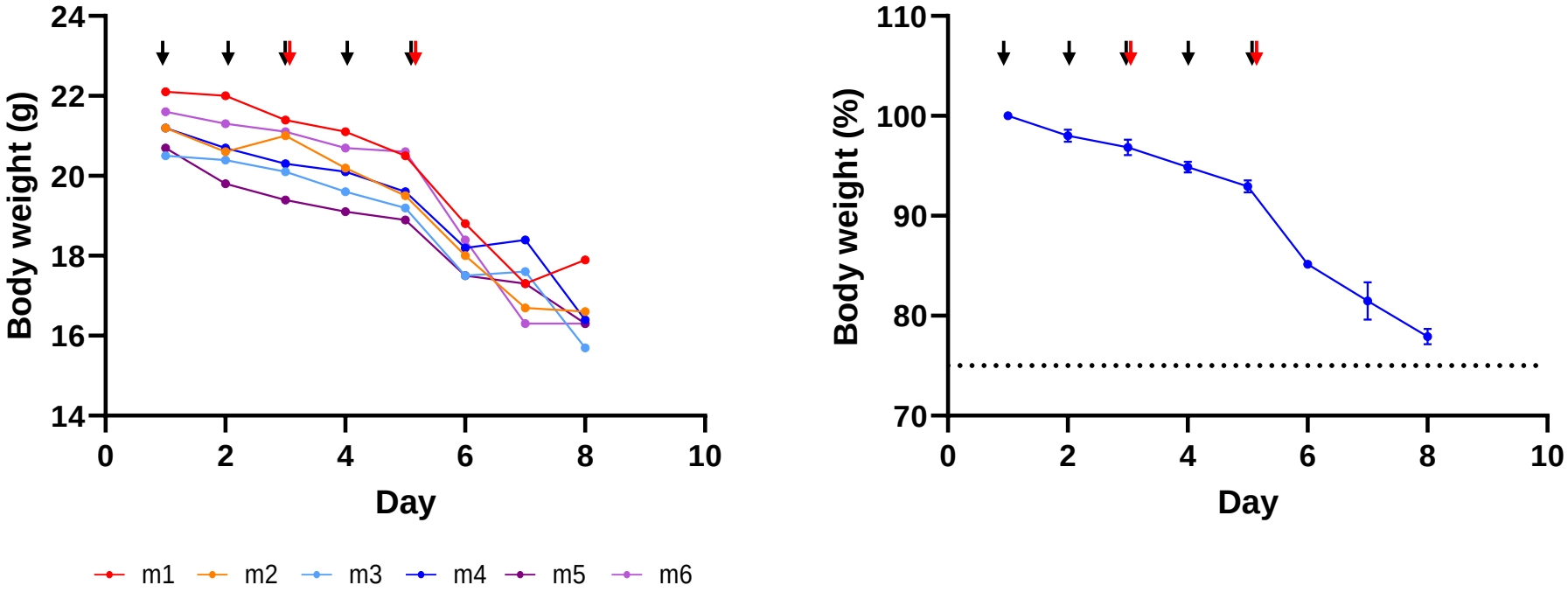

Figure 6.4. Step 3 (an addition dose of vincristine) was not tolerated. Body weight (individual, g; left and % mean ± SEM; right) following administration of cisplatin (2 mg/kg, IP; black), and vincristine (1.5 mg/kg, IP; red). The addition of an extra vincristine dose was not tolerated, and all mice were humanely culled on day 8.

6.4.2.4. Optimisation step 4

The increased dose of cyclophosphamide (from 60 to 150 mg/kg, assessed in regimen 2) was well tolerated. Next, the cyclophosphamide dose was further increased to 200 mg/kg. As the additional dose of vincristine was not tolerated in regimen 3, it can be hypothesised that one dose of vincristine per cycle was effective in this *in vivo* chemotherapy combination.

For step 4 of the chemotherapy optimisation, the increased dose of cyclophosphamide (200 mg/kg) was assessed by building on regimen 2, rather than regimen 3 as originally planned, an updated overview is shown in Table 6.4. Regimen 4 consisted of the administration of cisplatin (day 1-5; 2 mg/kg, IP), vincristine (day 5; 1.5 mg/kg, IP) and cyclophosphamide (day 10; 200 mg/kg, IV). Mice (n=6) were dosed at approximately 7 weeks old, once a minimum weight of 20g was reached (Figure 6.5).

Receipt of combination chemotherapy regimen 4 was tolerated; the majority of mice (n=4/6) tolerated 2 cycles of regimen 4 and survived until the study end point (day 53). During cycle 1, one mouse (m4) was culled due to excessive weight loss and poor general health (at day 9, prior to cyclophosphamide). Towards the end of cycle 2, all mice experienced moderate weight loss, though for most this was overcome with supportive care and mice recovered once the dosing period ended (1 mouse [m3] was culled at day 35).

Regimen	Drug	Day	Dose (per day, mg/kg)	Total dose (per cycle, mg/kg)	Route	Reasoning
1	Cisplatin	1-5	2	10	IP	Addition of cyclophosphamide to previously published regimen, modified by removing etoposide and adding cyclophosphamide at 1/5th MTD
	Vincristine	5	1.5	1.5	IP	
	Cyclophosphamide	10	60	60	IV	
2	Cisplatin	1-5	2	10	IP	Regimen 1 + increased dose of cyclophosphamide at ½ MTD
	Vincristine	5	1.5	1.5	IP	
	Cyclophosphamide	10	150	150	IV	
3	Cisplatin	1-5	2	10	IP	Regimen 2 + extra dose of vincristine
	Vincristine	3+5	1.5	3	IP	
	Cyclophosphamide	10	150	150	IV	
4	Cisplatin	1-5	2	10	IP	Regimen 2 + increased dose of cyclophosphamide at desired concentration
	Vincristine	5	1.5	3	IP	
	Cyclophosphamide	10	200	200	IV	

Table 6.4. Updated dosing schedule. Regimen 4 was modified from the original design as regimen 3 was not tolerated. Yellow highlight depicts the modifications made to regimen 4. Red text depicts the new element being assessed in each regimen.

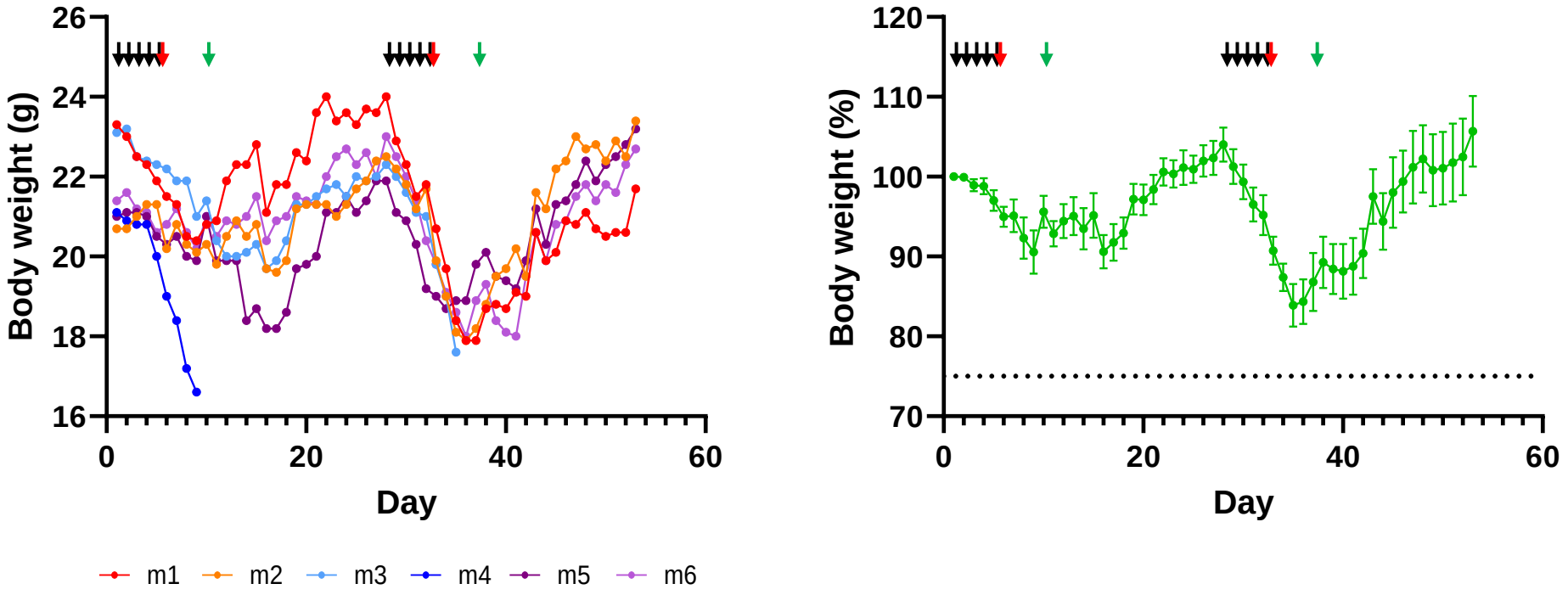

Figure 6.5. Step 4 (increasing cyclophosphamide dose) was tolerated. Body weight (individual, g; left and % mean ± SEM; right) following administration of cisplatin (2 mg/kg, IP; black), vincristine (1.5 mg/kg, IP; red) and an increased dose of cyclophosphamide (200 mg/kg, IV; green). Regimen 4 was tolerated; 4/6 mice tolerated 2 cycles of regimen 4 and survived until the study end point (day 53; 2 mice were humanely culled [at day 9 and day 35]).

6.4.3. Increased dose of cyclophosphamide induced increased frailty

6.4.3.1. Chemotherapy reduces body weight

Combination chemotherapy leads to a decrease in body weight. As shown in chapter 6.4.2, body weight decreased during the chemotherapy dosing period. Following dosing body weight recovers, however, mice remained at a smaller size than untreated controls (Figure 6.6).

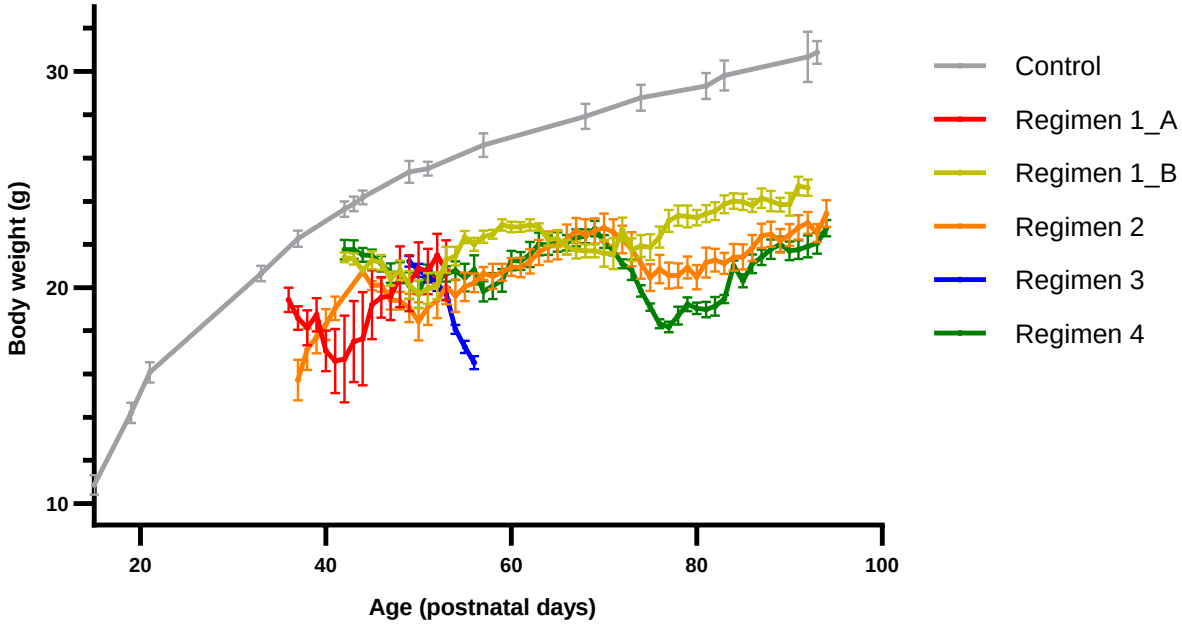

Figure 6.6. Reduced body weight following combination chemotherapy treatment. Body weight was lower following combination chemotherapy than control C57Bl/6 male mice (n=24).

6.4.3.2. Chemotherapy induces premature ageing

Frailty was assessed using a 30-parameter frailty index, following recovery from the chemotherapy dosing period (regain of any weight loss). Frailty assessment was conducted 2 weeks after the final dose of chemotherapy (day 46-51; ~PND 90, human-equivalent approximately 22 years old), on mice that received two cycles of regimen 1 (group 2 only; n=3), regimen 2 (n=5) or regimen 4 (n=4). No frailty assessment was conducted on group 1 of regimen 1 (prior to a minimum weight criterion; n=3), or any mouse that received regimen 3 (additional dose of vincristine; n=6) as all mice were culled within the first cycle of chemotherapy.

All groups received a total of 10 doses of 2 mg/kg cisplatin (day 1-5 of each cycle), 2 doses of 1.5 mg/kg vincristine (day 5 of each cycle) and 2 doses of varying quantities of cyclophosphamide (day 10 of each cycle; regimen 1: 60 mg/kg, regimen 2: 150 mg/kg and regimen 4: 200 mg/kg). Despite the concentration of cyclophosphamide increasing from 60-150 mg/kg, this did not increase overall frailty; frailty index was equivalent in mice receiving regimen 1 and 2 (mean FI: 0.059 and 0.057 respectively, p=0.883; Figure 6.7). Frailty in mice following receipt of regimen 4 (200mg/kg cyclophosphamide) was markedly higher than mice that received regimen 1 or 2 (mean FI: 0.102). However, this different was not significant (p=0.119 and 0.052, respectively), likely due to the low number of mice in each group.

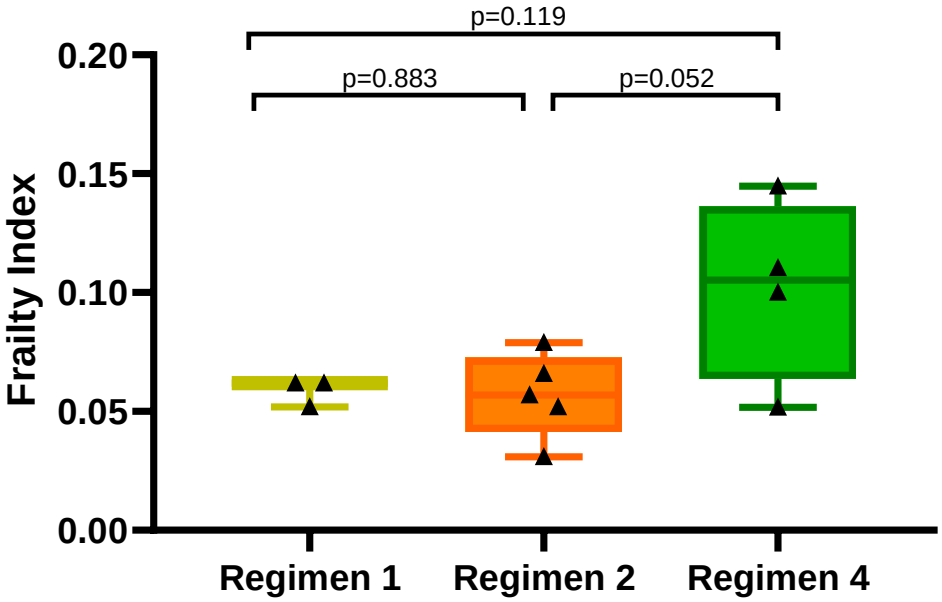

Figure 6.7. Frailty index following chemotherapy. Frailty index score following 2 cycles of regimen 1 (n=3; ~PND 91), regimen 2 (n=5, ~PND 93) and regimen 4 (n=4, ~PND 92). All groups received 10 doses of 2 mg/kg cisplatin (day 1-5 of each cycle), 2 doses of 1.5 mg/kg vincristine (day 5 of each cycle) and 2 doses of test dose of cyclophosphamide (day 10 of each cycle; regimen 1: 60 mg/kg, regimen 2: 150 mg/kg and regimen 4: 200 mg/kg).

6.5. Discussion

Chemotherapy-induced late-effects such as peripheral neuropathy, cardiotoxicity, ototoxicity and secondary malignant neoplasms (SMNs) are commonly experienced by cancer survivors. However, biological understanding of their development is lacking, and is hindered by a paucity of suitable models that can recapitulate contemporary combination chemotherapy *in vivo*. The development of an *in vivo* MB-equivalent chemotherapy regimen provides a baseline model for the future assessment of chemotherapy-induced late-effects.

This MB-chemotherapy model was developed to recapitulate Packer regimen B chemotherapy (the most commonly used chemotherapy regimen; summarised in Table 6.1), consisting of cisplatin, vincristine and cyclophosphamide. As there was no evidence of in vivo delivery of this regimen in the literature, this regimen was a refinement of a previously published in vivo ependymoma regimen consisting of cisplatin, vincristine, and etoposide (Table 6.2 (Nimmervoll *et al.*, 2018)). To recapitulate Packer regimen B chemotherapy, cyclophosphamide was added, and the dose increased incrementally, alongside an additional dose of vincristine. Etoposide is not widely used in the treatment of childhood MB and was therefore not included in this regimen. To minimise potential toxicity, modifications were made incrementally across 4 optimisation regimens (regimen 1-4). The additional of cyclophosphamide in combination with cisplatin and vincristine was well tolerated at low doses (60 mg/kg; 1/5th MTD). Thus, the dose was incrementally increased to achieve the higher doses associated with human MB chemotherapy. The highest dose (200mg/kg) was tolerated, and the majority of mice (n=4/6) tolerated 2 cycles of regimen 4 and survived until the study end point. As expected, regimen 4 (consisting of the highest dose of cyclophosphamide), induced higher frailty than with lower doses of cyclophosphamide. Childhood cancer survivors often experience higher rates of frailty in comparison to siblings, which has, in part, been associated with receipt of high doses of chemotherapy (Hayek *et al.*, 2020). All mice exhibited weight loss during receipt of chemotherapy, though this was within the expected limits and mice recovered once the dosing period ended. Chemotherapy is associated with significant weight loss in childhood MB patients, typically due to reduced dietary intake from emesis, nausea, mucositis and diarrhoea during treatment (Bakish *et al.*, 2003). In this model, body weight recovered following dosing, however, mice remained at a smaller size than untreated controls. Mice were followed up for approximately 2 weeks after cessation of chemotherapy. Despite a lower body weight than controls, it is not possible to

determine whether this reduction in body weight was due to reduced caloric intake during the dosing period, or whether the receipt of chemotherapy stunted overall growth. Monitoring of food intake and longer follow-up would provide insight into the extent of reduced caloric intake and whether body weight returns to that of untreated controls.

In this model, high acute toxicity occurred when chemotherapy was administered to small, young mice (5 weeks old, human-equivalent 6 years old). Chemotherapy dose was calculated according to weight (mg/kg), however, at a young age tolerability is further reduced (Saghir;Ansari and Dorato, 2020). Following the introduction of a minimum weight (set at 20g), tolerance to chemotherapy improved. High acute toxicity was also present following administration of the additional dose of vincristine in regimen 3 (2 doses at 1.5 mg/kg). Administration of chemotherapy via multiple lower doses increases tolerability compared to a single dose with same cumulative dose. In a study by Geisler *et al*, twice weekly vincristine at 1.5 mg/kg (for 4 weeks) was well tolerated and induced mild weight loss equivalent to the receipt of a single weekly dose at 1 mg/kg (Geisler *et al.*, 2016). Vincristine is tolerated at higher doses (Harrison, 1983; Thompson *et al.*, 1999; Geisler *et al.*, 2016; Liu *et al.*, 2018), though as a single agent and therefore the increased toxicity seen within regimen 3 is likely due to combination effects with additional chemotherapeutic agents. Vincristine can result in myelosuppression and therefore monitoring peripheral blood may provide an indication of acute toxicity. When given in combination vincristine is typically given at lower doses, or with a longer recovery period between doses (Nimmervoll *et al.*, 2018; Mañas *et al.*, 2022). Route of administration can also influence tolerability, as bioavailability is typically lower following IP injection than IV injection. In the study by Nimmervoll *et al*, vincristine (1.6 mg/kg) was administered intravenously and tolerated in combination with cisplatin at the same dose at this model (Nimmervoll *et al.*, 2018). Here vincristine was administered via IP rather than IV injection, and therefore drug concentration with the blood plasma were expected to be lower than via IP injection (Al Shoyaib;Archie and Karamyan, 2019). However, this was not assessed during this study. In humans, vincristine and cyclophosphamide are typically delivered intravenously. However, in mice, IV injections via the lateral tail veins can cause damage to the veins, and more stress than IP injections, therefore chemotherapy delivery via this route was minimised where possible. As shown in previous studies, cyclophosphamide induces neurocognitive impairment following IV and IP administration, though impaired cognition is less readily seen *in vivo* when cyclophosphamide is delivered via IP injections (Janelsins *et al.*,

2010; Yang *et al.*, 2010; Janelsins *et al.*, 2016) and therefore in this model, cyclophosphamide was delivered through the IV route. One of the main side-effects experienced by patients receiving vincristine is peripheral neuropathy. In animal models of vincristine-induced peripheral neuropathy, toxicity is typically induced through IP vincristine administration (Harrison, 1983; Geisler *et al.*, 2016; Liu *et al.*, 2018; Mañas *et al.*, 2022).

6.6. Chapter summary

In this chapter an *in vivo* model that recapitulates childhood MB chemotherapy was developed, using a widely used combination of cisplatin, vincristine and cyclophosphamide. The aim was to develop a dosing regimen that struck the balance of inducing obvious insult (weight loss, poor condition, frailty), but not too aggressive that it was intolerable. This model provides a baseline regimen for future assessment of chemotherapy-induced late-effects.

The tolerability of receiving 2 cycles of 1) a modified, previously published combination of cisplatin and vincristine; 2) the addition of cyclophosphamide to this combination, and 3) increasing the doses of cyclophosphamide and vincristine, was assessed. Receipt of cisplatin and vincristine (cisplatin: day 1-5; 2 mg/kg, IP, vincristine: day 5; 1.5 mg/kg, IP) was not well tolerated in young, small mice (age 5 weeks old, and under 20g). Following a minimum start weight of 20g, cisplatin and vincristine induced weight loss, though with the provision of supportive care this was generally well tolerated (n=2/12 [regimen 2 and 4] were culled prior to receipt of cyclophosphamide due to excessive weight loss).

The addition of cyclophosphamide was well tolerated at both 60 mg/kg and 150 mg/kg, with the majority of mice tolerating two cycles of combination chemotherapy (n=3/3 and n=5/6, respectively). An increase in cyclophosphamide dose to 200 mg/kg induced moderate weight loss, yet most mice were able to recover with the addition of supportive care (n=4/6). Two doses of vincristine (1.5 mg/kg at day 3 and 5) were not tolerated; all mice exhibited rapid weight loss, despite supportive care and were humanely culled on day 8. However, a single dose of vincristine per cycle (1.5 mg/kg at day 5) was well tolerated.

Two cycles of regimen 4 (cisplatin: day 1-5; 2 mg/kg, IP, vincristine: day 5; 1.5 mg/kg, IP, and cyclophosphamide: day 10; 200 mg/kg, IV), recapitulated chemotherapy in childhood MB patients. This dosing regimen was intensive enough to induce acute toxicity, yet not too aggressive that it was not tolerated, and any acute side-effects were typically managed with supportive care. Following recovery from dosing regimen 4, increased frailty was apparent, in comparison to receipt of regimen 1 and 2. Administration of combination chemotherapy using regimen 4 provides a useful basis for further investigation of late-effects. During this chapter, mice received chemotherapy over a period of approximately 35 days and were subsequently followed up for 2 weeks. Whilst mice recovered well post-chemotherapy, further assessment is required into the late-effects of this model.

The development of this *in vivo* MB-equivalent chemotherapy regimen can be utilised for 1) investigation into the biological mechanisms underpinning late-effect onset, 2) a baseline model for the appraisal of pharmacological interventions, and 3) a baseline model for the comparison of new primary treatments with standard of care on survivorship outcomes. Moreover, as childhood MB survivors experience multimodal treatment, it is important to progress understanding of the late effects associated with receiving multimodal therapy. The development of this combination chemotherapy regimen provides the potential for future combination with an *in vivo* model of MB-radiotherapy, and appraisal of subsequent late-effects.

Chapter 7. Overarching summary and discussion

7.1. Summary of findings

There is an urgent need for the development of interventions to prevent or alleviate the late-effect burden faced by MB survivors, however their development has been hindered by a lack of appropriate model systems. An overarching summary of this thesis is shown in Figure 7.1. During this study an *in vivo* model system was developed that recapitulates MB radiotherapy delivery, dose and targeting at an equivalent developmental stage, with comprehensive longitudinal assessment. Mice received 37.5 Gy CRT with 48.75 Gy PFB via the SARRP and underwent comprehensive longitudinal follow up for over one year. Despite mice receiving high-dose cranial-irradiation, there were no deaths due to acute toxicities and they continued to grow at the same rate as non-irradiated controls (Chapter 3). Longitudinal assessment revealed that CRT induced frailty and deficits in physical functioning deficits early and which persisted over the life course, similar to the human disease (Chapter 3). Likewise, following cranial-irradiation, mice exhibited neurocognitive impairment; CRT mice were initially slower to learn, had impaired long-term memory function, and brain size was smaller. Interestingly, receipt of PFB did not induce a worse late-effect profile (Chapter 3). The development of this *in vivo* model of MB radiotherapy-induced late-effects provides a platform to assess the progression of late-effects and understand the mechanisms underpinning late-effect development.

Ex vivo biological assessments were conducted on tissue harvested approximately 1 year post-irradiation (Chapter 4.). RNA sequencing revealed CRT did not induce consistent widespread, global, transcriptional modifications and instead distinct pathways including interferon-alpha and -gamma response, epithelial-mesenchymal transition, and oestrogen response (early and late) were downregulated. Quantification of pro-inflammatory proteins, using IHC, showed higher abundance following CRT, though response was not dose dependent. Utilising a prebuilt epigenetic clock, predicted epigenetic age increased with chronological age, though this was more accurate in DNA from peripheral blood than brain tissue. CRT did not induce a significantly accelerated epigenetic age.

To understand the acute radiation insult response, human-equivalent radiation was delivered *in vitro* and the Luminex assay was utilised to develop a novel, multi-analyte assessment of molecular insult response to MB-equivalent radiation (Chapter 5.). Markers of inflammation increased 1-hour post-irradiation, and typically increased further at 48-hours. Increased

inflammation was expected and is thought to play a major role in the development of radiation-induced late effects.

Finally, to provide a preclinical platform for the future investigation of chemotherapy-induced late-effects, a MB-like chemotherapy regimen was developed (Chapter 6.). The appropriate scheduling/dosing regimen replicated the popular Packer-style chemotherapy. The final regimen struck the balance of inducing obvious insult (weight loss, poor condition, and frailty), but not too aggressive that it was intolerable.

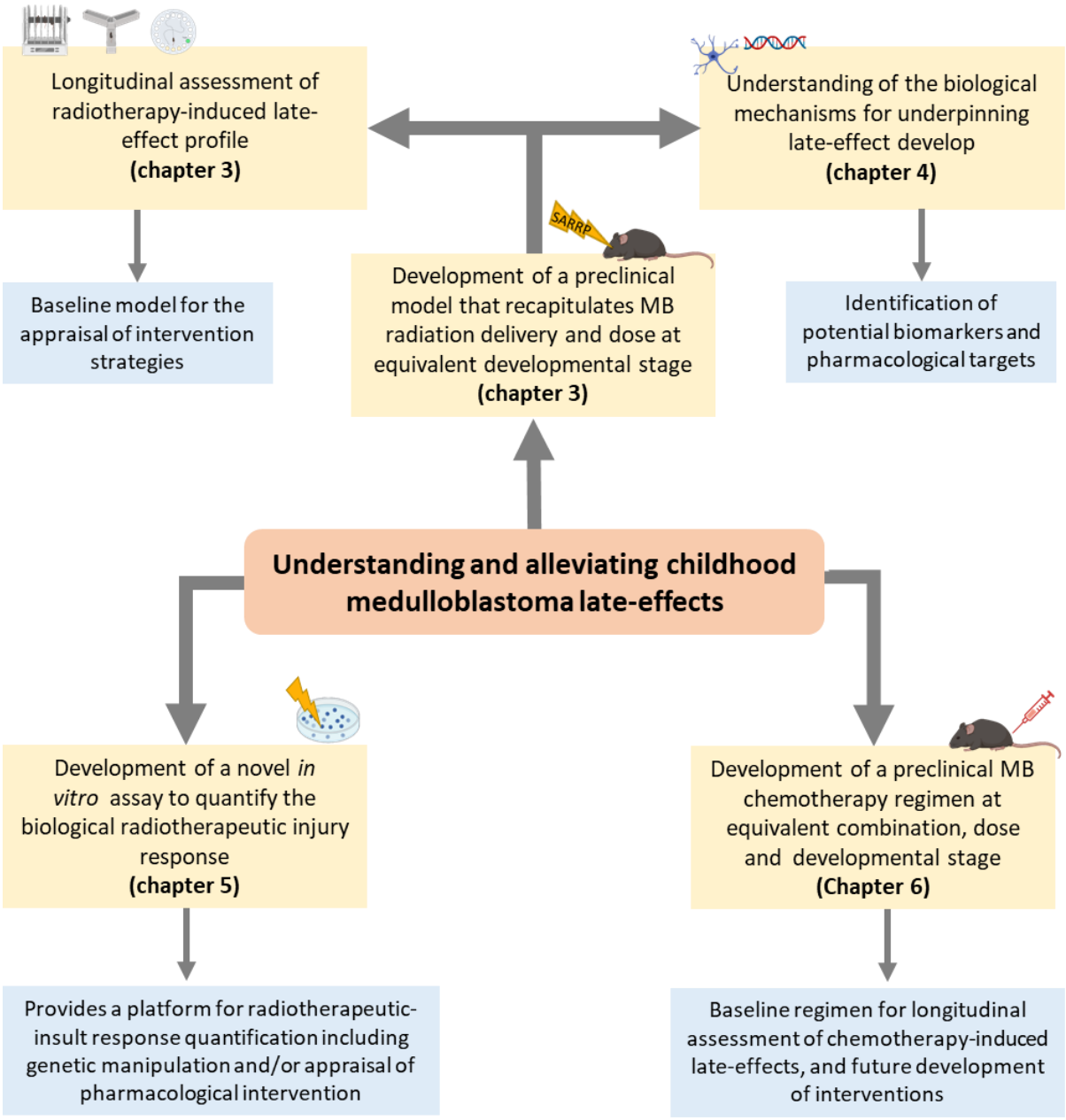

Figure 7.1. Overarching summary of the thesis.

7.2. Study strengths and limitations

7.2.1. In vivo modelling of MB cranial radiation, at a clinically-relevant dose, targeting regimen and developmental stage

Typically, studies have investigated the impact of cranial irradiation in rodent models through delivery of whole-head irradiation: the body is lead-shielded and the whole-head is exposed to the radiation (Wong-Goodrich *et al.*, 2010; Rodgers *et al.*, 2016; Ungvari *et al.*, 2017; de Guzman *et al.*, 2019; Tang *et al.*, 2019). However, delivery via this modality does not recapitulate childhood MB radiotherapy protocols; radiation delivery to the whole-head is not precise, non-target regions such as the mouth, ears and eyes are in the radiation field, and it is not possible to deliver the posterior fossa boost. The use of the SARRP enables precise delivery of X-ray radiation at a known intensity, with very minimal radiation received by non-target areas (<1mm precision) (Wong *et al.*, 2008). Through this precise targeting it was possible to deliver an additional boost dose to the posterior fossa (total dose equivalent to 49 Gy), mirroring the radiotherapy regimens experienced by childhood MB patients. The use of the SARRP to deliver high-dose cranial radiation is not novel to this study, however, previous SARRP-enabled studies typically used tumour-bearing adult mice and did not assess radiation-induced late-effects (Morrissy *et al.*, 2016; Nimmervoll *et al.*, 2018). Repeated anaesthesia, particularly at a young age, has been associated with neurotoxicity and poorer learning and memory in later life (Yon *et al.*, 2005; Murphy and Baxter, 2013; Bakri *et al.*, 2015). To ensure any observed deficits were a result of radiotherapeutic-insult, CRT mice were compared to a control group that received sham-irradiation; control mice were also anaesthetised and placed in the SARRP but did not receive any radiation.

A crucial novelty of this study is the combination of delivering a clinically-relevant, targeted radiation dose to mice at an equivalent developmental stage to childhood MB patients, which has been lacking in earlier studies (previously summarised in chapter 1.4 and Table 1.7). Most studies use adult mice, however, as a younger age during receipt of radiotherapy is often associated with a poorer late-effect profile (Mulhern *et al.*, 1989; Kiltie;Lashford and Gattamaneni, 1997; Jenkin;Danjoux and Greenberg, 1998), it is critical that *in vivo* models of MB radiotherapy-induced late-effects reflect the equivalent developmental age. Several studies have delivered cranial-irradiation in very young mice; however, young mice received a sub-clinically relevant dose and studies were often short and/or conducted limited

assessment of late-effects (Sándor *et al.*, 2014; Ruddy *et al.*, 2020; Yuen *et al.*, 2021). Within this novel model, no mice died from acute radiation-toxicity and body weight was equivalent to the sham-irradiation group over the course of the study. Therefore, this model strikes the balance of recapitulating childhood MB radiotherapy delivery at an appropriate developmental stage, whilst maintaining good survival rates.

7.2.2. Longitudinal assessment of physical functioning, frailty and neurocognitive performance, post-irradiation

Previous studies that model the late-effects of radiotherapeutic insult typically focus on a specific late-effects rather than the wider profile of late-effects experienced by childhood MB survivors (previously summarised in chapter 1.4 and Table 1.7). This newly developed model provides a comprehensive overview of the neurocognitive deficits, physical functioning and frailty that is induced following receipt of high-dose cranial radiation at a young age. Whilst endocrine impairment is a common late-effect experienced by childhood MB survivors who received cranial radiotherapy (Johnson *et al.*, 1994; Heikens *et al.*, 1998; Walter *et al.*, 1999; Ribi *et al.*, 2005; Frange *et al.*, 2009; Chevignard *et al.*, 2017), it was omitted from the profile of late-effects assessed in this study. Endocrine dysfunction is relatively well understood, and interventions are frequently used within the clinic (Johnson *et al.*, 1994; Heikens *et al.*, 1998; Walter *et al.*, 1999; Ribi *et al.*, 2005; Frange *et al.*, 2009; Chevignard *et al.*, 2017).

The development of late-effects can present and persist in the years following treatment, with others having a longer latency; adult survivors of childhood brain tumours develop numerous co-morbidities (Kahalley *et al.*, 2013; Salloum *et al.*, 2019; Dixon *et al.*, 2023) and become more frail over their life-course (Ness *et al.*, 2013). In addition to delivering clinically relevant, targeted radiation at a young age, another major novelty of this model is the longitudinal assessment whereby mice were assessed for over one year. Comprehensive longitudinal testing enables appraisal of late-effect progression throughout the life-course, however, is lacking in most studies. Typically, previous studies favour short term follow up, with those that conduct longer-term follow up focusing on a single specific late-effect (summarised in table 1.7). Whilst both Fielder *et al* and Ungvari *et al* did conduct a more comprehensive long-term follow-up of radiotherapeutic injury, this was not following the delivery of a clinically-relevant, targeted radiation dose to mice at an equivalent developmental stage to childhood MB patients (Ungvari *et al.*, 2017; Fielder *et al.*, 2019). In

this model, assessments were carried out from PND 97 to PND 394, from human-equivalent of early adulthood until middle-age (all timepoints are summarised in Table 3.2). A limitation of this model is the lack of a baseline/pre-irradiation assessment; however, this was not possible due to the travel restrictions in place during the COVID-19 pandemic.

Through comprehensive longitudinal assessment, the progression of late-effect development following MB-equivalent cranial radiation was characterised to provide a platform for the development of future interventions and surveillance strategies. Assessments were selected to cover the breadth of the late-effect profile, however, were typically wide-ranging and overlapped somewhat: for example, an animal with poor grip strength, would also perform worse of the hanging wire test. Therefore, to precisely measure key late-effects, additional testing methods would be required. Perhaps one of the most debilitating late-effects of cranial radiation is the lasting neurocognitive deficits with drastically reduce their quality of survivorship. Survivors often experience attention deficits, slower processing speed and impaired working memory which in turn results in poor psychosocial satisfaction, intellectual disability, low levels of academic attainment, and reduced independence in adulthood (Dennis *et al.*, 1996; Maddrey *et al.*, 2005; Chevignard *et al.*, 2017; Pazzaglia *et al.*, 2020). Neurocognitive function is typically assessed *in vivo* using maze-based tests that utilise a mouse's innate instinct to explore a novel environment. Y-maze and T-maze assess working memory by assessing the ability to enter novel arms, in mazes the shape of a 'T' and 'Y' respectively (Kraeuter;Guest and Sarnyai, 2019). The order of arm entry is recorded for a set time, and the proportion of novel arm choices provides the discrimination index (DI). It is generally assumed that a higher DI is due to better working memory, however environmental factors could also have an influence if the result if the test is not carried out correctly (Li *et al.*, 2018; Kraeuter;Guest and Sarnyai, 2019; Yoshizaki;Asai and Hara, 2020). The Y maze is most common neurocognitive test used *in vivo*, but other cognitive tests include Barnes maze, Morris water maze, and the open field test (Barnes, 1979; Sousa;Almeida and Wotjak, 2006; Vorhees and Williams, 2006). Morris water maze and the Barnes maze assess spatial learning and working memory by training the mouse to locate a target hole/platform and assessing either the ability to retain learned behaviour or performance in the novel object recognition test (Barnes, 1979; Ennaceur and Meliani, 1992; Vorhees and Williams, 2006; Berta Sunyer *et al.*, 2007). Whilst these assessments provide an insight into overall neurocognitive functioning

such a learning and memory, they are unable to discriminate specific neurocognitive domains such as attention, processing speed and executive function. A potential refinement of the model developed within this thesis could include assessments capable of precisely delineating neurocognitive domains. The Bussey-Saksida Touch Screen Chamber system uses human-equivalent CANTAB-based tasks in rodents to assess subdomains of neurocognitive impairment, and is directly comparable to the human CANTAB battery (Horner *et al.*, 2013)positioning it optimally for *in vivo* translational studies.

In vivo assessments of neurocognition and physical functioning can be influenced by behaviour, environmental and additional factors (Sousa;Almeida and Wotjak, 2006). For example, different strains and sexes can exhibit behavioural differences which can ultimately influence performance outcomes. To minimise variability, this model was developed in one sex of a single inbred strain (male C57Bl/6), however future development with both sexes and the inclusion of addition strains may provide a more comprehensive representation of natural variability. Moreover, environmental factors such as loud or high frequency sounds, strong smells, single-housing, and the timing of the tests can also influence assessment outcomes, and therefore were minimised/kept consistent within this study. The researcher conducting the test can have a large impact on results (Sousa;Almeida and Wotjak, 2006). As it is best practise, the same experimenter was maintained throughout the study (myself), which is particularly important when results are subjective, such as in behavioural assessments (Sousa;Almeida and Wotjak, 2006). Additional limitations of this model development include small group sizes (n=12 per treatment). Any animal work was completed under the guiding ethical principles of the 3Rs (reduction, replacement and refinement) (Russell;Burch and Hume, 1959). Therefore, groups were small to avoid the unnecessary use of additional animals, whilst maintaining power to detect significant changes. However, external factors related to animal welfare (e.g., mice fighting) further reduced the group sizes. For increased power during statistical analysis, the CRT and CRT+PFB groups were combined following the conclusion of cranial radiation-induced impairments were independent of receipt of PFB.

7.2.3. Understanding the biological response to radiotherapeutic-insult

The biological mechanisms underpinning late-effect onset are relatively undefined. Cranial irradiation damages healthy brain tissue through mechanisms such as inflammation, oxidative stress, DNA damage, and ultimately leads to cell death/senescence, reduced neurogenesis, damage to vasculature, demyelination and white matter necrosis (Zhao;Diz and Robbins, 2007; Moravan *et al.*, 2011; Greene-Schloesser *et al.*, 2012; Baskar *et al.*, 2014; Lumniczky;Szatmári and Sáfrány, 2017).

7.2.3.1. The late biological response

To investigate the late molecular response to MB-equivalent cranial radiation, *ex vivo* analysis was conducted on brain and peripheral blood collected from the *in vivo* model system that recapitulates MB radiotherapy delivery, dose and targeting at an equivalent developmental stage. A summary of the samples used in the *ex vivo* analysis is shown in Table 7.1.

Technique	Sample type	Collection timepoint (~PND)	Treatment group	n
RNAseq	Cerebellum	394	CRT+PFB	11
			Sham	12
IHC	Cerebellum	394	CRT	3
			CRT+PFB	3
			Sham	3
	Hippocampus	394	CRT	3
			CRT+PFB	3
			Sham	3
DNA methylation	Peripheral blood	150	CRT+PFB	11
			Sham	7
	Cerebellum	394	CRT+PFB	11
			Sham	7

Table 7.1. Summary of ex vivo biology samples. Samples from the brain (cerebellum and hippocampus) and peripheral blood were collected from mice following CRT, CRT+PFB or sham-irradiation, for RNA-sequencing (RNAseq), immunohistochemistry (IHC) and DNA methylation array (DNA methylation).

Assessment of transcriptional modifications approximately one-year post-irradiation showed decreased expression of interferon-alpha and -gamma response, epithelial-mesenchymal transition, and oestrogen response (early and late) pathways. Interferon-alpha and -gamma response pathways have been previously associated with neuroinflammation following radiation and brain injury, yet these pathways are typically over expressed. Whereas, in this model, at one-year post-irradiation, both pathways were downregulated (negatively enriched) compared to sham-irradiation. Epithelial-mesenchymal transition has previously been shown to occur following radiation, and is induced through various signalling pathways including TGF-β, tyrosine kinase, WNT and SMO, as well as inflammation and hypoxia (Jung *et al.*, 2007; Lamouille;Xu and Derynck, 2014; Liu *et al.*, 2014). Though at one-year post-irradiation EMT signalling was downregulated in the CRT+PFB group, compared to the sham group. Oestrogen signalling plays a role in regulating many physiological functions, including reproduction, bone density, brain function and control of inflammation (Liang and Shang, 2013). Within the brain, oestrogen signalling has a neuroprotective role, and has been linked to learning, memory and behaviour through modulation of inflammation and oxidative stress, increasing expression growth factors and promoting cell survival (Wallace *et al.*, 2006; Mitra *et al.*, 2023). In this model, at 12 months post-CRT+PFB, both early and late oestrogen signalling was downregulated compared to sham-irradiated mice. Mice that received CRT also exhibited impaired memory function, suggesting that reduced oestrogen signalling may have played a role in the development of neurocognitive deficits. However, as the appraisal of transcriptional modification was conducted at a single, late timepoint, when neurocognitive deficits had already developed, it is not possible to conclude a causative role of oestrogen signalling, and further assessment is required. Characterising the transcriptional modifications longitudinally from the initial radiation-insult until after the development of late-effects could highlight key time-periods where pharmacological intervention approaches may be most suitable. To investigate the late transcriptional modifications that occurred following the highest dose of radiation, RNAseq was analysed from RNA extracted from the cerebellum following CRT+PFB and compared to sham-irradiation. However, further analysis should be conducted on the CRT only group to explore any dose-dependent response within the cerebellum. Moreover, it may not be possible to generalise the findings of one substructure to all brain regions; brain substructures including the hippocampus, corpus callosum and frontal white matter exhibit increased sensitivity to radiation and

neurocognitive impairment (Acharya *et al.*, 2022), and therefore full characterisation would require further transcriptional analysis of each major substructure.

Cranial radiation induces acute and sustained neuroinflammation; inflammation initially peaks in the acute response, however, can be sustained for over 1 year (Moravan *et al.*, 2011; Han *et al.*, 2016). To explore sustained neuroinflammation, the pro-inflammatory response was assessed in the cerebellum and hippocampus one-year post cranial-irradiation (CRT only, CRT+PFB or sham-irradiation; summarised in Table 7.1), using immunohistochemistry staining. Again, overall abundance was not consistently higher one year following CRT only or CRT+PFB compared to sham-irradiation, though abundance of GFAP, a marker of activated astrocytes, was higher following CRT only than sham-irradiation. During CNS injury and disease astrocytes undergo functional remodelling and can become activated into either neurotoxic or neuroprotective phenotypes. Typically following an insult, cytokines released from activated microglia induce activation of the neurotoxic astrocyte phenotype, resulting in reduced neuronal survival, synaptogenesis, induced neuronal and oligodendrocyte cell death (Liddelow *et al.*, 2017). Astrocytes play an important role in synaptic plasticity within the hippocampus, which is imperative for acquisition of learning and memory (Wang *et al.*, 2021). Interestingly, abundance of GFAP was higher in the hippocampus than the cerebellum following CRT+PFB, suggesting a higher presence of activated astrocytes, however the CRT only and sham groups did not follow this trend, and further investigation is required. In this study, abundance of pro-inflammatory proteins in the cerebellum and hippocampus one year after CRT only, CRT+PFB or sham-irradiation, enabled assessment in both a dose-dependent and substructure-specific context, however, this was limited due to the small sample size. The quantification of a subset of pro-inflammatory proteins, in combination with the RNAseq analysis, describes the altered molecular pathways at one-year post-irradiation. However, as significant deficits were present at this time, additional earlier timepoints throughout the life course are required to fully decipher the biological mechanisms that underpin the development and progression of late-effects.

As discussed previously, survivors of childhood cancers experience increased frailty and age prematurely as a result of their cancer treatment (Oeffinger *et al.*, 2006; Diller *et al.*, 2009a; Ness *et al.*, 2013). Changes in DNA methylation patterns occur with normal ageing and have been associated with premature aging and age-related diseases and may be a useful

biomarker for overall health (Mozhui and Pandey, 2017; Kling;Wenger and Carén, 2020). The characterisation of such patterns has led to the development of epigenetic clocks, that aim to predict epigenetic age; a higher estimated epigenetic age acceleration (EAA) has been previously seen in childhood cancer survivors and linked to prior treatment with radiotherapy or alkylating chemotherapy (Field *et al.*, 2018; Salameh;Bejaoui and El Hajj, 2020; Qin *et al.*, 2021). In this study, EAA was assessed using DNA samples taken from the cerebellum and peripheral blood following either CRT+PFB or sham-irradiation over two timepoints (a sample summary is shown in Table 7.1). The mean epigenetic age calculated from the cerebellum (harvested a ~PND 394, approximately one-year post-irradiation) was higher following CRT+PFB than sham-irradiation, though this was not significant, likely due to the high variability in predicted ages. Inaccurate predictions of EAA may occur depending on the types of tissue used during the development of the epigenetic clock; differences in tissue-specific methylation signatures may account for the variance observed between peripheral blood and cerebellum EAA (Zhou *et al.*, 2022). This clock was previously developed using 26 tissue and cell types (including foetal brain, frontal lobe brain and hind brain) and therefore was expected to provide an accurate estimation of epigenetic age across various tissue types. However, the brain has a higher abundance of methylated DNA than most tissues (Ehrlich *et al.*, 1982), and perhaps a generic clock developed with multiple tissue types is not the most suitable for estimating age specifically within the brain. The use of EAA has potential as a future biomarker for identifying premature ageing prior to the manifestation of physical symptoms, however the use of cerebellum DNA for this purpose is not feasible.

The use of peripheral blood offers a relatively non-invasive option for longitudinal appraisal of EAA, to identify survivors at risk of developing premature ageing symptoms. In this study, EAA predicted from peripheral blood was estimated to be close to the chronological age and was considerably less variable than EAA obtained from the cerebellum. There was no significant difference in EAA between the CRT+PFB and sham groups, suggesting an equivalent epigenetic age. However, by this age, the CRT group were showing physical signs of premature ageing and were significantly more frail than sham-irradiated mice. Whilst the use of peripheral blood offers a relatively non-invasive approach for longitudinal surveillance, further investigation is required; within this *in vivo* model of radiotherapy-induced late-effects, this epigenetic clock did not detect a significant difference in EAA, despite the

presence of physical symptoms of premature ageing. This limitation may be due to i) a lack of sensitivity of the epigenetic clock used or ii) cranial-irradiation may not invoke systemic epigenetic changes. Both of which may be explored further using alternative epigenetic clocks, and investigation of individual CpG sites both within the radiation field and systemically. However, EAA in peripheral blood was only assessed at one timepoint, and further appraisal of additional timepoints and with larger group sizes should be conducted to fully explore the utility as a potential biomarker.

7.2.3.2. The early biological response

The biological mechanisms underpinning the development of radiotherapy-induced late-effects remain relatively undefined. To investigate the early response to a clinically-relevant radiotherapeutic-insult, a novel *in vitro* assay was developed utilising the Luminex assay. The Luminex® Discovery Assay, is a bead-based immunoassay that precisely measures multiple analytes in one sample. Whilst the enzyme-linked immunosorbent assay (ELISA) is typically considered the gold-standard for quantification of single biomarkers, the Luminex Discovery assay supports detection of up to 100 analytes simultaneously. The custom panel of 57 analytes covered the inflammatory and SASP response indicated in the literature to be involved in radiotherapeutic insult response. The early response following exposure to a clinically relevant 30Gy irradiation dose, was characterised using the novel assay. Whilst this assay was developed in a single, non-brain-derived cell line, several potentially interesting proteins were significantly overexpressed compared to non-irradiated controls (as discussed in chapter 5.5), showing promising utility for this model. For example, FSTL1 regulates cytokine production and proliferation of inflammatory cells, is highly expressed within the brain, and has been linked to impaired neurodevelopment through the increasing astrocyte activation (Mattiotti *et al.*, 2018; Yamada *et al.*, 2018; Li *et al.*, 2020). BDNF is primarily associated with promoting neuronal survival, growth and maintaining synaptic plasticity and cognition (Zhao *et al.*, 2017), and is thought to protect against hypoxia and inflammation (Prakash and Martin, 2014; Hartman *et al.*, 2015; Charlton *et al.*, 2023). In the MRC-5 cells, levels of BDNF increased at 48 hours post-irradiation suggesting this protective response may not occur immediately, though additional timepoints are required to assess the exact timing of this response. Following the initial development of this assay, its use in more biologically relevant cells lines will further understanding of the early biological response and provide a

platform for the future identification of key pathways and appraisal potential pharmacological interventions.

7.2.4. Developing a clinically-relevant regimen of MB chemotherapy, in vivo

Adjuvant chemotherapy is currently recommended for all childhood MB patients regardless of risk status (Tait *et al.*, 1990; Millard and De Braganca, 2016). Many survivors of childhood cancers are faced with chemotherapy-induced late-effects, including ototoxicity, peripheral neuropathy, cardiotoxicity, and secondary malignant neoplasms (Gurney *et al.*, 2003; Diller *et al.*, 2009a). However, the development of such late-effects is not well understood and pose a large challenge within the cancer research field; understanding and preventing chemotherapy-induced neurotoxicity and neuropathy is a theme of the 2023 Cancer Grand Challenges. Understanding the development of chemotherapy-induced late-effects is currently hindered by a lack of appropriate model systems that recapitulate standard-of-care paediatric MB chemotherapy regimens and longitudinally assess the subsequent late-effect profile. This is likely in part due to the complexity and variation of chemotherapy regimens between treatment centres. Previous *in vivo* rodent model systems typically assess i) tumour response to chemotherapy in combination with a novel pharmacological agent (Morfouace *et al.*, 2014; Endersby *et al.*, 2021; Mañas *et al.*, 2022), ii) late-effects induced from a single chemotherapeutic drug (Yang *et al.*, 2010; Geisler *et al.*, 2016; Janelsins *et al.*, 2016; Zhou;Kavelaars and Heijnen, 2016; Chiu *et al.*, 2017; Crouch *et al.*, 2017; Liu *et al.*, 2018) and/or iii) use non-MB standard-of care chemotherapy combinations (Bisen-Hersh;Hineline and Walker, 2013; Nimmervoll *et al.*, 2018). The 'Packer Regimen' is perhaps the most widely used MB chemotherapy regimen and consists of two alternating regimens of which regimen B is most commonly used (comprising of cisplatin, vincristine, and cyclophosphamide; details are provided in Table 6.1). There is currently no evidence of mouse models in the literature that recapitulate Packer regimen B chemotherapy.

A close-to-human, Packer-style chemotherapy regimen was developed in age-equivalent mice. The developed chemotherapy regimen drew heavily on a previously published *in vivo* ependymoma chemotherapy regimen by Nimmervoll et al, consisting of etoposide, cisplatin, vincristine (details are provided in Table 6.2) (Nimmervoll et al., 2018). Dosing intensities were gradually increased up to a clinically-relevant dose, though further pharmacokinetic (PK) analysis would be required to fully decipher the exact blood plasma concentrations.

Childhood cancer survivors are often more frail than their siblings, which has, in part, been associated with receipt of high doses of chemotherapy (Hayek *et al.*, 2020). Following recovery from dosing regimen 4, increased frailty was apparent, in comparison to earlier iterations. As previously discussed in Chapter 6.5, previous *in vivo* studies have shown cisplatin, vincristine and cyclophosphamide to induce a variety of late-effects when administered as single agents (e.g. ototoxicity, peripheral neuropathy and neurocognitive impairment), however further appraisal of the late-effect profile following this combination of chemotherapy is required. The development of this *in vivo* MB-equivalent chemotherapy regimen provides the basis for i) further investigation of the biological mechanisms underpinning late-effect development, ii) a baseline model for the appraisal of pharmacological interventions, and iii) a baseline model for the comparison of new primary treatments with standard of care on survivorship outcomes, and iv) future development of multimodal *in vivo* MB treatment models.

7.3. Future work

7.3.1. Pharmacological interventions to ameliorate late-effect development

Currently there are no pharmacological interventions routinely given to prevent the development of treatment-induced late-effects. As many MB survivors experience attention deficits and reduced processing speed, one potential therapeutic intervention could be the use of stimulants. Stimulants have been used to treat attention deficit hyperactivity disorder (ADHD) since the 1990s; methylphenidate is most commonly prescribed (Gadow, 1992; Conklin *et al.*, 2010a). Methylphenidate improves attention and concentration in approximately 70% of children with ADHD, through inhibition of dopamine reuptake (Safer;Zito and Fine, 1996; Conklin *et al.*, 2010a). Several small trials have assessed the use of methylphenidate in childhood cancer survivors, showing significant improvements in attention (Thompson *et al.*, 2001; Mulhern *et al.*, 2004; Conklin *et al.*, 2010b). A small scale pilot study assessed the effect on brain tumour survivors with learning impairments. There were significant improvements in processing speed, attention regulation, social skills academic ability and QoL (Watts *et al.*, 2018). Methylphenidate is showing great promise and may be a potential new adjuvant therapeutic, however the underlying mechanisms of actions remain unclear. The mechanistic effect of methylphenidate, alone and in combination with other drugs, requires further investigation to form a basis for future larger clinical trials.

Understanding the underlying mechanisms underpinning late-effect onset would enable the development of pharmacological interventions to target the specific pathways involved. For example, chronic inflammation, senescence, SASP and ROS production are thought to be involved in the onset of radiation-induced late-effects such as neurocognitive impairment and reduced physical functioning (Bentzen, 2006; Begg;Stewart and Vens, 2011; Moravan *et al.*, 2011; Montay-Gruel *et al.*, 2019). Drugs targeted to these key pathways may reduce late-effects in childhood MB survivors; previous studies have shown senolytic and senostatic drugs reduce premature frailty in preclinical mouse models (Short *et al.*, 2019; Kirkland and Tchkonia, 2020). Metformin, widely used to treat type-2 diabetes, has been suggested to have senolytic action (Chen *et al.*, 2016; Śmieszek *et al.*, 2017). In mouse models, metformin may promote neurogenesis and enhances spatial memory (Luo *et al.*, 2012); metformin is thought to have an antioxidant role and reduce radiation- and chemotherapy-induced DNA damage and ROS production in healthy cells (Xu *et al.*, 2015; Mortezaee *et al.*, 2019; Tohamy *et al.*, 2021). In childhood brain tumour survivors, metformin has shown to improve radiation-

induced neurocognitive deficits, such as working memory, in a small trial (Ayoub *et al.*, 2020), though further investigation is required. Additionally, as radiation induces neurocognitive decline through reduced neurogenesis, therapies that can prevent or induce neurogenesis may pose a suitable therapeutic option. When used *in vivo,* lithium increased proliferation of neural progenitor cell, and rescued radiation-induced cell cycle arrest (Zanni *et al.*, 2021). Moreover, following radiation, mice treated with lithium had better neurocognitive functioning, including learning and memory, and hippocampal neurons were protected from apoptosis (Yazlovitskaya *et al.*, 2006; Zhou *et al.*, 2017).

However, currently there are no pharmacological interventions routinely given to prevent the development of treatment-induced late-effects. Due to a previous lack of *in vivo* models that can recapitulate MB treatment and subsequent late-effect profile, appraisal of such interventions was not possible. Through the development of an *in vivo* model that recapitulates MB radiotherapy delivery and late-effect profile, the appraisal of such interventions is now possible.

7.3.2. Investigation of injury-induced white matter remodelling

Neurocognitive decline as a result of cranial irradiation is associated with a reduction in white matter volume, with MB patients having decreased volume when compared to patients with low grade astrocytoma (who do not receive radiotherapy) (Mulhern *et al.*, 1999). Mulhern *et al* found that a lower IQ was associated with having lower white matter volume than matched controls, with white matter volume showing a significant positive correlation with both verbal IQ (VIQ) and full-scale IQ (FSIQ) (Mulhern *et al.*, 1999). Additionally, Plas *et* al showed that the relationship between white matter remodelling and neurocognition was not exclusive to those that received radiotherapy; acute lymphoblastic leukaemia (ALL) survivors who were treated with chemotherapy only all had poor working memory index, which was significantly correlated with the volume of the amygdala, thalamus and corpus callosum, as well as reduced white and grey matter (van der Plas *et al.*, 2017). Nieman *et al* showed that survivors who receive cranial radiation had an initial decline in white matter volume, with the hippocampus and olfactory bulb also showing significant decline. After the initial decline, growth then continues at the normal rate, but does not reach that of healthy controls, except for the olfactory bulb which continues to grow at a slower rate (Nieman *et al.*, 2015). They also showed that the volumetric changes that occur in human brain tumour survivors are recapitulated in mice (de Guzman *et al.*, 2015; Nieman *et al.*, 2015).

The development of newer techniques has shown that, in addition to volumetric changes, changes to the functional composition of white matter are also evident. Diffusion tensor imaging (DTI) assesses subtle changes within structures to calculate fractional anisotropy (FA). The FA is based on the ability for ion diffusion and scored on a scale of 0-1 (0: isotropic movement of water, e.g. CSF; 1: anisotropic movement of water, e.g. fibre bundles) (Ment;Scheinost and Constable, 2017). Changes in FA have also been linked with reduced neurocognition in childhood brain tumour survivors (Uh *et al.*, 2021). Similarly, in *in vivo* models, following cranial radiation, significant cognitive decline was associated with structural changes including myelin integrity and neuronal network organisation, as well as decreased FA (Tang *et al.*, 2019). CD3 T-cells and dendritic cells have been shown to be selectively recruited to white matter areas with radiotherapeutic injury in both *in vivo* ageing models and cranial irradiation models, perhaps explaining the white matter remodelling seen in MB survivors (Moravan et al., 2011, Stichel and Luebbert, 2007).

7.3.3. Modelling MB multi-modal treatment-induced late-effects

Childhood MB treatment is multimodal, typically consisting of surgery, radiotherapy, and chemotherapy. Therefore, to accurately model the full late-effect profile of paediatric MB survivors, a preclinical model should consider all modalities of treatment as well as the subsequent late-effect profile. However, such models are lacking. Most studies that replicate MB treatment typically use tumour-bearing mice, whereby the goal is to investigate novel therapeutics on primary tumours, rather than to consider the late-effect profile, consequently, there are no published models that effectively recapitulate all stages of brain tumour treatment, at clinically relevant doses. Nimmervoll *et al* established a mouse model of supratentorial ependymoma and choroid plexus carcinoma; mice were orthotopically implanted with cell lines and then underwent surgical resection of the tumours, received 54 Gy cranial irradiation, and then treated with gemcitabine (Nimmervoll et al., 2018). Unfortunately, no assessments of late-effects were conducted as this platform was used for the assessment of novel treatment.

The development of an *in vivo* model that recapitulates MB radiotherapy delivery and late-effect profile (discussed in Chapter 3.) together with a clinically-relevant regimen of MB chemotherapy (discussed in Chapter 6.), provides the potential for the appraisal of combination chemoradiation associated late-effects. To fully recapitulate the late-effect profile of multimodal MB treatment regimens, the optimal *in vivo* model would involve

surgical resection of an orthotopic MB, followed by radiotherapy and chemotherapy at clinically relevant doses. However, one barrier to this is the different radio-sensitivities between different strains; mouse strains such as C57BL/6 can withstand high doses of radiation, whereas immunocompromised strains, which are often required for modelling tumours, are partially sensitive to radiotherapeutic insult. Saki *et al* showed that immunocompromised NSG (NOD-scid IL2Rgamma-null) mice, typically used in tumour-bearing studies, died within 8 days of receiving 4 Gy whole-body irradiation, thus making long-term follow up of clinically-relevant radiation in tumour bearing mice difficult (Saki *et al.*, 2020). Consequently, there are currently no models that recapitulate the late-effect profile following multimodal childhood MB therapy.

The successful development of an *in vivo* model that recapitulates MB radiotherapy (delivery, dose and targeting) at an equivalent developmental stage, coupled with comprehensive longitudinal assessment of MB radiotherapy-induced late-effects, provides a platform to further understand late effect development, and the appraisal of intervention strategies for their amelioration (Castle *et al.*, 2024).

Chapter 8. References

Acharya, S., Guo, Y., Patni, T., Li, Y., Wang, C., Gargone, M., Ashford, J.M., Wilson, L., Faught, A., Reddick, W.E., Patay, Z., Gajjar, A., Conklin, H.M. and Merchant, T.E. (2022) 'Association Between Brain Substructure Dose and Cognitive Outcomes in Children With Medulloblastoma Treated on SJMB03: A Step Toward Substructure-Informed Planning', *J Clin Oncol*, 40(1), pp. 83-95.
Adkins, D.L., Ferguson, L., Lance, S., Pevtsov, A., McDonough, K., Stamschror, J., Jones, T.A. and Kozlowski, D.A. (2015) 'Combining Multiple Types of Motor Rehabilitation Enhances Skilled Forelimb Use Following Experimental Traumatic Brain Injury in Rats', *Neurorehabil Neural Repair*, 29(10), pp. 989-1000.
Airaksinen, M.S. and Saarma, M. (2002) 'The GDNF family: Signalling, biological functions and therapeutic value', *Nature Reviews Neuroscience*, 3(5), pp. 383-394.
Al Shoyaib, A., Archie, S.R. and Karamyan, V.T. (2019) 'Intraperitoneal Route of Drug Administration: Should it Be Used in Experimental Animal Studies?', *Pharm Res*, 37(1), p. 12.
Anderson, V., Godber, T., Smibert, E. and Ekert, H. (1997) 'Neurobehavioural sequelae following cranial irradiation and chemotherapy in children: an analysis of risk factors', *Pediatr Rehabil*, 1(2), pp. 63-76.
Armenian, S.H. and Robison, L.L. (2013) 'Childhood cancer survivorship: an update on evolving paradigms for understanding pathogenesis and screening for therapy-related late effects', *Curr Opin Pediatr*, 25(1), pp. 16-22.
Armstrong, G.T., Jain, N., Liu, W., Merchant, T.E., Stovall, M., Srivastava, D.K., Gurney, J.G., Packer, R.J., Robison, L.L. and Krull, K.R. (2010) 'Region-specific radiotherapy and neuropsychological outcomes in adult survivors of childhood CNS malignancies', *Neuro Oncol*, 12(11), pp. 1173-86.
Armstrong, G.T., Liu, Q., Yasui, Y., Huang, S., Ness, K.K., Leisenring, W., Hudson, M.M., Donaldson, S.S., King, A.A., Stovall, M., Krull, K.R., Robison, L.L. and Packer, R.J. (2009) 'Long-term outcomes among adult survivors of childhood central nervous system malignancies in the Childhood Cancer Survivor Study', *J Natl Cancer Inst*, 101(13), pp. 946-58.
Aston, W.J., Hope, D.E., Nowak, A.K., Robinson, B.W., Lake, R.A. and Lesterhuis, W.J. (2017) 'A systematic investigation of the maximum tolerated dose of cytotoxic chemotherapy with and without supportive care in mice', *BMC Cancer*, 17(1), p. 684.
Avula, S., Mallucci, C., Kumar, R. and Pizer, B. (2015) 'Posterior fossa syndrome following brain tumour resection: review of pathophysiology and a new hypothesis on its pathogenesis', *Childs Nerv Syst*, 31(10), pp. 1859-67.
Ayoub, R., Ruddy, R.M., Cox, E., Oyefiade, A., Derkach, D., Laughlin, S., Ades-aron, B., Shirzadi, Z., Fieremans, E., MacIntosh, B.J., de Medeiros, C.B., Skocic, J., Bouffet, E., Miller, F.D., Morshead, C.M. and Mabbott, D.J. (2020) 'Assessment of cognitive and neural recovery in survivors of pediatric brain tumors in a pilot clinical trial using metformin', *Nature Medicine*, 26(8), pp. 1285-1294.
Bailey, S., André, N., Gandola, L., Massimino, M., Rutkowski, S. and Clifford, S.C. (2022) 'Clinical Trials in High-Risk Medulloblastoma: Evolution of the SIOP-Europe HR-MB Trial', *Cancers (Basel)*, 14(2).
Bailey, S., Jacobs, S., Kourti, M., Massimino, M., Andre, N., Doz, F., Dufour, C., Vennarini, S., Padovani, L., Aquilina, K., Thomale, U., Joshi, A., Pietsch, T., Avula, S., Morana, G., Rutkowski, S., Pizer, B. and Clifford, S.C. (2025) 'Medulloblastoma therapy: Consensus treatment recommendations from SIOP-Europe and the European Reference Network', *EJC Paediatric Oncology*, 5, p. 100205.
Bakish, J., Hargrave, D., Tariq, N., Laperriere, N., Rutka, J.T. and Bouffet, E. (2003) 'Evaluation of dietetic intervention in children with medulloblastoma or supratentorial primitive neuroectodermal tumors', *Cancer*, 98(5), pp. 1014-1020.
Bakri, M.H., Ismail, E.A., Ali, M.S., Elsedfy, G.O., Sayed, T.A. and Ibrahim, A. (2015) 'Behavioral and emotional effects of repeated general anesthesia in young children', *Saudi J Anaesth*, 9(2), pp. 161-6.
Banyal, A., Tiwari, S., Sharma, A., Chanana, I., Patel, S.K.S., Kulshrestha, S. and Kumar, P. (2023) 'Vinca alkaloids as a potential cancer therapeutics: recent update and future challenges', *3 Biotech*, 13(6), p. 211.
Barnes, C.A. (1979) 'Memory deficits associated with senescence: a neurophysiological and behavioral study in the rat', *J Comp Physiol Psychol*, 93(1), pp. 74-104.

Baskar, R., Dai, J., Wenlong, N., Yeo, R. and Yeoh, K.W. (2014) 'Biological response of cancer cells to radiation treatment', *Front Mol Biosci*, 1, p. 24.
Batista, M.L., Jr., Lopes, R.D., Seelaender, M.C. and Lopes, A.C. (2009) 'Anti-inflammatory effect of physical training in heart failure: role of TNF-alpha and IL-10', *Arq Bras Cardiol*, 93(6), pp. 643-51, 692-700.
Baumann, B.C., Benci, J.L., Santoiemma, P.P., Chandrasekaran, S., Hollander, A.B., Kao, G.D. and Dorsey, J.F. (2012) 'An integrated method for reproducible and accurate image-guided stereotactic cranial irradiation of brain tumors using the small animal radiation research platform', *Transl Oncol*, 5(4), pp. 230-7.
Beera, K.G., Li, Y.Q., Dazai, J., Stewart, J., Egan, S., Ahmed, M., Wong, C.S., Jaffray, D.A. and Nieman, B.J. (2018) 'Altered brain morphology after focal radiation reveals impact of off-target effects: implications for white matter development and neurogenesis', *Neuro Oncol*, 20(6), pp. 788-798.
Begg, A.C., Stewart, F.A. and Vens, C. (2011) 'Strategies to improve radiotherapy with targeted drugs', *Nat Rev Cancer*, 11(4), pp. 239-53.
Belcher, E.K., Sweet, T.B., Karaahmet, B., Dionisio-Santos, D.A., Owlett, L.D., Leffler, K.A., Janelsins, M.C., Williams, J.P., Olschowka, J.A. and O'Banion, M.K. (2020) 'Cranial irradiation acutely and persistently impairs injury-induced microglial proliferation', *Brain Behav Immun Health*, 4, p. 100057.
Belka, C., Budach, W., Kortmann, R.D. and Bamberg, M. (2001) 'Radiation induced CNS toxicity--molecular and cellular mechanisms', *Br J Cancer*, 85(9), pp. 1233-9.
Bentzen, S.M. (2006) 'Preventing or reducing late side effects of radiation therapy: radiobiology meets molecular pathology', *Nat Rev Cancer*, 6(9), pp. 702-13.
Berta Sunyer, Sudarshan Patil, Harald Höger and Lubec, G. (2007) 'Barnes maze, a useful task to assess spatial reference memory in the mice', *Protocol Exchange*.
Bisen-Hersh, E.B., Hineline, P.N. and Walker, E.A. (2013) 'Effects of Early Chemotherapeutic Treatment on Learning in Adolescent Mice: Implications for Cognitive Impairment and Remediation in Childhood Cancer Survivors', *Clinical Cancer Research*, 19(11), pp. 3008-3018.
Bloom, H.J. (1982) 'Medulloblastoma in children: increasing survival rates and further prospects', *Int J Radiat Oncol Biol Phys*, 8(11), pp. 2023-7.
Bothwell, S.W., Janigro, D. and Patabendige, A. (2019) 'Cerebrospinal fluid dynamics and intracranial pressure elevation in neurological diseases', *Fluids and Barriers of the CNS*, 16(1), p. 9.
Bouët, V., Freret, T., Toutain, J., Divoux, D., Boulouard, M. and Schumann-Bard, P. (2007) 'Sensorimotor and cognitive deficits after transient middle cerebral artery occlusion in the mouse', *Exp Neurol*, 203(2), pp. 555-67.
Brain Basics: Know Your Brain (2025). Available at: https://www.ninds.nih.gov/health-information/public-education/brain-basics/brain-basics-know-your-brain#:~:text=The%20brain%20can%20be%20divided,as%20respiration%20and%20heart%20rate.
Bray, N.W., Smart, R.R., Jakobi, J.M. and Jones, G.R. (2016) 'Exercise prescription to reverse frailty', *Appl Physiol Nutr Metab*, 41(10), pp. 1112-1116.
Brière, M.E., Scott, J.G., McNall-Knapp, R.Y. and Adams, R.L. (2008) 'Cognitive outcome in pediatric brain tumor survivors: delayed attention deficit at long-term follow-up', *Pediatr Blood Cancer*, 50(2), pp. 337-40.
Broniscer, A., Ke, W., Fuller, C.E., Wu, J., Gajjar, A. and Kun, L.E. (2004) 'Second neoplasms in pediatric patients with primary central nervous system tumors: the St. Jude Children's Research Hospital experience', *Cancer*, 100(10), pp. 2246-52.
Brook, I. (2020) 'Late side effects of radiation treatment for head and neck cancer', *Radiat Oncol J*, 38(2), pp. 84-92.
Brown, W.R., Blair, R.M., Moody, D.M., Thore, C.R., Ahmed, S., Robbins, M.E. and Wheeler, K.T. (2007) 'Capillary loss precedes the cognitive impairment induced by fractionated whole-brain irradiation: a potential rat model of vascular dementia', *J Neurol Sci*, 257(1-2), pp. 67-71.
Bui, T.M., Wiesolek, H.L. and Sumagin, R. (2020) 'ICAM-1: A master regulator of cellular responses in inflammation, injury resolution, and tumorigenesis', *J Leukoc Biol*, 108(3), pp. 787-799.

Bull, K.S., Kennedy, C.R., Bailey, S., Ellison, D.W. and Clifford, S.C. (2014) 'Improved health-related quality of life outcomes associated with SHH subgroup medulloblastoma in SIOP-UKCCSG PNET3 trial survivors', *Acta Neuropathol*, 128(1), pp. 151-3.
Câmara-Costa, H., Resch, A., Kieffer, V., Lalande, C., Poggi, G., Kennedy, C., Bull, K., Calaminus, G., Grill, J., Doz, F., Rutkowski, S., Massimino, M., Kortmann, R.D., Lannering, B., Dellatolas, G. and Chevignard, M. (2015) 'Neuropsychological Outcome of Children Treated for Standard Risk Medulloblastoma in the PNET4 European Randomized Controlled Trial of Hyperfractionated Versus Standard Radiation Therapy and Maintenance Chemotherapy', *Int J Radiat Oncol Biol Phys*, 92(5), pp. 978-985.
Casciati, A., Dobos, K., Antonelli, F., Benedek, A., Kempf, S.J., Bellés, M., Balogh, A., Tanori, M., Heredia, L., Atkinson, M.J., Toerne, C.v., Azimzadeh, O., Saran, A., Sáfrány, G., Benotmane, M.A., Linares-Vidal, M.V., Tapio, S., Lumniczky, K. and Pazzaglia, S. (2016) 'Age-related effects of X-ray irradiation on mouse hippocampus', *Oncotarget*, 7(19).
Castle, J., Shaw, G., Weller, D., Fielder, E., Egnuni, T., Singh, M., Skinner, R., von Zglinicki, T., Clifford, S.C., Short, S.C., Miwa, S. and Hicks, D. (2024) 'In vivo modelling recapitulates radiotherapy delivery and late-effect profile for childhood medulloblastoma', *Neuro-Oncology Advances*.
Cenci, M.A., Whishaw, I.Q. and Schallert, T. (2002) 'Animal models of neurological deficits: how relevant is the rat?', *Nat Rev Neurosci*, 3(7), pp. 574-9.
Chang, C.H., Housepian, E.M. and Herbert, C., Jr. (1969) 'An operative staging system and a megavoltage radiotherapeutic technic for cerebellar medulloblastomas', *Radiology*, 93(6), pp. 1351-9.
Charlton, T., Prowse, N., McFee, A., Heiratifar, N., Fortin, T., Paquette, C. and Hayley, S. (2023) 'Brain-derived neurotrophic factor (BDNF) has direct anti-inflammatory effects on microglia', *Front Cell Neurosci*, 17, p. 1188672.
Chen, D., Xia, D., Pan, Z., Xu, D., Zhou, Y., Wu, Y., Cai, N., Tang, Q., Wang, C., Yan, M., Zhang, J.J., Zhou, K., Wang, Q., Feng, Y., Wang, X., Xu, H., Zhang, X. and Tian, N. (2016) 'Metformin protects against apoptosis and senescence in nucleus pulposus cells and ameliorates disc degeneration in vivo', *Cell Death Dis*, 7(10), p. e2441.
Cherbuin, N., Kumar, R., Sachdev, P.S. and Anstey, K.J. (2014) 'Dietary Mineral Intake and Risk of Mild Cognitive Impairment: The PATH through Life Project', *Front Aging Neurosci*, 6, p. 4.
Chevignard, M., Câmara-Costa, H., Doz, F. and Dellatolas, G. (2017) 'Core deficits and quality of survival after childhood medulloblastoma: a review', *Neurooncol Pract*, 4(2), pp. 82-97.
Chiang, C.S., McBride, W.H. and Withers, H.R. (1993) 'Radiation-induced astrocytic and microglial responses in mouse brain', *Radiother Oncol*, 29(1), pp. 60-8.
Chichagova, V., Georgiou, M., Carter, M., Dorgau, B., Hilgen, G., Collin, J., Queen, R., Chung, G., Ajeian, J., Moya-Molina, M., Kustermann, S., Pognan, F., Hewitt, P., Schmitt, M., Sernagor, E., Armstrong, L. and Lako, M. (2023) 'Incorporating microglia-like cells in human induced pluripotent stem cell-derived retinal organoids', *J Cell Mol Med*, 27(3), pp. 435-445.
Chiu, G.S., Maj, M.A., Rizvi, S., Dantzer, R., Vichaya, E.G., Laumet, G., Kavelaars, A. and Heijnen, C.J. (2017) 'Pifithrin-μ Prevents Cisplatin-Induced Chemobrain by Preserving Neuronal Mitochondrial Function', *Cancer Research*, 77(3), pp. 742-752.
Conklin, H.M., Helton, S., Ashford, J., Mulhern, R.K., Reddick, W.E., Brown, R., Bonner, M., Jasper, B.W., Wu, S., Xiong, X. and Khan, R.B. (2010a) 'Predicting methylphenidate response in long-term survivors of childhood cancer: a randomized, double-blind, placebo-controlled, crossover trial', *J Pediatr Psychol*, 35(2), pp. 144-55.
Conklin, H.M., Reddick, W.E., Ashford, J., Ogg, S., Howard, S.C., Morris, E.B., Brown, R., Bonner, M., Christensen, R., Wu, S., Xiong, X. and Khan, R.B. (2010b) 'Long-Term Efficacy of Methylphenidate in Enhancing Attention Regulation, Social Skills, and Academic Abilities of Childhood Cancer Survivors', *Journal of Clinical Oncology*, 28(29), pp. 4465-4472.
Coppé, J.P., Desprez, P.Y., Krtolica, A. and Campisi, J. (2010) 'The senescence-associated secretory phenotype: the dark side of tumor suppression', *Annu Rev Pathol*, 5, pp. 99-118.

Crouch, M.-L., Knowels, G., Stuppard, R., Ericson, N.G., Bielas, J.H., Marcinek, D.J. and Syrjala, K.L. (2017) 'Cyclophosphamide leads to persistent deficits in physical performance and in vivo mitochondria function in a mouse model of chemotherapy late effects', *PLOS ONE*, 12(7), p. e0181086.
Cuollo, L., Antonangeli, F., Santoni, A. and Soriani, A. (2020) 'The Senescence-Associated Secretory Phenotype (SASP) in the Challenging Future of Cancer Therapy and Age-Related Diseases', *Biology (Basel)*, 9(12).
De Benedictis, C.A., Haffke, C., Hagmeyer, S., Sauer, A.K. and Grabrucker, A.M. (2021) 'Expression Analysis of Zinc Transporters in Nervous Tissue Cells Reveals Neuronal and Synaptic Localization of ZIP4', *Int J Mol Sci*, 22(9).
de Boer, A.G., Verbeek, J.H. and van Dijk, F.J. (2006) 'Adult survivors of childhood cancer and unemployment: A metaanalysis', *Cancer*, 107(1), pp. 1-11.
De Braganca, K.C. and Packer, R.J. (2013) 'Treatment Options for Medulloblastoma and CNS Primitive Neuroectodermal Tumor (PNET)', *Curr Treat Options Neurol*, 15(5), pp. 593-606.
de Guzman, A.E., Ahmed, M., Li, Y.Q., Wong, C.S. and Nieman, B.J. (2019) 'p53 Loss Mitigates Early Volume Deficits in the Brains of Irradiated Young Mice', *Int J Radiat Oncol Biol Phys*, 103(2), pp. 511-520.
de Guzman, A.E., Gazdzinski, L.M., Alsop, R.J., Stewart, J.M., Jaffray, D.A., Wong, C.S. and Nieman, B.J. (2015) 'Treatment age, dose and sex determine neuroanatomical outcome in irradiated juvenile mice', *Radiat Res*, 183(5), pp. 541-9.
de Waal Malefyt, R., Abrams, J., Bennett, B., Figdor, C.G. and de Vries, J.E. (1991) 'Interleukin 10(IL-10) inhibits cytokine synthesis by human monocytes: an autoregulatory role of IL-10 produced by monocytes', *J Exp Med*, 174(5), pp. 1209-20.
Deasy, J.O., Moiseenko, V., Marks, L., Chao, K.S., Nam, J. and Eisbruch, A. (2010) 'Radiotherapy dose-volume effects on salivary gland function', *Int J Radiat Oncol Biol Phys*, 76(3 Suppl), pp. S58-63.
Dennis, M., Spiegler, B.J., Hetherington, C.R. and Greenberg, M.L. (1996) 'Neuropsychological sequelae of the treatment of children with medulloblastoma', *J Neurooncol*, 29(1), pp. 91-101.
Dent, P., Yacoub, A., Contessa, J., Caron, R., Amorino, G., Valerie, K., Hagan, M.P., Grant, S. and Schmidt-Ullrich, R. (2003) 'Stress and radiation-induced activation of multiple intracellular signaling pathways', *Radiat Res*, 159(3), pp. 283-300.
Dhall, G., Grodman, H., Ji, L., Sands, S., Gardner, S., Dunkel, I.J., McCowage, G.B., Diez, B., Allen, J.C., Gopalan, A., Cornelius, A.S., Termuhlen, A., Abromowitch, M., Sposto, R. and Finlay, J.L. (2008) 'Outcome of children less than three years old at diagnosis with non-metastatic medulloblastoma treated with chemotherapy on the "Head Start" I and II protocols', *Pediatric Blood & Cancer*, 50(6), pp. 1169-1175.
Diller, L., Chow, E.J., Gurney, J.G., Hudson, M.M., Kadan-Lottick, N.S., Kawashima, T.I., Leisenring, W.M., Meacham, L.R., Mertens, A.C., Mulrooney, D.A., Oeffinger, K.C., Packer, R.J., Robison, L.L. and Sklar, C.A. (2009a) 'Chronic Disease in the Childhood Cancer Survivor Study Cohort: A Review of Published Findings', *Journal of Clinical Oncology*, 27(14), pp. 2339-2355.
Diller, L., Chow, E.J., Gurney, J.G., Hudson, M.M., Kadin-Lottick, N.S., Kawashima, T.I., Leisenring, W.M., Meacham, L.R., Mertens, A.C., Mulrooney, D.A., Oeffinger, K.C., Packer, R.J., Robison, L.L. and Sklar, C.A. (2009b) 'Chronic disease in the Childhood Cancer Survivor Study cohort: a review of published findings', *J Clin Oncol*, 27(14), pp. 2339-55.
Dilruba, S. and Kalayda, G.V. (2016) 'Platinum-based drugs: past, present and future', *Cancer Chemother Pharmacol*, 77(6), pp. 1103-24.
Dixon, S.B., Liu, Q., Chow, E.J., Oeffinger, K.C., Nathan, P.C., Howell, R.M., Leisenring, W.M., Ehrhardt, M.J., Ness, K.K., Krull, K.R., Mertens, A.C., Hudson, M.M., Robison, L.L., Yasui, Y. and Armstrong, G.T. (2023) 'Specific causes of excess late mortality and association with modifiable risk factors among survivors of childhood cancer: a report from the Childhood Cancer Survivor Study cohort', *The Lancet*, 401(10386), pp. 1447-1457.
Donkena, K.V., Young, C.Y. and Tindall, D.J. (2010) 'Oxidative stress and DNA methylation in prostate cancer', *Obstet Gynecol Int*, 2010, p. 302051.

Donya, M., Radford, M., ElGuindy, A., Firmin, D. and Yacoub, M.H. (2014) 'Radiation in medicine: Origins, risks and aspirations', *Glob Cardiol Sci Pract*, 2014(4), pp. 437-48.
Dunkerson, J., Moritz, K.E., Young, J., Pionk, T., Fink, K., Rossignol, J., Dunbar, G. and Smith, J.S. (2014) 'Combining enriched environment and induced pluripotent stem cell therapy results in improved cognitive and motor function following traumatic brain injury', *Restor Neurol Neurosci*, 32(5), pp. 675-87.
Dutta, S. and Sengupta, P. (2016) 'Men and mice: Relating their ages', *Life Sci*, 152, pp. 244-8.
Edelstein, K., Spiegler, B.J., Fung, S., Panzarella, T., Mabbott, D.J., Jewitt, N., D'Agostino, N.M., Mason, W.P., Bouffet, E., Tabori, U., Laperriere, N. and Hodgson, D.C. (2011) 'Early aging in adult survivors of childhood medulloblastoma: long-term neurocognitive, functional, and physical outcomes', *Neuro Oncol*, 13(5), pp. 536-45.
Eden, A., Gaudet, F., Waghmare, A. and Jaenisch, R. (2003) 'Chromosomal instability and tumors promoted by DNA hypomethylation', *Science*, 300(5618), p. 455.
Ehrlich, M., Gama-Sosa, M.A., Huang, L.H., Midgett, R.M., Kuo, K.C., McCune, R.A. and Gehrke, C. (1982) 'Amount and distribution of 5-methylcytosine in human DNA from different types of tissues of cells', *Nucleic Acids Res*, 10(8), pp. 2709-21.
Ellenberg, L., Liu, Q., Gioia, G., Yasui, Y., Packer, R.J., Mertens, A., Donaldson, S.S., Stovall, M., Kadan-Lottick, N., Armstrong, G., Robison, L.L. and Zeltzer, L.K. (2009) 'Neurocognitive status in long-term survivors of childhood CNS malignancies: a report from the Childhood Cancer Survivor Study', *Neuropsychology*, 23(6), pp. 705-17.
Endersby, R., Whitehouse, J., Pribnow, A., Kuchibhotla, M., Hii, H., Carline, B., Gande, S., Stripay, J., Ancliffe, M., Howlett, M., Schoep, T., George, C., Andradas, C., Dyer, P., Schluck, M., Patterson, B., Tacheva-Gigorova, S.K., Cooper, M.N., Robinson, G., Stewart, C., Pfister, S.M., Kool, M., Milde, T., Gajjar, A., Johns, T., Wechsler-Reya, R.J., Roussel, M.F. and Gottardo, N.G. (2021) 'Small-molecule screen reveals synergy of cell cycle checkpoint kinase inhibitors with DNA-damaging chemotherapies in medulloblastoma', *Sci Transl Med*, 13(577).
Ennaceur, A. and Meliani, K. (1992) 'A new one-trial test for neurobiological studies of memory in rats. III. Spatial vs. non-spatial working memory', *Behav Brain Res*, 51(1), pp. 83-92.
Evans, A.E., Jenkin, R.D., Sposto, R., Ortega, J.A., Wilson, C.B., Wara, W., Ertel, I.J., Kramer, S., Chang, C.H., Leikin, S.L. and et al. (1990) 'The treatment of medulloblastoma. Results of a prospective randomized trial of radiation therapy with and without CCNU, vincristine, and prednisone', *J Neurosurg*, 72(4), pp. 572-82.
Field, A.E., Robertson, N.A., Wang, T., Havas, A., Ideker, T. and Adams, P.D. (2018) 'DNA Methylation Clocks in Aging: Categories, Causes, and Consequences', *Molecular Cell*, 71(6), pp. 882-895.
Fielder, E., Tweedy, C., Wilson, C., Oakley, F., LeBeau, F.E.N., Passos, J.F., Mann, D.A., von Zglinicki, T. and Jurk, D. (2020) 'Anti-inflammatory treatment rescues memory deficits during aging in nfkb1(-/-) mice', *Aging Cell*, 19(10), p. e13188.
Fielder, E., Wan, T., Alimohammadiha, G., Ishaq, A., Low, E., Weigand, B.M., Kelly, G., Parker, C., Griffin, B., Jurk, D., Korolchuk, V.I., von Zglinicki, T. and Miwa, S. (2022) 'Short senolytic or senostatic interventions rescue progression of radiation-induced frailty and premature ageing in mice', *Elife*, 11.
Fielder, E., Weigand, M., Agneessens, J., Griffin, B., Parker, C., Miwa, S. and von Zglinicki, T. (2019) 'Sublethal whole-body irradiation causes progressive premature frailty in mice', *Mech Ageing Dev*, 180, pp. 63-69.
Filley, C.M. and Kleinschmidt-DeMasters, B.K. (2001) 'Toxic leukoencephalopathy', *N Engl J Med*, 345(6), pp. 425-32.
Fischer, D.S. (2005) 'Cancer Chemotherapeutic Agents', in Wexler, P. (ed.) *Encyclopedia of Toxicology (Second Edition)*. New York: Elsevier, pp. 384-401.
Flanigan, T.J., Anderson, J.E., Elayan, I., Allen, A.R. and Ferguson, S.A. (2017) 'Effects of Cyclophosphamide and/or Doxorubicin in a Murine Model of Postchemotherapy Cognitive Impairment', *Toxicological Sciences*, 162(2), pp. 462-474.

Fossati, P., Ricardi, U. and Orecchia, R. (2009) 'Pediatric medulloblastoma: Toxicity of current treatment and potential role of protontherapy', *Cancer Treatment Reviews*, 35(1), pp. 79-96.
Fowler, J.F. (1989) 'The linear-quadratic formula and progress in fractionated radiotherapy', *Br J Radiol*, 62(740), pp. 679-94.
Frange, P., Alapetite, C., Gaboriaud, G., Bours, D., Zucker, J.M., Zerah, M., Brisse, H., Chevignard, M., Mosseri, V., Bouffet, E. and Doz, F. (2009) 'From childhood to adulthood: long-term outcome of medulloblastoma patients. The Institut Curie experience (1980-2000)', *J Neurooncol*, 95(2), pp. 271-279.
Fromont-Hankard, G., Philippe-Chomette, P., Delezoide, A.L., Nessmann, C., Aigrain, Y. and Peuchmaur, M. (2002) 'Glial cell-derived neurotrophic factor expression in normal human lung and congenital cystic adenomatoid malformation', *Arch Pathol Lab Med*, 126(4), pp. 432-6.
Gadow, K.D. (1992) 'Pediatric psychopharmacotherapy: a review of recent research', *J Child Psychol Psychiatry*, 33(1), pp. 153-95.
Gajjar, A., Robinson, G.W., Smith, K.S., Lin, T., Merchant, T.E., Chintagumpala, M., Mahajan, A., Su, J., Bouffet, E., Bartels, U., Schechter, T., Hassall, T., Robertson, T., Nicholls, W., Gururangan, S., Schroeder, K., Sullivan, M., Wheeler, G., Hansford, J.R., Kellie, S.J., McCowage, G., Cohn, R., Fisher, M.J., Krasin, M.J., Stewart, C.F., Broniscer, A., Buchhalter, I., Tatevossian, R.G., Orr, B.A., Neale, G., Klimo, P., Jr., Boop, F., Srinivasan, A., Pfister, S.M., Gilbertson, R.J., Onar-Thomas, A., Ellison, D.W. and Northcott, P.A. (2021) 'Outcomes by Clinical and Molecular Features in Children With Medulloblastoma Treated With Risk-Adapted Therapy: Results of an International Phase III Trial (SJMB03)', *J Clin Oncol*, 39(7), pp. 822-835.
Geisler, S., Doan, R.A., Strickland, A., Huang, X., Milbrandt, J. and DiAntonio, A. (2016) 'Prevention of vincristine-induced peripheral neuropathy by genetic deletion of SARM1 in mice', *Brain*, 139(12), pp. 3092-3108.
Gielis, M., Dirix, V., Vanderhenst, E., Uyttebroeck, A., Feys, H., Sleurs, C. and Jacobs, S. (2022) 'Better detection of reduced motor functioning in brain tumor survivors based on objective motor assessments: an incentive for improved standardized follow-up', *Eur J Pediatr*, 181(7), pp. 2731-2740.
Goddard, J., Castle, J., Southworth, E., Fletcher, A., Crosier, S., Martin-Guerrero, I., García-Ariza, M., Navajas, A., Masliah-Planchon, J., Bourdeaut, F., Dufour, C., Ayrault, O., Goschzik, T., Pietsch, T., Sill, M., Pfister, S.M., Rutkowski, S., Richardson, S., Hill, R.M., Williamson, D., Bailey, S., Schwalbe, E.C., Clifford, S.C. and Hicks, D. (2023) 'Molecular characterisation defines clinically-actionable heterogeneity within Group 4 medulloblastoma and improves disease risk-stratification', *Acta Neuropathol*, 145(5), pp. 651-666.
Goldstein, M. and Kastan, M.B. (2015) 'The DNA damage response: implications for tumor responses to radiation and chemotherapy', *Annu Rev Med*, 66, pp. 129-43.
Gomez, R., Vance, A. and Watson, S.D. (2016) 'Structure of the Wechsler Intelligence Scale for Children - Fourth Edition in a Group of Children with ADHD', *Front Psychol*, 7, p. 737.
Goschzik, T., Schwalbe, E.C., Hicks, D. and al, e. (2018) 'Prognostic effect of whole chromosomal aberration signatures in standard-risk, non-WNT/non-SHH medulloblastoma: a retrospective, molecular analysis of the HIT-SIOP PNET 4 trial', *The Lancet Oncology*, 19(12), pp. 1602-1616.
Gottardo, N.G. and Gajjar, A. (2006) 'Current therapy for medulloblastoma', *Curr Treat Options Neurol*, 8(4), pp. 319-34.
Granowetter, L., Rosenstock, J.G. and Packer, R.J. (1983) 'Enhanced cis-platinum neurotoxicity in pediatric patients with brain tumors', *J Neurooncol*, 1(4), pp. 293-7.
Greene-Schloesser, D., Robbins, M.E., Peiffer, A.M., Shaw, E.G., Wheeler, K.T. and Chan, M.D. (2012) 'Radiation-induced brain injury: A review', *Front Oncol*, 2, p. 73.
Grewal, S., Merchant, T., Reymond, R., McInerney, M., Hodge, C. and Shearer, P. (2010) 'Auditory late effects of childhood cancer therapy: a report from the Children's Oncology Group', *Pediatrics*, 125(4), pp. e938-50.
Grill, J., Renaux, V.K., Bulteau, C., Viguier, D., Levy-Piebois, C., Sainte-Rose, C., Dellatolas, G., Raquin, M.-A., Jambaqué, I. and Kalifa, C. (1999) 'Long-term intellectual outcome in children with posterior

fossa tumors according to radiation doses and volumes', *International Journal of Radiation Oncology*Biology*Physics*, 45(1), pp. 137-145.
Grundmann, O., Mitchell, G.C. and Limesand, K.H. (2009) 'Sensitivity of salivary glands to radiation: from animal models to therapies', *J Dent Res*, 88(10), pp. 894-903.
Gupta, T., Kalra, B., Goswami, S., Deodhar, J., Rane, P., Epari, S., Moiyadi, A., Dasgupta, A., Chatterjee, A. and Chinnaswamy, G. (2022) 'Neurocognitive function and survival in children with average-risk medulloblastoma treated with hyperfractionated radiation therapy alone: Long-term mature outcomes of a prospective study', *Neurooncol Pract*, 9(3), pp. 236-245.
Gurfein, B.T., Stamm, A.W., Bacchetti, P., Dallman, M.F., Nadkarni, N.A., Milush, J.M., Touma, C., Palme, R., Di Borgo, C.P., Fromentin, G., Lown-Hecht, R., Konsman, J.P., Acree, M., Premenko-Lanier, M., Darcel, N., Hecht, F.M. and Nixon, D.F. (2012) 'The calm mouse: an animal model of stress reduction', *Mol Med*, 18(1), pp. 606-17.
Gurney, J.G., Kadan-Lottick, N.S., Packer, R.J., Neglia, J.P., Sklar, C.A., Punyko, J.A., Stovall, M., Yasui, Y., Nicholson, H.S., Wolden, S., McNeil, D.E., Mertens, A.C. and Robison, L.L. (2003) 'Endocrine and cardiovascular late effects among adult survivors of childhood brain tumors: Childhood Cancer Survivor Study', *Cancer*, 97(3), pp. 663-73.
Gurney, J.G., Krull, K.R., Kadan-Lottick, N., Nicholson, H.S., Nathan, P.C., Zebrack, B., Tersak, J.M. and Ness, K.K. (2009) 'Social outcomes in the Childhood Cancer Survivor Study cohort', *J Clin Oncol*, 27(14), pp. 2390-5.
Han, W., Umekawa, T., Zhou, K., Zhang, X.M., Ohshima, M., Dominguez, C.A., Harris, R.A., Zhu, C. and Blomgren, K. (2016) 'Cranial irradiation induces transient microglia accumulation, followed by long-lasting inflammation and loss of microglia', *Oncotarget*, 7(50), pp. 82305-82323.
Harao, T., Yamada, A., Kinoshita, M., Kamimura, S. and Moritake, H. (2020) 'Prevention of cisplatin-induced hearing-loss by sodium thiosulfate in medulloblastoma', *Pediatr Int*, 62(10), pp. 1204-1206.
Hardy, K.K., Willard, V.W., Gioia, A., Sharkey, C. and Walsh, K.S. (2018) 'Attention-mediated neurocognitive profiles in survivors of pediatric brain tumors: comparison to children with neurodevelopmental ADHD', *Neuro Oncol*, 20(5), pp. 705-715.
Harrison, S.D., Jr. (1983) 'An investigation of the mouse as a model for vincristine toxicity', *Cancer Chemother Pharmacol*, 11(1), pp. 62-5.
Hartman, W., Helan, M., Smelter, D., Sathish, V., Thompson, M., Pabelick, C.M., Johnson, B. and Prakash, Y.S. (2015) 'Role of Hypoxia-Induced Brain Derived Neurotrophic Factor in Human Pulmonary Artery Smooth Muscle', *PLOS ONE*, 10(7), p. e0129489.
Hayek, S., Gibson, T.M., Leisenring, W.M., Guida, J.L., Gramatges, M.M., Lupo, P.J., Howell, R.M., Oeffinger, K.C., Bhatia, S., Edelstein, K., Hudson, M.M., Robison, L.L., Nathan, P.C., Yasui, Y., Krull, K.R., Armstrong, G.T. and Ness, K.K. (2020) 'Prevalence and Predictors of Frailty in Childhood Cancer Survivors and Siblings: A Report From the Childhood Cancer Survivor Study', *J Clin Oncol*, 38(3), pp. 232-247.
Heikens, J., Michiels, E.M., Behrendt, H., Endert, E., Bakker, P.J. and Fliers, E. (1998) 'Long-term neuro-endocrine sequelae after treatment for childhood medulloblastoma', *Eur J Cancer*, 34(10), pp. 1592-7.
Herranz, N. and Gil, J. (2018) 'Mechanisms and functions of cellular senescence', *J Clin Invest*, 128(4), pp. 1238-1246.
Hicks, D., Rafiee, G., Schwalbe, E.C., Howell, C.I., Lindsey, J.C., Hill, R.M., Smith, A.J., Adidharma, P., Steel, C., Richardson, S., Pease, L., Danilenko, M., Crosier, S., Joshi, A., Wharton, S.B., Jacques, T.S., Pizer, B., Michalski, A., Williamson, D., Bailey, S. and Clifford, S.C. (2021) 'The molecular landscape and associated clinical experience in infant medulloblastoma: prognostic significance of second-generation subtypes', *Neuropathol Appl Neurobiol*, 47(2), pp. 236-250.
Hoffman, K.E. and Yock, T.I. (2009) 'Radiation therapy for pediatric central nervous system tumors', *J Child Neurol*, 24(11), pp. 1387-96.
HomeOffice (2004) 'Mice, rats, gerbils, hamsters and guinea pigs. In: Code of Practice for the Housing and Care of Animals Bred, Supplied or Used for Scientific Purposes', *Her Majesty's Stationery Office*.

Hormuth, D.A., 2nd, Eldridge, S.L., Weis, J.A., Miga, M.I. and Yankeelov, T.E. (2018) 'Mechanically Coupled Reaction-Diffusion Model to Predict Glioma Growth: Methodological Details', *Methods Mol Biol*, 1711, pp. 225-241.
Horner, A.E., Heath, C.J., Hvoslef-Eide, M., Kent, B.A., Kim, C.H., Nilsson, S.R., Alsiö, J., Oomen, C.A., Holmes, A., Saksida, L.M. and Bussey, T.J. (2013) 'The touchscreen operant platform for testing learning and memory in rats and mice', *Nat Protoc*, 8(10), pp. 1961-84.
Hovestadt, V., Ayrault, O., Swartling, F.J., Robinson, G.W., Pfister, S.M. and Northcott, P.A. (2020) 'Medulloblastomics revisited: biological and clinical insights from thousands of patients', *Nat Rev Cancer*, 20(1), pp. 42-56.
Huang, R.-X. and Zhou, P.-K. (2020) 'DNA damage response signaling pathways and targets for radiotherapy sensitization in cancer', *Signal Transduction and Targeted Therapy*, 5(1), p. 60.
Huang, Z., Huang, L., Waters, M.J. and Chen, C. (2020) 'Insulin and Growth Hormone Balance: Implications for Obesity', *Trends Endocrinol Metab*, 31(9), pp. 642-654.
Hughes, C.E. and Nibbs, R.J.B. (2018) 'A guide to chemokines and their receptors', *Febs j*, 285(16), pp. 2944-2971.
Jabarkheel, R., Amayiri, N., Yecies, D., Huang, Y., Toescu, S., Nobre, L., Mabbott, D.J., Sudhakar, S.V., Malik, P., Laughlin, S., Swaidan, M., Al Hussaini, M., Musharbash, A., Chacko, G., Mathew, L.G., Fisher, P.G., Hargrave, D., Bartels, U., Tabori, U., Pfister, S.M., Aquilina, K., Taylor, M.D., Grant, G.A., Bouffet, E., Mankad, K., Yeom, K.W. and Ramaswamy, V. (2020) 'Molecular correlates of cerebellar mutism syndrome in medulloblastoma', *Neuro Oncol*, 22(2), pp. 290-297.
Janelsins, M.C., Heckler, C.E., Thompson, B.D., Gross, R.A., Opanashuk, L.A. and Cory-Slechta, D.A. (2016) 'A clinically relevant dose of cyclophosphamide chemotherapy impairs memory performance on the delayed spatial alternation task that is sustained over time as mice age', *NeuroToxicology*, 56, pp. 287-293.
Janelsins, M.C., Roscoe, J.A., Berg, M.J., Thompson, B.D., Gallagher, M.J., Morrow, G.R., Heckler, C.E., Jean-Pierre, P., Opanashuk, L.A. and Gross, R.A. (2010) 'IGF-1 partially restores chemotherapy-induced reductions in neural cell proliferation in adult C57BL/6 mice', *Cancer Invest*, 28(5), pp. 544-53.
Jenkin, D., Danjoux, C. and Greenberg, M. (1998) 'Subsequent quality of life for children irradiated for a brain tumor before age four years', *Med Pediatr Oncol*, 31(6), pp. 506-11.
Jham, B.C. and da Silva Freire, A.R. (2006) 'Oral complications of radiotherapy in the head and neck', *Braz J Otorhinolaryngol*, 72(5), pp. 704-8.
Jiang, W.W., Zhang, Z.Z., He, P.P., Jiang, L.P., Chen, J.Z., Zhang, X.T., Hu, M., Zhang, Y.K. and Ouyang, X.P. (2021) 'Emerging roles of growth differentiation factor-15 in brain disorders (Review)', *Exp Ther Med*, 22(5), p. 1270.
Johnson, D.L., McCabe, M.A., Nicholson, H.S., Joseph, A.L., Getson, P.R., Byrne, J., Brasseux, C., Packer, R.J. and Reaman, G. (1994) 'Quality of long-term survival in young children with medulloblastoma', *J Neurosurg*, 80(6), pp. 1004-10.
Jung, J.W., Hwang, S.Y., Hwang, J.S., Oh, E.S., Park, S. and Han, I.O. (2007) 'Ionising radiation induces changes associated with epithelial-mesenchymal transdifferentiation and increased cell motility of A549 lung epithelial cells', *Eur J Cancer*, 43(7), pp. 1214-24.
Juraschka, K. and Taylor, M.D. (2019) 'Medulloblastoma in the age of molecular subgroups: a review', *Journal of Neurosurgery: Pediatrics PED*, 24(4), p. 353.
Kahalley, L.S., Conklin, H.M., Tyc, V.L., Hudson, M.M., Wilson, S.J., Wu, S., Xiong, X. and Hinds, P.S. (2013) 'Slower processing speed after treatment for pediatric brain tumor and acute lymphoblastic leukemia', *Psychooncology*, 22(9), pp. 1979-86.
Keeling, C., Davies, S., Goddard, J., Ramaswamy, V., Schwalbe, E.C., Bailey, S., Hicks, D. and Clifford, S.C. (2024) 'The clinical significance of sub-total surgical resection in childhood medulloblastoma: a multi-cohort analysis of 1100 patients', *EClinicalMedicine*, 69, p. 102469.
Ketelut-Carneiro, N. and Fitzgerald, K.A. (2022) 'Apoptosis, Pyroptosis, and Necroptosis—Oh My! The Many Ways a Cell Can Die', *Journal of Molecular Biology*, 434(4), p. 167378.

Kiltie, A.E., Lashford, L.S. and Gattamaneni, H.R. (1997) 'Survival and late effects in medulloblastoma patients treated with craniospinal irradiation under three years old', *Med Pediatr Oncol*, 28(5), pp. 348-54.
Kim, G.S., Harmon, E., Gutierrez, M., Stephenson, J., Chauhan, A., Banerjee, A., Wise, Z., Doan, A., Wu, T., Lee, J., Jung, J.E., McCullough, L., Wythe, J. and Marrelli, S. (2023) 'Single-cell analysis identifies Ifi27l2a as a novel gene regulator of microglial inflammation in the context of aging and stroke', *Res Sq*.
Kim, W., Choy, W., Dye, J., Nagasawa, D., Safaee, M., Fong, B. and Yang, I. (2011) 'The tumor biology and molecular characteristics of medulloblastoma identifying prognostic factors associated with survival outcomes and prognosis', *J Clin Neurosci*, 18(7), pp. 886-90.
King, A.A., Seidel, K., Di, C., Leisenring, W.M., Perkins, S.M., Krull, K.R., Sklar, C.A., Green, D.M., Armstrong, G.T., Zeltzer, L.K., Wells, E., Stovall, M., Ullrich, N.J., Oeffinger, K.C., Robison, L.L. and Packer, R.J. (2017) 'Long-term neurologic health and psychosocial function of adult survivors of childhood medulloblastoma/PNET: a report from the Childhood Cancer Survivor Study', *Neuro Oncol*, 19(5), pp. 689-698.
Kirchhoff, A.C., Krull, K.R., Ness, K.K., Armstrong, G.T., Park, E.R., Stovall, M., Robison, L.L. and Leisenring, W. (2011) 'Physical, mental, and neurocognitive status and employment outcomes in the childhood cancer survivor study cohort', *Cancer Epidemiol Biomarkers Prev*, 20(9), pp. 1838-49.
Kirkland, J.L. and Tchkonia, T. (2020) 'Senolytic drugs: from discovery to translation', *J Intern Med*, 288(5), pp. 518-536.
Klein, T. and Bischoff, R. (2011) 'Physiology and pathophysiology of matrix metalloproteases', *Amino Acids*, 41(2), pp. 271-90.
Kling, T., Wenger, A. and Carén, H. (2020) 'DNA methylation-based age estimation in pediatric healthy tissues and brain tumors', *Aging (Albany NY)*, 12(21), pp. 21037-21056.
Kong, D.H., Kim, Y.K., Kim, M.R., Jang, J.H. and Lee, S. (2018) 'Emerging Roles of Vascular Cell Adhesion Molecule-1 (VCAM-1) in Immunological Disorders and Cancer', *Int J Mol Sci*, 19(4).
Kool, M., Korshunov, A., Remke, M., Jones, D.T., Schlanstein, M., Northcott, P.A., Cho, Y.J., Koster, J., Schouten-van Meeteren, A., van Vuurden, D., Clifford, S.C., Pietsch, T., von Bueren, A.O., Rutkowski, S., McCabe, M., Collins, V.P., Bäcklund, M.L., Haberler, C., Bourdeaut, F., Delattre, O., Doz, F., Ellison, D.W., Gilbertson, R.J., Pomeroy, S.L., Taylor, M.D., Lichter, P. and Pfister, S.M. (2012) 'Molecular subgroups of medulloblastoma: an international meta-analysis of transcriptome, genetic aberrations, and clinical data of WNT, SHH, Group 3, and Group 4 medulloblastomas', *Acta Neuropathol*, 123(4), pp. 473-84.
Kortmann, R.D., Kühl, J., Timmermann, B., Mittler, U., Urban, C., Budach, V., Richter, E., Willich, N., Flentje, M., Berthold, F., Slavc, I., Wolff, J., Meisner, C., Wiestler, O., Sörensen, N., Warmuth-Metz, M. and Bamberg, M. (2000) 'Postoperative neoadjuvant chemotherapy before radiotherapy as compared to immediate radiotherapy followed by maintenance chemotherapy in the treatment of medulloblastoma in childhood: results of the German prospective randomized trial HIT '91', *Int J Radiat Oncol Biol Phys*, 46(2), pp. 269-79.
Koziol, L.F., Budding, D., Andreasen, N., D'Arrigo, S., Bulgheroni, S., Imamizu, H., Ito, M., Manto, M., Marvel, C., Parker, K., Pezzulo, G., Ramnani, N., Riva, D., Schmahmann, J., Vandervert, L. and Yamazaki, T. (2014) 'Consensus paper: the cerebellum's role in movement and cognition', *Cerebellum*, 13(1), pp. 151-77.
Kraeuter, A.K., Guest, P.C. and Sarnyai, Z. (2019) 'The Y-Maze for Assessment of Spatial Working and Reference Memory in Mice', *Methods Mol Biol*, 1916, pp. 105-111.
Kurt, B.A., Armstrong, G.T., Cash, D.K., Krasin, M.J., Morris, E.B., Spunt, S.L., Robison, L.L. and Hudson, M.M. (2008) 'Primary care management of the childhood cancer survivor', *J Pediatr*, 152(4), pp. 458-66.
Kyrkanides, S., Olschowka, J.A., Williams, J.P., Hansen, J.T. and O'Banion, M.K. (1999) 'TNF alpha and IL-1beta mediate intercellular adhesion molecule-1 induction via microglia-astrocyte interaction in CNS radiation injury', *J Neuroimmunol*, 95(1-2), pp. 95-106.

Lafay-Cousin, L., Bouffet, E., Hawkins, C., Amid, A., Huang, A. and Mabbott, D.J. (2009) 'Impact of radiation avoidance on survival and neurocognitive outcome in infant medulloblastoma', *Curr Oncol*, 16(6), pp. 21-8.
Lafay-Cousin, L., Bouffet, E., Strother, D., Rudneva, V., Hawkins, C., Eberhart, C., Horbinski, C., Heier, L., Souweidane, M., Williams-Hughes, C., Onar-Thomas, A., Billups, C.A., Fouladi, M., Northcott, P., Robinson, G. and Gajjar, A. (2020) 'Phase II Study of Nonmetastatic Desmoplastic Medulloblastoma in Children Younger Than 4 Years of Age: A Report of the Children's Oncology Group (ACNS1221)', *J Clin Oncol*, 38(3), pp. 223-231.
Lamouille, S., Xu, J. and Derynck, R. (2014) 'Molecular mechanisms of epithelial–mesenchymal transition', *Nature Reviews Molecular Cell Biology*, 15(3), pp. 178-196.
Lannering, B., Rutkowski, S., Doz, F., Pizer, B., Gustafsson, G., Navajas, A., Massimino, M., Reddingius, R., Benesch, M., Carrie, C., Taylor, R., Gandola, L., Björk-Eriksson, T., Giralt, J., Oldenburger, F., Pietsch, T., Figarella-Branger, D., Robson, K., Forni, M., Clifford, S.C., Warmuth-Metz, M., von Hoff, K., Faldum, A., Mosseri, V. and Kortmann, R. (2012) 'Hyperfractionated versus conventional radiotherapy followed by chemotherapy in standard-risk medulloblastoma: results from the randomized multicenter HIT-SIOP PNET 4 trial', *J Clin Oncol*, 30(26), pp. 3187-93.
Law, N., Greenberg, M., Bouffet, E., Taylor, M.D., Laughlin, S., Strother, D., Fryer, C., McConnell, D., Hukin, J., Kaise, C., Wang, F. and Mabbott, D.J. (2012) 'Clinical and neuroanatomical predictors of cerebellar mutism syndrome', *Neuro Oncol*, 14(10), pp. 1294-303.
Lazarini, F., Mouthon, M.-A., Gheusi, G., de Chaumont, F., Olivo-Marin, J.-C., Lamarque, S., Abrous, D.N., Boussin, F.D. and Lledo, P.-M. (2009a) 'Cellular and Behavioral Effects of Cranial Irradiation of the Subventricular Zone in Adult Mice', *PLOS ONE*, 4(9), p. e7017.
Lazarini, F., Mouthon, M.A., Gheusi, G., de Chaumont, F., Olivo-Marin, J.C., Lamarque, S., Abrous, D.N., Boussin, F.D. and Lledo, P.M. (2009b) 'Cellular and behavioral effects of cranial irradiation of the subventricular zone in adult mice', *PLoS One*, 4(9), p. e7017.
Leach, J.K., Van Tuyle, G., Lin, P.S., Schmidt-Ullrich, R. and Mikkelsen, R.B. (2001) 'Ionizing radiation-induced, mitochondria-dependent generation of reactive oxygen/nitrogen', *Cancer Res*, 61(10), pp. 3894-901.
Lee, I.C., Chiu, Y.H. and Lee, C.Y. (2016) 'Exploration of the importance of geriatric frailty on health-related quality of life', *Psychogeriatrics*, 16(6), pp. 368-375.
Lee, M., Wisoff, J.H., Abbott, R., Freed, D. and Epstein, F.J. (1994) 'Management of hydrocephalus in children with medulloblastoma: prognostic factors for shunting', *Pediatr Neurosurg*, 20(4), pp. 240-7.
Li, D., Ke, Y., Zhan, R., Liu, C., Zhao, M., Zeng, A., Shi, X., Ji, L., Cheng, S., Pan, B., Zheng, L. and Hong, H. (2018) 'Trimethylamine-N-oxide promotes brain aging and cognitive impairment in mice', *Aging Cell*, 17(4), p. e12768.
Li, W., Alahdal, M., Deng, Z., Liu, J., Zhao, Z., Cheng, X., Chen, X., Li, J., Yin, J., Li, Y., Wang, G., Wang, D., Tang, K. and Zhang, J. (2020) 'Molecular functions of FSTL1 in the osteoarthritis', *International Immunopharmacology*, 83, p. 106465.
Liang, J. and Shang, Y. (2013) 'Estrogen and cancer', *Annu Rev Physiol*, 75, pp. 225-40.
Liddelow, S.A., Guttenplan, K.A., Clarke, L.E., Bennett, F.C., Bohlen, C.J., Schirmer, L., Bennett, M.L., Münch, A.E., Chung, W.S., Peterson, T.C., Wilton, D.K., Frouin, A., Napier, B.A., Panicker, N., Kumar, M., Buckwalter, M.S., Rowitch, D.H., Dawson, V.L., Dawson, T.M., Stevens, B. and Barres, B.A. (2017) 'Neurotoxic reactive astrocytes are induced by activated microglia', *Nature*, 541(7638), pp. 481-487.
Limond, J.A., Bull, K.S., Calaminus, G., Kennedy, C.R., Spoudeas, H.A. and Chevignard, M.P. (2015) 'Quality of survival assessment in European childhood brain tumour trials, for children aged 5 years and over', *Eur J Paediatr Neurol*, 19(2), pp. 202-10.
Liu, C.N., Berryman, E., Zakur, D., Shoieb, A.M., Pardo, I.D., Boucher, M., Somps, C.J., Bagi, C.M. and Cook, J.C. (2018) 'A novel endpoint for the assessment of chemotherapy-induced peripheral neuropathy in rodents: biomechanical properties of peripheral nerve', *J Appl Toxicol*, 38(2), pp. 193-200.

Liu, W., Huang, Y.J., Liu, C., Yang, Y.Y., Liu, H., Cui, J.G., Cheng, Y., Gao, F., Cai, J.M. and Li, B.L. (2014) 'Inhibition of TBK1 attenuates radiation-induced epithelial-mesenchymal transition of A549 human lung cancer cells via activation of GSK-3β and repression of ZEB1', *Lab Invest*, 94(4), pp. 362-70.
Louis, D.N., Perry, A., Reifenberger, G., von Deimling, A., Figarella-Branger, D., Cavenee, W.K., Ohgaki, H., Wiestler, O.D., Kleihues, P. and Ellison, D.W. (2016) 'The 2016 World Health Organization Classification of Tumors of the Central Nervous System: a summary', *Acta Neuropathol*, 131(6), pp. 803-20.
Louis, D.N., Perry, A., Wesseling, P., Brat, D.J., Cree, I.A., Figarella-Branger, D., Hawkins, C., Ng, H.K., Pfister, S.M., Reifenberger, G., Soffietti, R., von Deimling, A. and Ellison, D.W. (2021) 'The 2021 WHO Classification of Tumors of the Central Nervous System: a summary', *Neuro Oncol*, 23(8), pp. 1231-1251.
Luine, V. and Frankfurt, M. (2013) 'Interactions between estradiol, BDNF and dendritic spines in promoting memory', *Neuroscience*, 239, pp. 34-45.
Lumniczky, K., Szatmári, T. and Sáfrány, G. (2017) 'Ionizing Radiation-Induced Immune and Inflammatory Reactions in the Brain', *Front Immunol*, 8, p. 517.
Luo, X.J., Li, M., Huang, L., Nho, K., Deng, M., Chen, Q., Weinberger, D.R., Vasquez, A.A., Rijpkema, M., Mattay, V.S., Saykin, A.J., Shen, L., Fernández, G., Franke, B., Chen, J.C., Chen, X.N., Wang, J.K., Xiao, X., Qi, X.B., Xiang, K., Peng, Y.M., Cao, X.Y., Li, Y., Shi, X.D., Gan, L. and Su, B. (2012) 'The interleukin 3 gene (IL3) contributes to human brain volume variation by regulating proliferation and survival of neural progenitors', *PLoS One*, 7(11), p. e50375.
Mabbott, D.J., Spiegler, B.J., Greenberg, M.L., Rutka, J.T., Hyder, D.J. and Bouffet, E. (2005) 'Serial evaluation of academic and behavioral outcome after treatment with cranial radiation in childhood', *J Clin Oncol*, 23(10), pp. 2256-63.
Maddrey, A.M., Bergeron, J.A., Lombardo, E.R., McDonald, N.K., Mulne, A.F., Barenberg, P.D. and Bowers, D.C. (2005) 'Neuropsychological performance and quality of life of 10 year survivors of childhood medulloblastoma', *J Neurooncol*, 72(3), pp. 245-53.
Mañas, A., Aaltonen, K., Andersson, N., Hansson, K., Adamska, A., Seger, A., Yasui, H., van den Bos, H., Radke, K., Esfandyari, J., Bhave, M.S., Karlsson, J., Spierings, D., Foijer, F., Gisselsson, D. and Bexell, D. (2022) 'Clinically relevant treatment of PDX models reveals patterns of neuroblastoma chemoresistance', *Science Advances*, 8(43), p. eabq4617.
Martinez, H.R., Salloum, R., Wright, E., Bueche, L., Khoury, P.R., Tretter, J.T. and Ryan, T.D. (2021) 'Echocardiographic myocardial strain analysis describes subclinical cardiac dysfunction after craniospinal irradiation in pediatric and young adult patients with central nervous system tumors', *Cardiooncology*, 7(1), p. 5.
Mattiotti, A., Prakash, S., Barnett, P. and van den Hoff, M.J.B. (2018) 'Follistatin-like 1 in development and human diseases', *Cell Mol Life Sci*, 75(13), pp. 2339-2354.
Maurice, T., Hiramatsu, M., Itoh, J., Kameyama, T., Hasegawa, T. and Nabeshima, T. (1994) 'Behavioral evidence for a modulating role of σ ligands in memory processes. I. Attenuation of dizocilpine (MK-801)-induced amnesia', *Brain Research*, 647(1), pp. 44-56.
McKenzie, A.T., Wang, M., Hauberg, M.E., Fullard, J.F., Kozlenkov, A., Keenan, A., Hurd, Y.L., Dracheva, S., Casaccia, P., Roussos, P. and Zhang, B. (2018) 'Brain Cell Type Specific Gene Expression and Co-expression Network Architectures', *Scientific Reports*, 8(1), p. 8868.
Ment, L.R., Scheinost, D. and Constable, T. (2017) '14 - Microstructural and Functional Connectivity in the Developing Brain', in Swaiman, K.F., Ashwal, S., Ferriero, D.M., Schor, N.F., Finkel, R.S., Gropman, A.L., Pearl, P.L. and Shevell, M.I. (eds.) *Swaiman's Pediatric Neurology (Sixth Edition)*. Elsevier, pp. 97-106.
Mertens, A.C., Liu, Q., Neglia, J.P., Wasilewski, K., Leisenring, W., Armstrong, G.T., Robison, L.L. and Yasui, Y. (2008) 'Cause-specific late mortality among 5-year survivors of childhood cancer: the Childhood Cancer Survivor Study', *J Natl Cancer Inst*, 100(19), pp. 1368-79.
Michalski, J.M., Janss, A.J., Vezina, L.G., Smith, K.S., Billups, C.A., Burger, P.C., Embry, L.M., Cullen, P.L., Hardy, K.K., Pomeroy, S.L., Bass, J.K., Perkins, S.M., Merchant, T.E., Colte, P.D., Fitzgerald, T.J., Booth,

T.N., Cherlow, J.M., Muraszko, K.M., Hadley, J., Kumar, R., Han, Y., Tarbell, N.J., Fouladi, M., Pollack, I.F., Packer, R.J., Li, Y., Gajjar, A. and Northcott, P.A. (2021) 'Children's Oncology Group Phase III Trial of Reduced-Dose and Reduced-Volume Radiotherapy With Chemotherapy for Newly Diagnosed Average-Risk Medulloblastoma', *J Clin Oncol*, 39(24), pp. 2685-2697.
Millard, N.E. and De Braganca, K.C. (2016) 'Medulloblastoma', *J Child Neurol*, 31(12), pp. 1341-53.
Miousse, I.R., Kutanzi, K.R. and Koturbash, I. (2017) 'Effects of ionizing radiation on DNA methylation: from experimental biology to clinical applications', *Int J Radiat Biol*, 93(5), pp. 457-469.
Mitby, P.A., Robison, L.L., Whitton, J.A., Zevon, M.A., Gibbs, I.C., Tersak, J.M., Meadows, A.T., Stovall, M., Zeltzer, L.K. and Mertens, A.C. (2003) 'Utilization of special education services and educational attainment among long-term survivors of childhood cancer: a report from the Childhood Cancer Survivor Study', *Cancer*, 97(4), pp. 1115-26.
Mitra, S., Dash, R., Sohel, M., Chowdhury, A., Munni, Y.A., Ali, M.C., Hannan, M.A., Islam, M.T. and Moon, I.S. (2023) 'Targeting Estrogen Signaling in the Radiation-induced Neurodegeneration: A Possible Role of Phytoestrogens', *Curr Neuropharmacol*, 21(2), pp. 353-379.
Monje, M.L., Mizumatsu, S., Fike, J.R. and Palmer, T.D. (2002) 'Irradiation induces neural precursor-cell dysfunction', *Nat Med*, 8(9), pp. 955-62.
Montay-Gruel, P., Acharya, M.M., Petersson, K., Alikhani, L., Yakkala, C., Allen, B.D., Ollivier, J., Petit, B., Jorge, P.G., Syage, A.R., Nguyen, T.A., Baddour, A.A.D., Lu, C., Singh, P., Moeckli, R., Bochud, F., Germond, J.F., Froidevaux, P., Bailat, C., Bourhis, J., Vozenin, M.C. and Limoli, C.L. (2019) 'Long-term neurocognitive benefits of FLASH radiotherapy driven by reduced reactive oxygen species', *Proc Natl Acad Sci U S A*, 116(22), pp. 10943-10951.
Montay-Gruel, P., Petersson, K., Jaccard, M., Boivin, G., Germond, J.F., Petit, B., Doenlen, R., Favaudon, V., Bochud, F., Bailat, C., Bourhis, J. and Vozenin, M.C. (2017) 'Irradiation in a flash: Unique sparing of memory in mice after whole brain irradiation with dose rates above 100Gy/s', *Radiother Oncol*, 124(3), pp. 365-369.
Moore, K.W., de Waal Malefyt, R., Coffman, R.L. and O'Garra, A. (2001) 'Interleukin-10 and the interleukin-10 receptor', *Annu Rev Immunol*, 19, pp. 683-765.
Moravan, M.J., Olschowka, J.A., Williams, J.P. and O'Banion, M.K. (2011) 'Cranial irradiation leads to acute and persistent neuroinflammation with delayed increases in T-cell infiltration and CD11c expression in C57BL/6 mouse brain', *Radiat Res*, 176(4), pp. 459-73.
Morfouace, M., Shelat, A., Jacus, M., Freeman, B.B., 3rd, Turner, D., Robinson, S., Zindy, F., Wang, Y.D., Finkelstein, D., Ayrault, O., Bihannic, L., Puget, S., Li, X.N., Olson, J.M., Robinson, G.W., Guy, R.K., Stewart, C.F., Gajjar, A. and Roussel, M.F. (2014) 'Pemetrexed and gemcitabine as combination therapy for the treatment of Group3 medulloblastoma', *Cancer Cell*, 25(4), pp. 516-29.
Morris, E.B., Gajjar, A., Okuma, J.O., Yasui, Y., Wallace, D., Kun, L.E., Merchant, T.E., Fouladi, M., Broniscer, A., Robison, L.L. and Hudson, M.M. (2007) 'Survival and late mortality in long-term survivors of pediatric CNS tumors', *J Clin Oncol*, 25(12), pp. 1532-8.
Morrissy, A.S., Garzia, L., Shih, D.J., Zuyderduyn, S., Huang, X., Skowron, P., Remke, M., Cavalli, F.M., Ramaswamy, V., Lindsay, P.E., Jelveh, S., Donovan, L.K., Wang, X., Luu, B., Zayne, K., Li, Y., Mayoh, C., Thiessen, N., Mercier, E., Mungall, K.L., Ma, Y., Tse, K., Zeng, T., Shumansky, K., Roth, A.J., Shah, S., Farooq, H., Kijima, N., Holgado, B.L., Lee, J.J., Matan-Lithwick, S., Liu, J., Mack, S.C., Manno, A., Michealraj, K.A., Nor, C., Peacock, J., Qin, L., Reimand, J., Rolider, A., Thompson, Y.Y., Wu, X., Pugh, T., Ally, A., Bilenky, M., Butterfield, Y.S., Carlsen, R., Cheng, Y., Chuah, E., Corbett, R.D., Dhalla, N., He, A., Lee, D., Li, H.I., Long, W., Mayo, M., Plettner, P., Qian, J.Q., Schein, J.E., Tam, A., Wong, T., Birol, I., Zhao, Y., Faria, C.C., Pimentel, J., Nunes, S., Shalaby, T., Grotzer, M., Pollack, I.F., Hamilton, R.L., Li, X.N., Bendel, A.E., Fults, D.W., Walter, A.W., Kumabe, T., Tominaga, T., Collins, V.P., Cho, Y.J., Hoffman, C., Lyden, D., Wisoff, J.H., Garvin, J.H., Jr., Stearns, D.S., Massimi, L., Schüller, U., Sterba, J., Zitterbart, K., Puget, S., Ayrault, O., Dunn, S.E., Tirapelli, D.P., Carlotti, C.G., Wheeler, H., Hallahan, A.R., Ingram, W., MacDonald, T.J., Olson, J.J., Van Meir, E.G., Lee, J.Y., Wang, K.C., et al. (2016) 'Divergent clonal selection dominates medulloblastoma at recurrence', *Nature*, 529(7586), pp. 351-7.

Mortezaee, K., Shabeeb, D., Musa, A.E., Najafi, M. and Farhood, B. (2019) 'Metformin as a Radiation Modifier; Implications to Normal Tissue Protection and Tumor Sensitization', *Curr Clin Pharmacol*, 14(1), pp. 41-53.
Moxon-Emre, I., Taylor, M.D., Bouffet, E., Hardy, K., Campen, C.J., Malkin, D., Hawkins, C., Laperriere, N., Ramaswamy, V., Bartels, U., Scantlebury, N., Janzen, L., Law, N., Walsh, K.S. and Mabbott, D.J. (2016) 'Intellectual Outcome in Molecular Subgroups of Medulloblastoma', *J Clin Oncol*, 34(34), pp. 4161-4170.
Mozhui, K. and Pandey, A.K. (2017) 'Conserved effect of aging on DNA methylation and association with EZH2 polycomb protein in mice and humans', *Mech Ageing Dev*, 162, pp. 27-37.
Mulhern, R.K. and Butler, R.W. (2004) 'Neurocognitive sequelae of childhood cancers and their treatment', *Pediatr Rehabil*, 7(1), pp. 1-14; discussion 15-6.
Mulhern, R.K., Horowitz, M.E., Kovnar, E.H., Langston, J., Sanford, R.A. and Kun, L.E. (1989) 'Neurodevelopmental status of infants and young children treated for brain tumors with preirradiation chemotherapy', *J Clin Oncol*, 7(11), pp. 1660-6.
Mulhern, R.K., Khan, R.B., Kaplan, S., Helton, S., Christensen, R., Bonner, M., Brown, R., Xiong, X., Wu, S., Gururangan, S. and Reddick, W.E. (2004) 'Short-term efficacy of methylphenidate: a randomized, double-blind, placebo-controlled trial among survivors of childhood cancer', *J Clin Oncol*, 22(23), pp. 4795-803.
Mulhern, R.K., Reddick, W.E., Palmer, S.L., Glass, J.O., Elkin, T.D., Kun, L.E., Taylor, J., Langston, J. and Gajjar, A. (1999) 'Neurocognitive deficits in medulloblastoma survivors and white matter loss', *Ann Neurol*, 46(6), pp. 834-41.
Müller, K., Mynarek, M., Zwiener, I., Siegler, N., Zimmermann, M., Christiansen, H., Budach, W., Henke, G., Warmuth-Metz, M., Pietsch, T., von Hoff, K., von Bueren, A., Bode, U., Rutkowski, S., Kortmann, R.D., Fleischhack, G. and Tippelt, S. (2014) 'Postponed is not canceled: role of craniospinal radiation therapy in the management of recurrent infant medulloblastoma--an experience from the HIT-REZ 1997 & 2005 studies', *Int J Radiat Oncol Biol Phys*, 88(5), pp. 1019-24.
Murphy, K.L. and Baxter, M.G. (2013) 'Long-term effects of neonatal single or multiple isoflurane exposures on spatial memory in rats', *Front Neurol*, 4, p. 87.
Mynarek, M., Milde, T., Padovani, L., Janssens, G.O., Kwiecien, R., Mosseri, V., Clifford, S.C., Doz, F. and Rutkowski, S. (2021) 'SIOP PNET5 MB Trial: History and Concept of a Molecularly Stratified Clinical Trial of Risk-Adapted Therapies for Standard-Risk Medulloblastoma', *Cancers (Basel)*, 13(23).
Mynarek, M., Obrecht, D., Sill, M., Sturm, D., Kloth-Stachnau, K., Selt, F., Ecker, J., von Hoff, K., Juhnke, B.O., Goschzik, T., Pietsch, T., Bockmayr, M., Kool, M., von Deimling, A., Witt, O., Schüller, U., Benesch, M., Gerber, N.U., Sahm, F., Jones, D.T.W., Korshunov, A., Pfister, S.M., Rutkowski, S. and Milde, T. (2023) 'Identification of low and very high-risk patients with non-WNT/non-SHH medulloblastoma by improved clinico-molecular stratification of the HIT2000 and I-HIT-MED cohorts', *Acta Neuropathol*, 145(1), pp. 97-112.
Mynarek, M., von Hoff, K., Pietsch, T., Ottensmeier, H., Warmuth-Metz, M., Bison, B., Pfister, S., Korshunov, A., Sharma, T., Jaeger, N., Ryzhova, M., Zheludkova, O., Golanov, A., Rushing, E.J., Hasselblatt, M., Koch, A., Schüller, U., von Deimling, A., Sahm, F., Sill, M., Riemenschneider, M.J., Dohmen, H., Monoranu, C.M., Sommer, C., Staszewski, O., Mawrin, C., Schittenhelm, J., Brück, W., Filipski, K., Hartmann, C., Meinhardt, M., Pietschmann, K., Haberler, C., Slavc, I., Gerber, N.U., Grotzer, M., Benesch, M., Schlegel, P.G., Deinlein, F., von Bueren, A.O., Friedrich, C., Juhnke, B.O., Obrecht, D., Fleischhack, G., Kwiecien, R., Faldum, A., Kortmann, R.D., Kool, M. and Rutkowski, S. (2020) 'Nonmetastatic Medulloblastoma of Early Childhood: Results From the Prospective Clinical Trial HIT-2000 and An Extended Validation Cohort', *J Clin Oncol*, 38(18), pp. 2028-2040.
Neglia, J.P., Robison, L.L., Stovall, M., Liu, Y., Packer, R.J., Hammond, S., Yasui, Y., Kasper, C.E., Mertens, A.C., Donaldson, S.S., Meadows, A.T. and Inskip, P.D. (2006) 'New primary neoplasms of the central nervous system in survivors of childhood cancer: a report from the Childhood Cancer Survivor Study', *J Natl Cancer Inst*, 98(21), pp. 1528-37.

Ness, K.K., Krull, K.R., Jones, K.E., Mulrooney, D.A., Armstrong, G.T., Green, D.M., Chemaitilly, W., Smith, W.A., Wilson, C.L., Sklar, C.A., Shelton, K., Srivastava, D.K., Ali, S., Robison, L.L. and Hudson, M.M. (2013) 'Physiologic frailty as a sign of accelerated aging among adult survivors of childhood cancer: a report from the St Jude Lifetime cohort study', *J Clin Oncol*, 31(36), pp. 4496-503.
Ness, K.K., Morris, E.B., Nolan, V.G., Howell, C.R., Gilchrist, L.S., Stovall, M., Cox, C.L., Klosky, J.L., Gajjar, A. and Neglia, J.P. (2010) 'Physical performance limitations among adult survivors of childhood brain tumors', *Cancer*, 116(12), pp. 3034-44.
Nieman, B.J., de Guzman, A.E., Gazdzinski, L.M., Lerch, J.P., Chakravarty, M.M., Pipitone, J., Strother, D., Fryer, C., Bouffet, E., Laughlin, S., Laperriere, N., Riggs, L., Skocic, J. and Mabbott, D.J. (2015) 'White and Gray Matter Abnormalities After Cranial Radiation in Children and Mice', *Int J Radiat Oncol Biol Phys*, 93(4), pp. 882-91.
Nimmervoll, B.V., Boulos, N., Bianski, B., Dapper, J., DeCuypere, M., Shelat, A., Terranova, S., Terhune, H.E., Gajjar, A., Patel, Y.T., Freeman, B.B., Onar-Thomas, A., Stewart, C.F., Roussel, M.F., Guy, R.K., Merchant, T.E., Calabrese, C., Wright, K.D. and Gilbertson, R.J. (2018) 'Establishing a Preclinical Multidisciplinary Board for Brain Tumors', *Clin Cancer Res*, 24(7), pp. 1654-1666.
Nitiss, J.L. (2009) 'Targeting DNA topoisomerase II in cancer chemotherapy', *Nat Rev Cancer*, 9(5), pp. 338-50.
Northcott, P.A., Buchhalter, I., Morrissy, A.S., Hovestadt, V., Weischenfeldt, J., Ehrenberger, T., Gröbner, S., Segura-Wang, M., Zichner, T., Rudneva, V.A., Warnatz, H.-J., Sidiropoulos, N., Phillips, A.H., Schumacher, S., Kleinheinz, K., Waszak, S.M., Erkek, S., Jones, D.T.W., Worst, B.C., Kool, M., Zapatka, M., Jäger, N., Chavez, L., Hutter, B., Bieg, M., Paramasivam, N., Heinold, M., Gu, Z., Ishaque, N., Jäger-Schmidt, C., Imbusch, C.D., Jugold, A., Hübschmann, D., Risch, T., Amstislavskiy, V., Gonzalez, F.G.R., Weber, U.D., Wolf, S., Robinson, G.W., Zhou, X., Wu, G., Finkelstein, D., Liu, Y., Cavalli, F.M.G., Luu, B., Ramaswamy, V., Wu, X., Koster, J., Ryzhova, M., Cho, Y.-J., Pomeroy, S.L., Herold-Mende, C., Schuhmann, M., Ebinger, M., Liau, L.M., Mora, J., McLendon, R.E., Jabado, N., Kumabe, T., Chuah, E., Ma, Y., Moore, R.A., Mungall, A.J., Mungall, K.L., Thiessen, N., Tse, K., Wong, T., Jones, S.J.M., Witt, O., Milde, T., Von Deimling, A., Capper, D., Korshunov, A., Yaspo, M.-L., Kriwacki, R., Gajjar, A., Zhang, J., Beroukhim, R., Fraenkel, E., Korbel, J.O., Brors, B., Schlesner, M., Eils, R., Marra, M.A., Pfister, S.M., Taylor, M.D. and Lichter, P. (2017) 'The whole-genome landscape of medulloblastoma subtypes', *Nature*, 547(7663), pp. 311-317.
Northcott, P.A., Robinson, G.W., Kratz, C.P., Mabbott, D.J., Pomeroy, S.L., Clifford, S.C., Rutkowski, S., Ellison, D.W., Malkin, D., Taylor, M.D., Gajjar, A. and Pfister, S.M. (2019) 'Medulloblastoma', *Nature Reviews Disease Primers*, 5(1), p. 11.
Northcott, P.A., Shih, D.J., Peacock, J., Garzia, L., Morrissy, A.S., Zichner, T., Stütz, A.M., Korshunov, A., Reimand, J., Schumacher, S.E., Beroukhim, R., Ellison, D.W., Marshall, C.R., Lionel, A.C., Mack, S., Dubuc, A., Yao, Y., Ramaswamy, V., Luu, B., Rolider, A., Cavalli, F.M., Wang, X., Remke, M., Wu, X., Chiu, R.Y., Chu, A., Chuah, E., Corbett, R.D., Hoad, G.R., Jackman, S.D., Li, Y., Lo, A., Mungall, K.L., Nip, K.M., Qian, J.Q., Raymond, A.G., Thiessen, N.T., Varhol, R.J., Birol, I., Moore, R.A., Mungall, A.J., Holt, R., Kawauchi, D., Roussel, M.F., Kool, M., Jones, D.T., Witt, H., Fernandez, L.A., Kenney, A.M., Wechsler-Reya, R.J., Dirks, P., Aviv, T., Grajkowska, W.A., Perek-Polnik, M., Haberler, C.C., Delattre, O., Reynaud, S.S., Doz, F.F., Pernet-Fattet, S.S., Cho, B.K., Kim, S.K., Wang, K.C., Scheurlen, W., Eberhart, C.G., Fèvre-Montange, M., Jouvet, A., Pollack, I.F., Fan, X., Muraszko, K.M., Gillespie, G.Y., Di Rocco, C., Massimi, L., Michiels, E.M., Kloosterhof, N.K., French, P.J., Kros, J.M., Olson, J.M., Ellenbogen, R.G., Zitterbart, K., Kren, L., Thompson, R.C., Cooper, M.K., Lach, B., McLendon, R.E., Bigner, D.D., Fontebasso, A., Albrecht, S., Jabado, N., Lindsey, J.C., Bailey, S., Gupta, N., Weiss, W.A., Bognár, L., Klekner, A., Van Meter, T.E., Kumabe, T., Tominaga, T., Elbabaa, S.K., Leonard, J.R., Rubin, J.B., et al. (2012) 'Subgroup-specific structural variation across 1,000 medulloblastoma genomes', *Nature*, 488(7409), pp. 49-56.
Oeffinger, K.C., Mertens, A.C., Sklar, C.A., Kawashima, T., Hudson, M.M., Meadows, A.T., Friedman, D.L., Marina, N., Hobbie, W., Kadan-Lottick, N.S., Schwartz, C.L., Leisenring, W. and Robison, L.L. (2006) 'Chronic health conditions in adult survivors of childhood cancer', *N Engl J Med*, 355(15), pp. 1572-82.

Ostrom, Q.T., Gittleman, H., Truitt, G., Boscia, A., Kruchko, C. and Barnholtz-Sloan, J.S. (2018) 'CBTRUS Statistical Report: Primary Brain and Other Central Nervous System Tumors Diagnosed in the United States in 2011-2015', *Neuro Oncol*, 20(suppl_4), pp. iv1-iv86.
Packer, R.J., Gurney, J.G., Punyko, J.A., Donaldson, S.S., Inskip, P.D., Stovall, M., Yasui, Y., Mertens, A.C., Sklar, C.A., Nicholson, H.S., Zeltzer, L.K., Neglia, J.P. and Robison, L.L. (2003) 'Long-term neurologic and neurosensory sequelae in adult survivors of a childhood brain tumor: childhood cancer survivor study', *J Clin Oncol*, 21(17), pp. 3255-61.
Packer, R.J., Sutton, L.N., Elterman, R., Lange, B., Goldwein, J., Nicholson, H.S., Mulne, L., Boyett, J., D'Angio, G., Wechsler-Jentzsch, K. and et al. (1994) 'Outcome for children with medulloblastoma treated with radiation and cisplatin, CCNU, and vincristine chemotherapy', *J Neurosurg*, 81(5), pp. 690-8.
Packer, R.J., Zhou, T., Holmes, E., Vezina, G. and Gajjar, A. (2013) 'Survival and secondary tumors in children with medulloblastoma receiving radiotherapy and adjuvant chemotherapy: results of Children's Oncology Group trial A9961', *Neuro Oncol*, 15(1), pp. 97-103.
Palmer, S.L., Armstrong, C., Onar-Thomas, A., Wu, S., Wallace, D., Bonner, M.J., Schreiber, J., Swain, M., Chapieski, L., Mabbott, D., Knight, S., Boyle, R. and Gajjar, A. (2013) 'Processing speed, attention, and working memory after treatment for medulloblastoma: an international, prospective, and longitudinal study', *J Clin Oncol*, 31(28), pp. 3494-500.
Palmer, S.L., Goloubeva, O., Reddick, W.E., Glass, J.O., Gajjar, A., Kun, L., Merchant, T.E. and Mulhern, R.K. (2001a) 'Patterns of intellectual development among survivors of pediatric medulloblastoma: a longitudinal analysis', *J Clin Oncol*, 19(8), pp. 2302-8.
Palmer, S.L., Goloubeva, O., Reddick, W.E., Glass, J.O., Gajjar, A., Kun, L., Merchant, T.E. and Mulhern, R.K. (2001b) 'Patterns of intellectual development among survivors of pediatric medulloblastoma: A longitudinal analysis', *Journal of Clinical Oncology*, 19(8), pp. 2302-2308.
Patro, R., Duggal, G., Love, M.I., Irizarry, R.A. and Kingsford, C. (2017) 'Salmon provides fast and bias-aware quantification of transcript expression', *Nature Methods*, 14(4), pp. 417-419.
Pazzaglia, S., Briganti, G., Mancuso, M. and Saran, A. (2020) 'Neurocognitive Decline Following Radiotherapy: Mechanisms and Therapeutic Implications', *Cancers (Basel)*, 12(1).
Pekny, M. and Nilsson, M. (2005) 'Astrocyte activation and reactive gliosis', *Glia*, 50(4), pp. 427-434.
Perreault, S., Ramaswamy, V., Achrol, A.S., Chao, K., Liu, T.T., Shih, D., Remke, M., Schubert, S., Bouffet, E., Fisher, P.G., Partap, S., Vogel, H., Taylor, M.D., Cho, Y.J. and Yeom, K.W. (2014) 'MRI surrogates for molecular subgroups of medulloblastoma', *AJNR Am J Neuroradiol*, 35(7), pp. 1263-9.
Peterson, K.M., Shao, C., McCarter, R., MacDonald, T.J. and Byrne, J. (2006) 'An analysis of SEER data of increasing risk of secondary malignant neoplasms among long-term survivors of childhood brain tumors', *Pediatr Blood Cancer*, 47(1), pp. 83-8.
Piscione, P.J., Bouffet, E., Mabbott, D.J., Shams, I. and Kulkarni, A.V. (2013) 'Physical functioning in pediatric survivors of childhood posterior fossa brain tumors', *Neuro-Oncology*, 16(1), pp. 147-155.
Pizer, B.L. and Clifford, S.C. (2009) 'The potential impact of tumour biology on improved clinical practice for medulloblastoma: progress towards biologically driven clinical trials', *Br J Neurosurg*, 23(4), pp. 364-75.
Porro, C., Cianciulli, A. and Panaro, M.A. (2020) 'The Regulatory Role of IL-10 in Neurodegenerative Diseases', *Biomolecules*, 10(7), p. 1017.
Prakash, Y.S. and Martin, R.J. (2014) 'Brain-derived neurotrophic factor in the airways', *Pharmacol Ther*, 143(1), pp. 74-86.
Provencher, V., Sirois, M.J., Émond, M., Perry, J.J., Daoust, R., Lee, J.S., Griffith, L.E., Batomen Kuimi, B.L., Despeignes, L.R., Wilding, L., Allain-Boulé, N. and Lebon, J. (2016) 'Frail older adults with minor fractures show lower health-related quality of life (SF-12) scores up to six months following emergency department discharge', *Health Qual Life Outcomes*, 14, p. 40.
Pulsifer, M.B., Duncanson, H., Grieco, J., Evans, C., Tseretopoulos, I.D., MacDonald, S., Tarbell, N.J. and Yock, T.I. (2018) 'Cognitive and Adaptive Outcomes After Proton Radiation for Pediatric Patients With Brain Tumors', *Int J Radiat Oncol Biol Phys*, 102(2), pp. 391-398.

Qin, N., Li, Z., Song, N., Wilson, C.L., Easton, J., Mulder, H., Plyler, E., Neale, G., Walker, E., Zhou, X., Pan, H., Hudson, M.M., Yasui, Y., Robison, L.L., Zhang, J., Ness, K.K. and Wang, Z. (2021) 'Epigenetic Age Acceleration and Chronic Health Conditions Among Adult Survivors of Childhood Cancer', *J Natl Cancer Inst*, 113(5), pp. 597-605.
Ramanan, S., Kooshki, M., Zhao, W., Hsu, F.C., Riddle, D.R. and Robbins, M.E. (2009) 'The PPARalpha agonist fenofibrate preserves hippocampal neurogenesis and inhibits microglial activation after whole-brain irradiation', *Int J Radiat Oncol Biol Phys*, 75(3), pp. 870-7.
Ramaswamy, V., Remke, M., Bouffet, E., Bailey, S., Clifford, S.C., Doz, F., Kool, M., Dufour, C., Vassal, G., Milde, T., Witt, O., von Hoff, K., Pietsch, T., Northcott, P.A., Gajjar, A., Robinson, G.W., Padovani, L., André, N., Massimino, M., Pizer, B., Packer, R., Rutkowski, S., Pfister, S.M., Taylor, M.D. and Pomeroy, S.L. (2016) 'Risk stratification of childhood medulloblastoma in the molecular era: the current consensus', *Acta Neuropathol*, 131(6), pp. 821-31.
Rang, F.J. and Boonstra, J. (2014) 'Causes and Consequences of Age-Related Changes in DNA Methylation: A Role for ROS?', *Biology (Basel)*, 3(2), pp. 403-25.
Rao, A.A., Ye, H., Decker, P.A., Howe, C.L. and Wetmore, C. (2011) 'Therapeutic doses of cranial irradiation induce hippocampus-dependent cognitive deficits in young mice', *J Neurooncol*, 105(2), pp. 191-8.
Remke, M. and Ramaswamy, V. (2018) 'Infant medulloblastoma — learning new lessons from old strata', *Nature Reviews Clinical Oncology*, 15(11), pp. 659-660.
Reulen, R.C., Frobisher, C., Winter, D.L., Kelly, J., Lancashire, E.R., Stiller, C.A., Pritchard-Jones, K., Jenkinson, H.C. and Hawkins, M.M. (2011) 'Long-term risks of subsequent primary neoplasms among survivors of childhood cancer', *Jama*, 305(22), pp. 2311-9.
Ribi, K., Relly, C., Landolt, M.A., Alber, F.D., Boltshauser, E. and Grotzer, M.A. (2005) 'Outcome of medulloblastoma in children: long-term complications and quality of life', *Neuropediatrics*, 36(6), pp. 357-65.
Ridola, V., Grill, J., Doz, F., Gentet, J.C., Frappaz, D., Raquin, M.A., Habrand, J.L., Sainte-Rose, C., Valteau-Couanet, D. and Kalifa, C. (2007) 'High-dose chemotherapy with autologous stem cell rescue followed by posterior fossa irradiation for local medulloblastoma recurrence or progression after conventional chemotherapy', *Cancer*, 110(1), pp. 156-63.
Ris, M.D., Packer, R., Goldwein, J., Jones-Wallace, D. and Boyett, J.M. (2001) 'Intellectual outcome after reduced-dose radiation therapy plus adjuvant chemotherapy for medulloblastoma: a Children's Cancer Group study', *J Clin Oncol*, 19(15), pp. 3470-6.
Robbins, M., Greene-Schloesser, D., Peiffer, A., Shaw, E., Chan, M. and Wheeler, K. (2012) 'Radiation-induced brain injury: A review', *Frontiers in Oncology*, 2(73).
Robinson, G.W., Rudneva, V.A., Buchhalter, I., Billups, C.A., Waszak, S.M., Smith, K.S., Bowers, D.C., Bendel, A., Fisher, P.G., Partap, S., Crawford, J.R., Hassall, T., Indelicato, D.J., Boop, F., Klimo, P., Sabin, N.D., Patay, Z., Merchant, T.E., Stewart, C.F., Orr, B.A., Korbel, J.O., Jones, D.T.W., Sharma, T., Lichter, P., Kool, M., Korshunov, A., Pfister, S.M., Gilbertson, R.J., Sanders, R.P., Onar-Thomas, A., Ellison, D.W., Gajjar, A. and Northcott, P.A. (2018) 'Risk-adapted therapy for young children with medulloblastoma (SJYC07): therapeutic and molecular outcomes from a multicentre, phase 2 trial', *The Lancet Oncology*, 19(6), pp. 768-784.
Rochfort, K.D. and Cummins, P.M. (2015) 'The blood-brain barrier endothelium: a target for pro-inflammatory cytokines', *Biochem Soc Trans*, 43(4), pp. 702-6.
Rockwood, K., Blodgett, J.M., Theou, O., Sun, M.H., Feridooni, H.A., Mitnitski, A., Rose, R.A., Godin, J., Gregson, E. and Howlett, S.E. (2017) 'A Frailty Index Based On Deficit Accumulation Quantifies Mortality Risk in Humans and in Mice', *Sci Rep*, 7, p. 43068.
Rodgers, S.P., Zawaski, J.A., Sahnoune, I., Leasure, J.L. and Gaber, M.W. (2016) 'Radiation-Induced Growth Retardation and Microstructural and Metabolite Abnormalities in the Hippocampus', *Neural Plast*, 2016, p. 3259621.
Roussel, M.F. and Robinson, G.W. (2013) 'Role of MYC in Medulloblastoma', *Cold Spring Harb Perspect Med*, 3(11).

Ruddy, R.M., Derkach, D., Dadwal, P. and Morshead, C.M. (2020) 'Cranial irradiation in juvenile mice leads to early and sustained defects in the stem and progenitor cell pools and late cognitive impairments', *Brain Res*, 1727, p. 146548.
Russell, W.M.S., Burch, R.L. and Hume, C.W. (1959) *The principles of humane experimental technique*. Methuen London.
Rutkowski, S., Bode, U., Deinlein, F., Ottensmeier, H., Warmuth-Metz, M., Soerensen, N., Graf, N., Emser, A., Pietsch, T., Wolff, J.E., Kortmann, R.D. and Kuehl, J. (2005) 'Treatment of early childhood medulloblastoma by postoperative chemotherapy alone', *N Engl J Med*, 352(10), pp. 978-86.
Rutkowski, S., von Hoff, K., Emser, A., Zwiener, I., Pietsch, T., Figarella-Branger, D., Giangaspero, F., Ellison, D.W., Garre, M.L., Biassoni, V., Grundy, R.G., Finlay, J.L., Dhall, G., Raquin, M.A. and Grill, J. (2010) 'Survival and prognostic factors of early childhood medulloblastoma: an international meta-analysis', *J Clin Oncol*, 28(33), pp. 4961-8.
Ryu, S.H., Park, J.H., Jeong, E.S., Choi, S.Y., Ham, S.H., Park, J.I., Jeon, H.Y., Kim, J.Y., Yoo, R.J., Lee, Y.J., Woo, S.K. and Choi, Y.K. (2016) 'Establishment of a mouse model of 70% lethal dose by total-body irradiation', *Lab Anim Res*, 32(2), pp. 116-21.
Safer, D.J., Zito, J.M. and Fine, E.M. (1996) 'Increased methylphenidate usage for attention deficit disorder in the 1990s', *Pediatrics*, 98(6 Pt 1), pp. 1084-8.
Saghir, S.A., Ansari, R.A. and Dorato, M.A. (2020) 'Rethinking toxicity testing: Influence of aging on the outcome of long-term toxicity testing and possible remediation', *Food and Chemical Toxicology*, 141, p. 111327.
Saki, M., Bhat, K., Sodhi, S.S., Nguyen, N.T., Kornblum, H.I. and Pajonk, F. (2020) 'Effects of Brain Irradiation in Immune-Competent and Immune-Compromised Mouse Models', *Radiat Res*, 193(2), pp. 186-194.
Salameh, Y., Bejaoui, Y. and El Hajj, N. (2020) 'DNA Methylation Biomarkers in Aging and Age-Related Diseases', *Frontiers in Genetics*, 11.
Salloum, R., Chen, Y., Yasui, Y., Packer, R., Leisenring, W., Wells, E., King, A., Howell, R., Gibson, T.M., Krull, K.R., Robison, L.L., Oeffinger, K.C., Fouladi, M. and Armstrong, G.T. (2019) 'Late Morbidity and Mortality Among Medulloblastoma Survivors Diagnosed Across Three Decades: A Report From the Childhood Cancer Survivor Study', *J Clin Oncol*, 37(9), pp. 731-740.
Sándor, N., Walter, F.R., Bocsik, A., Sántha, P., Schilling-Tóth, B., Léner, V., Varga, Z., Kahán, Z., Deli, M.A., Sáfrány, G. and Hegyesi, H. (2014) 'Low Dose Cranial Irradiation-Induced Cerebrovascular Damage Is Reversible in Mice', *PLOS ONE*, 9(11), p. e112397.
Santivasi, W.L. and Xia, F. (2014) 'Ionizing radiation-induced DNA damage, response, and repair', *Antioxid Redox Signal*, 21(2), pp. 251-9.
Saraiva, M. and O'Garra, A. (2010) 'The regulation of IL-10 production by immune cells', *Nature Reviews Immunology*, 10(3), pp. 170-181.
Sayler, E., Dolney, D., Avery, S. and Koch, C. (2013) 'Shielding considerations for the small animal radiation research platform (SARRP)', *Health Phys*, 104(5), pp. 471-80.
Schnegg, C.I., Greene-Schloesser, D., Kooshki, M., Payne, V.S., Hsu, F.C. and Robbins, M.E. (2013) 'The PPARδ agonist GW0742 inhibits neuroinflammation, but does not restore neurogenesis or prevent early delayed hippocampal-dependent cognitive impairment after whole-brain irradiation', *Free Radic Biol Med*, 61, pp. 1-9.
Schönfeld, L.-M., Dooley, D., Jahanshahi, A., Temel, Y. and Hendrix, S. (2017a) 'Evaluating rodent motor functions: Which tests to choose?', *Neuroscience & Biobehavioral Reviews*, 83, pp. 298-312.
Schönfeld, L.M., Jahanshahi, A., Lemmens, E., Schipper, S., Dooley, D., Joosten, E., Temel, Y. and Hendrix, S. (2017b) 'Long-Term Motor Deficits after Controlled Cortical Impact in Rats Can Be Detected by Fine Motor Skill Tests but Not by Automated Gait Analysis', *J Neurotrauma*, 34(2), pp. 505-516.
Schwalbe, E.C., Lindsey, J.C., Nakjang, S. and al, e. (2017) 'Novel molecular subgroups for clinical classification and outcome prediction in childhood medulloblastoma: a cohort study', *The Lancet Oncology*, 18(7), pp. 958-971.

Seibert, T.M., Karunamuni, R., Kaifi, S., Burkeen, J., Connor, M., Krishnan, A.P., White, N.S., Farid, N., Bartsch, H., Murzin, V., Nguyen, T.T., Moiseenko, V., Brewer, J.B., McDonald, C.R., Dale, A.M. and Hattangadi-Gluth, J.A. (2017) 'Cerebral Cortex Regions Selectively Vulnerable to Radiation Dose-Dependent Atrophy', *Int J Radiat Oncol Biol Phys*, 97(5), pp. 910-918.
Sharma, T., Schwalbe, E.C., Williamson, D. and al, e. (2019) 'Second-generation molecular subgrouping of medulloblastoma: an international meta-analysis of Group 3 and Group 4 subtypes', *Acta Neuropathologica*, 138, pp. 309-326.
Shimura, T., Sasatani, M., Kawai, H., Kamiya, K., Kobayashi, J., Komatsu, K. and Kunugita, N. (2018) 'Radiation-Induced Myofibroblasts Promote Tumor Growth via Mitochondrial ROS-Activated TGFβ Signaling', *Mol Cancer Res*, 16(11), pp. 1676-1686.
Shin, S.J., Dodd-Eaton, E.B., Gao, F., Bojadzieva, J., Chen, J., Kong, X., Amos, C.I., Ning, J., Strong, L.C. and Wang, W. (2020) 'Penetrance Estimates Over Time to First and Second Primary Cancer Diagnosis in Families with Li-Fraumeni Syndrome: A Single Institution Perspective', *Cancer Research*, 80(2), pp. 347-353.
Short, S., Fielder, E., Miwa, S. and von Zglinicki, T. (2019) 'Senolytics and senostatics as adjuvant tumour therapy', *EBioMedicine*, 41, pp. 683-692.
Siddiqui, J.A., Pothuraju, R., Khan, P., Sharma, G., Muniyan, S., Seshacharyulu, P., Jain, M., Nasser, M.W. and Batra, S.K. (2022) 'Pathophysiological role of growth differentiation factor 15 (GDF15) in obesity, cancer, and cachexia', *Cytokine & Growth Factor Reviews*, 64, pp. 71-83.
Simmons, D.A., Lartey, F.M., Schüler, E., Rafat, M., King, G., Kim, A., Ko, R., Semaan, S., Gonzalez, S., Jenkins, M., Pradhan, P., Shih, Z., Wang, J., von Eyben, R., Graves, E.E., Maxim, P.G., Longo, F.M. and Loo, B.W., Jr. (2019) 'Reduced cognitive deficits after FLASH irradiation of whole mouse brain are associated with less hippocampal dendritic spine loss and neuroinflammation', *Radiother Oncol*, 139, pp. 4-10.
Śmieszek, A., Stręk, Z., Kornicka, K., Grzesiak, J., Weiss, C. and Marycz, K. (2017) 'Antioxidant and Anti-Senescence Effect of Metformin on Mouse Olfactory Ensheathing Cells (mOECs) May Be Associated with Increased Brain-Derived Neurotrophic Factor Levels-An Ex Vivo Study', *Int J Mol Sci*, 18(4).
Smoll, N.R. (2012) 'Relative survival of childhood and adult medulloblastomas and primitive neuroectodermal tumors (PNETs)', *Cancer*, 118(5), pp. 1313-22.
Sousa, N., Almeida, O.F. and Wotjak, C.T. (2006) 'A hitchhiker's guide to behavioral analysis in laboratory rodents', *Genes Brain Behav*, 5 Suppl 2, pp. 5-24.
Spiegler, B.J., Bouffet, E., Greenberg, M.L., Rutka, J.T. and Mabbott, D.J. (2004) 'Change in neurocognitive functioning after treatment with cranial radiation in childhood', *Journal of Clinical Oncology*, 22(4), pp. 706-713.
Stanley, T. (2012) 'Diagnosis of growth hormone deficiency in childhood', *Curr Opin Endocrinol Diabetes Obes*, 19(1), pp. 47-52.
Streit, W.J., Mrak, R.E. and Griffin, W.S. (2004) 'Microglia and neuroinflammation: a pathological perspective', *J Neuroinflammation*, 1(1), p. 14.
Suckert, T., Beyreuther, E., Müller, J., Azadegan, B., Meinhardt, M., Raschke, F., Bodenstein, E., von Neubeck, C., Lühr, A., Krause, M. and Dietrich, A. (2021) 'Late Side Effects in Normal Mouse Brain Tissue After Proton Irradiation', *Frontiers in Oncology*, 10.
Sun, Y., Coppé, J.P. and Lam, E.W. (2018) 'Cellular Senescence: The Sought or the Unwanted?', *Trends Mol Med*, 24(10), pp. 871-885.
Suri, J.S., Rednam, S., Teh, B.S., Butler, E. and Paulino, A.C. (2013) 'Subsequent Malignancies in Patients With Li-Fraumeni Syndrome Treated With Radiation Therapy', *International Journal of Radiation Oncology*Biology*Physics*, 87(2, Supplement), pp. S71-S72.
Tait, D.M., Thornton-Jones, H., Bloom, H.J., Lemerle, J. and Morris-Jones, P. (1990) 'Adjuvant chemotherapy for medulloblastoma: the first multi-centre control trial of the International Society of Paediatric Oncology (SIOP I)', *Eur J Cancer*, 26(4), pp. 464-9.

Takeda, A., Takada, S., Ando, M., Itagaki, K., Tamano, H., Suzuki, M., Iwaki, H. and Oku, N. (2010) 'Impairment of recognition memory and hippocampal long-term potentiation after acute exposure to clioquinol', *Neuroscience*, 171(2), pp. 443-50.
Tang, T.T., Zawaski, J.A., Kesler, S.R., Beamish, C.A., Reddick, W.E., Glass, J.O., Carney, D.H., Sabek, O.M., Grosshans, D.R. and Gaber, M.W. (2019) 'A comprehensive preclinical assessment of late-term imaging markers of radiation-induced brain injury', *Neurooncol Adv*, 1(1), p. vdz012.
Taylor, M.D., Northcott, P.A., Korshunov, A., Remke, M., Cho, Y.J., Clifford, S.C., Eberhart, C.G., Parsons, D.W., Rutkowski, S., Gajjar, A., Ellison, D.W., Lichter, P., Gilbertson, R.J., Pomeroy, S.L., Kool, M. and Pfister, S.M. (2012) 'Molecular subgroups of medulloblastoma: the current consensus', *Acta Neuropathol*, 123(4), pp. 465-72.
Taylor, R.E., Bailey, C.C., Robinson, K., Weston, C.L., Ellison, D., Ironside, J., Lucraft, H., Gilbertson, R., Tait, D.M., Walker, D.A., Pizer, B.L., Imeson, J. and Lashford, L.S. (2003) 'Results of a randomized study of preradiation chemotherapy versus radiotherapy alone for nonmetastatic medulloblastoma: The International Society of Paediatric Oncology/United Kingdom Children's Cancer Study Group PNET-3 Study', *J Clin Oncol*, 21(8), pp. 1581-91.
Taylor, R.E., Bailey, C.C., Robinson, K.J., Weston, C.L., Ellison, D., Ironside, J., Lucraft, H., Gilbertson, R., Tait, D.M., Saran, F., Walker, D.A., Pizer, B.L. and Lashford, L.S. (2004) 'Impact of radiotherapy parameters on outcome in the International Society of Paediatric Oncology/United Kingdom Children's Cancer Study Group PNET-3 study of preradiotherapy chemotherapy for M0-M1 medulloblastoma', *Int J Radiat Oncol Biol Phys*, 58(4), pp. 1184-93.
Taylor, R.E., Bailey, C.C., Robinson, K.J., Weston, C.L., Walker, D.A., Ellison, D., Ironside, J., Pizer, B.L. and Lashford, L.S. (2005) 'Outcome for patients with metastatic (M2–3) medulloblastoma treated with SIOP/UKCCSG PNET-3 chemotherapy', *European Journal of Cancer*, 41(5), pp. 727-734.
Teo, W.Y., Shen, J., Su, J.M., Yu, A., Wang, J., Chow, W.Y., Li, X., Jones, J., Dauser, R., Whitehead, W., Adesina, A.M., Chintagumpala, M., Man, T.K. and Lau, C.C. (2013) 'Implications of tumor location on subtypes of medulloblastoma', *Pediatr Blood Cancer*, 60(9), pp. 1408-10.
Thompson, E.M., Hielscher, T., Bouffet, E., Remke, M., Luu, B., Gururangan, S., McLendon, R.E., Bigner, D.D., Lipp, E.S., Perreault, S., Cho, Y.J., Grant, G., Kim, S.K., Lee, J.Y., Rao, A.A.N., Giannini, C., Li, K.K.W., Ng, H.K., Yao, Y., Kumabe, T., Tominaga, T., Grajkowska, W.A., Perek-Polnik, M., Low, D.C.Y., Seow, W.T., Chang, K.T.E., Mora, J., Pollack, I.F., Hamilton, R.L., Leary, S., Moore, A.S., Ingram, W.J., Hallahan, A.R., Jouvet, A., Fèvre-Montange, M., Vasiljevic, A., Faure-Conter, C., Shofuda, T., Kagawa, N., Hashimoto, N., Jabado, N., Weil, A.G., Gayden, T., Wataya, T., Shalaby, T., Grotzer, M., Zitterbart, K., Sterba, J., Kren, L., Hortobágyi, T., Klekner, A., László, B., Pócza, T., Hauser, P., Schüller, U., Jung, S., Jang, W.Y., French, P.J., Kros, J.M., van Veelen, M.C., Massimi, L., Leonard, J.R., Rubin, J.B., Vibhakar, R., Chambless, L.B., Cooper, M.K., Thompson, R.C., Faria, C.C., Carvalho, A., Nunes, S., Pimentel, J., Fan, X., Muraszko, K.M., López-Aguilar, E., Lyden, D., Garzia, L., Shih, D.J.H., Kijima, N., Schneider, C., Adamski, J., Northcott, P.A., Kool, M., Jones, D.T.W., Chan, J.A., Nikolic, A., Garre, M.L., Van Meir, E.G., Osuka, S., Olson, J.J., Jahangiri, A., Castro, B.A., Gupta, N., Weiss, W.A., Moxon-Emre, I., Mabbott, D.J., Lassaletta, A., Hawkins, C.E., Tabori, U., Drake, J., Kulkarni, A., et al. (2016) 'Prognostic value of medulloblastoma extent of resection after accounting for molecular subgroup: a retrospective integrated clinical and molecular analysis', *Lancet Oncol*, 17(4), pp. 484-495.
Thompson, J., George, E.O., Poquette, C.A., Cheshire, P.J., Richmond, L.B., de Graaf, S.S., Ma, M., Stewart, C.F. and Houghton, P.J. (1999) 'Synergy of topotecan in combination with vincristine for treatment of pediatric solid tumor xenografts', *Clin Cancer Res*, 5(11), pp. 3617-31.
Thompson, S.J., Leigh, L., Christensen, R., Xiong, X., Kun, L.E., Heideman, R.L., Reddick, W.E., Gajjar, A., Merchant, T., Pui, C.H., Hudson, M.M. and Mulhern, R.K. (2001) 'Immediate neurocognitive effects of methylphenidate on learning-impaired survivors of childhood cancer', *J Clin Oncol*, 19(6), pp. 1802-8.
Tohamy, A.F., Hussein, S., Moussa, I.M., Rizk, H., Daghash, S., Alsubki, R.A., Mubarak, A.S., Alshammari, H.O., Al-Maary, K.S. and Hemeg, H.A. (2021) 'Lucrative antioxidant effect of metformin against cyclophosphamide induced nephrotoxicity', *Saudi J Biol Sci*, 28(5), pp. 2755-2761.

Tomé, W.A., Gökhan, Ş., Brodin, N.P., Gulinello, M.E., Heard, J., Mehler, M.F. and Guha, C. (2015) 'A mouse model replicating hippocampal sparing cranial irradiation in humans: A tool for identifying new strategies to limit neurocognitive decline', *Sci Rep*, 5, p. 14384.
Turnquist, C., Beck, J.A., Horikawa, I., Obiorah, I.E., Von Muhlinen, N., Vojtesek, B., Lane, D.P., Grunseich, C., Chahine, J.J., Ames, H.M., Smart, D.D., Harris, B.T. and Harris, C.C. (2019) 'Radiation-induced astrocyte senescence is rescued by Δ133p53', *Neuro Oncol*, 21(4), pp. 474-485.
Turnquist, C., Harris, B.T. and Harris, C.C. (2020a) 'Radiation-induced brain injury: current concepts and therapeutic strategies targeting neuroinflammation', *Neurooncol Adv*, 2(1), p. vdaa057.
Turnquist, C., Harris, B.T. and Harris, C.C. (2020b) 'Radiation-induced brain injury: current concepts and therapeutic strategies targeting neuroinflammation', *Neuro-Oncology Advances*, 2(1).
Uh, J., Merchant, T.E., Conklin, H.M., Ismael, Y., Li, Y., Han, Y., Sabin, N.D., Babajani-Feremi, A., Indelicato, D.J. and Hua, C.H. (2021) 'Diffusion Tensor Imaging-Based Analysis of Baseline Neurocognitive Function and Posttreatment White Matter Changes in Pediatric Patients With Craniopharyngioma Treated With Surgery and Proton Therapy', *Int J Radiat Oncol Biol Phys*, 109(2), pp. 515-526.
Ungvari, Z., Podlutsky, A., Sosnowska, D., Tucsek, Z., Toth, P., Deak, F., Gautam, T., Csiszar, A. and Sonntag, W.E. (2013) 'Ionizing radiation promotes the acquisition of a senescence-associated secretory phenotype and impairs angiogenic capacity in cerebromicrovascular endothelial cells: role of increased DNA damage and decreased DNA repair capacity in microvascular radiosensitivity', *J Gerontol A Biol Sci Med Sci*, 68(12), pp. 1443-57.
Ungvari, Z., Tarantini, S., Hertelendy, P., Valcarcel-Ares, M.N., Fülöp, G.A., Logan, S., Kiss, T., Farkas, E., Csiszar, A. and Yabluchanskiy, A. (2017) 'Cerebromicrovascular dysfunction predicts cognitive decline and gait abnormalities in a mouse model of whole brain irradiation-induced accelerated brain senescence', *Geroscience*, 39(1), pp. 33-42.
van der Plas, E., Schachar, R.J., Hitzler, J., Crosbie, J., Guger, S.L., Spiegler, B.J., Ito, S. and Nieman, B.J. (2017) 'Brain structure, working memory and response inhibition in childhood leukemia survivors', *Brain Behav*, 7(2), p. e00621.
Varedi, M., Lu, L., Phillips, N.S., Partin, R.E., Brinkman, T.M., Armstrong, G.T., Chase, E., Khan, R.B., Powell, D., McKenna, R.F., Robison, L.L., Hudson, M.M. and Ness, K.K. (2021) 'Balance impairment in survivors of pediatric brain cancers: risk factors and associated physical limitations', *J Cancer Surviv*, 15(2), pp. 311-324.
von Bueren, A.O., von Hoff, K., Pietsch, T., Gerber, N.U., Warmuth-Metz, M., Deinlein, F., Zwiener, I., Faldum, A., Fleischhack, G., Benesch, M., Krauss, J., Kuehl, J., Kortmann, R.D. and Rutkowski, S. (2011) 'Treatment of young children with localized medulloblastoma by chemotherapy alone: results of the prospective, multicenter trial HIT 2000 confirming the prognostic impact of histology', *Neuro Oncol*, 13(6), pp. 669-79.
Vorhees, C.V. and Williams, M.T. (2006) 'Morris water maze: procedures for assessing spatial and related forms of learning and memory', *Nat Protoc*, 1(2), pp. 848-58.
Wallace, M., Luine, V., Arellanos, A. and Frankfurt, M. (2006) 'Ovariectomized rats show decreased recognition memory and spine density in the hippocampus and prefrontal cortex', *Brain Research*, 1126(1), pp. 176-182.
Walter, A.W., Mulhern, R.K., Gajjar, A., Heideman, R.L., Reardon, D., Sanford, R.A., Xiong, X. and Kun, L.E. (1999) 'Survival and neurodevelopmental outcome of young children with medulloblastoma at St Jude Children's Research Hospital', *J Clin Oncol*, 17(12), pp. 3720-8.
Wang, B., Kohli, J. and Demaria, M. (2020) 'Senescent Cells in Cancer Therapy: Friends or Foes?', *Trends Cancer*, 6(10), pp. 838-857.
Wang, S., Lai, X., Deng, Y. and Song, Y. (2020) 'Correlation between mouse age and human age in anti-tumor research: Significance and method establishment', *Life Sciences*, 242, p. 117242.
Wang, Y., Boerma, M. and Zhou, D. (2016) 'Ionizing Radiation-Induced Endothelial Cell Senescence and Cardiovascular Diseases', *Radiat Res*, 186(2), pp. 153-61.

Wang, Y., Fu, W.Y., Cheung, K., Hung, K.W., Chen, C., Geng, H., Yung, W.H., Qu, J.Y., Fu, A.K.Y. and Ip, N.Y. (2021) 'Astrocyte-secreted IL-33 mediates homeostatic synaptic plasticity in the adult hippocampus', *Proc Natl Acad Sci U S A*, 118(1).
Watts, S.J., Halliday, G., Ryles, J. and Bailey, S. (2018) 'QOL-06. METHYLPHENIDATE IMPROVES HEALTH-RELATED QUALITY OF LIFE AND ATTENTIONAL IMPAIRMENT IN PAEDIATRIC NEURO-ONCOLOGY SURVIVORS', *Neuro Oncol*, 20(Suppl 2), p. i158.
Whitehead, J.C., Hildebrand, B.A., Sun, M., Rockwood, M.R., Rose, R.A., Rockwood, K. and Howlett, S.E. (2014) 'A clinical frailty index in aging mice: comparisons with frailty index data in humans', *J Gerontol A Biol Sci Med Sci*, 69(6), pp. 621-32.
Williamson, D., Schwalbe, E.C., Hicks, D., Aldinger, K.A., Lindsey, J.C., Crosier, S., Richardson, S., Goddard, J., Hill, R.M., Castle, J., Grabovska, Y., Hacking, J., Pizer, B., Wharton, S.B., Jacques, T.S., Joshi, A., Bailey, S. and Clifford, S.C. (2022) 'Medulloblastoma group 3 and 4 tumors comprise a clinically and biologically significant expression continuum reflecting human cerebellar development', *Cell Rep*, 40(5), p. 111162.
Winocur, G., Wojtowicz, J.M., Sekeres, M., Snyder, J.S. and Wang, S. (2006) 'Inhibition of neurogenesis interferes with hippocampus-dependent memory function', *Hippocampus*, 16(3), pp. 296-304.
Wolfe, K.R., Hunter, G.R., Madan-Swain, A., Reddy, A.T., Baños, J. and Kana, R.K. (2012) 'Cardiorespiratory fitness in survivors of pediatric posterior fossa tumor', *J Pediatr Hematol Oncol*, 34(6), pp. e222-7.
Wong-Goodrich, S.J., Pfau, M.L., Flores, C.T., Fraser, J.A., Williams, C.L. and Jones, L.W. (2010) 'Voluntary running prevents progressive memory decline and increases adult hippocampal neurogenesis and growth factor expression after whole-brain irradiation', *Cancer Res*, 70(22), pp. 9329-38.
Wong, J., Armour, E., Kazanzides, P., Iordachita, I., Tryggestad, E., Deng, H., Matinfar, M., Kennedy, C., Liu, Z., Chan, T., Gray, O., Verhaegen, F., McNutt, T., Ford, E. and DeWeese, T.L. (2008) 'High-resolution, small animal radiation research platform with x-ray tomographic guidance capabilities', *Int J Radiat Oncol Biol Phys*, 71(5), pp. 1591-9.
Xu, G., Wu, H., Zhang, J., Li, D., Wang, Y., Wang, Y., Zhang, H., Lu, L., Li, C., Huang, S., Xing, Y., Zhou, D. and Meng, A. (2015) 'Metformin ameliorates ionizing irradiation-induced long-term hematopoietic stem cell injury in mice', *Free Radic Biol Med*, 87, pp. 15-25.
Yabluchanskiy, A., Tarantini, S., Balasubramanian, P., Kiss, T., Csipo, T., Fülöp, G.A., Lipecz, A., Ahire, C., DelFavero, J., Nyul-Toth, A., Sonntag, W.E., Schwartzman, M.L., Campisi, J., Csiszar, A. and Ungvari, Z. (2020) 'Pharmacological or genetic depletion of senescent astrocytes prevents whole brain irradiation-induced impairment of neurovascular coupling responses protecting cognitive function in mice', *Geroscience*, 42(2), pp. 409-428.
Yamada, S., Itoh, N., Nagai, T., Nakai, T., Ibi, D., Nakajima, A., Nabeshima, T. and Yamada, K. (2018) 'Innate immune activation of astrocytes impairs neurodevelopment via upregulation of follistatin-like 1 and interferon-induced transmembrane protein 3', *Journal of Neuroinflammation*, 15(1), p. 295.
Yang, M., Kim, J.S., Song, M.S., Kim, S.H., Kang, S.S., Bae, C.S., Kim, J.C., Wang, H., Shin, T. and Moon, C. (2010) 'Cyclophosphamide impairs hippocampus-dependent learning and memory in adult mice: Possible involvement of hippocampal neurogenesis in chemotherapy-induced memory deficits', *Neurobiol Learn Mem*, 93(4), pp. 487-94.
Yazlovitskaya, E.M., Edwards, E., Thotala, D., Fu, A., Osusky, K.L., Whetsell, W.O., Jr., Boone, B., Shinohara, E.T. and Hallahan, D.E. (2006) 'Lithium Treatment Prevents Neurocognitive Deficit Resulting from Cranial Irradiation', *Cancer Research*, 66(23), pp. 11179-11186.
Yock, T.I., Yeap, B.Y., Ebb, D.H., Weyman, E., Eaton, B.R., Sherry, N.A., Jones, R.M., MacDonald, S.M., Pulsifer, M.B., Lavally, B., Abrams, A.N., Huang, M.S., Marcus, K.J. and Tarbell, N.J. (2016) 'Long-term toxic effects of proton radiotherapy for paediatric medulloblastoma: a phase 2 single-arm study', *Lancet Oncol*, 17(3), pp. 287-298.

Yon, J.H., Daniel-Johnson, J., Carter, L.B. and Jevtovic-Todorovic, V. (2005) 'Anesthesia induces neuronal cell death in the developing rat brain via the intrinsic and extrinsic apoptotic pathways', *Neuroscience*, 135(3), pp. 815-27.
Yoshizaki, K., Asai, M. and Hara, T. (2020) 'High-Fat Diet Enhances Working Memory in the Y-Maze Test in Male C57BL/6J Mice with Less Anxiety in the Elevated Plus Maze Test', *Nutrients*, 12(7).
Yousuf, S., Brat, D.J., Shu, H.-K., Wang, Y., Stein, D.G. and Atif, F. (2017) 'Progesterone improves neurocognitive outcomes following therapeutic cranial irradiation in mice', *Hormones and Behavior*, 96, pp. 21-30.
Yuen, N., Szulc-Lerch, K.U., Li, Y.-Q., Morshead, C.M., Mabbott, D.J., Wong, C.S. and Nieman, B.J. (2021) 'Metformin effects on brain development following cranial irradiation in a mouse model', *Neuro-Oncology*, 23(9), pp. 1523-1536.
Zanni, G., Goto, S., Fragopoulou, A.F., Gaudenzi, G., Naidoo, V., Di Martino, E., Levy, G., Dominguez, C.A., Dethlefsen, O., Cedazo-Minguez, A., Merino-Serrais, P., Stamatakis, A., Hermanson, O. and Blomgren, K. (2021) 'Lithium treatment reverses irradiation-induced changes in rodent neural progenitors and rescues cognition', *Molecular Psychiatry*, 26(1), pp. 322-340.
Zhang, D., Zhou, W., Lam, T.T., Weng, C., Bronk, L., Ma, D., Wang, Q., Duman, J.G., Dougherty, P.M. and Grosshans, D.R. (2018) 'Radiation induces age-dependent deficits in cortical synaptic plasticity', *Neuro Oncol*, 20(9), pp. 1207-1214.
Zhao, H., Alam, A., San, C.Y., Eguchi, S., Chen, Q., Lian, Q. and Ma, D. (2017) 'Molecular mechanisms of brain-derived neurotrophic factor in neuro-protection: Recent developments', *Brain Res*, 1665, pp. 1-21.
Zhao, W., Diz, D.I. and Robbins, M.E. (2007) 'Oxidative damage pathways in relation to normal tissue injury', *The British Journal of Radiology*, 80(special_issue_1), pp. S23-S31.
Zhou, K., Xie, C., Wickström, M., Dolga, A.M., Zhang, Y., Li, T., Xu, Y., Culmsee, C., Kogner, P., Zhu, C. and Blomgren, K. (2017) 'Lithium protects hippocampal progenitors, cognitive performance and hypothalamus–pituitary function after irradiation to the juvenile rat brain', *Oncotarget*, 8(21).
Zhou, W., Hinoue, T., Barnes, B., Mitchell, O., Iqbal, W., Lee, S.M., Foy, K.K., Lee, K.H., Moyer, E.J., VanderArk, A., Koeman, J.M., Ding, W., Kalkat, M., Spix, N.J., Eagleson, B., Pospisilik, J.A., Szabó, P.E., Bartolomei, M.S., Vander Schaaf, N.A., Kang, L., Wiseman, A.K., Jones, P.A., Krawczyk, C.M., Adams, M., Porecha, R., Chen, B.H., Shen, H. and Laird, P.W. (2022) 'DNA methylation dynamics and dysregulation delineated by high-throughput profiling in the mouse', *Cell Genom*, 2(7).
Zhou, W., Kavelaars, A. and Heijnen, C.J. (2016) 'Metformin Prevents Cisplatin-Induced Cognitive Impairment and Brain Damage in Mice', *PLoS One*, 11(3), p. e0151890.
Zhou, W., Triche, T.J., Jr., Laird, P.W. and Shen, H. (2018) 'SeSAMe: reducing artifactual detection of DNA methylation by Infinium BeadChips in genomic deletions', *Nucleic Acids Res*, 46(20), p. e123.

Appendix 1: Comparison of body weight between sham and CRT+/- PFB (Chapter 3)

Day	P (CRT only vs sham)	P (CRT+PFB vs sham)
28	0.989	0.983
30	0.989	0.983
42	0.563	0.983
43	0.489	0.983
44	0.489	0.983
45	0.489	0.983
46	0.489	0.983
49	0.489	0.983
50	0.489	0.983
51	0.489	0.983
52	0.489	0.983
53	0.489	0.983
60	0.489	0.983
93	0.670	0.983
101	0.563	0.983
108	0.489	0.983
115	0.517	0.983
122	0.590	0.983
129	0.621	0.983
136	0.670	0.983
143	0.670	0.983
150	0.670	0.983
164	0.670	0.983
171	0.783	0.983
178	0.889	0.983
185	0.935	0.983
191	0.935	0.983
200	0.935	0.983
206	0.935	0.983
213	0.889	0.983
220	0.989	1.000
227	0.948	0.983
233	0.989	0.983
241	0.989	0.983
248	0.989	0.983
254	0.989	0.983
261	0.989	0.983
269	0.989	0.983
277	0.989	0.983
283	0.989	0.983
290	0.989	0.983
297	0.989	0.983
304	0.989	0.983
311	0.989	0.983
317	0.989	0.983
324	0.989	0.983
332	0.989	0.983
338	0.989	0.983
347	0.989	0.983
355	0.989	0.983
361	0.989	0.983
368	0.989	0.983
376	0.989	0.983
382	0.989	0.983
389	0.989	0.983
394	0.989	0.983

Comparison of body weight relative to start weight for CRT only and CRT+PFB vs sham-irradiation.
Adjusted p-values following independent t-tests.

Appendix 2: Mouse ENCODE transcription data (Chapter 5)

ICAM-1

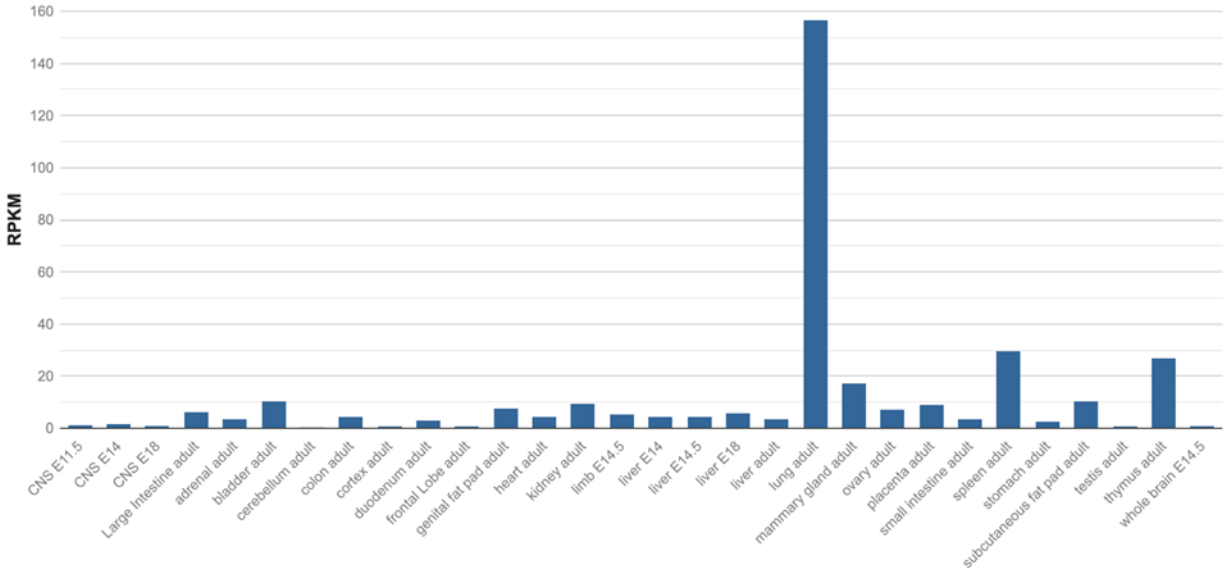

MCP-1

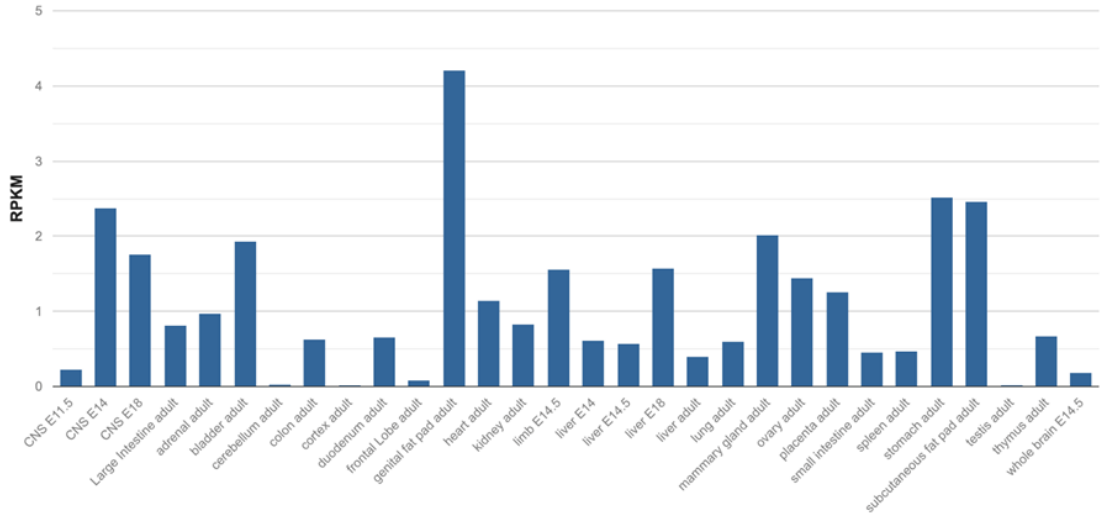

TNF-alpha

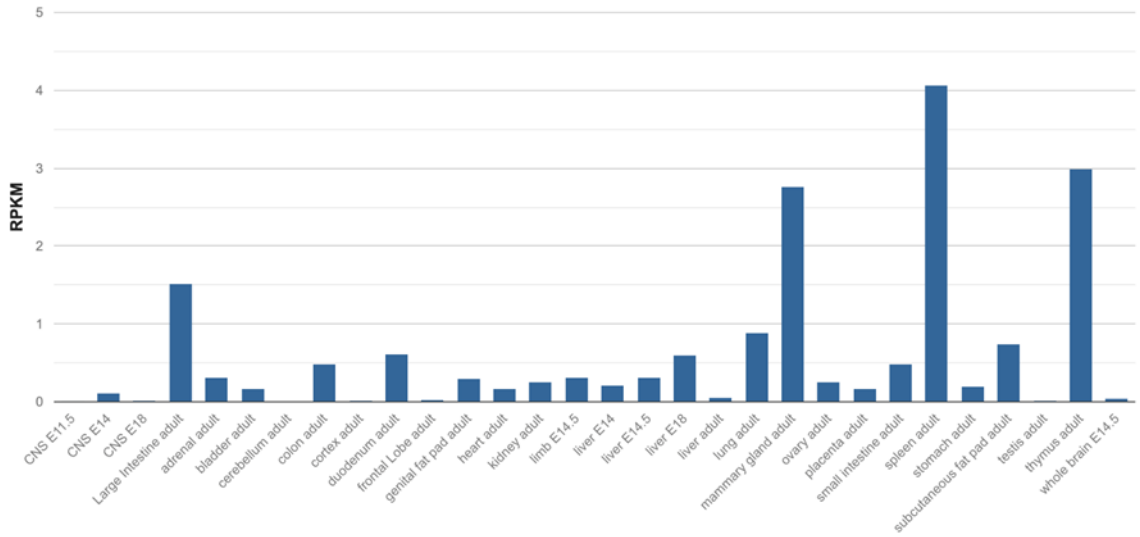

MHCII

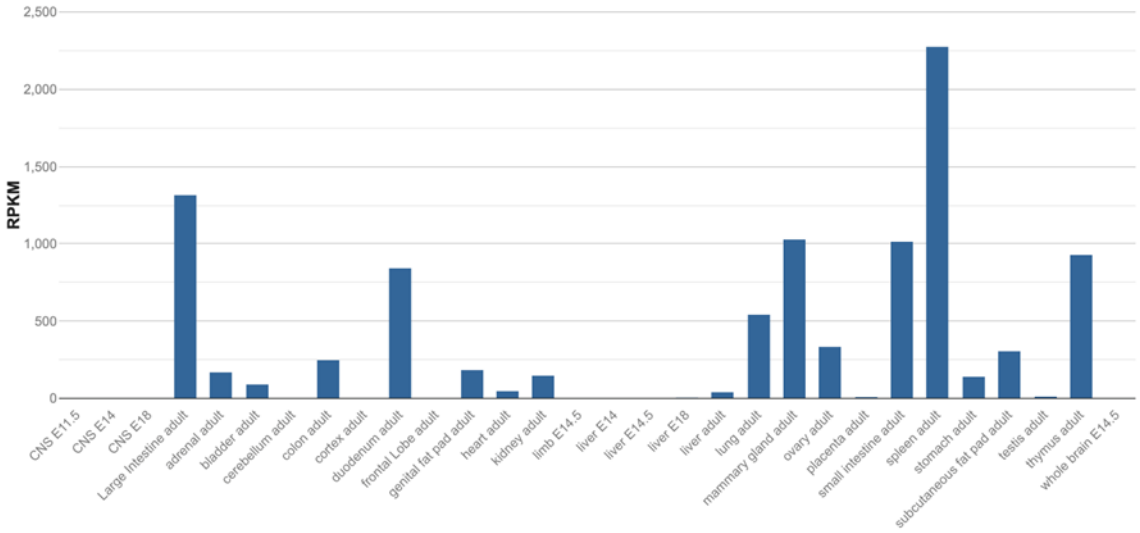

GFAP

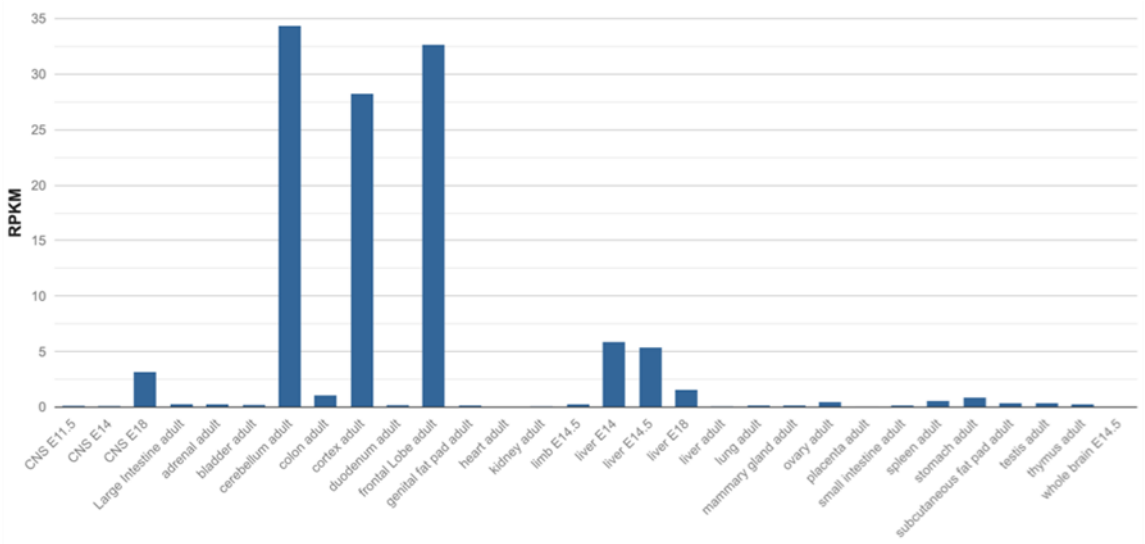

CD3

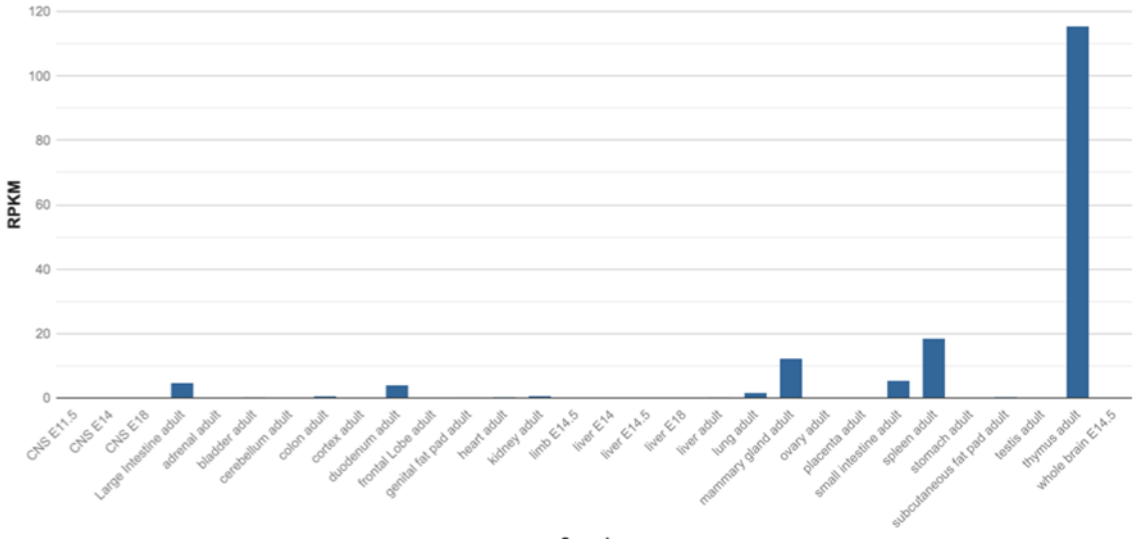

Images copied directly from the NIH National Library of Medicine, National Centre for Biotechnology Information [www.ncbi.nlm.nih.gov/gene/]

Appendix 3: RNA quality control data (Chapter 5)

Sample ID	Treatment group	RIN	Concentration (ng/µL)	Quantity (ng)	Action
1955m1	Sham	8.3	644	9016	Proceed
1955m2	Sham	8.6	27.8	389.2	Proceed
1955m3	Sham	8.9	26.4	369.6	Proceed
1956m1	Sham	9.2	10.2	142.8	Re-extract
1956m2	Sham	7.9	723	10122	Proceed
1956m3	Sham	8.2	778	10892	Proceed
1961m1	Sham	8.8	134	1876	Proceed
1961m2	Sham	7.9	836	10868	Proceed
1961m3	Sham	8.4	370	5180	Proceed
1962m1	Sham	8.6	389	5446	Proceed
1962m2	Sham	8.6	348	4872	Proceed
1962m3	Sham	8.3	485	6790	Proceed
1964	CRT+PFB	8.2	436	6104	Proceed
2164	CRT+PFB	-	3.95	55.3	Re-extract
1957m1	CRT+PFB	8.9	156	2184	Proceed
1957m2	CRT+PFB	8.5	408	5712	Proceed
1957m3	CRT+PFB	8.6	238	3332	Proceed
1958m1	CRT+PFB	9.2	92.6	1296.4	Proceed
1958m2	CRT+PFB	9.1	150	2100	Proceed
1958m3	CRT+PFB	8.8	201	2814	Proceed
1963m1	CRT+PFB	8.3	326	4564	Proceed
1963m2	CRT+PFB	8	519	7266	Proceed
1963m3	CRT+PFB	8.1	626	8764	Proceed
1956m1	sham	8.6	251	3514	Proceed
2164	CRT+PFB	8	794	11116	Proceed

Quality control (QC) of total RNA extracted from cerebellum. QC criteria consisted of quality (RIN ≥7) and quantity (≥150 ng) of RNA extracted from the cerebellum. Samples that passed QC were sent for RNAseq (action = proceed) and samples that failed QC (red; action = re-extract) required RNA extraction from a new piece of the tissue. Repeat extractions are shown at the bottom of the table.

Appendix 4: DNA quality control data (Chapter 5)

		DNA from peripheral blood			DNA from cerebellum		
Sample ID	Treatment group	Concentration (ng/µL)	Quantity (ng)	Sent for methylation array	Concentration (ng/µL)	Quantity (ng)	Sent for methylation array
1956m1	Sham	<1	-	No	51.8	7770	No
1956m2	Sham	2.01	397.98	Yes	7.1	355	Yes
1956m3	Sham	3.36	665.28	Yes	8.56	428	Yes
1955m1	Sham	3.29	651.42	Yes	218	10900	Yes
1955m2	Sham	7.21	1427.58	Yes	934	46700	Yes
1955m3	Sham	3.25	643.5	Yes	79.2	3960	No
1961m1	Sham	4.44	213.12	Yes	4.02	603	Yes
1961m2	Sham	5.98	287.04	Yes	93.2	4660	No
1961m3	Sham	13.9	667.2	Yes	107	5350	Yes
1962m1	Sham	7.01	336.48	Yes	64.6	3230	No
1962m2	Sham	10.2	489.6	Yes	98.8	4940	Yes
1962m3	Sham	26.2	1257.6	Yes	72.2	3610	No
1963m1	CRT+PFB	3.18	629.64	Yes	73.4	11010	Yes
1963m2	CRT+PFB	4.36	863.28	Yes	43.2	2160	Yes
1963m3	CRT+PFB	5.07	1003.86	Yes	60.6	3030	Yes
1964	CRT+PFB	5.84	1156.32	Yes	7.9	395	Yes
2164	CRT+PFB	3.33	659.34	Yes	72	3600	Yes
1958m1	CRT+PFB	6.09	292.32	Yes	24.6	3690	Yes
1958m2	CRT+PFB	8.9	427.2	Yes	26.2	3930	Yes
1958m3	CRT+PFB	15.2	729.6	Yes	13.1	1965	Yes
1957m1	CRT+PFB	12.7	609.6	Yes	40.4	6060	Yes
1957m2	CRT+PFB	22.3	1070.4	Yes	23	3450	Yes
1957m3	CRT+PFB	13.2	633.6	Yes	2.38	357	Yes

DNA extracted from peripheral blood and cerebellum. Red text depicts samples that failed QC. Some samples were not sent for methylation array (despite passing QC) due to limited space on the array.

Neuro-Oncology Advances

6(1), vdae091, 2024 | https://doi.org/10.1093/noajnl/vdae091 | Advance Access date 6 June 2024

In vivo modeling recapitulates radiotherapy delivery and late-effect profile for childhood medulloblastoma

Jemma Castle, Gary Shaw, Dominic Weller, Edward Fielder, Teklu Egnuni, Mankaran Singh, Roderick Skinner, Thomas von Zglinicki, Steven C. Clifford, Susan C. Short‡, Satomi Miwa‡, and Debbie Hicks‡,

All author affiliations are listed at the end of the article

Corresponding Author: Debbie Hicks, PhD, Wolfson Childhood Cancer Research Centre, Newcastle University Centre for Cancer, Translational and Clinical Research Institute, Newcastle University, Newcastle upon Tyne, UK (debbie.Hicks@ncl.ac.uk).

‡These authors contributed equally.

Abstract

Background. Medulloblastoma (MB) is the most common malignant pediatric brain tumor, with 5-year survival rates > 70%. Cranial radiotherapy (CRT) to the whole brain, with posterior fossa boost (PFB), underpins treatment for non-infants; however, radiotherapeutic insult to the normal brain has deleterious consequences to neurocognitive and physical functioning, and causes accelerated aging/frailty. Approaches to ameliorate radiotherapy-induced late-effects are lacking and a paucity of appropriate model systems hinders their development.

Methods. We have developed a clinically relevant in vivo model system that recapitulates the radiotherapy dose, targeting, and developmental stage of childhood medulloblastoma. Consistent with human regimens, age-equivalent (postnatal days 35–37) male C57Bl/6J mice received computerized tomography image-guided CRT (human-equivalent 37.5 Gy EQD2, $n = 12$) ± PFB (human-equivalent 48.7 Gy EQD2, $n = 12$), via the small animal radiation research platform and were longitudinally assessed for > 12 months.

Results. CRT was well tolerated, independent of PFB receipt. Compared to a sham-irradiated group ($n = 12$), irradiated mice were significantly frailer following irradiation (frailty index; $P = .0002$) and had reduced physical functioning; time to fall from a rotating rod (rotarod; $P = .026$) and grip strength ($P = .006$) were significantly lower. Neurocognitive deficits were consistent with childhood MB survivors; irradiated mice displayed significantly worse working memory (Y-maze; $P = .009$) and exhibited spatial memory deficits (Barnes maze; $P = .029$). Receipt of PFB did not induce a more severe late-effect profile.

Conclusions. Our in vivo model mirrored childhood MB radiotherapy and recapitulated features observed in the late-effect profile of MB survivors. Our clinically relevant model will facilitate both the elucidation of novel/target mechanisms underpinning MB late effects and the development of novel interventions for their amelioration.

Key Points

1. In vivo model system recapitulates the radiotherapy dose, targeting, and developmental stage of childhood medulloblastoma.
2. Irradiated mice display MB-like deficits to neurocognitive and physical functioning, and frailty, independent of receipt of PFB dose.

Intensified therapies for children with cancer have led to 5-year survival rates approaching 85%[1]; however, this has come at a huge cost. Survivors have a high risk of developing life-changing or life-threatening late effects as a result of cancer treatment that affects the majority of physiological and psychosocial systems; examples include cardiotoxicity, renal

© The Author(s) 2024. Published by Oxford University Press, the Society for Neuro-Oncology and the European Association of Neuro-Oncology.
This is an Open Access article distributed under the terms of the Creative Commons Attribution License (https://creativecommons.org/licenses/by/4.0/), which permits unrestricted reuse, distribution, and reproduction in any medium, provided the original work is properly cited.

Importance of the Study

Eighty percent of children diagnosed with a brain tumor now become 5-year survivors, driven by the delivery of combination and intensified treatments. This exposure to intensive treatments leaves pediatric brain tumor survivors at increased risk of detrimental life-long late effects associated with their disease and its therapy. Medulloblastoma (MB) survivors are particularly burdened due to the routine use of curative high-dose regimens that include irradiation to the whole brain (CRT) plus an additional posterior fossa boost (PFB) dose. The development of effective pharmacological or other interventions aimed at prevention/treatment of therapy-associated deficits is a major clinical goal; however, a paucity of appropriate model systems hinders their development. Our highly disease-relevant model recapitulates childhood MB radiotherapy dose, targeting, and late-effect profile, at an equivalent developmental stage. Thus, our clinically relevant model provides an essential platform that will both facilitate the elucidation of novel/target mechanisms underpinning MB late effects and the development of novel neurointerventional strategies.

toxicity, ototoxicity, endocrine impairment, subsequent malignancies, neurocognitive deficits, impaired neuromuscular function, and accelerated aging.[2–6]

Cranial radiotherapy (CRT), the mainstay of pediatric brain tumor treatment in non-infants, is a causative factor in lasting neurocognitive deficits, with survivors suffering intellectual disability, low levels of academic attainment, poor psychosocial satisfaction, and reduced independence in adulthood.[7–9] Many survivors experience impaired physical functioning,[10] and neurological difficulties such as ataxia and co-ordination disorders, as well as reduced fine motor skills.[11] While these deficits present and persist in the years following treatment, others have a longer latency; adult survivors of childhood brain tumors develop numerous co-morbidities[12,13] and become more frail over their life course.[14]

Medulloblastoma (MB), the most common malignant pediatric brain tumor, is typically treated with high doses of craniospinal irradiation (CSI) including CRT (up to 36 Gy) with a posterior fossa boost dose (PFB; total dose up to 54 Gy).[15] CSI is omitted from treatment protocols for the very youngest patients due to its intolerable toxicity and late-effect profile in this age group and is reserved for children aged over either 3 or 5 years, depending on national treatment philosophies. High-dose CRT promotes the greatest intellectual impairment; the mean loss of IQ points is between 2.5 and 3.9 per year,[16–18] reaching a plateau of impairment around 2 standard deviations below average. 70%–90% of this group demonstrate a significant impairment in global intellectual functioning; many survivors experience attention deficits, slower processing speed, and impaired working memory,[11,19–21] which are in turn strongly correlated with decreased quality of life.[22–25]

There is a critical need for the development of interventions to prevent or ameliorate the MB late effects that burden survivors throughout their adolescent and adult life.[12,13] However, the development of such interventions is hindered by a lack of suitable experimental model systems. Previous in vivo cranial irradiation studies have typically failed to fully model pediatric brain tumor regimens (Supplementary Table 1). Many have been limited by a common tradeoff, which was either the use of clinically relevant radiotherapy doses in adult mice[26–32] or sub-relevant doses in juvenile mice.[33–38] Furthermore, traditional approaches did not allow for the delivery of targeted cranial irradiation, and instead typically employed whole-head irradiation, incorporating vulnerable structures such as the ears, eyes, and mouth in the radiation field,[27,33,39–42] resulting in high levels of acute toxicity with little clinical relevance.[43,44] Moreover, non-targeted radiation approaches are not able to deliver radiation specifically to substructures of the brain, and therefore cannot recapitulate the PFB commonly used in MB radiotherapy regimens. Previous studies have also typically focused solely on neurocognition to the exclusion of other facets of the late-effect profile, and have rarely characterized models beyond 6 months post-irradiation, therefore failing to describe the chronic burden over the life course.[27,28,41,45–47] To address these limitations, we developed a novel in vivo model through the combination of the delivery of MB-like fractionated high-dose radiotherapy to juvenile mice, to mirror those MB treatment paradigms that result in the greatest risk of severe late-effects. We performed longitudinal assessments across the life course up to human-equivalent middle age, to model the long-term burden suffered by survivors of childhood brain tumors.

Materials and Methods

Mice

Juvenile male C57BL/6J mice ($n = 36$) were purchased from Charles River post-weaning (aged 21 postnatal days) and maintained in groups of 3 littermates in individually ventilated cages. Cages contained sawdust, paper bedding, and environmental enrichment. Mice were housed at 20 ± 2 °C under a 12-hour light/12-hour dark photoperiod. They received standard rodent-pelleted chow ad libitum (Special Diets Services, Witham, UK). Age (approximate postnatal days; ~PND) was calculated using the mean age at the start of each procedure. Human-equivalent life stage details are provided in Supplementary Table 2. At the end of the study (~PND 394), mice were humanely culled via cervical dislocation. The work was licensed by the UK Home Office (PBDAFDFB0 and P67C4EBE4) and complied with the guiding principles for the care and use of laboratory animals. Ethical approval was granted by Newcastle University Animal Welfare and Ethics Review Body.

Table 1. Small Animal Radiation Research Platform Irradiation Regimen

Group	Radiation dose	Radiation schedule	Equivalent radiation dose in 2 Gy fractions (EQD2)
CRT only	Whole brain: 10F × 3 Gy (30 Gy)	5 days per week for 2 weeks	Whole-brain: 37.5 Gy
CRT + PFB	Posterior fossa only: 3F × 3 Gy (9 Gy) Whole brain: 10F × 3 Gy (30 Gy)	3 consecutive days 5 days per week for 2 weeks	PF only: 11.25 Gy [48.75 total] Whole-brain: 37.5 Gy
Sham	*Did not receive radiation*		

Radiation dose and frequency for cranial-radiation (CRT) only, CRT with posterior fossa boost (CRT + PFB), and sham-irradiated control group (sham); $n = 12$ for each group. The total human-equivalent radiation dose per area is given in brackets. While < 2 Gy per fraction is typical for human MB radiotherapy regimens, regulatory limitations necessitated the delivery of 3 Gy per fraction in our model, resulting in an overall dose equivalent to 37.5 Gy EQD2. Anesthesia (isoflurane) was administered to all groups independent of receipt of CRT.

Cranial-Irradiation With PFB

We used the small animal radiation research platform (SARRP) to precisely deliver MB-like CRT with PFB via computerized tomography imaging guidance.[48] Irradiation was performed at Leeds University. Mice were randomly allocated into 3 treatment groups: cranial (whole-brain) irradiation ("CRT only," human-equivalent 37.5 Gy EQD2; $n = 12$), cranial-irradiation with an additional PFB ("CRT+PFB," human-equivalent 37.5 Gy EQD2 with 11.25 Gy EQD2 [48.75 Gy EQD2 to the posterior fossa]; $n = 12$) and a control group that did not receive any irradiation (sham, 0 Gy, $n = 12$). Doses were calculated with an equivalent dose in 2Gy fractions (EQD2) assuming an α/β ratio of 2. Irradiation was delivered at a dose rate of 3.66 Gy/min. For mice in the CRT-only group, treatment began on PND 35 and lasted for 10 days. For the CRT + PFB group, treatment commenced at PND 37 and required an additional 3 days of treatment (details are provided in Supplementary Figure 1). All mice ($n = 36$) including the sham group were anesthetized with isoflurane and placed into the SARRP, independent of receipt of radiation. A 10 × 10 mm collimator with arc from –60 to 60 °C was used to deliver both CRT and the high-dose boost to the posterior fossa. While MB patients receive CSI, here spinal cord irradiation was omitted to limit the development of acute toxicities arising from off-target radiation to the thoracic cavity. Beam angles were selected to avoid the oral cavity, olfactory bulbs, ear, and ear canal. Dose verification was carried out by end-to-end testing by NPL and Innovate UK. This was carried out using 10 × 10 mm and 5 × 5 collimators with both static and arc beams. Differences between alanine pellets and gafchromic film were calculated when exposed to a dose of 12 Gy in a mouse phantom model. The difference between the treatment planning system dose and the measured dose was approximately 5% for film and 3% for pellets. Radiation protocols for each treatment group are summarized in Table 1 and a detailed timeline is provided in Supplementary Figure 1.

Following recovery, mice were transferred to Newcastle University (~PND 63) for subsequent assessment, where assessors were blind to the allocation of radiation group. After acclimatization, mice received radiofrequency identification (RFID; IMI-500 Read Only Transponder), implanted subcutaneously under general anesthesia. Mice were longitudinally assessed for over one year (up to ~PND 394).

Frailty Assessment

Frailty assessment was carried out using the Rockwood-style FI as previously described.[49] Briefly, 30 parameters of frailty (summarized in Supplementary Table 3) were scored on a scale from 0 (no impairment) to 1 (severe impairment). Grip strength was measured using the BIO-GS3 (BIOSEB), and the mean of 3 attempts was calculated from the maximal peak force generated (grams, g) from the forepaws. Body weight, body temperature, and grip strength were scored according to degrees of standard deviation (S.D.) from the mean of age- and sex-matched controls (0: < 1SD; 0.3: 1SD–2SD; 0.7: 2SD–3SD; 1: ≥ 3SD). To minimize subjectivity, assessors ($n = 2$) were kept the same throughout and blind to the allocation of radiation group; however, some unavoidable visual indications of therapy receipt were present.

Physical Functioning Assessment

Grip strength.—Neuromuscular function was assessed using the Grip Strength Test (BIO-GS3, BIOSEB) on forepaws. Mice were lowered via the tail onto the device, and the maximal peak force was recorded (grams, g). The mean was calculated from 3 attempts.

Rotarod.—To assess balance, co-ordination, and endurance, mice were placed on the rotarod (Roto-Rod Series 8, IITC Life Science), which began to rotate at an initial speed of 4 rpm, and gradually accelerated by 7.2 rpm per minute.[50] Time on the rod (seconds) was recorded automatically when mice fell from the rotarod. Quiet, low-light conditions were used to minimize stress during testing. Mice were tested 3 times per day, for 2 consecutive days, with approximately 20-minute intervals between trials. The mean was calculated using scores across both days.

Neurocognitive Assessment

The Y-maze was used to assess working memory.[51] The maze consisted of 3 arms made of dark gray plastic; each arm was 40 cm long, 5 cm wide, and 10 cm high. Mice were placed in arm A and observed for 8 minutes; arm entry was manually recorded. Quiet, low-light conditions were used to minimize stress during testing. Spontaneous alternation

was defined as the frequency of a mouse entering a novel arm of the maze in 3 consecutive entries (eg, A-B-C), divided by the total arm entries, minus 2.

Learning, short- and long-term memory (LTM) was assessed using the Barnes maze (BM) as previously described.[52] The BM consisted of 20 holes, surrounded by visual cues (square, circle, cross, and triangle). The target hole contained an escape box underneath. Target hole allocation was randomly assigned across visual cues and treatment groups. The maze was thoroughly cleaned and rotated 90° between each mouse and trial to remove potential olfactory cues. Briefly, testing consisted of 4 steps. (1) Day 1: Initial acclimatization—the mouse was placed in an opaque holding chamber for 10 seconds, then gently guided to the target hole. The mouse stayed in the escape box for 2 minutes. (2) Day 1–4: Spatial acquisition (training period)—after 10 seconds in the holding chamber, the mouse attempted to locate the target hole for up to 3 minutes, after which the mouse remained in the escape box for 1 minute. This was repeated for 4 trials per day for 4 days, with approximately 25 minutes between trials for memory consolidation. (3) Day 5: Probe 1 (short-term memory [STM] test)—24 hours after the final day of spatial acquisition, the escape box was removed from the target hole and the mice explored the maze for 90 seconds. 4) Day 12: Probe 2 (LTM test)—7 days after probe 1, the escape box was removed from the target hole and the mice explored the maze for 90 seconds. No training/testing took place on days 6–11. primary latency (PL) was defined as the time taken to locate the target hole.

Statistical Analysis

Statistical analysis and data visualization were carried out using SPSS statistics (IBM, version 27) and R Studio (version 4.2.2). T-tests (independent and paired), linear regression, and ANOVA with post-hoc Tukey tests were used to compare group means between continuous variables. Significant associations were defined as having a $p < 0.05$. Where appropriate, the Benjamini-Hochberg procedure was used to correct for multiple tests. Kaplan–Meier curves with log-rank tests were used to visualize survival, and deaths not related to irradiation were right censored (details provided in Supplementary Table 4).

Results and Discussion

Development of a Clinically Relevant, High-Dose, Targeted Cranial-Irradiation Model of MB Treatment

While previous in vivo modeling studies each contain critical limitations (a summary is provided in Supplementary Table 1), ours is the only model to (1) deliver fractioned high-dose radiotherapy, (2) use juvenile mice, and (3) perform longitudinal and comprehensive long-term follow-up, making it optimally positioned for use in future interventional development.

Previous studies typically utilized traditional approaches to deliver radiation to the whole head, with lead shielded from the body.[26,27,39,53,54] Delivery via this modality renders non-target regions such as the mouth, ears, and eyes are in the radiation field. Consequently, whole-head irradiation comes with high levels of acute toxicity, (eg,. damage to the salivary gland, mouth ulceration, eye dryness, and weight loss).[43,44] Moreover, whole-head irradiation cannot deliver targeted radiation to specific brain regions, which prevents the delivery of a PFB dose. Thus, irradiation using these methodologies cannot fully recapitulate the dose and targeting used in MB regimens.

Childhood MB patients with high-risk disease typically receive 36 Gy CRT with 54 Gy to the posterior fossa; these high doses are associated with the most severe late effects and represent the greatest clinical need.[15,55] By utilizing a pre-clinical radiotherapy platform (SARRP) to deliver computerized tomography image-guided, arc-delivered, fractionated radiotherapy CRT (Supplementary Figure 1), we were able to deliver up to an equivalent of 48.75 Gy EQD2 to the posterior fossa, very close to the high-dose PFB used in medulloblastoma regiments.[56]

Radiotherapeutic insult to the brain results in substantial damage to healthy tissue, including damage to the vasculature and demyelination, resulting in impaired neurogenesis.[57] As significant brain development occurs in early childhood, young children are particularly vulnerable to the deleterious consequences of CRT in treating a brain tumor.[58] We delivered CRT to cohorts of young mice at ~PND 36, equivalent to the juvenile life stage in humans and peak stage of MB diagnosis.[15]

While previous studies have assessed the effects of cranial irradiation in young mice, often this is for a relatively short period.[35,38,46] We followed up with our mouse cohort for over a year (up to ~PND 394); longitudinal assessments of frailty, physical functioning (grip strength and rotarod), and neurocognition (Y maze and BM) were performed to determine their sensitivity to CRT, additional negative consequences of PFB, and the extent to which our model recapitulated MB late-effect severity and durability (Figure 1).

Our Human-Equivalent CRT Regimen was Well Tolerated, Acutely, and Mice Thrived Post-treatment

High-dose CRT was well tolerated; no animals died due to severe acute toxicity either during or immediately following irradiation (Figure 2A). Over the course of the experiment, 5 mice were culled (though not attributable to cranial irradiation; Supplementary Table 4). Following irradiation, mice thrived and continued to grow at the same rate as sham-irradiated controls, independent of receipt of PFB (Figure 2B, *P*-values shown in Supplementary Table 5), throughout the life course.

Outcomes for the CRT + PFB group were equivalent to the CRT group across the vast majority of measures ($n = 163/166$) of frailty, physical functioning, and neurocognition tested, indicating there was no additional impact of the PFB dose (Figure 2C and Supplementary Tables 6A–C). Previous studies have shown that the dose of cranial irradiation is the major driver of poor neuropsychological outcomes in children treated for posterior fossa tumours[55] and others have reported a selective vulnerability of specific neuro-anatomical

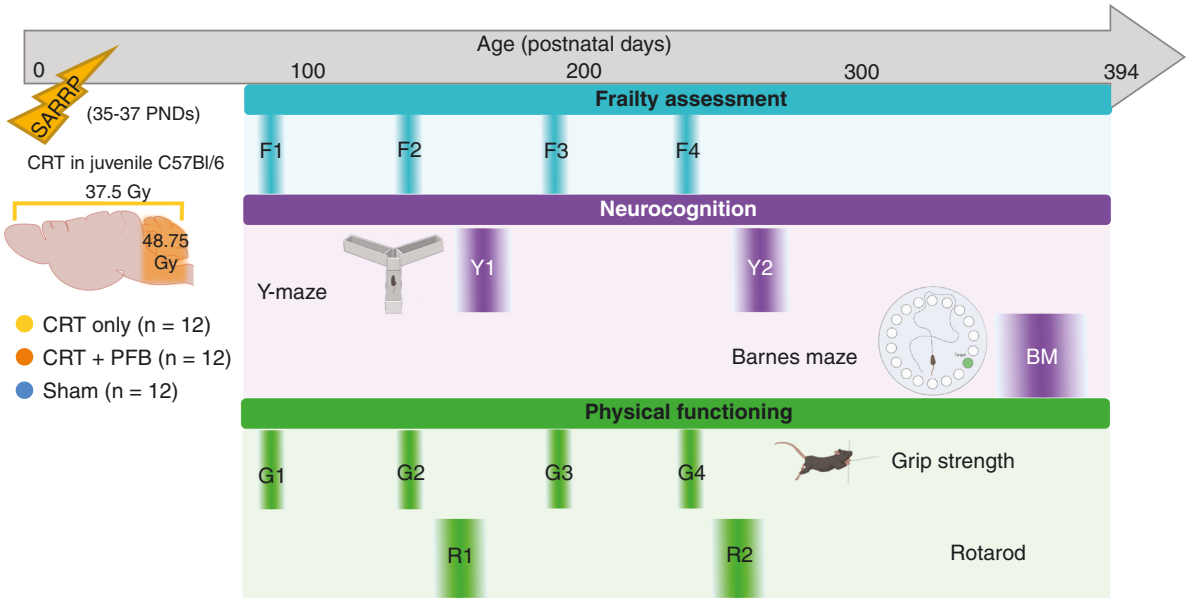

Figure 1. Schematic overview of the development of a clinically relevant, high-dose, targeted cranial-irradiation model. An overview of the study design. Juvenile C57Bl/6J mice (age 35–37 PNDs) received either CRT only (37.5 Gy human equivalent EQD2, $n = 12$), CRT + PFB (total dose of 48.75 Gy EQD2 to the posterior fossa, human-equivalent), or sham-irradiation ($n = 12$) via the small animal radiation research platform. Following irradiation, mice were subjected to longitudinal functional assessments. Assessments of frailty (frailty assessment at 4 timepoints [F1: ~PND 97, F2: ~PND 130, F3:~PND 191 and F4: ~PND 233]), neurocognition (Y-maze at 2 timepoints [Y1: ~PND 179 and Y2: ~PND 266] and Barnes maze [BM: ~PND 369]) and physical functioning (grip strength test at 4 timepoints [G1: ~PND 97, G2: ~PND 130, G3:~PND 191, and G4: ~PND 233] and RotaRod at 2 timepoints 1-2 [R1: ~PND 172 and R2: ~PND 249]) were carried out up to ~PND 394.

substructures to radiation injury, implicating the hippocampus and frontal- and temporal lobes in determining neurocognitive function, rather than the posterior fossa,[59–61] supporting our findings. Given that PFB is not associated with late-effect severity in our model, CRT only and CRT + PFB groups were subsequently combined for further analyses (henceforth collectively referred to as CRT) for comparison against sham-irradiated control mice.

CRT Drives Accelerated Frailty

Survivors of childhood MB experience increased frailty.[2,14,62] To assess whether CRT induced frailty in our model, we used the frailty index (FI), a measure used to provide an overall picture of general health and well-being in both mice and humans. The FI is also predictive of mortality across species.[63,64] The mouse FI exhibits key features of the FI used in humans and is therefore useful to quantify deficits relevant to human frailty and aging. The FI can be influenced by stress; however, in our study, this was minimized by acclimatization to handling prior to assessments and maintaining low levels of environmental noise. Frailty was assessed longitudinally (at ~PND 97, 130, 191, and 233; time points F1-4, respectively, Figure 3A) in our mice by scoring 30 age-related conditions on a scale of 0 (no frailty) to 1 (severe frailty), and calculating an average to produce a FI as described (Figure 3B).[49,65]

As expected, the FI for sham-irradiated mice increased along over the life course ($r^2 = 0.101$), representing a normal, healthy, aging profile.[64] However, CRT-induced accelerated frailty manifested early; at F1 (~PND 97; human-equivalent of early adulthood) FI was significantly higher in the CRT group than the sham-irradiated group ($P = .001$) and this persisted at all time points (F2, $P = .0001$; F3, $P = .007$ and F4, $P = .002$, Figure 3C). The rate of FI increase was significantly higher following CRT ($r^2 = 0.166$, $P < .0001$; Figure 3C). Vision loss, loss of fur color, piloerection, and high breathing rate were the most common FI parameters following CRT (Figure 3B; representative images are shown in Figure 3D and E). FI scores for distinct CRT only and CRT + PFB groups are summarized in supplementary figure 3.

Physical Functioning is Impaired Following Cranial-Irradiation

Physical functioning was assessed longitudinally using the grip strength test (at ~PND 97, 130, 191, and 233; time points G1-4, respectively) and rotarod (~PND 172 and 249; time points R1-2, respectively, Figure 4A). The grip strength of the CRT group was worse than sham-irradiated mice at all time points; this was significant at G2 (~PND 130, $P = .031$) and G4 (~PND 233, $P = .006$; Figure 4B). Both CRT and sham-irradiated groups exhibited a similar reduction in grip strength with age (Figure 4B).

To assess endurance, and neurological function related to balance and coordination, the mice were subjected to the rotarod at ~PND 172 and ~PND 249 (time points R1 and

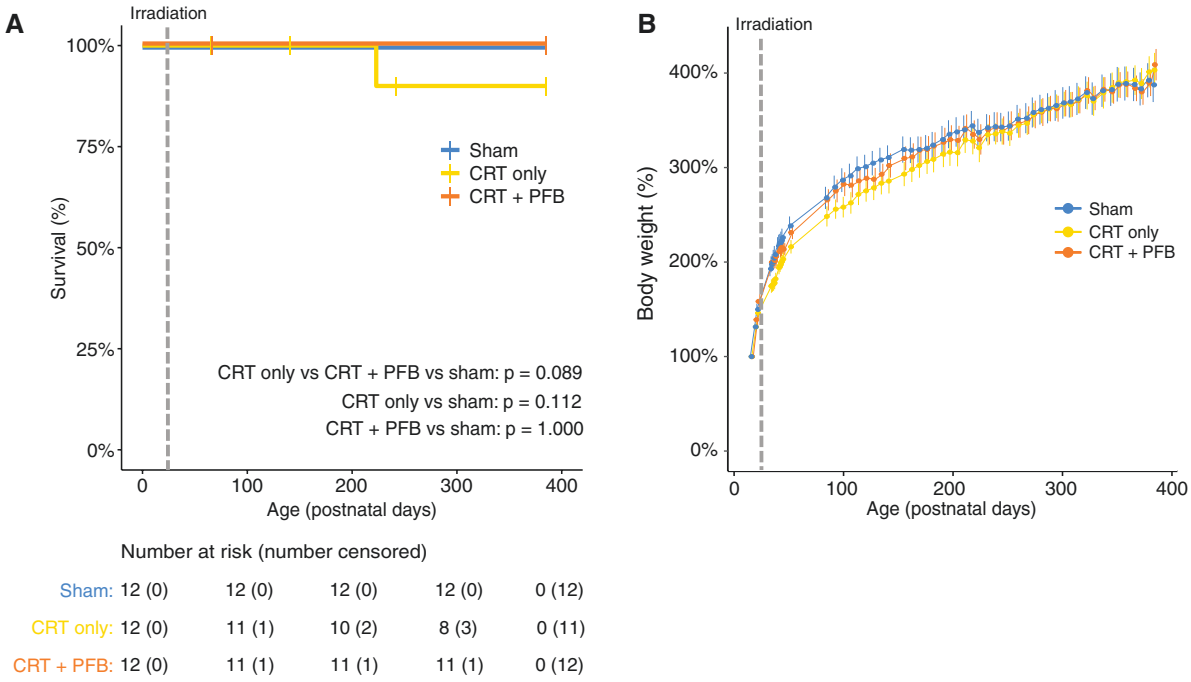

C

		Assessment	p-value (CRT only vs CRT + PFB)
Frailty		Frailty index	0.966 (F1) 1.000 (F2) 1.000 (F3) 1.000 (F4)
Physical functioning	Grip strength	Forelimb grip strength	0.719 (G1) 1.000 (G2) 0.929 (G3) 0.649 (G4)
	Rotarod	Time on the rod	0.719 (R1) 0.649 (R2)
Neurocognitive function	Y-maze	Spontaneous alternation	0.712 (Y1) 0.736 (Y2)
	Barnes maze	Spatial acquisition	1.000 (day 1) 1.000 (day 2) 1.000 (day 3) 0.736 (day 4)
		Probe 1: short-term memory	0.871 (day 5)
		Probe 2: long-term memory	1.000 (day 12)

Figure 2. Clinically relevant, high-dose, targeted cranial irradiation is well tolerated and mice thrive independent of posterior fossa boost. (A) Kaplan–Meier plot of survival by cranial-radiation group. Deaths not related to radiation were right-censored (details are provided in Supplementary Table 4) Receipt of cranial irradiation is depicted by the dotted line. (B) Mean body weight (+ SEM) was measured at least weekly over the course of the study, pre- and post-irradiation (*P*-values given in Supplementary Table 5). The receipt of cranial irradiation is depicted by the dotted line. (C) Summary of the performance of CRT only versus CRT + PFB groups. Adjusted *P*-values following independent *t*-tests between CRT only and CRT + PFB for all assessments of frailty, physical functioning (grip strength and Rotarod), and neurocognition (Y-maze and Barnes maze). A full comparison of all measures tested is provided in Supplementary Tables 6A–C).

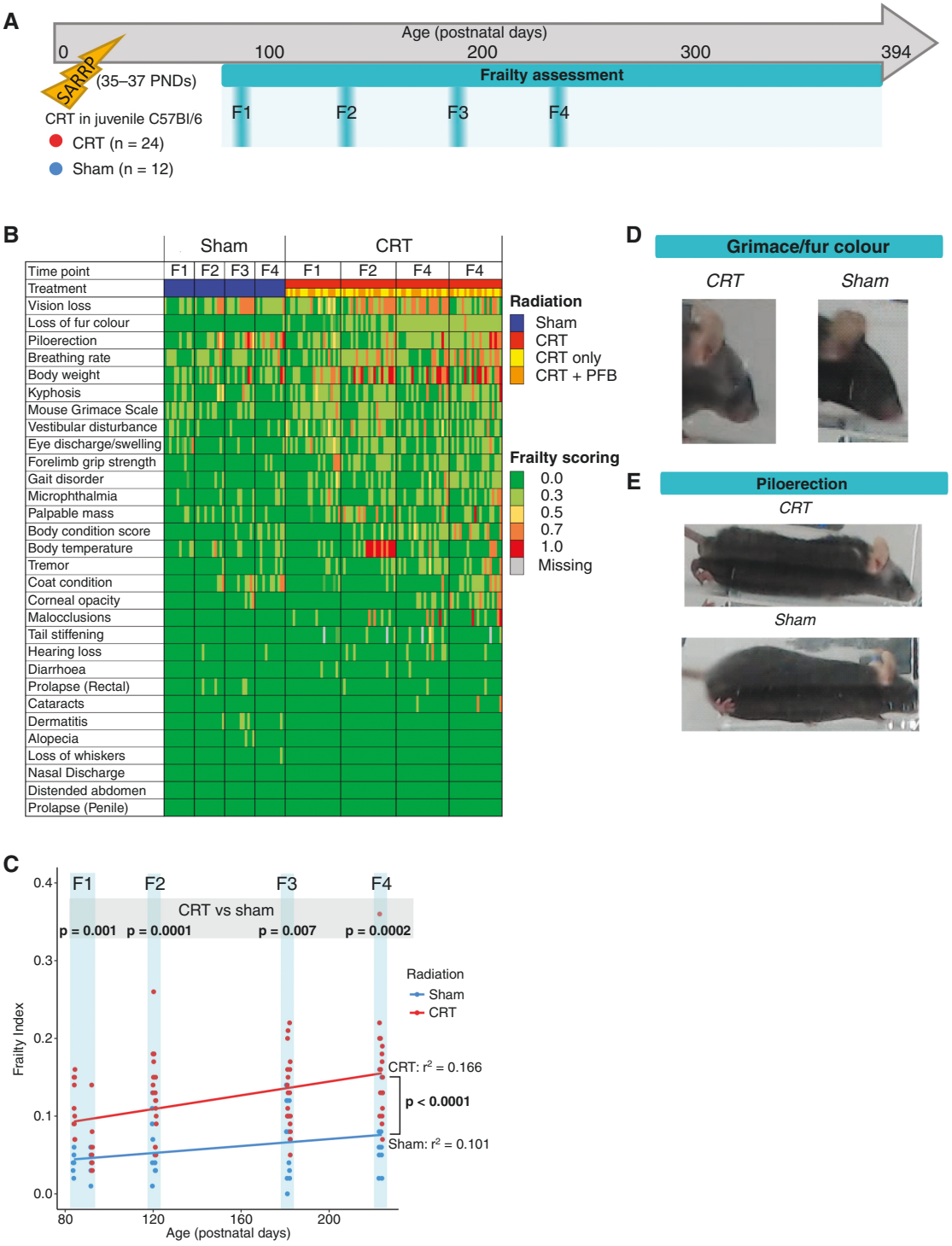

Figure 3. CRT drives accelerated development of frailty. (A) Timeline of longitudinal frailty assessment (F1: ~PND 97, F2: ~PND 130, F3: ~PND 191 and F4: ~PND 233). (B) Increased frailty scores following CRT. Heatmap showing frailty scores for all 30 frailty parameters following CRT or sham-irradiation. Individual frailty criteria were scored from 0 (no impairment, green) to 1 (severe frailty, red). Gray shading depicts missing data. Criterion are ordered from most commonly impaired to least commonly impaired (top to bottom). (C) CRT drives accelerated frailty. Mean frailty index (FI) following longitudinal frailty assessment at F1-4. Each point represents individual mice scores for CRT (red) and sham (blue) groups. Rate of frailty increase is higher in CRT-treated mice. Goodness of fit is denoted by r^2, *P*-value represents linear regression. Significant *P*-values ($P < .05$) are in bold text. Examples of commonly impaired features following CRT or sham-irradiation: Are grimace and loss of fur color following CRT (D) and piloerection following CRT (E).

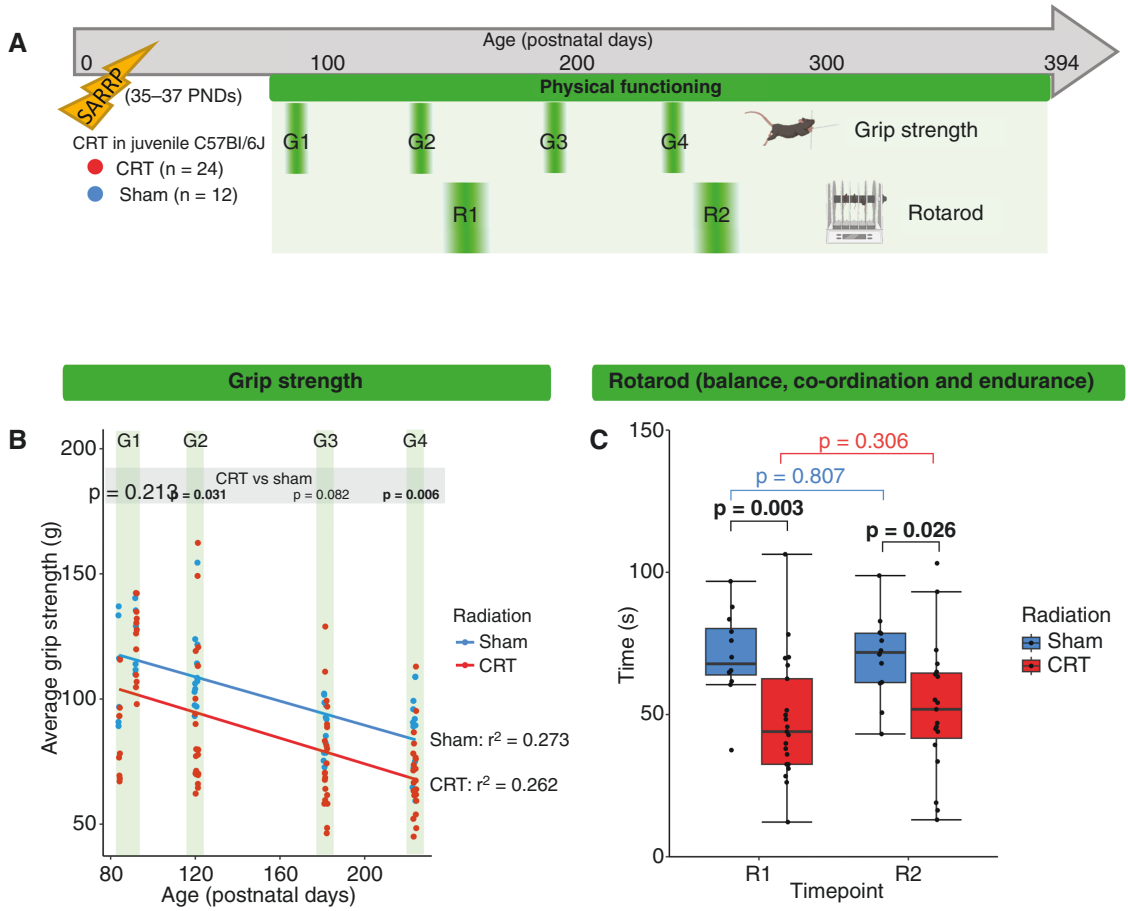

Figure 4. Physical functioning is impaired following cranial irradiation. (A) Timeline of longitudinal physical functioning assessment via the Grip Strength test (G1: ~PND 97, G2: ~PND 130, G3: ~PND 191 and G4: ~PND 233), and the RotaRod (R1: ~PND 172 and R2: ~PND 249). (B) Grip strength was poorer following CRT than sham-irradiation. Scatterplot showing longitudinal grip strength (mean of 3 attempts) at G1-4, where each point represents individual mice for CRT (red) and sham (blue) groups with linear regression fit lines. Significance was assessed via independent *t*-tests. Grip strength declines over time. Goodness of fit is denoted by r^2. (C) Balance, coordination, and endurance are worse following CRT than sham-irradiation. Average time on the Rotarod (mean time across 6 trials) at R1 and R2. Each point represents individual mice. Significance was assessed via independent *t*-tests (black [at both R1 and R2]) and paired *t*-tests (red [R1 vs. R2 in the CRT group] and blue [R1 vs. R2 in the sham-irradiation group]). Significant *P*-values ($P < .05$) are in bold text.

R2, respectively, Figure 4C). The CRT group were able to stay on the rotarod for significantly less time at both R1 (mean time 48.2 vs. 70.7 s, $P = .003$) and R2 (52.3 vs. 70.2 s, $P = .026$, Figure 4C). There was no age-associated decline in rotarod performance either group (Figure 4C). Physical functioning for distinct CRT only and CRT + PFB groups are summarized in Supplementary Figure 4.

The impaired physical functioning induced by CRT in our model mirrors that of childhood brain tumor survivors. Many survivors of childhood medulloblastoma experience below-average physical functioning, particularly within motor functioning, exhibiting difficulties such as ataxia and coordination disorders, as well as reduced fine motor skills.[10,11,66,67] While impaired physical functioning may be a result of the tumor itself, younger age at diagnosis and combination treatment approaches including surgical resection, and the use of chemoradiation have been identified as risk factors for neurological dysfunction.[67]

CRT Induces Deficits in Memory and Learning

Neurocognitive impairment is common in childhood MB survivors.[7,55] Neurocognitive function was assessed by the Y-maze (at ~PND 179 and ~PND 266; time points Y1 and Y2, respectively) and BM (at ~PND 369; time point BM), and brain weight was measured at the study endpoint (~PND 394; Figure 5A). CRT has been shown to reduce brain volume in both humans and mice,[68] which has also been linked to lower IQ scores in childhood MB survivors.[69] In our clinically relevant model, CRT significantly reduced brain size; brain weight was significantly less in the CRT group than in sham-irradiated controls (median weight: 0.46 and 0.50 g, respectively, $P < .001$; Figure 5B). CRT has been linked with decreased total brain volume, decreased white matter, and reduced neurogenesis; however, further investigation into the specific substructure vulnerabilities is required.[68,70]

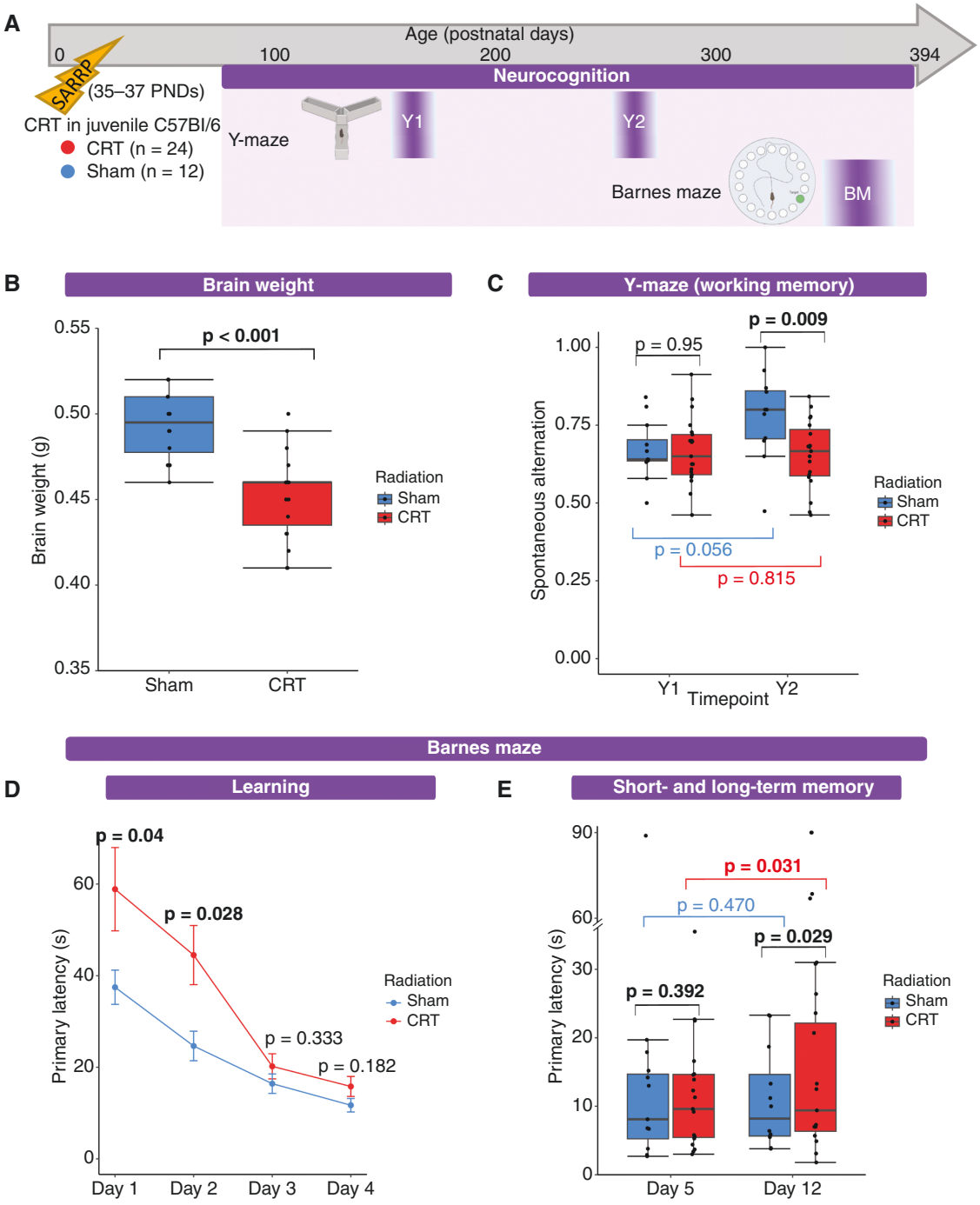

Figure 5. CRT induces deficits in memory and learning. (A) Timeline of longitudinal neurocognitive assessment using the Y-maze (working memory [spontaneous alternation] at Y1: ~PND 179 and Y2: ~PND 266) and the Barnes maze (learning, short- and long-term memory [BM: ~PND 369]). (B) Brain weight is lower following CRT than sham-irradiation. Brain weight (g) at ~PND 394, where each point represents individual mice. Significance was assessed via independent *t*-test. (C) Working memory is poorer following CRT than sham-irradiation. Spontaneous alternation at Y1 and Y2, where each point represents individual mice. Significance was assessed via independent *t*-test (black [at both Y1 and Y2]) and paired *t*-tests (red [Y1 vs. Y2 in CRT group] and blue [Y1 vs. Y2 in sham-irradiation group]). (D) Mice receiving CRT showed initial learning deficits but overcame this by day 3. Mean time is taken to find the target hole (primary latency, s) during spatial acquisition (days 1–4, 4 trials per day). Significance was assessed via independent *t*-tests. (E) Following CRT mice had deficits in long-term memory but not short-term memory. Primary latency on day 5 (short-term memory, STM) and day 12 (long-term memory, LTM), where each point represents individual mice. Significance was assessed via independent *t*-tests (black [at both days 5 and 12]) and paired *t*-tests (red [day 5 vs. 12 in CRT group] and blue [days 5 vs. 12 in sham-irradiation group]). Significant *P*-values ($P < .05$) are in bold text.

Neurocognitive function was assessed by the Y-maze (spontaneous alternation) and BM (PL). To assess working memory, mice were subjected to the Y-maze at ~PND 179 and ~PND 266 (time points Y1 and Y2, respectively, Figure 5A). CRT-induced working memory deficits (Figure 5C). While at Y1, early in the life course, the CRT group performed equivalently to the sham-irradiated group ($P = .95$), at Y2 (~PND 266; human-equivalent of early middle age) spontaneous alternation was significantly lower than sham-irradiated mice (mean spontaneous alternation: 0.655 vs. 0.781, $P = .009$, Figure 5C).

The ability to learn and retain learned behavior was assessed using the BM at ~PND 369 (human-equivalent of middle age; Figure 5A). Mice were trained for 4 days to locate the target hole (spatial acquisition [days 1–4], 4 trials per day); search strategy and time to locate the target hole improved following training (as shown in the pre- and post- training video [online resource 1 and 2]). Mice in the CRT group were initially slower to locate the target hole, presumably in part attributable to their worse physical functioning; at days 1 and 2 PL (time to locate target hole) was significantly higher in the CRT group than the sham-irradiated group (day 1 PL: 58.9 vs. 37.5 s [$P = .04$] and day 2 PL: 44.5 vs. 24.6 s [$P = .028$]). However, the CRT group performed equivalently to the sham-irradiated controls by the end of the spatial acquisition period; at day 3 and day 4 PL was equivalent in the CRT and sham-irradiated groups ($P = .333$ and $P = .182$, respectively, Figure 5D). Neurocognitive function for distinct CRT only and CRT + PFB groups are summarized in Supplementary Figure 5.

CRT-induced deficits in LTM but not STM (Figure 5E). A probe trial to assess STM function was performed one day after the spatial acquisition period (day 5). The CRT group showed no deficit in STM; PL was equivalent in CRT and sham-irradiated groups ($P = .392$). After 1 week, with no further training, a second probe trial was conducted to assess LTM (day 12). Despite having performed equally at day 5, mice that received CRT had impaired LTM and took significantly longer to locate the target hole; PL was significantly higher for the CRT group than sham-irradiated controls (day 12 mean PL 27.4 vs. 10.9 s, $P = .029$, Figure 5E). LTM impairment following CRT is analogous to human MB survivors, where the majority of survivors report memory problems.[71]

The neurocognitive deficits induced by CRT in our model mirror those seen in childhood MB survivors. Reduced attention, slower processing speeds, and poor working memory are characteristic of medulloblastoma patients who have received cranial radiotherapy.[21,69,72–77] Such domains support the acquisition of new learning such that childhood brain tumor survivors acquire new information at half the rate of unaffected peers.[16] This cranial radiation-induced neurocognitive impairment was mirrored within our in vivo model system; following CRT mice displayed reduced working memory and LTM function. 70%–90% of childhood brain tumor survivors demonstrate significant impairment in global intellectual functioning,[20,21] which is in turn strongly correlated with decreased quality of life.[22,23,25,77]

Receipt of CRT, particularly at a young age, results in a wide range of deleterious late effects that can drastically reduce the quality of life of childhood cancer survivors.[11,16,71,78] We conclude that delivery of childhood MB-equivalent radiotherapy is tolerated in vivo and following longitudinal, multi-parameter assessments, invokes an equivalent late-effect profile to the human disease. Thus, our clinically relevant model provides an essential platform that will both facilitate the elucidation of novel/target mechanisms underpinning MB late effects and the development of novel neuro-interventional strategies to alleviate the burden of surviving childhood MB.

Supplementary material

Supplementary material is available online at *Neuro-Oncology Advances* (https://academic.oup.com/noa).

Keywords

late-effects | medulloblastoma | modelling | radiotherapy | survivorship

Funding

This work was supported by Children's Cancer North, a Cancer Research UK Pioneer grant (C12161/A24009), ERC WIDESPREAD TEAMING grant (DLV-857524), UK SPINE Proof of Concept fund, H2020 WIDESPREAD (Project: 857524, MIA Portugal), University of Leeds Alumni Office "Brain cancer Research at Leeds" (Ref. 95501064), Cancer Research UK RadNet Leeds (Ref. A28832).

Authorship statement

All authors contributed to the study's conception and design. Material preparation, data collection, and analysis were performed by J.C., G.S., D.W., E.F., and M.S.. The first draft of the manuscript was written by J.C. and D.H. and all authors commented on previous versions of the manuscript. All authors read and approved the final manuscript.

Conflict of interest

The authors have no conflicts of interest to declare.

Ethics approval

The work was licensed by the UK Home Office (PBDAFDFB0 and P67C4EBE4) and complied with the guiding principles for the care and use of laboratory animals. Ethical approval was granted by Newcastle University Animal Welfare and Ethics Review Body.

Data availability

The data that support the study's findings are available from the corresponding author (DH) upon reasonable request.

Affiliations

Wolfson Childhood Cancer Research Centre, Newcastle University Centre for Cancer, Translational and Clinical Research Institute, Newcastle University, Newcastle upon Tyne, UK (J.C., D.W., M.S., R.S., S.C.C., D.H.); Leeds Institute of Medical Research, Wellcome Trust Brenner Building, St James's University Hospital, Beckett St, Leeds, UK (G.S., T.E., S.C.S.); Biosciences Institute, Campus for Ageing and Vitality, Newcastle University, Newcastle upon Tyne, UK (E.F., T.Z., S.M.)

References

1. Childhood Cancer Statistics. *England Annual report 2018*. UK: Public Health England.
2. Oeffinger KC, Mertens AC, Sklar CA, et al; Childhood Cancer Survivor Study. Chronic health conditions in adult survivors of childhood cancer. *N Engl J Med*. 2006;355(15):1572–1582.
3. MacDonald C, Theurer JA, Doyle PC. "Cured" but not "healed": The application of principles of palliative care to cancer survivorship. *Soc Sci Med*. 2021;275(1):113802.
4. Khalil J, Chaabi S, Oberlin O, et al. Medulloblastoma in childhood: What effects on neurocognitive functions? *Cancer Radiother*. 2019;23(5):370–377.
5. Limond JA, Bull KS, Calaminus G, et al; Brain Tumour Quality of Survival Group, International Society of Paediatric Oncology (Europe; SIOP-E). Quality of survival assessment in European childhood brain tumour trials, for children aged 5 years and over. *Eur J Paediatr Neurol*. 2015;19(2):202–210.
6. Edelstein K, Spiegler BJ, Fung S, et al. Early aging in adult survivors of childhood medulloblastoma: long-term neurocognitive, functional, and physical outcomes. *Neuro Oncol*. 2011;13(5):536–545.
7. Spiegler BJ, Bouffet E, Greenberg ML, Rutka JT, Mabbott DJ. Change in neurocognitive functioning after treatment with cranial radiation in childhood. *J Clin Oncol*. 2004;22(4):706–713.
8. Robbins M, Greene-Schloesser D, Peiffer A, et al. Radiation-induced brain injury: A review. *Front Oncol*. 2012;2(73):1–16.
9. Gupta T, Kalra B, Goswami S, et al. Neurocognitive function and survival in children with average-risk medulloblastoma treated with hyperfractionated radiation therapy alone: Long-term mature outcomes of a prospective study. *Neurooncol. Pract.*. 2022;9(3):236–245.
10. Piscione PJ, Bouffet E, Mabbott DJ, Shams I, Kulkarni AV. Physical functioning in pediatric survivors of childhood posterior fossa brain tumors. *Neuro-Oncology*. 2013;16(1):147–155.
11. Chevignard M, Câmara-Costa H, Doz F, Dellatolas G. Core deficits and quality of survival after childhood medulloblastoma: A review. *Neurooncol. Pract.*. 2017;4(2):82–97.
12. Salloum R, Chen Y, Yasui Y, et al. Late morbidity and mortality among medulloblastoma survivors diagnosed across three decades: A Report From the Childhood Cancer Survivor Study. *J Clin Oncol*. 2019;37(9):731–740.
13. Dixon SB, Liu Q, Chow EJ, et al. Specific causes of excess late mortality and association with modifiable risk factors among survivors of childhood cancer: A report from the Childhood Cancer Survivor Study cohort. *Lancet*. 2023;401(10386):1447–1457.
14. Ness KK, Krull KR, Jones KE, et al. Physiologic frailty as a sign of accelerated aging among adult survivors of childhood cancer: A report from the St Jude Lifetime cohort study. *J Clin Oncol*. 2013;31(36):4496–4503.
15. Ramaswamy V, Remke M, Bouffet E, et al. Risk stratification of childhood medulloblastoma in the molecular era: The current consensus. *Acta Neuropathol*. 2016;131(6):821–831.
16. Palmer SL, Goloubeva O, Reddick WE, et al. Patterns of intellectual development among survivors of pediatric medulloblastoma: A longitudinal analysis. *J Clin Oncol*. 2001;19(8):2302–2308.
17. Ris MD, Packer R, Goldwein J, Jones-Wallace D, Boyett JM. Intellectual outcome after reduced-dose radiation therapy plus adjuvant chemotherapy for medulloblastoma: A Children's Cancer Group study. *J Clin Oncol*. 2001;19(15):3470–3476.
18. Walter AW, Mulhern RK, Gajjar A, et al. Survival and neurodevelopmental outcome of young children with medulloblastoma at St Jude Children's Research Hospital. *J Clin Oncol*. 1999;17(12):3720–3728.
19. Pazzaglia S, Briganti G, Mancuso M, Saran A. Neurocognitive decline following radiotherapy: Mechanisms and therapeutic implications. *Cancers (Basel)*. 2020;12(1):146.
20. Dennis M, Spiegler BJ, Hetherington CR, Greenberg ML. Neuropsychological sequelae of the treatment of children with medulloblastoma. *J Neurooncol*. 1996;29(1):91–101.
21. Maddrey AM, Bergeron JA, Lombardo ER, et al. Neuropsychological performance and quality of life of 10 year survivors of childhood medulloblastoma. *J Neurooncol*. 2005;72(3):245–253.
22. Mitby PA, Robison LL, Whitton JA, et al; Childhood Cancer Survivor Study Steering Committee. Utilization of special education services and educational attainment among long-term survivors of childhood cancer: A report from the Childhood Cancer Survivor Study. *Cancer*. 2003;97(4):1115–1126.
23. Mabbott DJ, Spiegler BJ, Greenberg ML, et al. Serial evaluation of academic and behavioral outcome after treatment with cranial radiation in childhood. *J Clin Oncol*. 2005;23(10):2256–2263.
24. Mulhern R K, Butler R W. Neurocognitive sequelae of childhood cancers and their treatment. *Pediatr Rehabil*. 2009;7(1):1–14discussion 15.
25. Gurney JG, Krull KR, Kadan-Lottick N, et al. Social outcomes in the Childhood Cancer Survivor Study cohort. *J Clin Oncol*. 2009;27(14):2390–2395.
26. Ungvari Z, Tarantini S, Hertelendy P, et al. Cerebromicrovascular dysfunction predicts cognitive decline and gait abnormalities in a mouse model of whole brain irradiation-induced accelerated brain senescence. *Geroscience*. 2017;39(1):33–42.
27. Wong-Goodrich SJ, Pfau ML, Flores CT, et al. Voluntary running prevents progressive memory decline and increases adult hippocampal neurogenesis and growth factor expression after whole-brain irradiation. *Cancer Res*. 2010;70(22):9329–9338.
28. Suckert T, Beyreuther E, Müller J, et al. Late side effects in normal mouse brain tissue after proton irradiation. *Front Oncol*. 2021;10(1):598360.
29. Belcher EK, Sweet TB, Karaahmet B, et al. Cranial irradiation acutely and persistently impairs injury-induced microglial proliferation. *Brain Behav Immun Health*. 2020;4(1):100057.
30. Baumann BC, Benci JL, Santoiemma PP, et al. An integrated method for reproducible and accurate image-guided stereotactic cranial irradiation of brain tumors using the small animal radiation research platform. *Transl Oncol*. 2012;5(4):230–237.
31. Lazarini F, Mouthon M-A, Gheusi G, et al. Cellular and behavioral effects of cranial irradiation of the subventricular zone in adult mice. *PLoS One*. 2009;4(9):e7017.

32. Moravan MJ, Olschowka JA, Williams JP, O'Banion MK. Cranial irradiation leads to acute and persistent neuroinflammation with delayed increases in T-cell infiltration and CD11c expression in C57BL/6 mouse brain. *Radiat Res.* 2011;176(4):459–473.
33. Yuen N, Szulc-Lerch KU, Li Y-Q, et al. Metformin effects on brain development following cranial irradiation in a mouse model. *Neuro-Oncology.* 2021;23(9):1523–1536.
34. Rao AA, Ye H, Decker PA, Howe CL, Wetmore C. Therapeutic doses of cranial irradiation induce hippocampus-dependent cognitive deficits in young mice. *J Neurooncol.* 2011;105(2):191–198.
35. Ruddy RM, Derkach D, Dadwal P, Morshead CM. Cranial irradiation in juvenile mice leads to early and sustained defects in the stem and progenitor cell pools and late cognitive impairments. *Brain Res.* 2020;1727(1):146548.
36. Beera KG, Li YQ, Dazai J, et al. Altered brain morphology after focal radiation reveals impact of off-target effects: Implications for white matter development and neurogenesis. *Neuro Oncol.* 2018;20(6):788–798.
37. Sándor N, Walter FR, Bocsik A, et al. Low dose cranial irradiation-induced cerebrovascular damage is reversible in mice. *PLoS One.* 2014;9(11):e112397.
38. Casciati A, Dobos K, Antonelli F, et al. Age-related effects of X-ray irradiation on mouse hippocampus. *Oncotarget.* 2016;7(19):28040–28058.
39. Tang TT, Zawaski JA, Kesler SR, et al. A comprehensive preclinical assessment of late-term imaging markers of radiation-induced brain injury. *Neurooncol. Adv..* 2019;1(1):vdz012.
40. Yabluchanskiy A, Tarantini S, Balasubramanian P, et al. Pharmacological or genetic depletion of senescent astrocytes prevents whole brain irradiation-induced impairment of neurovascular coupling responses protecting cognitive function in mice. *Geroscience.* 2020;42(2):409–428.
41. Zanni G, Goto S, Fragopoulou AF, et al. Lithium treatment reverses irradiation-induced changes in rodent neural progenitors and rescues cognition. *Mol Psychiatry.* 2021;26(1):322–340.
42. Yousuf S, Brat DJ, Shu H-K, et al. Progesterone improves neurocognitive outcomes following therapeutic cranial irradiation in mice. *Horm Behav.* 2017;96(1):21–30.
43. Brook I. Late side effects of radiation treatment for head and neck cancer. *Radiat Oncol J.* 2020;38(2):84–92.
44. Jham BC, da Silva Freire AR. Oral complications of radiotherapy in the head and neck. *Braz J Otorhinolaryngol.* 2006;72(5):704–708.
45. Zhang D, Zhou W, Lam TT, et al. Radiation induces age-dependent deficits in cortical synaptic plasticity. *Neuro Oncol.* 2018;20(9):1207–1214.
46. Zhou K, Xie C, Wickström M, et al. Lithium protects hippocampal progenitors, cognitive performance and hypothalamus–pituitary function after irradiation to the juvenile rat brain. *Oncotarget.* 2017;8(21):34111–34127.
47. Tomé WA, Gökhan S, Brodin NP, et al. A mouse model replicating hippocampal sparing cranial irradiation in humans: A tool for identifying new strategies to limit neurocognitive decline. *Sci Rep.* 2015;5(1):14384.
48. Wong J, Armour E, Kazanzides P, et al. High-resolution, small animal radiation research platform with x-ray tomographic guidance capabilities. *Int J Radiat Oncol Biol Phys.* 2008;71(5):1591–1599.
49. Fielder E, Weigand M, Agneessens J, et al. Sublethal whole-body irradiation causes progressive premature frailty in mice. *Mech Ageing Dev.* 2019;180(1):63–69.
50. Graber TG, Ferguson-Stegall L, Kim J-H, Thompson LV. C57BL/6 neuromuscular healthspan scoring system. *J Gerontol A Biol Sci Med Sci.* 2013;68(11):1326–1336.
51. Maurice T, Hiramatsu M, Itoh J, et al. Behavioral evidence for a modulating role of σ ligands in memory processes. I. Attenuation of dizocilpine (MK-801)-induced amnesia. *Brain Res.* 1994;647(1):44–56.
52. Fielder E, Tweedy C, Wilson C, et al. Anti-inflammatory treatment rescues memory deficits during aging in nfkb1(-/-) mice. *Aging Cell.* 2020;19(10):e13188.
53. de Guzman AE, Ahmed M, Li YQ, Wong CS, Nieman BJ. p53 loss mitigates early volume deficits in the brains of irradiated young mice. *Int J Radiat Oncol Biol Phys.* 2019;103(2):511–520.
54. Rodgers SP, Zawaski JA, Sahnoune I, Leasure JL, Gaber MW. Radiation-induced growth retardation and microstructural and metabolite abnormalities in the hippocampus. *Neural Plast.* 2016;2016(1):3259621.
55. Grill J, Renaux VK, Bulteau C, et al. Long-term intellectual outcome in children with posterior fossa tumors according to radiation doses and volumes. *Int J Radiat Oncol Biol Phys.* 1999;45(1):137–145.
56. Northcott PA, Robinson GW, Kratz CP, et al. Medulloblastoma. *Nat Rev Dis Primers.* 2019;5(1):11.
57. Belka C, Budach W, Kortmann RD, Bamberg M. Radiation induced CNS toxicity--molecular and cellular mechanisms. *Br J Cancer.* 2001;85(9):1233–1239.
58. Greene-Schloesser D, Robbins ME, Peiffer AM, et al. Radiation-induced brain injury: A review. *Front Oncol.* 2012;2(1):73.
59. Acharya S, Guo Y, Patni T, et al. Association between brain substructure dose and cognitive outcomes in children with medulloblastoma treated on SJMB03: A step toward substructure-informed planning. *J Clin Oncol.* 2022;40(1):83–95.
60. Seibert TM, Karunamuni R, Kaifi S, et al. Cerebral cortex regions selectively vulnerable to radiation dose-dependent atrophy. *Int J Radiat Oncol Biol Phys.* 2017;97(5):910–918.
61. Armstrong GT, Jain N, Liu W, et al. Region-specific radiotherapy and neuropsychological outcomes in adult survivors of childhood CNS malignancies. *Neuro Oncol.* 2010;12(11):1173–1186.
62. Diller L, Chow EJ, Gurney JG, et al. Chronic disease in the Childhood Cancer Survivor Study cohort: A review of published findings. *J Clin Oncol.* 2009;27(14):2339–2355.
63. Rockwood K, Blodgett JM, Theou O, et al. A frailty index based on deficit accumulation quantifies mortality risk in humans and in mice. *Sci Rep.* 2017;7(1):43068.
64. Whitehead JC, Hildebrand BA, Sun M, et al. A clinical frailty index in aging mice: Comparisons with frailty index data in humans. *J Gerontol A Biol Sci Med Sci.* 2014;69(6):621–632.
65. Fielder E, Wan T, Alimohammadiha G, et al. Short senolytic or senostatic interventions rescue progression of radiation-induced frailty and premature ageing in mice. *Elife.* 2022;11(1):e75492.
66. Varedi M, Lu L, Phillips NS, et al. Balance impairment in survivors of pediatric brain cancers: Risk factors and associated physical limitations. *J Cancer Surviv.* 2021;15(2):311–324.
67. Gielis M, Dirix V, Vanderhenst E, et al. Better detection of reduced motor functioning in brain tumor survivors based on objective motor assessments: An incentive for improved standardized follow-up. *Eur J Pediatr.* 2022;181(7):2731–2740.
68. Nieman BJ, de Guzman AE, Gazdzinski LM, et al. White and gray matter abnormalities after cranial radiation in children and mice. *Int J Radiat Oncol Biol Phys.* 2015;93(4):882–891.
69. Mulhern RK, Reddick WE, Palmer SL, et al. Neurocognitive deficits in medulloblastoma survivors and white matter loss. *Ann Neurol.* 1999;46(6):834–841.
70. Filley CM, Kleinschmidt-DeMasters BK. Toxic leukoencephalopathy. *N Engl J Med.* 2001;345(6):425–432.
71. King AA, Seidel K, Di C, et al. Long-term neurologic health and psychosocial function of adult survivors of childhood medulloblastoma/PNET: A report from the Childhood Cancer Survivor Study. *Neuro Oncol.* 2017;19(5):689–698.

72. Anderson V, Godber T, Smibert E, Ekert H. Neurobehavioural sequelae following cranial irradiation and chemotherapy in children: An analysis of risk factors. *Pediatr Rehabil*. 1997;1(2):63–76.
73. Brière ME, Scott JG, McNall-Knapp RY, Adams RL. Cognitive outcome in pediatric brain tumor survivors: Delayed attention deficit at long-term follow-up. *Pediatr Blood Cancer*. 2008;50(2):337–340.
74. Hardy KK, Willard VW, Gioia A, Sharkey C, Walsh KS. Attention-mediated neurocognitive profiles in survivors of pediatric brain tumors: comparison to children with neurodevelopmental ADHD. *Neuro Oncol*. 2018;20(5):705–715.
75. Kahalley LS, Conklin HM, Tyc VL, et al. Slower processing speed after treatment for pediatric brain tumor and acute lymphoblastic leukemia. *Psychooncology*. 2013;22(9):1979–1986.
76. Câmara-Costa H, Resch A, Kieffer V, et al; Quality of Survival Working Group of the Brain Tumour Group of SIOP-Europe. Neuropsychological outcome of children treated for standard risk medulloblastoma in the PNET4 European randomized controlled trial of hyperfractionated versus standard radiation therapy and maintenance chemotherapy. *Int J Radiat Oncol Biol Phys*. 2015;92(5):978–985.
77. Mulhern RK, Butler RW. Neurocognitive sequelae of childhood cancers and their treatment. *Pediatr Rehabil*. 2004;7(1):1–14; discussion 15.
78. Palmer SL, Armstrong C, Onar-Thomas A, et al. Processing speed, attention, and working memory after treatment for medulloblastoma: An international, prospective, and longitudinal study. *J Clin Oncol*. 2013;31(28):3494–3500.